



## *D2.2: Final concurrent design report*

July 2021

PIPISTREL  
VERTICAL  
SOLUTIONS



POLITECNICO  
MILANO 1863

TU Delft

Delft University of Technology



This project has received funding from the Clean Sky 2 Joint Undertaking (JU) under grant agreement No 864901. The JU receives support from the European Union's Horizon 2020 research and innovation programme and the Clean Sky 2 JU members other than the Union

  
Clean Sky 2



## Document Control Sheet

Project Number	864901
Project Acronym	UNIFIER19
Project Full Title	Community Friendly Miniliner 19
Project URL	<a href="https://www.unifier19.eu/">https://www.unifier19.eu/</a>
Work Package	WP2
Document URL	<a href="https://pipistrel.sharepoint.com/sites/UNIFIER19">https://pipistrel.sharepoint.com/sites/UNIFIER19</a>
Issue Date	12.7.2021
Author(s)	David Eržen, Pipistrel Vertical Solutions Lorenzo Trainelli, Politecnico di Milano Carlo E. D Riboldi, Politecnico di Milano Alberto Rolando, Politecnico di Milano Francesco Salucci, Politecnico di Milano Fabrizio Oliviero, Technical University Delft Jernej Pirnar, Pipistrel Vertical Solutions Thomas Koopman, Pipistrel Vertical Solutions Andres Žnidar, Pipistrel Vertical Solutions Matej Andrejašič, Pipistrel Vertical Solutions Rok Lapuh, Pipistrel Vertical Solutions Johannes Soikkeli, Pipistrel Vertical Solutions Gregor Čretnik, Pipistrel Vertical Solutions
Nature	Document
Dissemination Level	Open

## Executive Summary

The present document constitutes deliverable D2.1 "Final concurrent design report - Complete report" resulting from the activities carried out in the WP2 "Initial concurrent design competition" of the UNIFIER19 - Community Friendly Miniliner project, funded by the Clean Sky JTI under GA no. 864901.

The document set the design framework for the UNIFIER19 design activities by

- discussing results of the market analysis for miniliner and microfeeder case, which form the basis of Top-Level Aircraft Requirements, defining technology assumptions for next 15 years and elaborating aircraft configurations down-selection methodology;
- outlining Conceptual design tools developed by POLIMI, PVS and TUDELFT, as well as introducing noise assessment methodology and marketability metrics;
- describing 4 preliminary candidate solutions, their design, sensitivity analysis and cross-check analysis;
- describing candidates' noise and marketability assessment as well as gaseous emissions assessment for conventionally powered reference aircraft;
- substantiating final candidate selection for further analysis in WP3.

A brochure, dedicated to the general public, is annexed, to explain in eye-catching way these innovative liquid hydrogen hybrid electric configurations.

# Table of contents

<b>1</b>	<b>Introduction</b>	<b>13</b>
1.1	Market analysis findings	13
1.1.1	Analysis of the potential market for microfeeder service: recap from D1.1	13
1.1.2	Intercity liner service analysis	14
1.2	Top Level Aircraft Requirements	19
1.2.1	Power generation system configuration	20
1.2.2	Technology assumptions	21
1.3	Aircraft configurations down-selection methodology	21
1.3.1	Politecnico di Milano activities	21
1.3.2	TUDELFT	30
<b>2</b>	<b>Conceptual design methods</b>	<b>36</b>
2.1	POLIMI	36
2.1.1	Outline of Hyperion preliminary sizing methodology	36
2.1.2	Aircraft configuration and detailed sizing in Argos	38
2.1.3	Conceptual design with Titan	40
2.2	PIPISTREL VERTICAL SOLUTIONS	41
2.2.1	Introduction	41
	Preliminary sizing loop description – pConcept	42
2.2.2		42
2.2.3	Main/DEP, Prop/Duct	44
2.2.4	Mass Breakdown	49
2.2.5	Packaging and W&B procedure	50
2.2.6	Aerodynamic analysis	51
2.2.7	Cooling drag assessment	54
2.2.8	Polars build-up	54
2.2.9	Mission Analysis	56
2.2.10	Noise assessment	59
2.2.11	Marketability – Life-cycle cost estimation	62
2.3	TUDELFT	64
<b>3</b>	<b>Preliminary candidate solutions</b>	<b>70</b>
3.1	Framework	70
3.1.1	POLIMI candidates	70
3.1.2	PVS candidate	71
3.1.3	Final candidate set	71
3.2	Configuration C3	71
6.2.1	General description	72
6.2.2	Sensitivity analysis	76
	Cross-check & assessment	83
3.2.1		83
3.3	Configuration C7A	87
3.3.1	General description	87
3.3.2	Sensitivity analysis	93
	Cross-check & assessment	97
3.3.3		97
3.4	Configuration C2	112
3.4.1	General description	113

3.4.2	<i>Sensitivity analysis</i> .....	118
	<i>Cross-check &amp; assessment</i> .....	122
3.4.3	.....	122
3.5	Configuration PVS1 .....	128
3.5.1	<i>General description</i> .....	128
3.5.2	<i>Sensitivity analysis</i> .....	137
3.5.3	<i>Cross-check &amp; assessment</i> .....	140
3.6	FlightStream General Discussion .....	143
<b>4</b>	<b>Noise assessment</b> .....	<b>146</b>
4.1	Approach .....	146
4.2	Example application.....	146
4.3	Candidate analysis and comparison .....	149
<b>5</b>	<b>Cost and marketability analysis</b> .....	<b>152</b>
5.1	Modifications after WP1.....	152
5.1.1	<i>Powertrain costs</i> .....	152
5.1.2	<i>Distributed Electric Propulsion (DEP)</i> .....	153
5.1.3	<i>Materials distribution</i> .....	153
5.1.4	<i>Economy parameters</i> .....	154
5.2	Results.....	154
5.2.1	<i>Cost comparison</i> .....	154
5.2.2	<i>Sensitivity studies</i> .....	157
<b>6</b>	<b>Gaseous Emissions</b> .....	<b>163</b>
6.1	Approach .....	163
6.2	Reference aircraft .....	163
6.3	Gaseous emission estimation methodology and results.....	167
<b>7</b>	<b>Final selection</b> .....	<b>168</b>
<b>8</b>	<b>Reply to M12 Assessment Report Comments and Recommendations</b> .....	<b>170</b>
<b>9</b>	<b>References</b> .....	<b>171</b>
<b>10</b>	<b>Brochure</b> .....	<b>172</b>

## List of Figures

Figure 1 Employed people commuting to another region within their country in Europe in 2018.....	14
Figure 2 Example of intercity service between Lucca and Milan (Bresso airport) .....	15
Figure 3 Potential demand estimation for an intercity service in Italy. Variation for different cruising speed values, considering runways longer than 800 m. ....	16
Figure 4 Potential demand estimation for an intercity service in Italy. Variation with respect to runway length, considering a cruising speed of 200 KTAS. ....	16
Figure 5 Distribution of towns and SAs involved in an intercity service in Italy with a range of 350 km, runways longer than 800 m and 200 KTAS cruising speed.....	17
Figure 6 Miniliner travel time and road time for all the town pairs, including trip constraints, for a choice of constraining values $t_{ref}$ and $k$ .....	18
Figure 7 Potential commuters with respect to overall airport time and time gain parameter. ....	19
Figure 8 Aircraft architecture option tree diagram .....	23
Figure 9 Serial hybrid-electric powertrain scheme.....	37
Figure 10 Flowchart of the Hyperion preliminary sizing tool .....	38
Figure 11 Flowchart of the main blocks of Argos .....	39
Figure 12 Flowchart of the main blocks of Titan .....	40
Figure 13 Pipistrel Class II Conceptual Design Loop .....	41
Figure 14 pConcept workflow diagram .....	43
Figure 15: Comparison between Hyperion and pConcept for C7A aircraft. Other aircraft have similar differences. ....	44
Figure 16 Propeller/wing configuration for augmented lift estimation .....	45
Figure 17 PVS1 DEP propeller geometry .....	45
Figure 18 PVS1 DEP propeller efficiency over velocity interval.....	46
Figure 19 C7A main propeller geometry .....	47
Figure 20 C7A main propeller efficiency.....	47
Figure 21 PVS1 ducted fan geometry (left: one blade; mid: rotor top view; right: duct, hub and blade cross section).....	48
Figure 22 PVS1 ducted fan efficiency in climb and cruise power settings .....	48
Figure 23 3D model of PVS1 aircraft candidate in OpenVSP .....	50
Figure 24 Flow chart of the aerodynamic analysis methodology.....	51
Figure 25 Aero-propulsive interaction within FlightStream. The impact of the propeller wake over the wing can be seen. ....	53
Figure 26: Description of polar curves used in the mission analysis. ....	54
Figure 27: First step of modification of FlightStream polars. ....	55
Figure 28: Relative correction of CL(AoA) and CD(AoA) curves (reference configuration) obtained with FlightStream based on the verification done with NUMECA CFD simulations. ....	56
Figure 29: Comparison of baseline and modified polars for C7A candidate (left), and modified polars and POLIMI polars (right).....	56
Figure 30: Prescribed mission, altitude vs time of the aircraft. ....	58
Figure 31: A/C speed comparison during the mission.....	59
Figure 32: Directivity of thickness, loading, and broadband noise. ....	60
Figure 33: A-, B-, and C-weighting. (Ginsberg, 2018) .....	61
Figure 34: TUD CS23-FC Class I estimation procedure .....	65

Figure 35: reference aircraft mass breakdown .....	66
Figure 36: powertrain components of the FC powertrain.....	67
Figure 37: Power breakdown for a preliminary study case.....	68
Figure 38: Output from the sizing procedure .....	69
Figure 43 : Candidate C3 top, side, front and ISO view.....	72
Figure 44 Sizing matrix plot for candidate C3.....	75
Figure 45 Mass breakdown of candidate C3. ....	75
Figure 42 Battery and tank level during the sizing mission for candidate C3. ....	76
Figure 47 Power utilization during the sizing mission for candidate C3. ....	76
Figure 48 Sensitivity of MTOM vs battery specific power.....	79
Figure 49 Sensitivity of gTOT vs cruise speed.....	79
Figure 46 f_tot versus battery specific power.....	79
Figure 47 MTOM versus battery specific power.....	79
Figure 48 f_tot versus fuel-cells specific power .....	80
Figure 49 MTOM versus fuel-cells specific power .....	80
Figure 50 f_tot versus CD0.....	81
Figure 51 MTOM versus CD0 .....	81
Figure 52 f_tot versus battery specific energy .....	82
Figure 53 MTOM versus battery specific energy.....	82
Figure 54 The geometry of the POLIMI C3 candidate used in the aerodynamic analysis.....	83
Figure 59 The lift coefficient of the POLIMI C3 candidate.....	84
Figure 60 The lift-to-drag coefficient of the POLIMI C3 candidate. ....	85
Figure 61 The pitching moment coefficient of the POLIMI C3 candidate. ....	85
Figure 58: Shaft power requirement comparison for C3 candidate between PVS and POLIMI analysis....	87
Figure 63 Candidate C7A top, side, front and ISO view.....	88
Figure 64 Sizing matrix plot for candidate C7A. ....	91
Figure 65 Mass breakdown of candidate C7A. ....	91
Figure 66 Battery and tank level during the sizing mission for candidate C7A.....	92
Figure 67 Power utilization during the sizing mission for candidate C7A. ....	92
Figure 64 f_tot versus battery specific power.....	93
Figure 65 MTOM versus battery specific power.....	94
Figure 66 f_tot versus fuel-cells specific power .....	94
Figure 67 MTOM versus fuel-cells specific power .....	95
Figure 68 f_tot versus CD0.....	95
Figure 69 MTOM versus CD0 .....	96
Figure 70 f_tot versus battery specific energy .....	96
Figure 71 MTOM versus battery specific energy.....	97
Figure 76 Sensitivity of MTOM vs battery specific power.....	97
Figure 77 Sensitivity of gTOT vs cruise speed.....	97
Figure 74 The geometry of the POLIMI C7A candidate used in the aerodynamic analysis.....	98
Figure 75 The fowler flap of the POLIMIC7A1 candidate. The fowler flap is modelled as continuous due to limitation in the modelling capabilities. ....	99
Figure 80 The lift coefficient of the Polimi C7A candidate. ....	99
Figure 81 The lift-to-drag coefficient of the Polimi C7A candidate.....	100
Figure 82 The pitching moment coefficient of the Polimi C7A candidate.....	100

Figure 79 Shaft power requirement comparison for C7A candidate between PVS and POLIMI analysis.	102
Figure 80 A/C speed comparison during the mission for C7A candidate between PVS and POLIMI analysis	103
Figure 81: C7A conceptual design.....	104
Figure 82: Position of primary powertrain components inside the fuselage.....	105
Figure 83: Passenger seating configuration.....	105
Figure 84: Schematic representation of the chosen fuselage structural concept (1).....	106
Figure 85: Wing-fuselage attachment of a tiltwing VTOL aircraft (2).....	107
Figure 86: Fuselage wing attachment concept of a high wing aircraft (3).....	108
Figure 87: Fuselage wing attachment of military transport aircraft.....	108
Figure 88: Example structure of the horizontal stabilizer.....	109
Figure 89: Critical lack of clearance between the pusher propeller and the vertical tail.....	110
Figure 90: Proposed design changes to mitigate the insufficient clearance between the pusher propeller and the vertical stabilizer.....	111
Figure 91: "Side stowing" main landing gear configuration on a novel VTOL aircraft design with limited space in the fuselage.....	112
Figure 96 Candidate C2 top, side, front and ISO view.....	113
Figure 97 Sizing matrix plot for candidate C2.....	116
Figure 98 Mass breakdown of candidate C2.....	116
Figure 99 Battery and tank level during the sizing mission for candidate C2.....	117
Figure 100 Power utilization during the sizing mission for candidate C2.....	117
Figure 97 $f_{tot}$ versus battery specific power.....	118
Figure 98 MTOM versus battery specific power.....	119
Figure 99 $f_{tot}$ versus fuel-cells specific power.....	119
Figure 100 MTOM versus fuel-cells specific power.....	120
Figure 101 $f_{tot}$ versus $CD_0$ .....	120
Figure 102 MTOM versus $CD_0$ .....	121
Figure 103 $f_{tot}$ versus battery specific energy.....	121
Figure 104 MTOM versus battery specific energy.....	122
Figure 109 Sensitivity of MTOM vs battery specific power.....	122
Figure 110 Sensitivity of $g_{TOT}$ vs cruise speed.....	122
Figure 107 The geometry of the POLIMI C2 candidate used in the aerodynamic analysis.....	123
Figure 112 The lift coefficient of the POLIMI C2 candidate.....	124
Figure 113 The lift-to-drag coefficient of the POLIMI C2 candidate.....	124
Figure 114 Pitching moment coefficient of the POLIMI C2 candidate.....	125
Figure 111: Shaft power requirement comparison for C2 candidate between PVS and POLIMI analysis.	127
Figure 112 PVS1 top, side, front and ISO view.....	129
Figure 113 The geometry of the PVS 1 candidate used in the aerodynamic analysis.....	130
Figure 114 The lift coefficient of the PVS 1 candidate.....	131
Figure 115 The lift-to-drag coefficient of the PVS 1 candidate.....	131
Figure 116 The pitching moment coefficient of the PVS 1 candidate.....	132
Figure 117: PVS 1 candidate main electric powertrain cooling system concept. Left: electric motor cooling circuit. Right: Power-controller cooling circuit.....	133



Figure 118: PVS 1 candidate DEP electric powertrain cooling system concept. Left: electric motors cooling circuit (one wing). Right: Power-controllers cooling circuit (one wing).....	134
Figure 119: PVS1 candidate fuel cells cooling system concept. ....	135
Figure 120: Shaft power requirement comparison between PVS1 candidate and C7A candidate. ....	136
Figure 121: Aircraft PVS1 weight and $f_{tot}$ versus airframe mass fraction. ....	137
Figure 122: Aircraft PVS1 weight and $f_{tot}$ versus battery power density. ....	138
Figure 123: Aircraft PVS1 weight and $f_{tot}$ versus battery energy density. ....	138
Figure 124: Aircraft PVS1 weight and $f_{tot}$ versus fuel cell efficiency.....	139
Figure 125: Aircraft PVS1 weight and $f_{tot}$ versus fuel cell power density. ....	139
Figure 126: Aircraft PVS1 weight and $f_{tot}$ versus glide ratio. ....	140
Figure 127 Sizing matrix plot for PVS1 obtained by Hyperion.....	142
Figure 128 Fuel, battery, and throttle level plot for PVS1 obtained by Hyperion.....	142
Figure 129 Power utilization during the sizing mission for PVS1 obtained by Hyperion. ....	143
Figure 130 The pitching moment behaviour between canard and conventional configuration. ....	145
Figure 131: Point of interest for generation of ground noise contour maps.....	146
Figure 132: PVS1 candidate main propeller <b>rotational</b> noise ground contour map.....	146
Figure 133: PVS1 candidate main propeller <b>broadband</b> noise ground contour map. ....	147
Figure 134: PVS1 candidate main propeller <b>total</b> noise ground contour map. ....	147
Figure 135: PVS1 candidate DEP propellers <b>rotational</b> noise ground contour map.....	148
Figure 136: PVS1 candidate DEP propellers <b>broadband</b> noise ground contour map. ....	148
Figure 137: PVS1 candidate DEP propellers <b>total</b> noise ground contour map.....	149
Figure 138: Comparison of candidates - noise ground footprint at $y = 0$ m (below aircraft). ....	151
Figure 139: Total DOC per flight, detailed per type of cost.....	155
Figure 140: DOC expressed in terms of Cost per Available Seat and Kilometre. ....	156
Figure 141: Aircraft purchase price for 500 units, including overhead margin and extras.....	156
Figure 142: Sensitivity study for C3, in percentages from the baseline DOC.....	159
Figure 143: Sensitivity study for C7A, in percentages from the baseline DOC. ....	160
Figure 144: Sensitivity study for C2, in percentages from the baseline DOC.....	161
Figure 145: Sensitivity study for PVS1, in percentages from the baseline DOC.....	162
Figure 146 Conventionally powered reference aircraft sizing matrix plot.....	165
Figure 147 Conventionally powered reference aircraft mass breakdown.....	165
Figure 148 Conventionally powered reference aircraft sizing mission simulation: altitude profile (black dashed), engine throttle (blue) and fuel tank level (red). ....	166
Figure 149 Conventionally powered reference aircraft sizing mission simulation: altitude profile (black dashed), electric motor input power (red) and output power (green).....	166
Figure 150 NOx emissions of turbine engines as a function of fuel flow .....	167

## List of Tables

Table 1 Top level aircraft requirements .....	19
Table 2 Performance values projection.....	21
Table 3 Aircraft architecture options considered in the initial design space sweep. ....	24
Table 4 Initial list of candidate configurations (part I). ....	25
Table 5 Initial list of candidate configurations (part II). ....	26
Table 6 Intermediate list of candidate configurations. ....	28
Table 7 AHP ranking of the intermediate list of candidate configurations.....	30
Table 8: Aircraft configuration selected for the first top-down selection (TUDELFT).....	31
Table 9: Weight for the trade-off criteria .....	33
Table 10: Scoring scale for the trade-off .....	33
Table 11: initial trade-off .....	34
Table 12 Mass breakdown for PVS1 candidate - main window .....	49
Table 13 FlightStream general settings .....	53
Table 14: Mission requirements. ....	57
Table 15 Material distribution for all UNIFIER19 candidate designs.....	64
Table 16 Complete specifications of candidate C3.....	73
Table 17 Variation of technological parameters for sensitivity analysis.....	77
Table 18 Variation of global design parameters for sensitivity analysis. ....	77
Table 19 Variation operational parameters for sensitivity analysis.....	77
Table 20 : Variation of aircraft range for C3 configuration and respective parameter changes. ....	78
Table 21: pConcept results. ....	83
Table 22 The analysis points of the POLIMI C3 candidate.....	83
Table 23: Input data (POLIMI 4) for cooling drag estimation – main electric powertrain.....	86
Table 24 Input data (POLIMI C3) for cooling drag estimation – FC. ....	86
Table 25: POLIMI C3 radiators size. ....	86
Table 26 Complete specifications of candidate C7A .....	89
Table 27 Variation of aircraft range for C7A configuration and respective parameter changes.....	93
Table 28: pConcept results. ....	97
Table 29 The analysis settings of the POLIMI C7A candidate.....	98
Table 30 Input data (POLIMI C7A) for cooling drag estimation – main electric powertrain.....	101
Table 31 Input data (POLIMI C7A) for cooling drag estimation – DEP electric powertrain. ....	101
Table 32 Input data (POLIMI C7A) for cooling drag estimation – FC.....	101
Table 33 POLIMI 1 (C7A) radiators size.....	102
Table 34 Complete specifications of candidate C2.....	114
Table 35 Variation of aircraft range for C2 configuration and respective parameter changes. ....	118
Table 36: pConcept results. ....	122
Table 37 The analysis settings of the POLIMI 3 candidate. ....	123
Table 38: Input data (POLIMI C2) for cooling drag estimation – main electric powertrain.....	125
Table 39: Input data (POLIMI C2) for cooling drag estimation – DEP electric powertrain.....	126
Table 40: Input data (POLIMI C2) for cooling drag estimation – FC.....	126
Table 41: POLIMI C2 radiators size. ....	126
Table 42 PVS1 geometrical and performance characteristics.....	129
Table 43: pConcept results. ....	129

Table 44 The analysis points of the PVS 1 candidate. ....	130
Table 45: Input data (PVS 1) for cooling drag estimation – main electric powertrain.....	133
Table 46: Input data (PVS1) for cooling drag estimation – DEP electric powertrain. ....	134
Table 47: Input data (PVS1) for cooling drag estimation – FC.....	135
Table 48: PVS1 radiators size.....	135
Table 49 Results of PVS1 cross-check using Hyperion.....	141
Table 50 Qualitative structural design assessment .....	143
Table 51: PVS1 operational data for propellers noise estimation.....	149
Table 52: POLIMI C7A operational data for propellers noise estimation.....	150
Table 53: POLIMI C2 operational data for propellers noise estimation. ....	150
Table 54: POLIMI C3 operational data for propellers noise estimation. ....	150
Table 55: POLIMI REFERENCE operational data for propellers noise estimation. ....	151
Table 56: Assumed material distribution for all UNIFIER 10 candidate designs. ....	153
Table 57 Conventionally powered reference aircraft main specifications.....	163
Table 58 Gaseous emissions of the conventional reference aircraft per passenger kilometer.....	167

## Abbreviations

A/C	aircraft
AHP	Analytical Hierarchy Process
BLI	Boundary-Layer Ingestion
CG	Center of Gravity
DAER	Department of Aerospace Science and Technology (POLIMI)
DEP	Distributed Electric Propulsion
FC	Fuel Cell
HT	Horizontal Tail
MCDM	Multi-Criteria Decision Making
PCA	Propulsion-Controlled Aircraft
POLIMI	Politecnico di Milano
PVS	Pipistrel Vertical Solutions
TBW	Truss-Braced Wing
TCP	Tail-Cone Propeller
TLAR	Top Level Aircraft Requirements
TUDELFT	Technical University Delft
VIW	Variable-Incidence Wing
VT	Vertical Tail
WP1	Work Package 1
WTP	Wing-Tip Propeller

# 1 Introduction

## 1.1 Market analysis findings

As highlighted in Section 2 of Deliverable 1.1 (D1.1), a relevant step in assessing the potential of novel electric-powered aircraft is the quantitative analysis of the air transport network they can sustain. Understanding the trade-offs between aircraft performance and captured demand on a potential theatre of operation allows to negotiate and define the top-level aircraft requirements for a new aircraft, capable of successfully carrying out an intended role in the air transportation network.

The revamping of secondary airports and smaller airfields (SAs), promoting them to nodes in a network served by community-friendly miniliners, is a key-enabler for the successful deployment of a novel hybrid-electric aircraft, of interest in UNIFIER19. As explained in the cited section of D1.1, two missions can be envisaged on a such network, namely a microfeeder operating on a hub-and-spoke basis between SAs and major airports, and an intercity liner, connecting SAs and especially suitable for a daily commuting service, in areas and on distances where ground infrastructure does not offer a suitable service.

In this section, at first we will draw upon the methodology to compute the captured demand documented in Chapter 2 of D1.1 and quickly recap some of the findings instrumental in the approach to top-level aircraft requirements (TLAR) definition. Next, we will complement the previous results with a market analysis specifically related to the intercity liner concept, concentrating on the Italian scenario as a test case.

### 1.1.1 Analysis of the potential market for microfeeder service: recap from D1.1

The idea behind the computation of captured demand in the case of a microfeeder is that of finding whether traveling to/from a primary airport and an SA is possible in a lower overall time than with other means of transportation (ground infrastructure). The evaluation is carried out considering also the overhead due to departure/arrival procedures in a larger airport, for instance when coming by car (e.g. parking, check-in and security in a larger airport).

It has been shown that the size and capillarity of the network are correlated to the characteristics of the aircraft intended to sustain it. In particular, take-off distance, cruising speed and range all bear an impact on the network potentially served by a specifically designed microfeeder, hence on the demand that the network may capture.

In D1.1 a thorough market analysis of the micro-feeder service has been presented, focusing on three example European regions (of Bruxelles, Venice and Riga) associated to different densities of the existing ground transportation network.

It has been demonstrated in D1.1 how in the considered test cases both cruising range and take-off distance have an intense effect on the captured demand, impacting the actual number of SAs which can be practically employed for the intended task.

A longer cruising range allows extending the area covered by the network, thus typically raising the number of SAs in it. Combined with a sufficiently high cruising speed, this effect clearly raises the captured demand correspondingly.

A shorter take-off distance allows to employ more SAs, thus in principle increasing the capillarity of the network (in practice, this also depends on the presence of more SAs with shorter runways in the area,

which become of use when the aircraft requires a shorter take-off distance), with a positive effect on captured demand.

Cruising speed is typically effective in competitive scenarios, where a microfeeder service would be employed in face of an existing and well-developed ground infrastructure. On the contrary, for scenarios where the existing infrastructure is less developed (like Riga, as shown in D1.1), this parameter does not produce any appreciable effect.

### 1.1.2 Intercity liner service analysis

The intercity liner service considered in this project is a point-to-point transportation system for day to day commuting and business travel. Similar to the microfeeder, the idea is that of providing a faster and greener alternative to ground-based systems, mostly fossil-fuel based like cars.

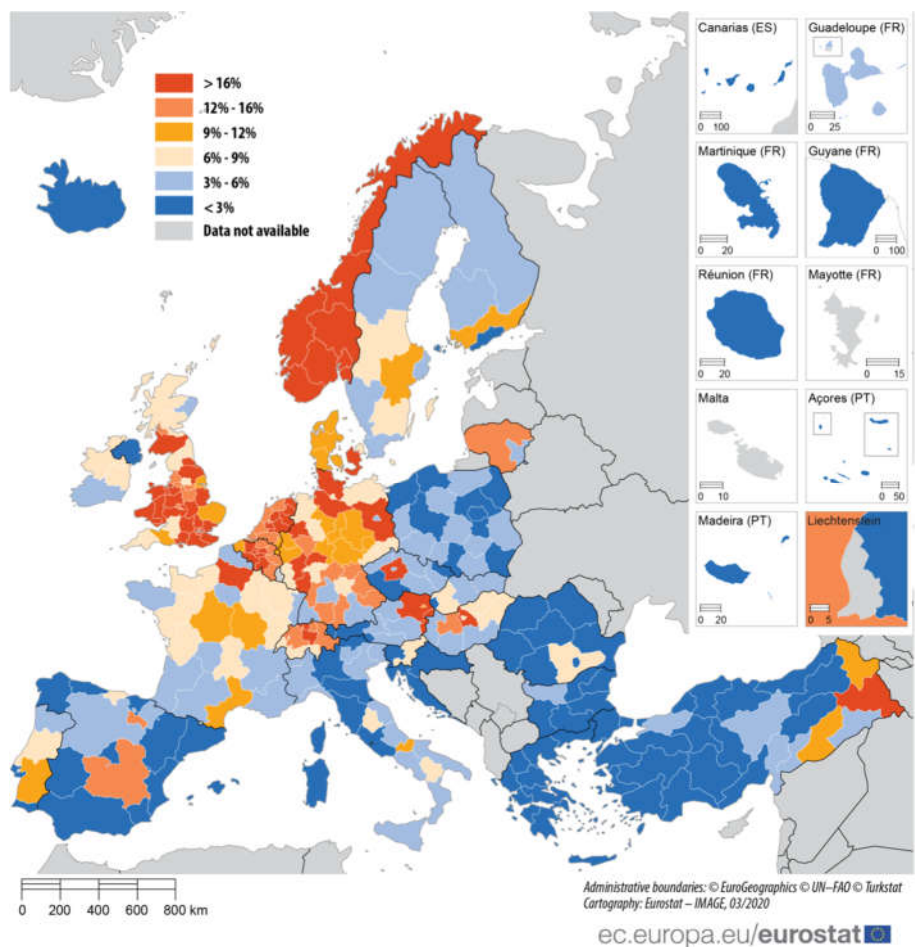


Figure 1 Employed people commuting to another region within their country in Europe in 2018

In a European perspective, there is a good portion of citizens who commute outside of the region where they live. Of them 6%, or 12 million, of the 193 million people working in the EU aged 15-64 years in 2018 commuted to work within their country of residence, from one area to another. The Benelux, the United Kingdom (formerly part of the EU at the time of the study) and, in particular, Norway have the highest share of interregional commuters with respect to the total number of employed people, as depicted in Figure 1.

In this deliverable, we are going to consider Italy as a case study for an intercity liner service. In this country, nearly half a million people cross regional borders every day to go to work or study (according to the latest 2011 census). Moreover, more than 75% of the commuting is done using private cars, with a very small fraction being shared (carpooling).

Car is predominant among workers, which makes up to 66% of total commuting population, while students prefer public means of transport.

It is expected that the intercity miniliner will be especially interesting in those cases where the commuting distance is longer. One example of the intercity liner service is depicted in Figure 2. A person living in Lucca (Tuscany) but working in Milan (Lombardy), could take the car to the nearest airport (Lucca-Tassignano Airport, 8.5 km from the city centre) and from there take the miniliner to Bresso Airport (LIMB), in the neighbourhood of Milan. The full car travel takes 3 h and 12 min without traffic. This time can be reduced to 1 h and 58 min, including 40 min extra time to check-in/check-out at the local airports and the car time from the SAs to the city centres.

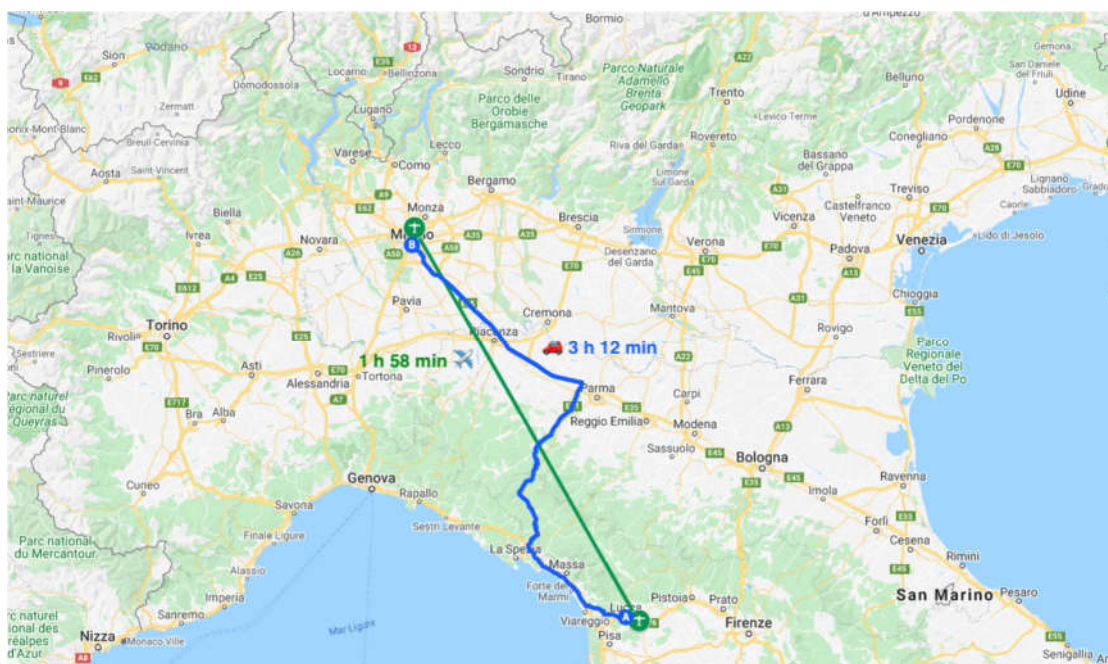


Figure 2 Example of intercity service between Lucca and Milan (Bresso airport)

### 1.1.2.1 Methodological aspects of demand estimation for the intercity liner service

In order to estimate the number of people interested in traveling between any two towns using the intercity liner service, data about commuting habits from the Italian National Institute of Statistics was considered. In particular, periodical censuses usually provide matrices of commuting habits estimating the number of people that commute daily for work or study reasons. The total traffic flow can be arranged in the form of a typical Origin-Destination (OD) matrix  $G$  such that

$$G = \begin{bmatrix} g_{11} & g_{12} & \dots & g_{1n} \\ g_{21} & g_{22} & \dots & g_{2n} \\ \vdots & & \ddots & \\ g_{n1} & & & g_{nn} \end{bmatrix}$$

where  $g_{ij}$  represents the commuter flow from the  $i$ -th town origin to the  $j$ -th destination. It is interesting to note that commuter traffic flow is bidirectional: those who travel in the morning will travel back in the afternoon/evening. Therefore, the return OD matrix is simply the transpose of the one-way OD matrix:

$$G_{return} = G_{one-way}.$$

By evaluating of all route catchment areas relative to each entry of the OD matrix, the total potential demand can be estimated. An example will be shown in the next sub-section.

### 1.1.2.2 Case study for the intercity liner: Italy

The Italian case is assumed for the study of the intercity service. In particular, in this deliverable we are using the commuting matrix  $G$  from the 15<sup>th</sup> population and housing census from 2011.

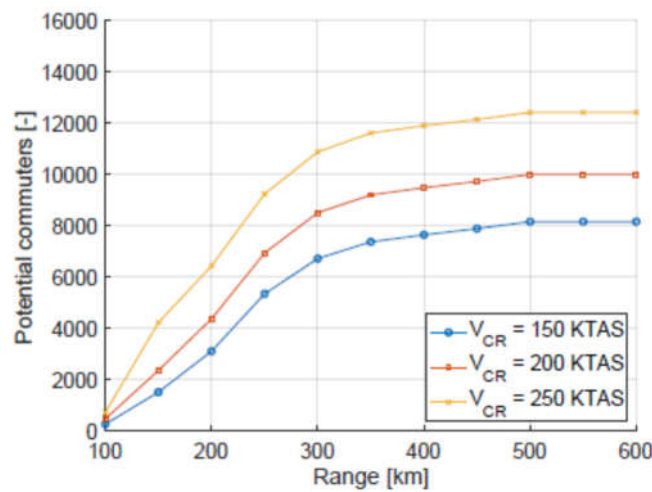


Figure 3 Potential demand estimation for an intercity service in Italy. Variation for different cruising speed values, considering runways longer than 800 m.

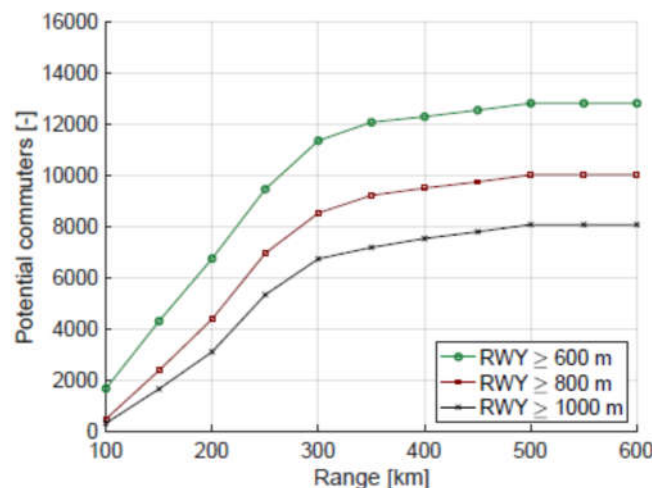


Figure 4 Potential demand estimation for an intercity service in Italy. Variation with respect to runway length, considering a cruising speed of 200 KTAS.



The captured traveling demand of Italian commuters is presented in Figure 3 and Figure 4 as a function of trip distance (range), cruising speed and runway length.

We can observe how the amount of potential commuters, clearly flattens towards a constant value, saturating around 300÷350 km trip distance. Significant differences for changing values of cruising speed and runway length are observed. For instance, from Figure 3, looking at the 350 km number of commuters, a cruising speed increment of 50 and 100 kn from 150 KTAS increases that number by 26% and 57%, respectively. The effect of runway length is similar (Figure 4): the number of potential commuters rises by 68% using 600 m long runways, and by 28% using 800 m long runways, with respect to the 1,000 m case.

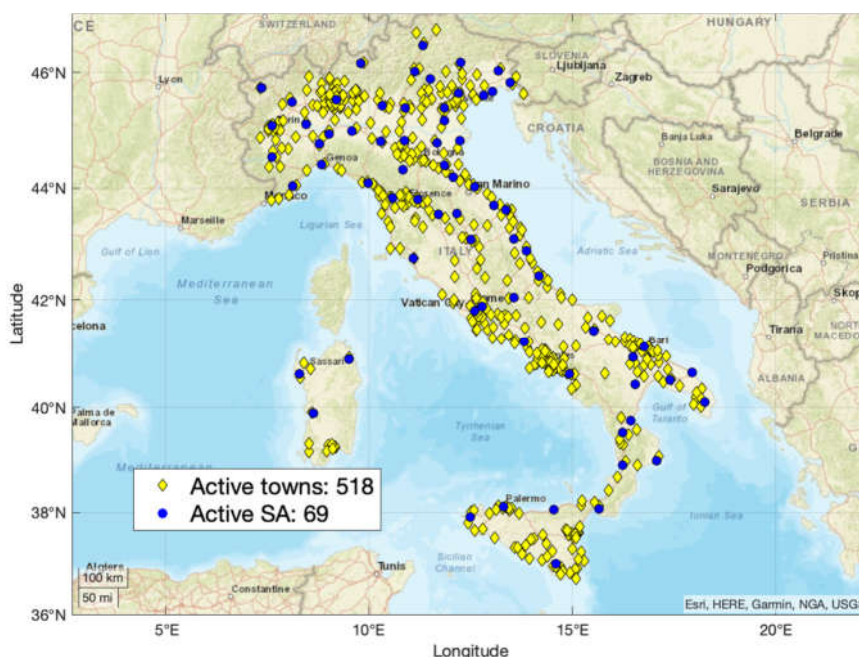


Figure 5 Distribution of towns and SAs involved in an intercity service in Italy with a range of 350 km, runways longer than 800 m and 200 KTAS cruising speed.

Figure 5 depicts a map of the network with considered towns and SAs, for an intermediate choice of the TLARs, showing the relevant potential both in terms of activated infrastructure (SAs) and towns served. In order to better capture the potential of a trade-off process in negotiating the TLAR, a sensitivity analysis has been performed on the constraining parameters  $t_{ref}$  and  $k$ , defined in the formulation introduced in D1.1, section 2.

Figure 6 displays an example of a choice of the minimum time gain ( $t_{ref}$ , time difference constraint boundary) and relative time advantage ( $k$ , time gain constraint boundary), producing the lines on the plot showing road travel time ( $t^{T1-T2}$  according to the notation D1.1, section 2) and travel time with an intercity service ( $t^{T1-S1} + t^{mf} + t^{T2-S2}$ ) for all pairs of SAs in Italy.

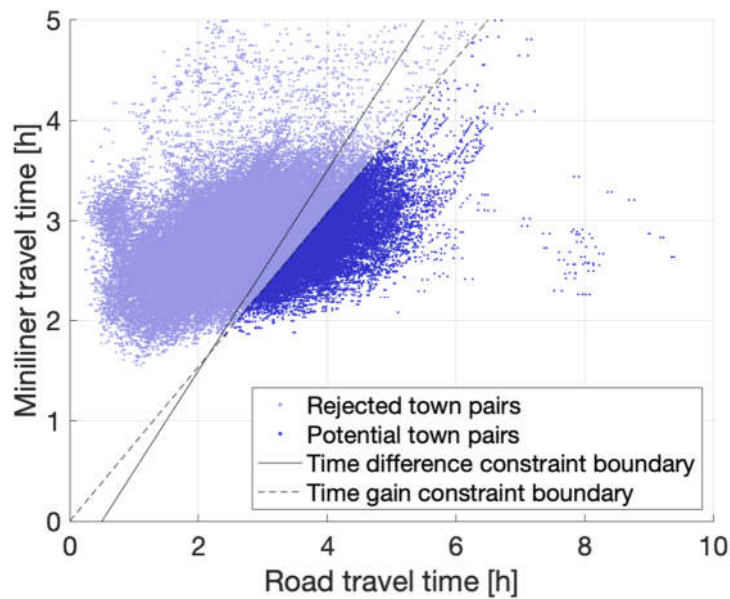


Figure 6 Miniliner travel time and road time for all the town pairs, including trip constraints, for a choice of constraining values  $t_{ref}$  and  $k$ .

In general, increasing or decreasing  $t_{ref}$  moves up and down the time difference constraint boundary, represented by the solid black line. However, this constraint has a limited effect, if any, in the considered configuration. Modifying  $k$  rotates around the origin the time gain constraint boundary represented by the dashed black line. In particular, decreasing  $k$  makes the boundary steeper and hence, less restrictive. Also, increasing the aircraft performance or reducing the airport times (the latter amounting to 40 minutes in this plot), moves down the data cloud, enabling more potential town pairs.

Airport procedures time and the time gain parameter  $k$  have a deep effect on the number of potential travellers. This is shown in Figure 7, where the absolute time difference  $t_{ref}$  is not considered due to its lower effect (as just explained). In the figure, a range of 200 km, a cruising speed of 200 KTAS and a minimum runway length required of 800 m are considered. Airport times are added up and treated as a block. Nominal airport times in this study were selected with the microfeeder service in mind, in which the passenger continues the trip after disembarking from the miniliner, to take an international flight. In the intercity liner, this is no longer the case. Commuters are expected to be “light travelers”, so shorter check-in, turnaround and, in general airport-related times could be achieved. Also, time gain expectations may be different for commuters.

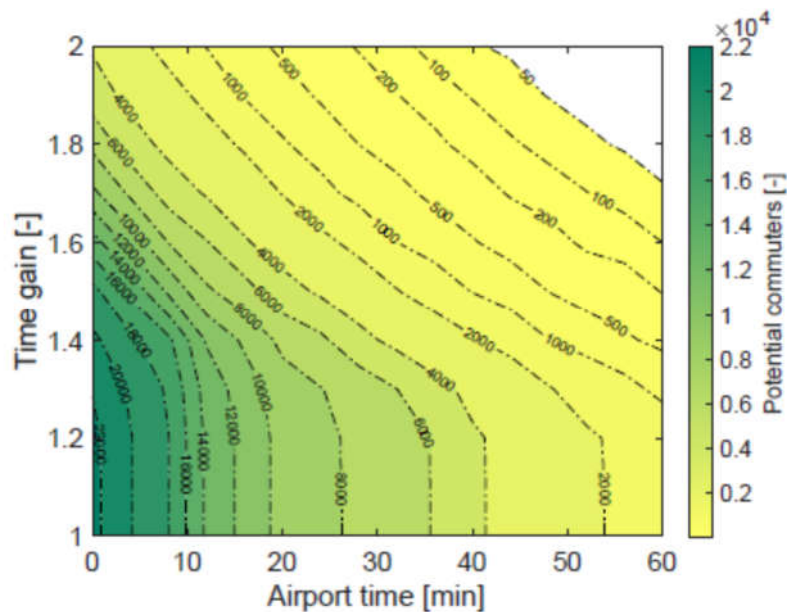


Figure 7 Potential commuters with respect to overall airport time and time gain parameter.

This result exposes the considerable impact airport times have on the potential demand. In the unrealistic case of vanishing airport times, more than 22,000 commuters are potentially willing to use the service. On the other hand, with airport times between 40 min (the nominal value) and 1 hour, this number is reduced by one order of magnitude, to 1,000÷4,000 commuters. The effect of increasing the time gain parameter  $k$  is less relevant, and provides an increase in the potential demand that quickly reduces in association with an increasing airport time.

## 1.2 Top Level Aircraft Requirements

Most of the Top Level Aircraft Requirements are derived from market analysis findings and specifications of the available airport network, such as mission requirements and runway minimum length. CS-23, EASA Certification Specification, is adapted as a basis for Unifier19 aircraft certification requirement with Commuter subcategory for minimum required manoeuvring envelope G limits. All requirements are presented in Table 1.

Table 1 Top level aircraft requirements

Leg	Type	Value	Note
<b>Take-off</b>	Runway length	800 m	50% of secondary aerodromes are 800m or longer
	Runway type	Grass	50% of secondary aerodromes are grass type
<b>Climb</b>	Initial gradient	7 degrees	Up to 1000ft AGL, airport near populated area
	ROC	850 ft/min	
<b>Cruise</b>	Block range	300 - 350 km	Block range is a sum of climb, cruise and descend distance → defined as one “hop”
	Altitude	max 8000 ft	

	Speed	150-200 kts	Potential demand increases up to 50 % (23%) moving from 150 kts to 200 kts, while the increase from 200 kts to 250 kts is limited to 12-15% (8%) for Microfeeder (Miniliner)
<b>Descent</b>	ROD	350 ft/min	Passenger comfort
<b>Landing</b>	Runway length	800 m	
<b>Reserves</b>	Diversion	100 km	90% of secondary aerodrome within 100 km
	Loiter	45 min	IFR requirement
<b>Airport operations</b>	Turnaround time	Max 45 min	
	Ground support	Battery recharge	
<b>General</b>	CS-23		Unpressurised cabin
	Cargo variant	3 x LD3 containers equivalent	
	Number of passengers	19	
	Passenger mass	100 kg + 20 kg	100 kg – passenger + carry-on baggage 20 kg – checked baggage
	Number of “hops”	min 4	To avoid having refuelling infrastructure on all small airports
	Number of pilots	1	Fly-by-wire system, suitable for autonomous or remotely-piloted conversion

### 1.2.1 Power generation system configuration

When it comes to the lofting of the power generation system (PGS), composed by a fuel cell system together with its LH2 tank(s), two main options may be considered:

1. **Concentrated lofting** – The PGS forms a single major assembly: a single (possibly, two) LH2 tank is placed in the fuselage, with the fuel cell system located nearby.
2. **Distributed lofting** – The PGS is separated in multiple units, each comprising a fuel cell system and a LH2 tank, to be placed in nacelles or underwing pods.

Each configuration has its pro’s and con’s, as usual. Among the main ones, in a concentrated lofting,

- the thermal and weight performance of the LH2 tank is maximized, due to the favourable surface-to-drag ratio of a large vessel;
- the layout of the PGS is simplified, due to the easier location in the fuselage;
- the cooling imposes a significant provision for an air intake in the fuselage, with inevitable degradation of drag performance.

On the other hand, in a distributed lofting,

- the thermal and weight performance of the LH2 tanks are degraded, due to the unfavourable surface-to-drag ratio of slender vessels;
- the layout of the PGS is significantly complicated, due to the need to provide hydrogen transfer from one wing subsystem to another in case of failures, with the related piping;
- the cooling may take advantage of the slender external nacelles or pods;

- the nacelles may degrade the wing performance and introduce difficulties in the integration of Distributed electric Propulsion (DEP);
- the underwing pods imply an inevitable degradation of drag performance.

Given the above, a decision was made to favour the general higher simplicity and efficiency of the concentrated lofting, after the cooling penalty was evaluated and assessed to be compatible with the preliminary sizing and performance of the aircraft, as seen in Section 6. In addition, as explained in Section 4.3, special attention has been given to an advanced aerodynamic configuration, which is not easily compatible with a distributed PGS configuration.

### 1.2.2 Technology assumptions

The aircraft is set to come into service in 2030. Due to rapid development in key technologies installed in this aircraft, current state-of-the-art subsystems, i.e. batteries and fuel cells, will be already obsolete at the time of their installation in the aircraft. Therefore, it is important in aircraft conceptual design stage to use a realistic and believable performance prediction in order to optimise the aircraft around the subsystems that will be available at the required moment in the future. Because of that, technology assumptions were made for time intervals of next 15 years. Five-year step projections of the battery and fuel cell performance as well as for liquid hydrogen storage system capabilities are listed in Table 2.

Table 2 Performance values projection

Type	Values per year			
	2020	2025	2030	2035
Batt. energy density [Wh/kg]	210	260	304	350
Batt. power density [W/kg]	1365	1670	1970	2275
LH2 tank gravimetric index	60%	60%	65%	65%
FC power density [W/kg]	800	2130	3460	4800
Batt. volum. energy density [Wh/m <sup>3</sup> ]	490	600	710	818

Values from technology assumption for year 2025 were used in the conceptual design.

## 1.3 Aircraft configurations down-selection methodology

### 1.3.1 Politecnico di Milano activities

#### 1.3.1.1 General approach

An articulated activity was set for the exploration of the aircraft configuration design space, providing an incremental down-selection of possible candidates for the UNIFIER19 mission. As a starting point, the availability of multiple configuration options was considered in order to seek an innovative solution capable of

- complying with the TLAR,
- constitute a significant departure from traditional designs, and
- to appear as an aesthetically attractive and fresh-looking solution.

Elements b and c in the above list have been considered relevant in view of the economic profitability of the final solution to be proposed. In fact, the envisaged miniliner market will need an improved degree of public acceptance for propeller-driven passenger aircraft. This will not be built on economics (ticket price), travel comfort and environmental friendliness only. It is generally known that passengers typically consider propeller-driven aircraft as obsolete and aesthetically clumsy. This perception is assumed to be one of the reasons that drove the majority among European regional carriers to switch from turboprop to jetliners such as the Bombardier CRJ, Embraer ERJ and E-Jet families. Therefore, it was assumed that an innovative look – which typically corresponds to refined aerodynamics and an original configuration – is a non-negligible addition to the UNIFIER19 customer appeal.

In addition, in the frame of the present effort, it was deemed important to invest in a significant research activity to bring to maturity an innovative formula in the aircraft configuration, instead of pursuing an already trodden path. This allows

- to depart from competing design choices, such as those exemplified by some industrial programs currently advertised, including the Heart Aerospace ES-19 (announced in September 2020), let alone the electric retrofit of existing aircraft;
- to build on some elements that have been developed within the H2020 MAHEPA project ([www.mahepa.eu](http://www.mahepa.eu)), such as DEP aero-propulsive modelling, further enhancing design methodologies dedicated to innovative aircraft that may be used in the initial stages of the design process, to explore the design solution space.

Also, it is expected that the UNIFIER19 activities will contribute insight and quantitative information on a novel configuration without established antecedents, that may be useful to assess its potential, by highlighting benefits, drawbacks, and trade-offs to be considered in future projects, possibly aiming at larger payload and sizes.

The approach adopted to select the candidate aircraft design solution delivered by POLIMI was developed through the following phases:

1. **Design Space Sweep** – An in-depth research is conducted to identify all the innovative technologies that are applicable for this aircraft family, proceeding from work done in WP1. The identified technologies are initially combined with a systematic approach to obtain all possible combinations. This leads to a large number of alternatives, of which many are not feasible or not practical.
2. **Qualitative Selection** – A set of selection criteria are chosen and used to perform a reduction of the initial list of candidates. The list is further reduced during a series of brain-storming in which the potential of each configuration is discussed. Some other configurations are added, as other secondary technologies are taken into account from discussions and from solutions of issues highlighted by conceptual hand-sketches. In the end, a subset of 15 candidate aircraft is used as input of an accurate selection based on the AHP (Analytical Hierarchy Process), obtaining the five most promising configurations.

The five selected aircraft are sized by taking advantage of the design tools developed internally at DAER-POLIMI, i.e. HYPERION (preliminary sizing) and TITAN (Class I design). This involved determining the necessary input data based on mission and certification requirements and updating the software tools to consider the new particular mission and the new technologies specific to these aircraft. The sizing results have been iteratively assessed and discussed, bringing to the update of some design requirements.

From the five selected aircraft, a further down-selection, discussed in Chapter 6, led to the proposition of three candidates for the subsequent UNIFIER19 developments.



Wing Body, Box Wing, TBW, VIW), others propulsion system (DEP, WTP, TCP and BLI), and other potentially beneficial technologies such as Propulsion-Controlled Aircraft (PCA) and Laminar Flow.

Table 3 Aircraft architecture options considered in the initial design space sweep.

Category	Elements		
<b>Layout</b>	<ul style="list-style-type: none"> <li>• canard</li> <li>• tailless</li> </ul>	<ul style="list-style-type: none"> <li>• three surface (TSA)</li> <li>• traditional aft tail</li> </ul>	
<b>Wing</b>	<ul style="list-style-type: none"> <li>• high aspect ratio supported wing (TBW, SBW)</li> <li>• box wing</li> </ul>	<ul style="list-style-type: none"> <li>• cantilever</li> </ul>	
<b>Propulsion</b>	<ul style="list-style-type: none"> <li>• blown-wing (DEP)</li> <li>• traditional nose or wing-mounted</li> </ul>	<ul style="list-style-type: none"> <li>• tail cone (TCP)</li> <li>• wing tip (WTP)</li> </ul>	
<b>Propeller</b>	<ul style="list-style-type: none"> <li>• contra-rotating</li> </ul>	<ul style="list-style-type: none"> <li>• single</li> </ul>	<ul style="list-style-type: none"> <li>• tubed fan</li> </ul>
<b>Architecture</b>	<ul style="list-style-type: none"> <li>• single source (fuel or electric energy)</li> <li>• hybrid-electric (series or parallel or complex)</li> </ul>		
<b>Energy Source</b>	<ul style="list-style-type: none"> <li>• batteries</li> <li>• hydrogen fuel cells with GH2 or LH2 storage system</li> </ul>	<ul style="list-style-type: none"> <li>• fossil-fuel</li> </ul>	
<b>Special</b>	<ul style="list-style-type: none"> <li>• flying-V</li> <li>• box wing or joined wing aircraft (BWA, JWA)</li> </ul>	<ul style="list-style-type: none"> <li>• blended wing body (BWB)</li> </ul>	

Table 3 shows a categorized list of technology options considered in the assembling of candidate solutions. A notional analysis of all possible combinations leads to over 200,000 possible permutations. Therefore, a first substantial reduction process was carried out, applying a qualitative judgement of the overall feasibility of the possible candidates. Removal of configurations deemed unfeasible or unable to provide any benefit, plus a number of preliminary assessments (also relying on hand-drawings to better define some particulars of less-intuitive solutions), helped to shrink the number of potential candidates to 45 for the initial list to be qualitatively assessed. This list is shown in Table 4 and Table 5.



Table 4 Initial list of candidate configurations (part I).

N°	Definition		
	Layout	Wing	Propulsion
1			Twin wing-mounted propellers
2			DEP and WTP
3		Cantilever	DEP, WTP and BLI
4			WTP and BLI
5			BLI and VIW
6	Aft Tail		DEP and WTP
7		TBW	DEP, WTP and BLI
8			WTP and BLI
9			BLI and VIW
10			DEP
11		Box Wing	DEP and BLI
12			BLI and VIW
13			DEP and WTP
14			DEP, WTP and BLI
15		Cantilever	WTP and BLI
16			BLI and VIW
17	Canard		DEP and WTP
18		TBW	DEP, WTP and BLI
19			WTP and BLI
20			BLI and VIW
21			DEP
22		Box Wing	DEP and BLI
23			BLI and VIW

Table 5 Initial list of candidate configurations (part II).

N°	Definition		
	Layout	Wing	Propulsion
24			DEP and WTP
25			DEP, WTP and BLI
26		Cantilever	WTP and BLI
27			BLI and VIW
28			DEP and WTP
29	Tailless	TBW	DEP, WTP and BLI
30			WTP and BLI
31			BLI and VIW
32			DEP
33		Box Wing	DEP and BLI
34			BLI and VIW
35			DEP and WTP
36			DEP, WTP and BLI
37		Cantilever	WTP and BLI
38			BLI and VIW
39			DEP and WTP
40	TSA	TBW	DEP, WTP and BLI
41			WTP and BLI
42			BLI and VIW
43			DEP
44		Box Wing	DEP and BLI
45			BLI and VIW

### 1.3.1.3 Qualitative Selection

The initial list of potential candidate configurations was subjected to a second selection process based on two steps:

1. Preliminary down-selection based on a set of rational criteria.
2. Accurate ranking of the surviving candidates.

#### **Down-selection**

The preliminary down-selection method is based on the following evaluation criteria:

- A. **One critical innovation at a time** – The embedding of multiple criticalities and challenges in a design impacts on the uncertainty of the estimated performance, and on the risk that the latter

cannot be achieved. Such considerations rule out some apparently less promising alternatives, which instead would win in an ideal future selection, as greater knowledge on a particular technology may reveal lower capabilities than predicted. For this reason, the candidate configurations should share an equivalent level of complexity, uncertainty and feasibility.

- B. **Keep all the innovative solutions** – Each attractive technology should be present at least in one of the down-selected configurations. At this step it is essential to not take away any innovative technology detected before, unless clear exceptional conditions are encountered to judge it absolutely inapplicable. In fact, the subsequent detailed assessment may change the game and promote an option over the others.
- C. **Remove all impractical configurations** – All the selected configuration must be feasible, so they are carefully analysed to detect possible inconsistencies and oddities. For instance, the configurations including a variable incidence box wing have been considered impractical, as the structural complexity of such a mechanism would likely trivialize any advantages.
- D. **Keep only solutions with proven benefits** – The high level of abstraction that naturally characterizes this generation and selection process may easily lead to assumptions that are not observed in practice, or to deviations toward different design goals. This coarse selection should maintain only those candidate configurations that show benefits only relative to the objective of this project, ignoring all those benefits that are not pertinent or not substantiated.

In practice, a series of reduced lists of candidate configurations have been proposed, discussed and combined together, until reaching a single list considered compliant with the selection criteria presented above. This intermediate list includes 15 candidates and is shown in Table 6.

Table 6 Intermediate list of candidate configurations.

Label	Definition		
	Layout	Wing	Propulsion
C1	Aft Tail	TBW	DEP and WTP
C2	Special Layout: Canard PCA with DEP, WTP and BLI		
C3	Special Layout: Canard with " <i>laminar flow fuselage</i> ", VIW and BLI		
C4	Special Layout: BWB with asymmetric BLI-DEP		
C5	Special Layout: BWA with DEP		
C6	Aft Tail	Cantilever	DEP, WTP and BLI
C7	Aft Tail	TBW	DEP, WTP and BLI
C8	Aft Tail	Box Wing	DEP
C9	Aft Tail	Box Wing	DEP and BLI
C10	Canard	Cantilever	DEP, WTP and BLI
C11	Tailless	Cantilever	DEP, WTP and BLI
C12	Tailless	TBW	DEP, WTP and BLI
C13	Tailless	Cantilever	WTP and BLI
C14	TSA	Cantilever	DEP, WTP and BLI
C15	TSA	TBW	DEP, WTP and BLI

## Ranking

An accurate ranking process was carried out on the intermediate list of candidates obtained above, by the application of a Multi-Criteria Decision Making (MCDM) methodology. MCDM methods have been proposed in the literature to make the selection process more formal, credible and transparent. Among these methods, the simple Pugh's Method<sup>1</sup> and the more articulated Analytical Hierarchy Process (AHP)<sup>2</sup> have been considered here.

Particularly, we shall discuss the results obtained by the application of the AHP. This is a widespread MCDM method able to deliver robust results. It has been implemented in a spreadsheets tool, as it involves a laborious procedure including a sequence of computations. The core of this process can be summarized into the following key steps:

1. Define the problem. The alternatives, the criteria, the goal and a scale of numbers to be used for judgements.
2. Structure the decision hierarchy. From the top (i.e. the goal of the decision), through the intermediate levels (e.g. criteria), to the lowest level (e.g. alternatives).

<sup>1</sup> S. Burge, The Systems Engineering Tool Box, 2009.

<sup>2</sup> T. L. Saaty, Decision Making with the Analytic Hierarchy Process, Int. J. Services Sciences, Vol. 1, No. 1, 2008.

3. Construct a set of pairwise comparison matrices. Each element is used to compare the elements in the level below. For examples: goals are used to compare criteria and criteria are used to compare alternatives.
4. Use priorities weight in the level below. For each element in the level below add its weighed values and obtain its global priority. Repeat this process of weighing and adding down to the bottom most level to obtain the priorities of the alternatives. For example: use the priorities of the criteria with respect to the goal to weight the priorities of the alternatives with respect to the criteria, then obtain the overall priorities by summing these weighted values.
















The synthesis is the part of the process in which the global priorities are obtained by multiplying each ranking by the priority of its criterion and summing them for each alternative.

The method has been implemented in both its "Relative Model" and "Rating Model" variants. In addition, it has been combined with a routine to get the outcomes of multiple different ratings. The criteria adopted for the ranking are the following:

1. **Airframe-Propulsion Interaction** – This criterion is used to judge how much a configuration is able to exploit the benefits of hybrid-electric architecture through innovative airframe-propulsion interactions. This has been selected because leveraging on propulsion is part of the foundation of the UNIFIER19 vision.
2. **Aerodynamic Efficiency** – The reduction of chemical emission is an important design goal that depends, at a first glance, on propulsion efficiency and aerodynamic efficiency. The former is somehow included in the previous criterion, the latter is assessed with this criterion.
3. **Structural Efficiency** – This has been selected because it indirectly affects emissions through fuel consumption, in fact an aeroplane with lower structural efficiency has higher airframe weight, thus requires more lift, more power and more fuel.
4. **Noise** – Reduction of acoustic emissions is another key target for the project. It is explicitly evaluated with this criterion despite all the previous have also effects on noise.
5. **Cost and Design Complexity** – Every element of complexity in the design should be taken into account here, as each configuration has its own. This criterion is used as a means to take into account all those aspects specific of each individual design, which ultimately impact on cost and design complexity.

Table 7 presents the results obtained with the application of the AHP method. The histogram on the left side depicts the ratings attained by each of the 15 candidates at the end of the complete evaluation procedure. The rank is the result of the geometric mean among multiple different applications of the AHP, considered for robustness. Colours show the natural clustering inspired by discrete jumps in the score values.

Table 7 AHP ranking of the intermediate list of candidate configurations.

Score	Label	Definition		
		Layout	Wing	Propulsion
	0.22759 C3	Canard with "laminar flow fuselage", VIW and BLI		
	0.20612 C12	Tailless	TBW	DEP, WTP and BLI
	0.20415 C2	Canard PCA with DEP, WTP and BLI		
	0.20373 C7	Aft Tail	TBW	DEP, WTP and BLI
	0.19857 C15	TSA	TBW	DEP, WTP and BLI
	0.19850 C6	Aft Tail	Cantilever	DEP, WTP and BLI
	0.19420 C4	BWB with with asymmetric BLI-DEP		
	0.19419 C9	Aft Tail	Box Wing	DEP and BLI
	0.19399 C11	Tailless	Cantilever	DEP, WTP and BLI
	0.19380 C10	Canard	Cantilever	DEP, WTP and BLI
	0.19188 C5	BWA with DEP		
	0.19121 C1	Aft Tail	TBW	DEP and WTP
	0.18676 C14	TSA	Cantilever	DEP, WTP and BLI
	0.18284 C13	Tailless	Cantilever	WTP and BLI
	0.17913 C8	Aft Tail	Box Wing	DEP

The top-ranking configuration C3 stands out thanks to its relatively simple design that ensure great aerodynamic and structural potential while exploiting propulsion-airframe interaction. Configuration C2 is also a canard realization, with the added complexity of DEP.

Concerning C12, C7 and C15, all representing TBW applications, it may be noted that they represent relatively similar solutions, ranked very close to each other, and the are expected to provide relatively similar performance.

### 1.3.2 TUDELFT

Similarly to the activities performed by POLIMI, the design space has been initially scanned by assembling "compatible" subsystems solutions reported in the Option Tree of Figure 8.

The resulting design space has been built following a hierarchical order where the wing configuration is considered first; for that, four possible design options have been considered: a conventional Tube-and-Wing, A Truss-Braced Wing (TBW), a Closed Box Wing or PrandtlPlane (PrP) and a Blended-Wing-Body (BWB).

For each wing configuration, several possible aero-propulsive solutions are consequently considered: concentrated propulsions (CP), Distributed Propulsion along the wing (DEP), Wing Tip Propellers (WTP), Ducted Fans (DF), Boundary Layer Ingestion fans (BLI). Therefore, a total of possible 18 candidates has been extrapolated and reported in the following Table 8.

Table 8: Aircraft configuration selected for the first top-down selection (TUDELFT)

N.	Aircraft Configuration	Aero Propulsive Solutions
1		CP (Wing Location)
2		DEP
3	Tube and Wing (TW)	DEP + WTP
4		DEP + DF
5		DF (no tail)
6		BLI (at tail)
7		
8		DEP + WTP
9	TBW	CP (Wing Location)
10		DEP + DF
11		DF (no tail)
12		BLI (at tail)
13		
14	PRP	CP (Wing Location)
15		DF (back fuselage)
16		DEP (above the wing)
17	BWB	CP (upper part of the body)
18		DF( upper part of the body)

Considering the options determined in Table 8, the following initial assumptions have influenced notably the determination of the initial design space:

- a. A fuel-cell based powertrain, with the presence of batteries as additional power supply is considered the only viable option to both ensure the fulfilment of the nominal mission and to achieve the ultimate goal of zero emission flight. Therefore, no actual trade-off has been performed for the selection of the power generation devices.
- b. Incompatible or ineffective coupling of Aero-propulsive solutions and aircraft configuration have been preliminarily discarded. AS an example, WTP is not an effective solution for a PRP wing configuration as the tip vortexes and the related induced drag is already minimized.
- c. For all the aircraft configuration (except the BWB), the DEP is assumed to be placed in front of the leading edge in a tractor configuration. Additional studies on the exact placement of the propulsion devices
- d. BLI devices are assumed to be located at the tail of the fuselage.

- e. TBW-DF and TW-DF solutions do not present a tail but stability and controllability requirements are in principle guaranteed by the control of the flow exiting from the DF.
- f. In the PRP-CP configuration the propulsion devices are assumed to be located in pod under the rear wing.

The 18 resulting configurations are then ranked between each other by mean of a qualitative trade-off study. The purpose of this trade-off is to determine whether or not a certain candidate presents significant advantages with respect to the other ones and which configurations will enter the full conceptual design phase.

This trade-off consists of several criteria and their correspondent weight. The selected criteria reflect the most important aspect of the ultimate goal of a zero emission aircraft capable to operate the mission with the given flight requirements; the identified criteria are listed below and briefly explained:

- **Aerodynamic Efficiency:** the increase of aerodynamic efficiency during most of the mission is paramount to minimize the required energy, hence the size of the powertrain and the amount of required energy onboard. In addition, aero-propulsive interaction effects are taken into account.
- **Propulsive Efficiency:** this criterion takes the overall capacity of convert the energy sources into useful power for motion into account. Additionally, also the facility to integrate the propulsion system in the airframe is considered.
- **Structural Efficiency:** the EOW/MTOW fraction gives a first indication of how a certain structure arrangement can be lightened still guarantying the necessary strnght under design load.
- **Production Costs:** this term account to possible difference in the acquisition costs that can influence notably the operative costs and hence the marketability of the final product.
- **Ground operations:** it takes into account how well the designs can be integrated into current airports and their operations. For this criterion the following sub-aspects are considered: ease of maintenance and accessibility, ground clearance, dimensions of the aircraft and ability to land on small airports.
- **TRL/Certification:** given the presence of non-conventioanl solution for both the wing configuration and the propulsion system it is also important to correlate the effectivity of a certain solution to the probability to have this technology available for the targeted Entry Into Service of the vehicle.

The weight to each criterion has been calculated by following an Analytic Hierarchy Process (AHP) method, commonly used in decision making problems.

In this contest, the relative importance of each criterion with respect to all the ones is sorted out. If a criterion A is more important of a criterion B, its importance score will be a value between 1 (equally important) and 9 (extremely more important). Viceversa the score will be the reciprocate of the values if the criterion A is less important than a criterion B. All the mutual scores are then gathered into a matrix that can be normalized by making equal to the unity the sum of each entries of each column. Finally the weight of each criterion is built by averaging the entries of each row of the normalized pairwise comparison matrix.

The resulting weight system is reported in the Table 9.



Table 9: Weight for the trade-off criteria

Criteria					
Aerodynamic efficiency	Propulsive Efficiency	Structural Efficiency	Production Costs	Ground Operations	TRL/Certification possibility
33,94	13,73	23,75	4,62	19,99	3,97

As expected, Production Costs and TRL criteria influence relatively low the design choices whereas the other four criteria have more importance as there are heavily affecting the feasibility of the design according to the chosen requirements.

In order to measure the consistency of the chosen weight factor a consistency ratio CR can be calculated by considering the first eigenvector of the normalized matrix. The resulting consistency ratio for the calculated weight is  $CR = 0.035$  well below the threshold limit of 0.1 under which the criteria selection and weighting is considered to be reliable and well formulated.

Once the Criteria and the correspondent weights are defined, it is possible to score all the 18 aircraft configuration. For each criterion, the score system ranges from 1 (the configuration is unacceptable) to 10 (the solution is optimal). The scoring scale is reported in the Table 10 below:

Table 10: Scoring scale for the trade-off

Scoring scale									
10	9	8	7	6	5	4	3	2	1
Optimal	Excellent	Very Good	Good	Acceptable	Easily Correctable	Correctable	Problematic	Hardly Feasible	Unfeasible

To assign a score to each criterion for each configuration, a first sizing procedure and experience gained in previous similar design projects have been used to determine a reliable range of values for the main parameters such as  $L/D$ ,  $\eta_{prop}$ , EOW/MTOW.

The TW-CP configuration has been used as a benchmark to compare all the other configurations with; for this reason, a 10 has been assigned to only its Production Costs and TRL level, whereas all the other criteria range in the acceptable/good range. In this way, potential benefits as well as possible disadvantages on the more technical criteria can be properly accounted.

When all the scored are assigned the total scored can be calculated by summing all the contribution, multiplied by the weight of each criterion; this total score is then normalized with respect the maximum total score present in the list. The overall scoring system is reported in Table 11.

Table 11: initial trade-off

N.	Aircraft Configuration	Aero Propulsive Solutions	Criteria							Total normalized score	Rank
			Aerodynamic efficiency 33,94	Propulsive Efficiency 13,73	Structural Efficiency 23,75	Production Costs 4,62	Ground Operations 19,99	TRL/Certification possibility 3,97			
1		Concentrated Propulsion (CP) (Wing Location)	5	5	7	10	7	8	3	0,94	3
2		DEP	7	6	6	8	7	6	6	1,00	1
3	Tube and Wing (TW)	DEP + WTP	8	7	5	5	4	6	6	0,92	6
4		DEP + DF	8	8	3	4	7	3	6	0,94	2
5		DF (no tail)	7	8	4	5	7	4	6	0,94	4
6		BLI (at tail)	7	7	3	4	5	4	6	0,81	17
7		DEP	5	6	7	7	6	6	6	0,90	11
8		DEP + WTP	6	7	7	5	4	6	6	0,89	12
9	TBW	CP (Wing Location)	4	6	8	8	6	9	6	0,91	8
10		DEP + DF	7	8	5	3	4	3	6	0,86	14
11		DF (no tail)	6	7	6	6	6	6	6	0,93	5
12		BLI (at tail)	6	7	5	4	4	4	6	0,80	18
13		DEP	7	5	3	5	6	6	6	0,82	16
14		PRP	CP (Wing Location)	7	6	4	7	6	7	6	0,90
15	DF (back fuselage)		8	7	2	6	5	6	6	0,85	15
16	DEP (above the wing)		9	5	6	2	2	5	5	0,88	13
17	BWB	CP (upper part of the body)	9	6	6	2	2	5	5	0,90	9
18		DF (upper part of the body)	9	6	6	2	2	6	6	0,91	7

When looking at the overall score, the tube and wing configuration still outperform almost all the other non-conventional wing configuration. Some relatively high ranks have been given to the Truss Braced Wing configuration where the relatively worse ground operation due to the bigger aspect ratio of the wing, shade possible advantages in terms of aerodynamics and propulsion system. TW-DEP ranked 1<sup>st</sup> due its relatively high advantages of having a small and efficient wing. Little differences have been noticed between TW-CP, TW-DEP+DF, TW-DF; therefore, the following configurations have been top-down selected on the basis of those results:

- TW-DEP
- TW-CP
- TW-DEP+DF
- TW-DF

## 2 Conceptual design methods

### 2.1 POLIMI

In order to carry out the conceptual design of an aircraft, POLIMI has envisaged a multi-stage methodology, based on two major cores. These have been named after Hyperion and Argos. Hyperion (Hybrid PERFORMANCE SimulatIOn), a preliminary aircraft sizing tool capable of dealing with hybrid-electric powertrains, is a major outcome of the MAHEPA project, and has been thoroughly analysed in previous deliverables (MAHEPA WP9). An outline of the tool will be proposed in the next sub-section. Argos (AiRcraft GeOmetry Sizing), which allows to carry out lofting and produce a more detailed definition of the aircraft configuration, starting from lumped values (overall mass, power, battery energy,...) like those put by Hyperion, will be introduced next.

These two cores, considered in sequence, constitute a conceptual design methodology, named Titan. This has been widely exploited in the production of proposed configurations, for evaluation and selection, in the present deliverable.

#### 2.1.1 Outline of Hyperion preliminary sizing methodology

The proposed sizing methodology is able to generate optimal purely electric and hybrid-electric preliminary sizing solutions to specified mission, technology, certification, and other applicable requirements. This amounts to determining the aircraft design gross mass (Maximum Take-off Mass, or MTOM), the top-level mass breakdown specifying the mass of each of the main aircraft subsystems, the power rating of all the power-generating components, and the reference wing area. Optimality involves the minimization of MTOM, but may also be extended to other elements in the design, such as the sizing of single power-train components or the in-flight energy and power management strategies.

In fact, the presented method also provides the complete time histories of numerous variables along the sizing mission. The method applies to propeller-driven airplanes with a general serial hybrid-electric power-train architecture. This implies an electric motor driving each propeller, fed by electric energy derived from the combination of a battery pack and an electric power generation system (PGS). The latter is included here in two fashions: in the THE (thermal) case, the PGS is an engine-generator combining an electrical generator and a hydrocarbon-burning, Internal Combustion Engine (ICE) (possibly a reciprocating or turboshaft engine), supplying energy to the electric motor and/or the battery pack. In the FCHE (fuel-cell hybrid-electric) case, the PGS is a hydrogen driven fuel cell system. Hydrogen can be stored in the gaseous or liquid form.

A general serial hybrid-electric architecture is outlined in Figure 9. The yellow box on the left represents the fuel tank, connected to the big orange box in the middle that represents the PGS. Then, the PGS is electrically linked (light blue line) to the electric motor (green box) which, in turn, is mechanically connected (red line) to the propeller. The blue box on top represents the battery pack, electrically linked to the PGS and to the electric motor.

Conveniently, the formulation can be implemented so that purely electric (battery-only) and conventional aircraft are easily obtained as extreme cases in the serial hybrid-electric spectrum: the former by eliminating the PGS and the latter by eliminating the electric components of the power-train, i.e. battery pack, electric motors and generators, and by 'plugging in' directly the ICE included in the PGS to the propellers.

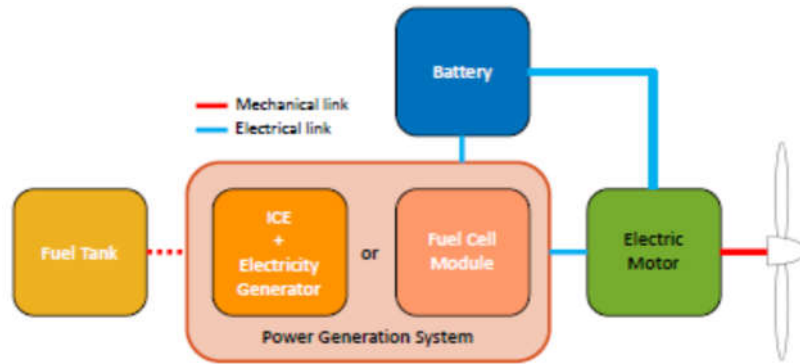


Figure 9 Serial hybrid-electric powertrain scheme

The methodology combines the ability to resort to historical-statistical estimations and the direct modelling of aircraft main subsystems, in a modular fashion. The corresponding submodules have been documented in detail in previous deliverables (in particular, the deliverables of WP9 of project MAHEPA). The flowchart of the implementation of Hyperion can be exposed as in Figure 10.

The methodology consists in a two-step procedure. First, the requirements from mission analysis are imposed together with certification standards, and other design specifications, a first-guess design point is chosen on the sizing matrix plot (SMP), and an iterative calculation is carried out for the weight sizing until convergence. This provides an initial solution in terms of mass breakdown, power sizing and wing sizing, together with the estimation of some basic quantities of geometric and aerodynamic nature (such as the wing aspect ratio and the aircraft drag polar curve). The initial solution is used to start another iterative computation in which the full sizing mission is simulated through a time-marching run. This step in the procedure allows to take into account the time evolution of the dynamics of the power-train in a finer manner, typically leading to adjustments on the initial estimation.

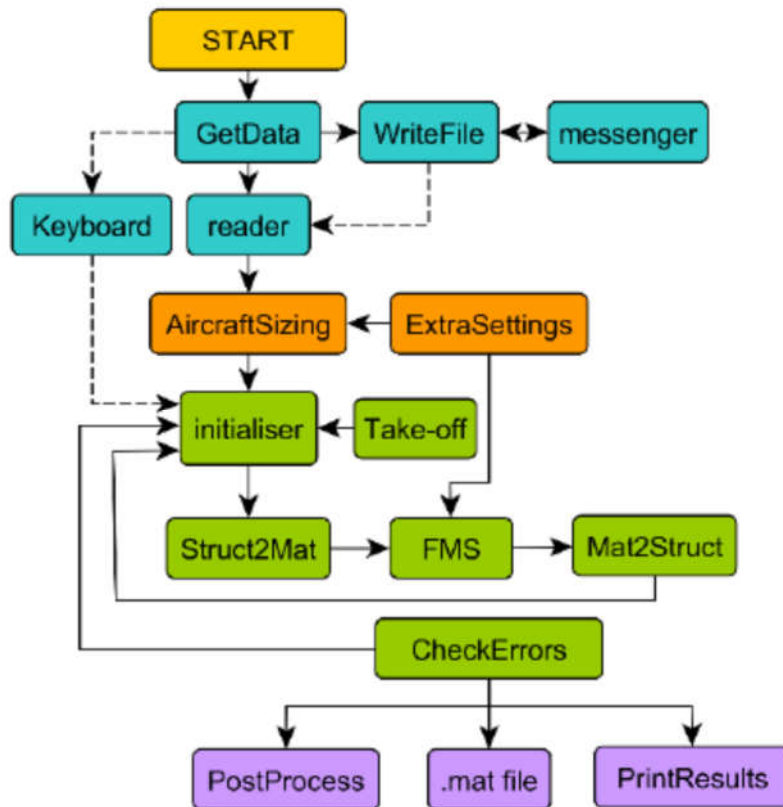


Figure 10 Flowchart of the Hyperion preliminary sizing tool

In Figure 10, the *AircraftSizing* block stands for the core of the operations leading to the initial solution, while *FMS* (Flight Mission Simulation) represents the time-marching computation block. The process starts by solving for an initial MTOM guess and looping until convergence, while accommodating all mission requirements and performance specifications derived by the applicable certification basis or other design considerations and bringing into play a number of parameters yielded by the market analysis and technology surveys, that are normally carried out prior to the start of conceptual design.

Within *AircraftSizing*, all components of weight are adjusted in a fully coupled fashion, taking into account changes in power and energy needs arising from changes in the various mass components, and seeking minimum gross design weight. Once convergence is achieved, the time simulation in *FMS* is deployed, and the masses of energy storage components, i.e. battery pack and fuel tank, are corrected in order to satisfy mission requirements. This typically leads to small adjustments that do not require adaption of other mass components, e.g. electric motors, power generation system and non-propulsive airframe. In case adjustments are more substantial, of course the process can be repeated feeding *AircraftSizing* with the *FMS* solution as a new initial guess.

### 2.1.2 Aircraft configuration and detailed sizing in Argos

Argos is a tool implementing Class I sizing methodologies for geometric sizing and can provide a better estimate of the subcomponent's weights and aerodynamic drag polar than Hyperion. However, Argos fully relies on Hyperion results for power-train sizing. In Figure 11 a flow chart of Argos is illustrated.

The first step is wing design. The airfoil is selected based on the required aerodynamic characteristics (target L/D or stall coefficient). After that, an innovative lifting line theory for twisted wings is used

through a function to compute the wing taper ratio, twist angle and incidence minimizing the induced drag.

The next step is fuselage sizing. The procedure for the fuselage can find the best external diameter and length based on the selection of an optimal slenderness ratio. The internal dimensions are calculated taking into account the cabin layout for passengers and cargo.

Successively, the external size of the fuselage is defined. An important aspect to determine in the sizing of the fuselage is the type of power-train (THE, FCHE). In many cases, there is a need to find room for hosting batteries, fuel tanks and a PGS. For what concerns hydrogen tanks, gaseous hydrogen tanks are typically placed on top of the cabin, because they take a large volume, and their shape is constrained due to their high inside pressure (cylindrical shape). This usually produces a fuselage diameter which is larger than it would have been on a conventional airplane. On the other hand, liquid hydrogen tanks can be fitted behind the passenger's cabin, as the shape is not constrained by pressurization limitations and the weight is usually much more contained than gaseous hydrogen tanks.

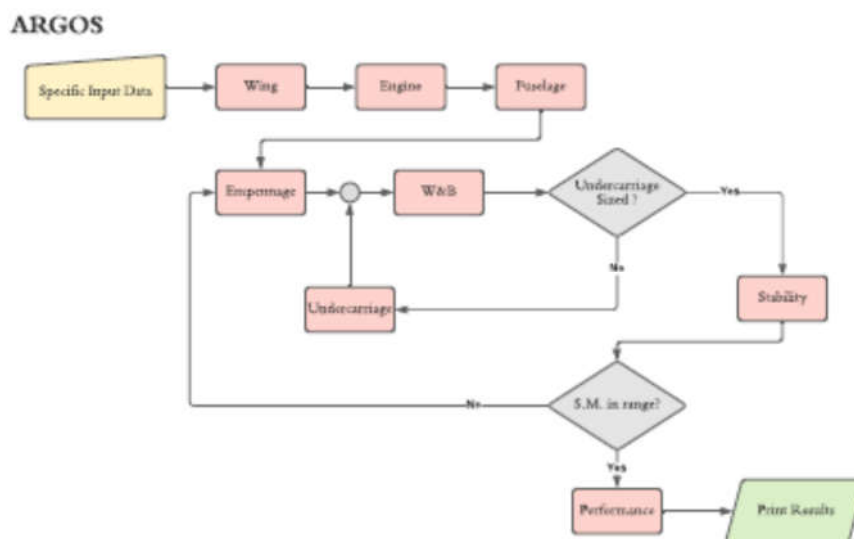


Figure 11 Flowchart of the main blocks of Argos

At this point, the other aircraft components are sized, such as the empennages and the landing gear. Finally, the weight and balance (W&B) module estimates all the weights and centre of gravity positions for all the subcomponents.

All the steps described above run inside an optimization loop that guarantees that the static margin remains within a required range. In particular, the size of the horizontal tail is tuned to meet the request. Once the complete configuration and geometry has been sized, the parasite drag coefficient is calculated. For each configuration (gear up/down, flaps up/down) it is possible to obtain the analytical drag polar and the performance indices (such as the lift-to-drag ratio), based on well-proven build-up methods (Roskam). The Argos code bends itself to a many extensions, dealing with virtually arbitrary possible configurations. This feature has been exploited in the present deliverable, to analyse concurrent designs, and selecting more promising configurations.

### 2.1.3 Conceptual design with Titan

The coupling of Hyperion and Argos in Titan represents a complete tool for the conceptual design of hybrid-electric aircraft. As pointed out, the design process begins when Hyperion provides an initial estimation of the overall wing sizing (surface and span), and a weight breakdown of the aircraft: non-propulsive air-frame mass, PGS system, fuel, batteries and electric motors, and hydrogen tanks in case of a FC-Hybrid architecture.

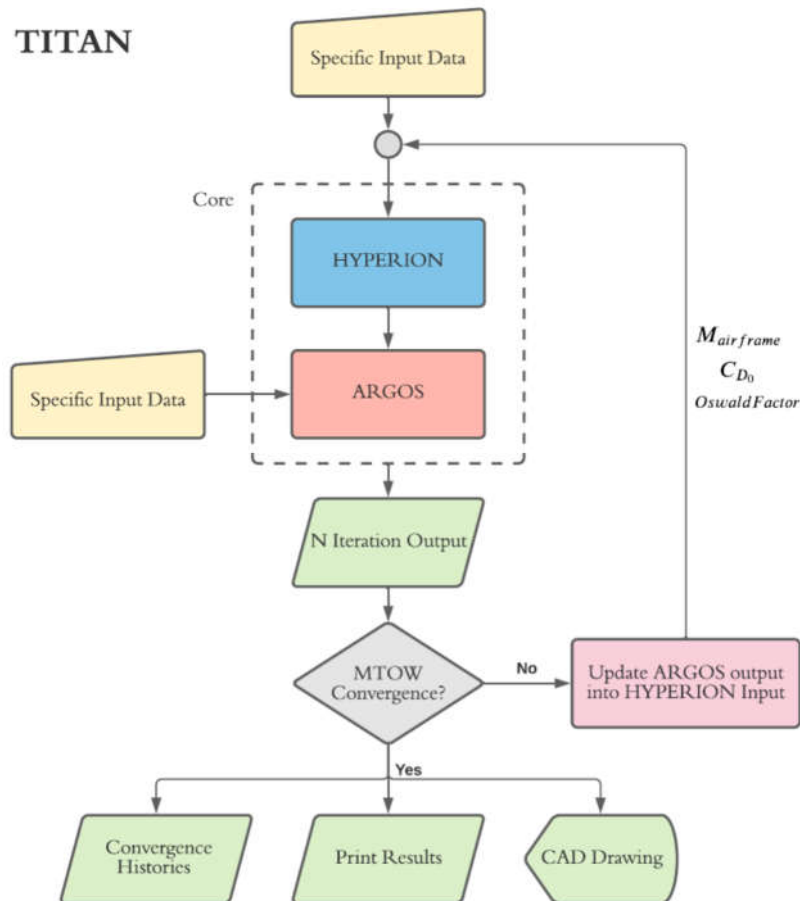


Figure 12 Flowchart of the main blocks of Titan

Afterwards, Argos uses input data from two different sources: the output data from Hyperion and a specific information about the aircraft configuration. For a reliable solution, the output weights from both tools must be equal. Thus, an iterative loop is implemented through Titan, in which the Argos output for the non-propulsive airframe mass and the aerodynamic data (parasite drag) is used to start a new solution of the Hyperion module. This process is repeated until the output MTOM from both converge. When they successfully collimate a solution, the convergence histories, as well as a CAD drawing and the related numerical results are printed. A schematic of this logic is in Figure 12.



## 2.2 PIPISTREL VERTICAL SOLUTIONS

### 2.2.1 Introduction

Pipistrel has developed an aircraft conceptual design procedure to perform the conceptual design of a CS23 category aircraft featuring a FC powertrain. Its basic workflow structure is shown in Figure 13, where individual building blocks are depicted by colour frames, workflow by dashed arrow and data flow by solid line arrows.

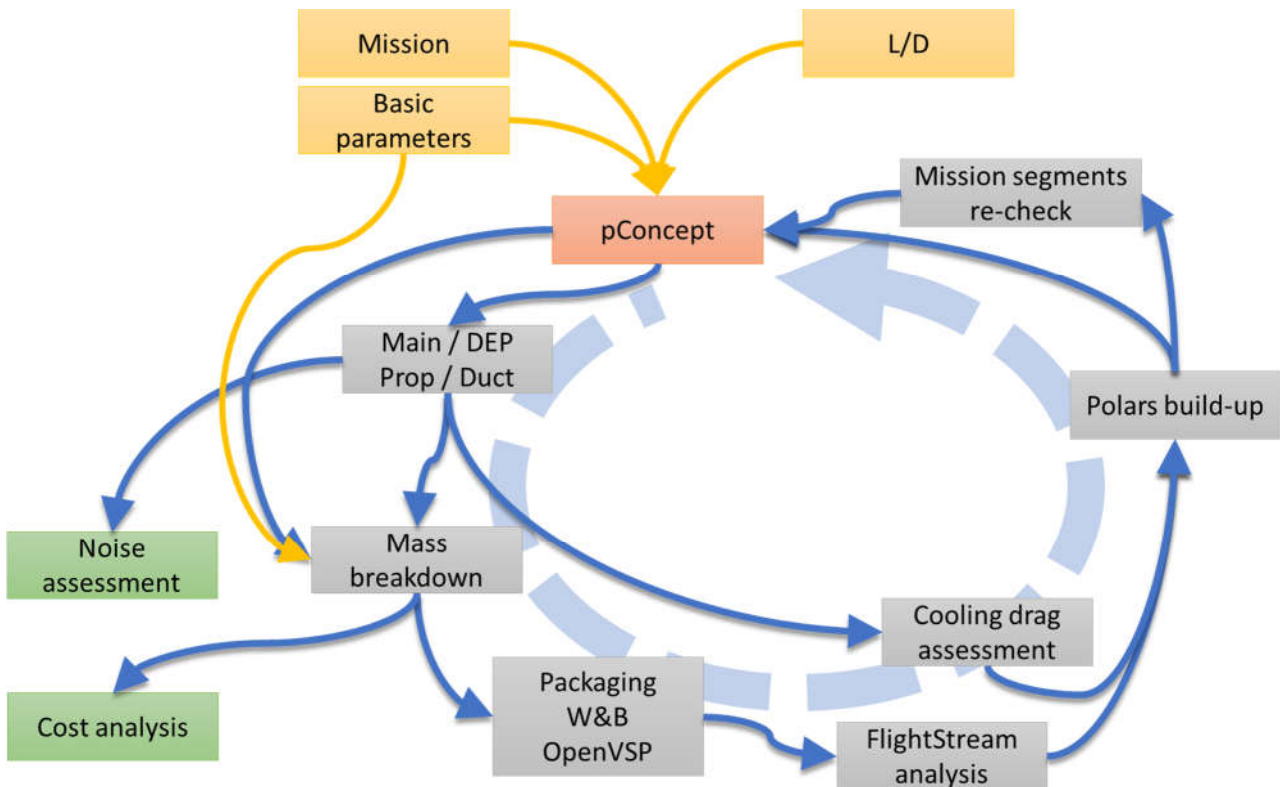


Figure 13 Pipistrel Class II Conceptual Design Loop

It is an iterative Class II conceptual design loop which has a preliminary sizing loop integrated in pConcept building block. There, the first sizing of the aircraft is performed with the purpose to identify key parameters as the Wing and Power Loading, Maximum Take Off Weight, initial dimensions of the main components. etc. The sizing is done on the basis of the operating requirements identified through the Market analysis of WP1 and, in addition, initial assumptions on some technologic parameters such as values on the gravimetric index for the hydrogen tank, energy and power density of the main propulsion components etc.

In the first iteration step, the pConcept input data comes from Mission definition, technology assumptions (Basic parameters) and L/D assumption (for each mission segment). However, in next steps, the L/D assumption is replaced with the actual polar (-s) information from aerodynamic analysis and cooling drag assessment combined in Polars build-up building block. The pConcept solution is then refined by means of more physic-based or semi-empirical models integrated in a Class II loop, where subsystems are sized. The tool allows to take into account also novel aero-propulsive solution such as Distributed Propulsion, Tail propeller, Wing Tip propeller, Ducted Fan.

As explained above, pConcept is just one part of the Class II conceptual design loop. This loop consists of several building blocks with mid-fidelity tools and/or more detailed analysis.

Main building blocks of the loop are:

- pConcept(Section 1.1.1): a new preliminary sizing loop was developed which is also capable of handling Class II loop results in subsequent iterations steps.
- Main / DEP, Prop / Duct(Section 2.2.3): an automated procedure for designing individual propellers /ducted fans using XROTOR (M. & H., xrotor, 2003) / DFDC (M & H, 2005) opensource software and for acquiring their performance map for subsequent iteration building blocks.
- Mass breakdown(Section 2.2.4): mass estimation procedure for aircraft components that are not evaluated in pConcept but are important for estimating the Center of Gravity location. Mass values are estimated by statistical regression or semi-empirical methods.
- Packaging and W&B procedure(Section 2.2.5): point masses from previous steps and TLAR defined masses are used for Center of Gravity (W&B procedure) location estimation. Each aircraft component location is checked in Packaging procedure by its volumetric requirement. The packaging is performed in OpenVSP (an open-source software for generating parametric geometry aircraft, (McDonald, 2016)).
- FlightStream analysis(Section 2.2.6): an automated procedure was developed where aerodynamic surfaces from the OpenVSP model are introduced to vorticity-based flow solver to analyse aircraft aerodynamic properties (polars) in all segments of the mission.
- Cooling Drag Assessment procedure(Section 2.2.7): a new cooling system design procedure was developed and validated on existing electric, hydrogen hybrid electric and ICE hybrid electric airplanes. The procedure returns cooling system basic design and cooling drag with respect to power rejection requirements.
- Polars build-up procedure(Section 2.2.8): a new methodology was established where aerodynamic information from previous steps is combined to form a realistic polar data of the whole aircraft. CFD correction factors are introduced as well.
- Mission segments re-check(Section 2.2.9): additional automatic procedure to check aircraft performance in each mission segment in time stepping manner was developed. The aircraft performance is compared with the next step of pConcept prediction.
- Noise assessment procedure(Section 2.2.10): an automated procedure was developed which combines XROTOR for propeller tonal noise estimation and Pegg's method for broadband noise estimation (see also D1.1)
- Cost analysis(Section 2.2.11): a new methodology, derived from four existing methodologies, was developed and validated on existing 19-seater category aircraft (see also D1.1)

## 2.2.2 Preliminary sizing loop description – pConcept

The pConcept tools is a preliminary sizing loop for aircraft sizing. In its core, the pConcept program runs a procedure that converges the aircraft weight. The idea behind the algorithm is heavily inspired by the sizing procedures from aircraft design books such as (Raymer, Aircraft Design: A Conceptual Approach, 2018) . The inner working of pConcept is sketched in Figure 14.

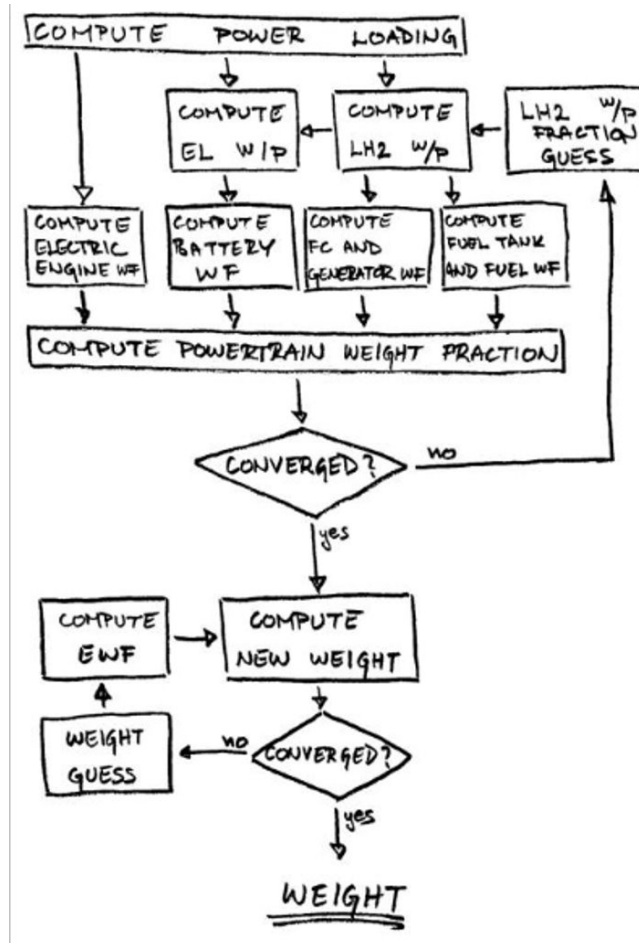


Figure 14 pConcept workflow diagram

The pConcept program was modified to handle serial hydrogen hybrids. The algorithm starts by computing the required shaft power loading (W/P) in each mission segment – that is, the ratio between required power and aircraft mass. For this purpose, the aircraft L/D needs to be assumed a-priori. This power requirement is then split between hydrogen and electrical propulsion which in turn gives the mass ratio between different components and the aircraft total mass. Fuel weight fraction is also computed here. Summation of all these ratios gives the powertrain weight fraction (WF). If needed, the ratio between electrical and hydrogen power can be amended with a goal to minimise the powertrain weight fraction.

If the powertrain weight fraction meets the requirements, the program moves into the next phase. Here powertrain weight fraction is combined with airframe mass fraction (EWF) and new aircraft mass is computed. If aircraft polars are available, the initial L/D assumption can be updated, and the powertrain weight fraction can be recomputed. If the airframe weight fraction is dependent on maximum aircraft weight, it can be updated as well. This cycle repeats until the aircraft weight converges.

The main output of the pConcept is therefore the total aircraft weight with additional mass breakdown for certain components. The power requirements are also available after the completion.

### 2.2.2.1 Comparison with Hyperion

The sizing results were compared with the results from Hyperion, which is POLIMI’s sizing tool. The differences between the tools were quite small, about one percent of mass difference for the whole aircraft and not more than five percent of a difference on a component level. The differences are believed to come from slightly different implementation and rounding and were not investigated further, as the match is deemed sufficient. For comparison between Hyperion and pConcept, see Figure 15.

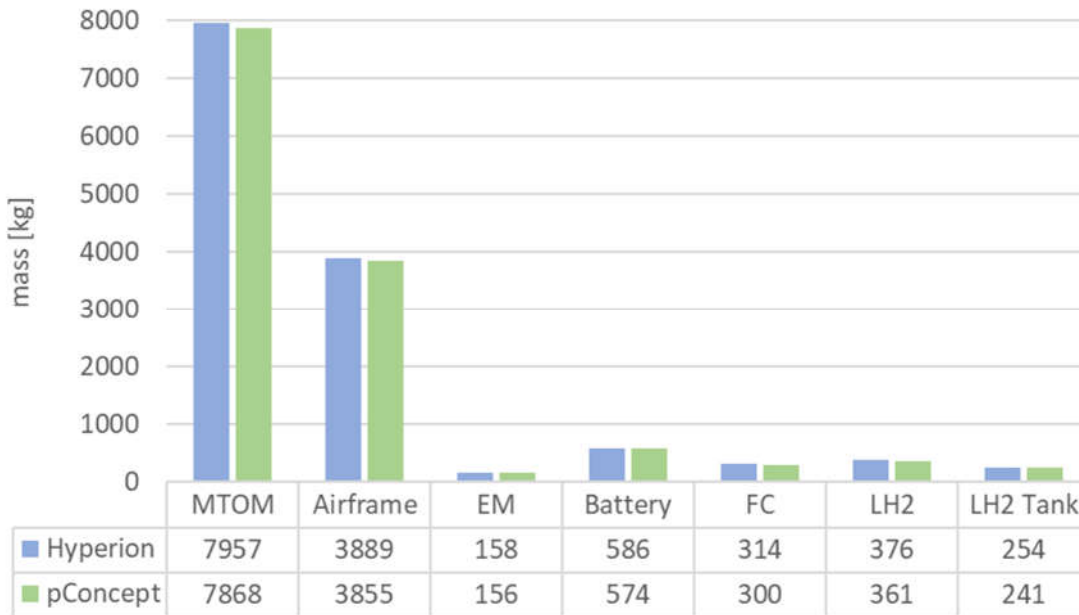


Figure 15: Comparison between Hyperion and pConcept for C7A aircraft. Other aircraft have similar differences.

### 2.2.3 Main/DEP, Prop/Duct

In this section, the methodology for main and distributed electric propulsion propeller design and for ducted fan design is presented.

The input data for propeller/ducted fan design comes mainly from the pConcept. It consists of total power required for each mission segment and required lift augmentation for take-off speed ( $=1.1 \cdot V_{\text{stall}}$  for take-off configuration (Raymer, Aircraft Design: A Conceptual Approach, 2018)).

#### 2.2.3.1 DEP propeller design

The lift augmentation is proportional to the axial slipstream velocity of the DEP propellers given by the following implicit formula (Michael D. Patterson):

$$\frac{\Delta L'}{L'_\infty} = \left( 1 - \frac{\beta V_p \sin i_p}{V_\infty \sin \alpha_a} \right) \frac{\sqrt{V_\infty^2 + 2V_\infty \beta V_p \cos(\alpha_a + i_p) + (\beta V_p)^2}}{V_\infty} - 1$$

where wing-propeller combination geometry is shown in (Figure 16):

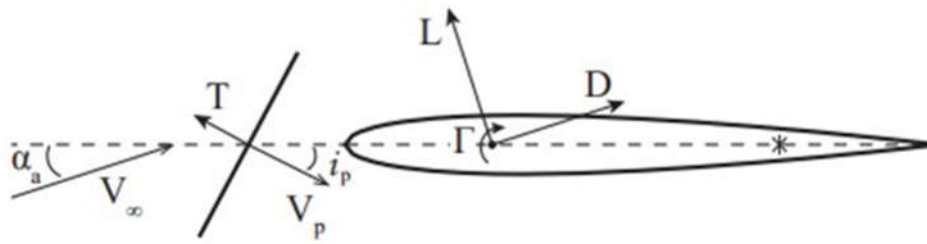


Figure 16 Propeller/wing configuration for augmented lift estimation

$\Delta L'$  – lift increase due to augmentation

$L'_\infty$  - lift without augmentation

$\beta$  – finite slipstream height factor

$V_p$  – average propeller slipstream

The propeller was designed using XROTOR opensource software, satisfying average slipstream velocity requirement at the take-off speed. The propeller performance map was automatically acquired on the aircraft velocity interval (where the DEP was switched on), keeping the propeller power value the same as in the design point. The propeller performance data (CT, CQ, rpm, efficiency) as well as physical properties (chord distribution, airfoil set data) were used in subsequent analysis (aerodynamic analysis of the whole aircraft, mission analysis, noise assessment, ...).

#### Example: PVS1 (see Section 3.5) DEP propeller

Distributed electric propulsion propeller for PVS1 aircraft candidate is designed in following design point:

$V = 39.4$  m/s

$P_{\text{shaft}} = 54$  kW

rot. speed = 1500/min

It is a 5-bladed, constant pitch propeller with a 1.47m diameter, shown in Figure 17. Odd number of blades is beneficial for lowering noise originating from propeller wake - wing interaction.

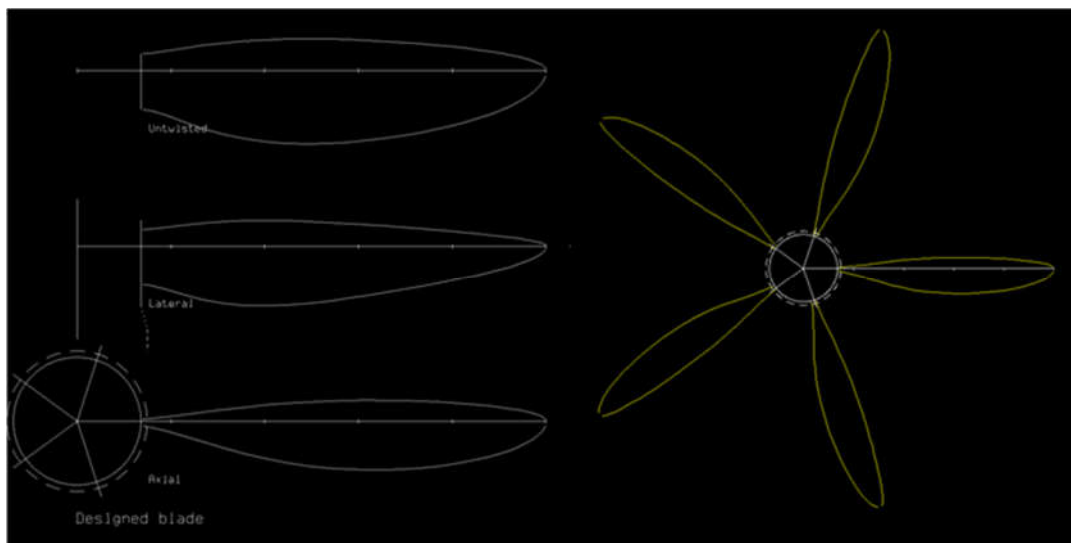


Figure 17 PVS1 DEP propeller geometry

The propeller efficiency was calculated for a range of aircraft velocities, depicted in Figure 18, assuming constant power over the velocity interval. Highlighted is DEP operational velocity range.

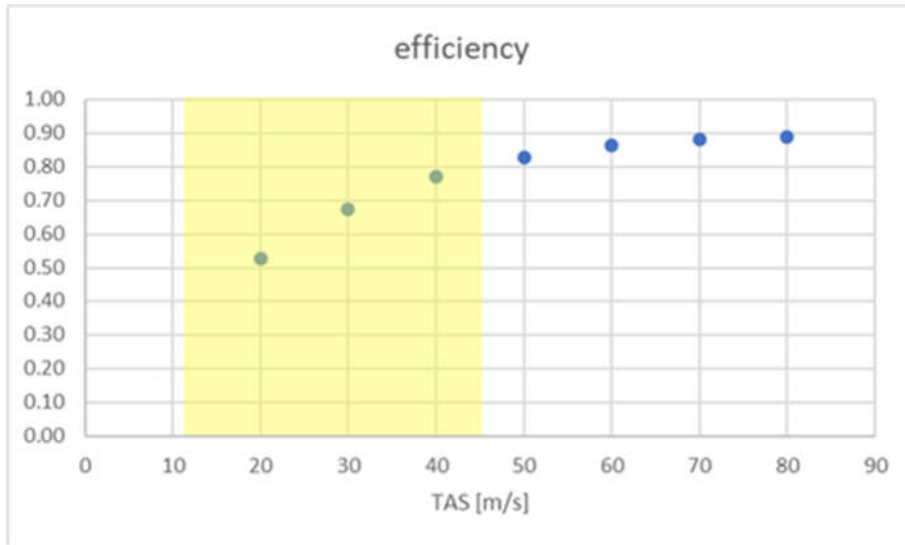


Figure 18 PVS1 DEP propeller efficiency over velocity interval

### 2.2.3.2 Main propulsion design

Main propulsion consists of one or two (counter-rotating) propellers on the tail cone (C7A, C2, C3), wing mounted propellers (REF) or ducted fan on the tail cone (PVS1).

Propellers were designed using XROTOR, providing maximum thrust for available power at take-off and maximizing efficiency at cruise speeds. The performance maps were acquired automatically with the same procedure as for DEP propellers.

#### Example: C7A (see Section 3.3) Main propeller

Main propeller (tail cone propeller) for POLIMI candidate C7A was designed in cruise design point conditions:

$V = 77.2 \text{ m/s}$

$P_{\text{shaft}} = 510 \text{ kW}$

rot. speed = 1500/min

It is a 5-bladed, 2.88 m diameter, constant-speed propeller with the efficiency of 87% in the design point (Figure 19).

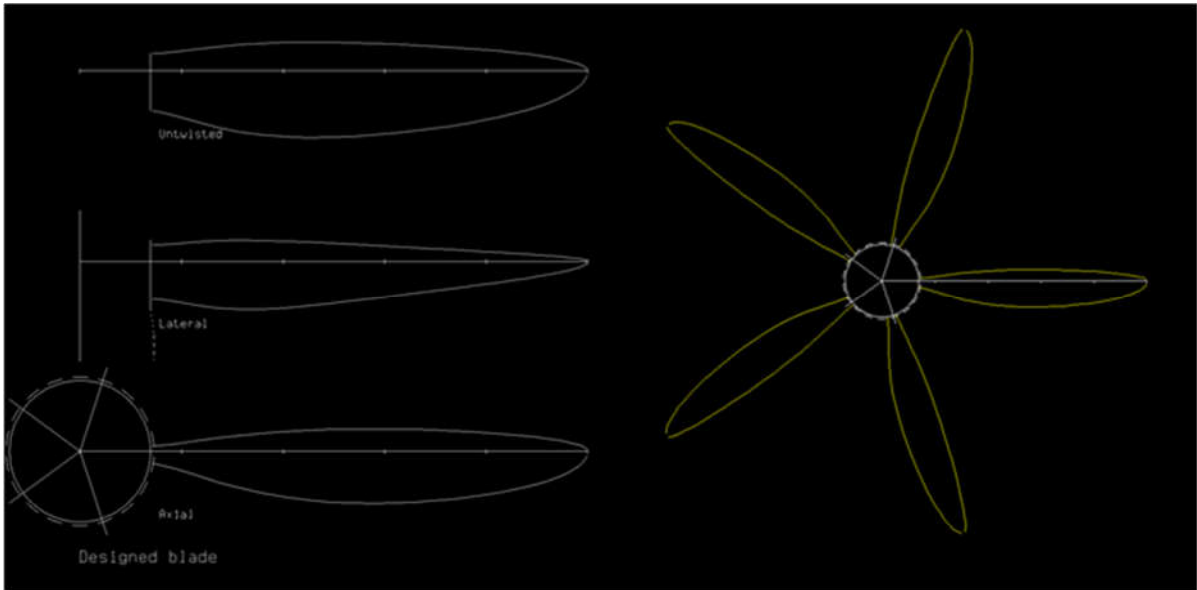


Figure 19 C7A main propeller geometry

In Figure 20, efficiency over the aircraft speed range is shown, where power and tip speed are constant (510 kW, 1500/min).

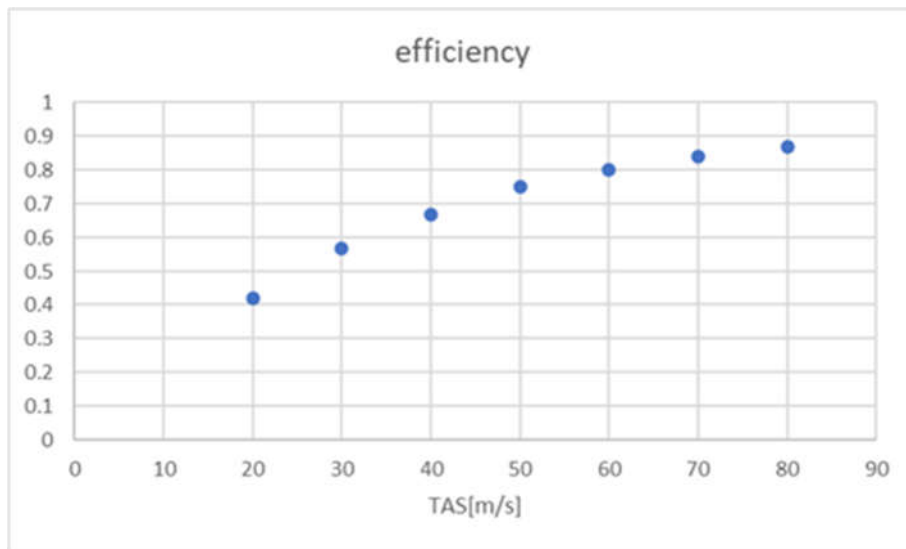


Figure 20 C7A main propeller efficiency

### 2.2.3.3 Ducted fan design

Ducted fan design procedure was using DFDC (M. D. , DFDC, 2005) opensource software for fan, stator and duct shape design. The procedure and performance map calculation was similar to propeller design using XROTOR. DFDC returns the total thrust of the ducted fan for a given operational point. The total thrust consists of propeller thrust, stator thrust and duct thrust (or drag at higher aircraft velocities). Since the duct and stator drag are already a part of total thrust value of the whole propulsion unit, the duct geometry is excluded from aerodynamic analysis in FlightStream.

**Example: PVS1 (see Section 3.5) ducted fan**

Only PVS1 aircraft candidate uses ducted fan as the main propulsion device.

The design point parameters are:

$V = 77.2 \text{ m/s}$

$P_{\text{shaft}} = 493 \text{ kW}$

rot. speed = 1300/min

No particular optimization was performed on the duct geometry, however, a reasonable geometry was selected based on DFDC author's recommendations.

In Figure 21, blade geometry (left), rotor geometry (mid) and duct/hub geometry is shown. It is a 7-bladed, 2.7m diameter, constant-pitch propeller fan with the efficiency of 80% in the design point (Figure 19).

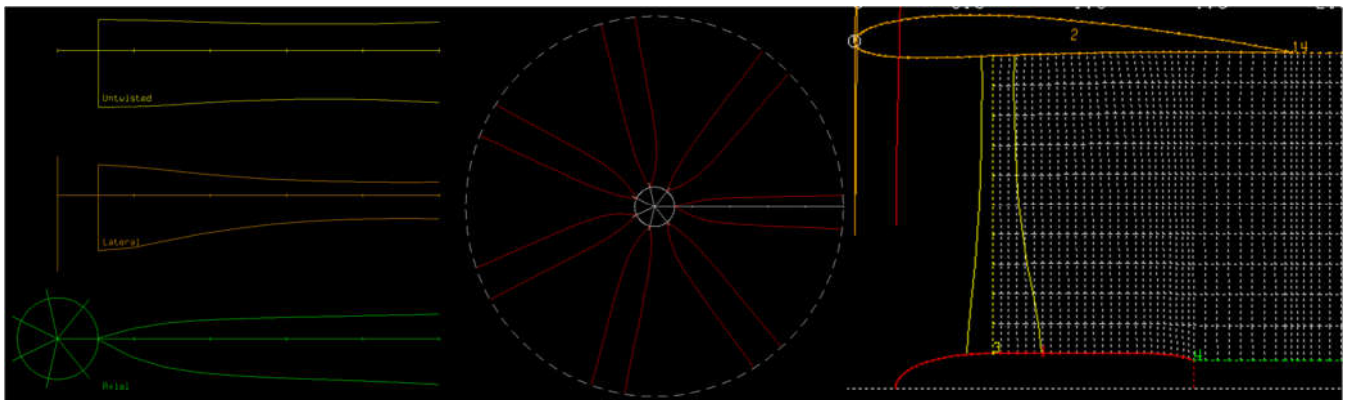


Figure 21 PVS1 ducted fan geometry (left: one blade; mid: rotor top view; right: duct, hub and blade cross section)

Efficiency maps for climb and cruise power setting are depicted in Figure 22.

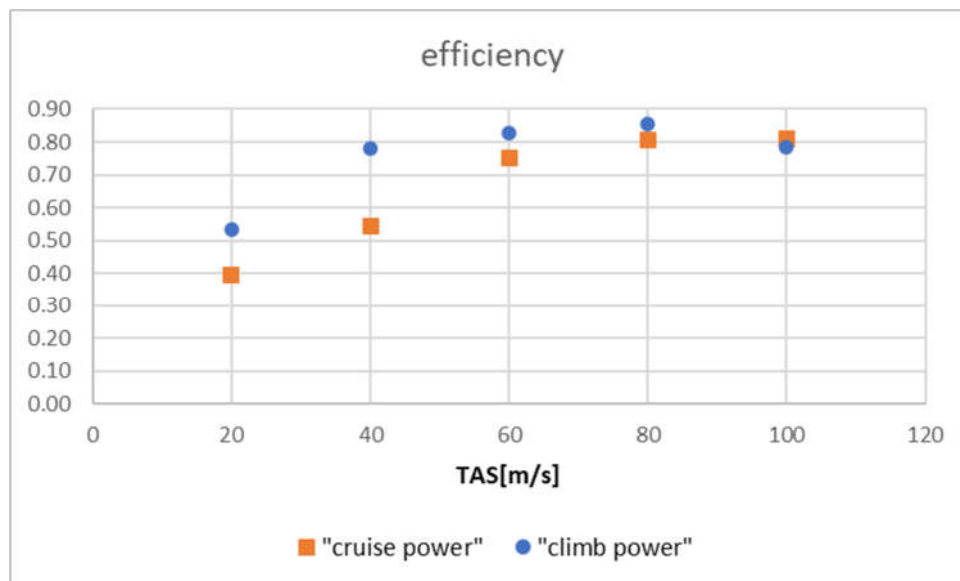


Figure 22 PVS1 ducted fan efficiency in climb and cruise power settings



## 2.2.4 Mass Breakdown

In this tool, individual aircraft component masses are defined in more detail. pConcept returns following mass information:

- Airframe
- Crew + payload (passengers or cargo)
- Battery
- Fuel cells
- LH2 tank
- LH2 fuel
- Electric engine

These components are, where applicable, split into subcomponents and a position coordinate is assigned to each subcomponent, which is used/updated iteratively with next design step (Packaging, W&B, OpenVSP).

Table 12 shows an example of mass breakdown and coordinates assigned to individual components for PVS1 aircraft candidate. Two more columns (“m\*x” and “contribution”) are added for CG position estimation. The right column (“contribution”) indicates degree of contribution of individual component to CG position, red colour being most critical aft component and green most favourable front component. For example, duct represents a critical component since it is a heavy aircraft building block positioned far behind the CG.

Table 12 Mass breakdown for PVS1 candidate - main window

PVS1				
	m	x	m*x	contribution
Wing	721	9.0	6487.198	-6%
Fuselage	1005	8.1	8135.714	3%
Duct	244	16.9	4120.934	-27%
Fuel fuselage	306	8.4	2558.16	0%
Landing gear	353	9.6	3385.92	-6%
Pilot	100	2.5	250	7%
Cargo	836	11.1	9237.8	-29%
Control surf	239	8.6	2055.4	-1%
duct engine + prop	154	16.0	2468.381	-15%
Instr. Nav	45	1.3	56.75	4%
Hydr. Pneu	8	5.0	40	0%
Electric syst	202	10.0	2020	-4%
Electronics	128	1.3	160	11%
Air cond anti ice	447	4.4	1986.456	22%
Furnishing	434	8.1	3510.095	1%
Passengers	1444	5.3	7653.2	55%
Battery	399	8.2	3283.77	0%
PGS	378	9.6	3609.9	-6%
Hydrogen tank	206	8.4	1722.16	0%
DEP	148	8.1	1196.213	0%
Vtail	80	17.4	1390.2	-9%
<b>MTOM</b>	<b>7877</b>			
<b>CG_X</b>	<b>8.3</b>			
<b>CG_X_aft</b>	<b>9.0</b>			

The masses of subcomponents are estimated by different methods (statistical regression, semi empirical, ...) and the sum of subcomponents set is compared with original pConcept component mass.

Examples of mass estimation methods:

- Wing: (Raymer, Aircraft Design: A Conceptual Approach, 2018) and (M. N. )
- Duct: (Dungen, 2017)
- Landing gear: (Raymer, Aircraft Design: A Conceptual Approach, 2018)

### 2.2.5 Packaging and W&B procedure

In Packaging and W&B procedure, 3D models of the aircraft building blocks are generated and their integration inside the available fuselage volume is checked.

The volumetric information from previous steps (TLAR, pConcept, Main/DEP Prop/Duct, Mass breakdown) is used to generate a 3D shape of the component. The packaging procedure is performed in OpenVSP, opensource software for parametric aircraft design, where 3D modelling of individual aircraft building blocks is adapted to the degree of volumetric information of each block.

For example, wing geometry is characterized by its cross-section points, span, taper, twist and dihedrals, and thus its 3D shape is well defined. On the other hand, fuel cells with the balance of plant or battery packs have less volumetric information at this design stage and thus are represented with a simpler model (box, cylinder, ...) or as a conformal element inside the fuselage in case of luggage compartment.

Figure 23 shows 3D model of the PVS1 aircraft candidate generated in OpenVSP. Inside the fuselage, the pilot, passengers, seats, LH2 tank (yellow) and luggage compartment (pink) are visible. All aircraft candidates have similar interior arrangement thus only PVS1 is shown.

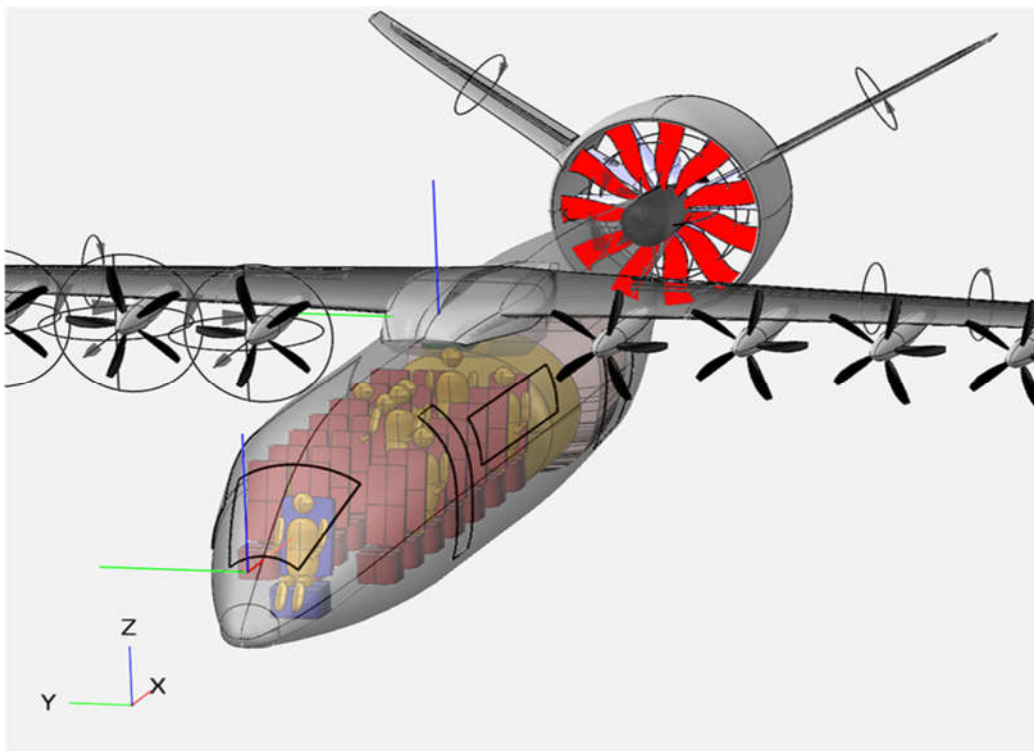


Figure 23 3D model of PVS1 aircraft candidate in OpenVSP

Coordinates of individual component from OpenVSP model can be used in W&B procedure (Table 12) to update the CG location. A particular attention should be given to positioning the components inside the fuselage, due to limited available space and components' strong effect on the CG location. Packaging and CG location estimation is an iterative process, where trade-off between suitable CG location and convenient interior arrangement is achieved.

At the end, a subset of 3D models generated in OpenVSP, representing aerodynamics surfaces, is exported to be used in Aerodynamic analysis (Section 2.2.6).

## 2.2.6 Aerodynamic analysis

In this section the methodology for assessing the aerodynamic performance of each candidate is discussed. Firstly, a brief overview of the methodology is given, and then, results of each candidate are presented. Finally, general observation regarding the aerodynamic performance of the candidates is discussed.

### 2.2.6.1 Methodology

Figure 24 illustrates the overall aerodynamic analysis flow chart. It can be seen that two external software tools are used to perform the analysis: OpenVSP and FlightStream. The input to the analysis is the candidate design data, which contains information about the external geometry of the aircraft (wing sizing etc.), as well as the propeller performance at desired design points. In the case of POLIMI candidates, the candidate geometry data is from the report file provided by POLIMI. In the case of PVS candidate the geometry is from PVS design toolchain. In order to assess the aero-propulsive performance, propeller performance data is needed. This data is gathered using PVS methods. Refer to Section 2.2.3 for discussion about the propeller performance analysis.

OpenVSP is used to generate the geometry which is used to generate the mesh. The mesh file is imported to FlightStream. In the FlightStream, the mesh is prepared for analysis by manually repairing meshing imperfections. The propellers are added as actuator disks. For each candidate, the performance is evaluated for selected operating points with props-on/props-off depending on the candidate design. Finally, FlightStream results are stored for each candidate.

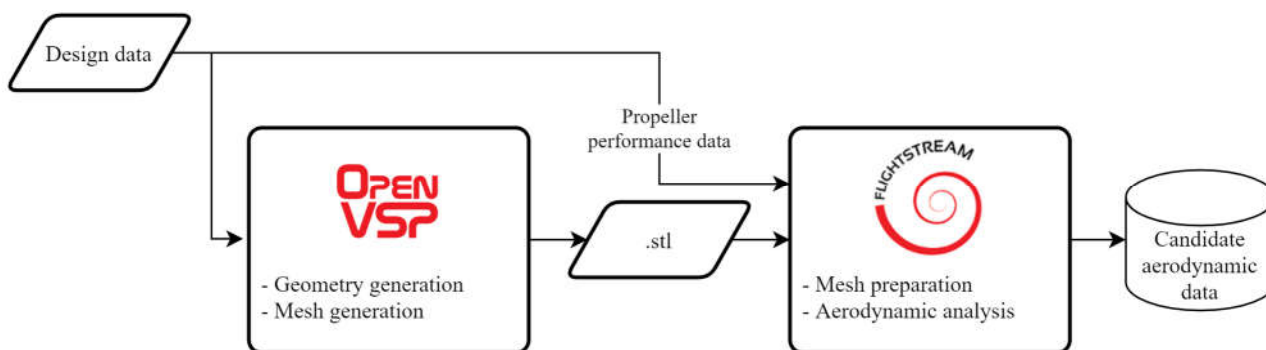


Figure 24 Flow chart of the aerodynamic analysis methodology.

### **2.2.6.1.1 FlightStream**

FlightStream is a surface vorticity solver developed by Research In Flight. The solver can analyse three-dimensional geometries, while also allowing to model powered flight. The solver contains models for skin friction and flow separation. Because the tool is a panel method, the required mesh is a surface mesh and not a volumetric; hence the computational time is significantly lower than on full volumetric CFD. The theoretical background of the FlightStream solver is presented and discussed in detail by (Ahuja & Hartfield, 2016). In general, the solver can be classified as a mid-fidelity analysis too, offering significantly more detail than conventional panel methods, like AVL or VSPAERO. Even though FlightStream contains flow separation capabilities, it can be considered indicative, as often stalling behaviour is a result of a more complex and detailed flow phenomena, which is particularly hard to capture using panel methods.

FlightStream can model arbitrary number of propellers for which the user must define blade diameter, thrust coefficient, and rotational speed. The propellers are modelled by potential flow actuator theory based on the work by (Conway, 1995). The actuator disks have elliptical propeller disk loading distribution. The actuator disk model of FlightStream has been seen to agree well with wind tunnel measurements. Interested reader is referred to validation study by (Soikkeli, 2020).

The skin friction drag and flow separation is predicted in FlightStream by using a two-dimensional integral boundary layer model along the local surface streamlines. The model can evaluate the laminar and turbulent boundary layer, as well as the boundary layer transition and flow separation. The laminar boundary layer is calculated based on the work by (Curle, 1967). During the computation of each point of the laminar boundary layer, a check is performed to detect whether the boundary layer continues laminar, naturally transitions, separates and attaches as turbulent, or separates with no reattachment. In case the flow is separating from the surface, the solver is shedding a vortex from the separation point. Thus, relaxing the Kutta condition. The boundary layer analysis in the FlightStream solver is based on the earlier work by the NASA developed PMARC panel code. Interested reader is referred to (Ashby, Dudley, Iguchi, & Browne, 1999).

### **2.2.6.1.2 Analysis points**

Because aero-propulsive interactions are not airspeed independent, the performance of each candidate cannot be assessed with one set of non-dimensional coefficients. Additionally, for some candidates the propulsion is only leveraged at certain phases of flight. Hence, for each candidate all the relevant operating conditions are assessed separately and for each operating point aerodynamic polars of force and moment coefficients are collected. Note that only longitudinal aerodynamic performance was analysed.

Note that only propellers that have aero-propulsive interaction affects are modelled. Also, only the impact of the propeller wake to the airframe is captured. In other words, neither forces nor moments due to propellers themselves are recorded.

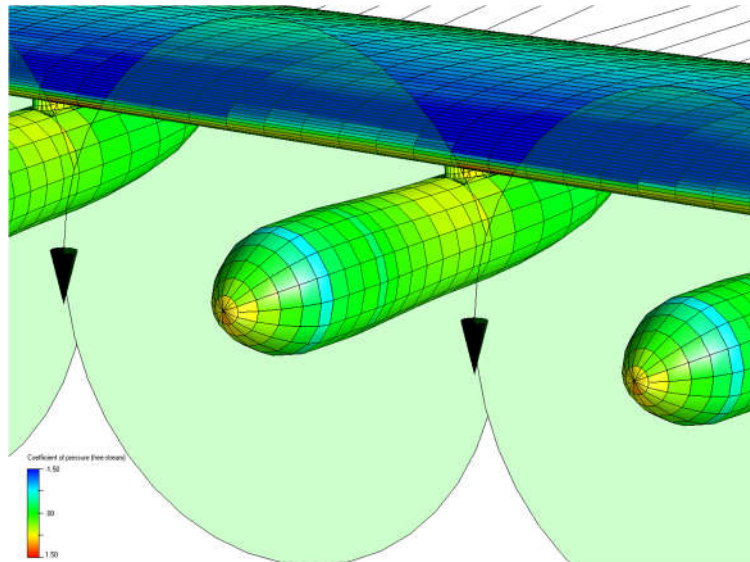


Figure 25 Aero-propulsive interaction within FlightStream. The impact of the propeller wake over the wing can be seen.

Note, that the candidate geometry used in the aerodynamic analysis differ from the previous sections of the conceptual design loop of assessment methodology. This is because certain simplifications of the geometry are required to produce reliable results with FlightStream. For each candidate, the modelled geometries contain lifting surfaces (wings, and stabilizers/canards), fuselage, and in the case of distributed electric propulsion, nacelles. The nacelle size was estimated based on the distributed electric propulsion power, based on the engineering judgement. No detailed design of the nacelle was performed, but a representative nacelle geometry was used. Neither antennas nor under carriage was modelled.

### 2.2.6.1.3 FlightStream General Settings

All the candidates received the same treatment via the aerodynamic analysis chain. No mesh dependency study was performed; however, proper mesh was selected for each candidate based on the engineering judgement. The FlightStream settings for each analysis point are presented in the Table 13. Note that for the analysis points with propellers-off, the flow was allowed to naturally transition from laminar to turbulent. However, flow over the fuselage was always fully turbulent with boundary trip wires placed at the nose of the fuselage. In the props-on analysis, the flow was forced to be turbulent on the entire geometry. This is because FlightStream cannot account for the turbulence in the actuator disk wake, and hence the flow might erroneously be laminar in the propeller wake.

Table 13 FlightStream general settings

<b>FlightStream Version</b>	2272021
<b>Lift Model</b>	Pressure
<b>Drag Model</b>	Vorticity
<b>Flow Separation</b>	On
<b>Moments Model</b>	Linear Pressure
<b>Surface Roughness</b>	6500 nm

<b>Boundary Layer</b>	Transitionally turbulent (for props-off) Turbulent (for props-on)
<b>Convergence criteria</b>	1e-5
<b>Compressibility</b>	Disabled (Mach < 0.3 for all candidates)

## 2.2.7 Cooling drag assessment

Because of powertrain components inefficiencies, a non-negligible amount of waste heat is generated simultaneously with useful work. Therefore, a dedicated cooling system is required for managing components thermal behaviour. Usually, waste heat is rejected to an ambient using radiators or cooling fins exposed to ram-air. In consequence of internal or external airflow through/around cooling bodies, the vehicle drag increases. To estimate this cooling related drag, a calculation procedure was developed (using Python coding) within UNIFIER19 project based on the theory presented by Hoerner (Hoerner, 1965). The comparison of UNIFIER19 candidates from the perspective of cooling drag is given in Results section.

## 2.2.8 Polars build-up

Because of the nature of the mission requirements, four different polars had to be prepared for each of the candidates, regardless if the A/C has DEP system implemented or not. An example configuration candidate with DEP system is presented in Figure 26. Such A/C needs the following polars curves (sorted by utilization of DEP and flaps):

- Polar 1: Cruise + Descend; both DEP system and flaps are retracted, cruise cooling is taken into account
- Polar 2: Climb; DEP system is ON, flaps are retracted, climb cooling is taken into account
- Polar 3: Take-off; DEP system is ON, flaps are in the take-off configuration, climb cooling is taken into account
- Polar 4: Landing; DEP system is ON, flaps are in the landing configuration, cruise cooling is taken into account

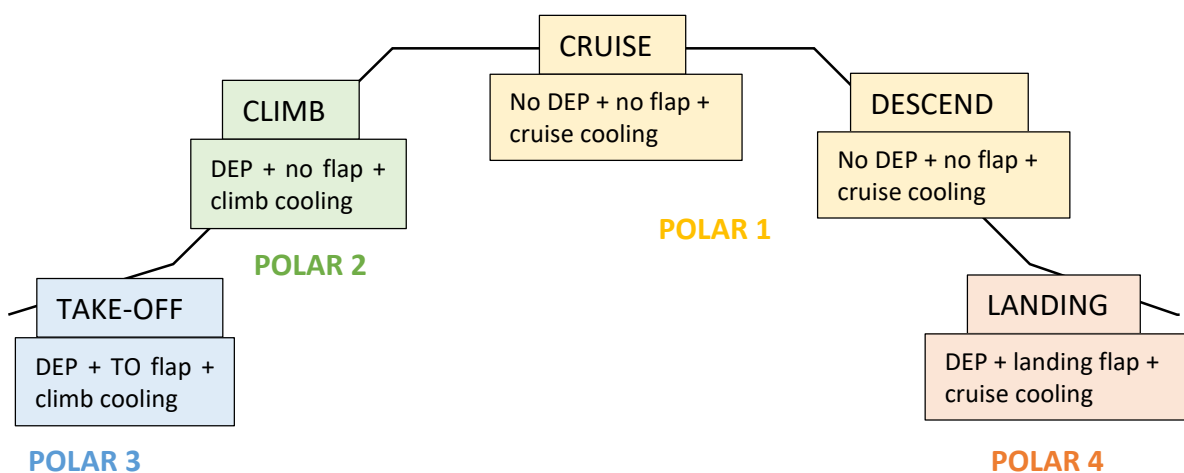


Figure 26: Description of polar curves used in the mission analysis.

For the configuration candidates without DEP system there is no geometrical difference between the A/C in climb regime and cruise regime. Which means that if there wasn't for the difference in cooling drag, polar 2 would be equal to polar 1.

Polar curve build-up was done in 4 steps.

1. Baseline: Polars at different flight regime were obtained with software Flightstream (Section 2.2.6).
2. Modification 1: As explained more in detail in Subsection 1.1.1, due to the limitation of the geometric modelling capabilities in Flightstream, POLIMI candidates were simulated with continuous fowler flap instead of a fowler flap with a slot. That is why, instead of using directly polar 3 (take-off flap setting) and polar 4 (landing flap setting), polar 2 (flaps retracted) fitted on the polar 3 and polar 4 at smaller AoAs is used, respectively. As can be seen in Figure 27, Polar 2 – Flightstream was fitted on Polar 3 – Flightstream on interval of AoAs below 8° (CL) and resulted in Polar 3 – modification 1. Similarly, Polar 2 – Flightstream was fitted on Polar 4 – Flightstream on interval of AoAs below 3° (CL) and resulted in Polar 4 – modification 1. And similar was done for the CD curves. Modification 1 was therefore applied only to the Polar 3 and Polar 4 curves of the POLIMI candidates.

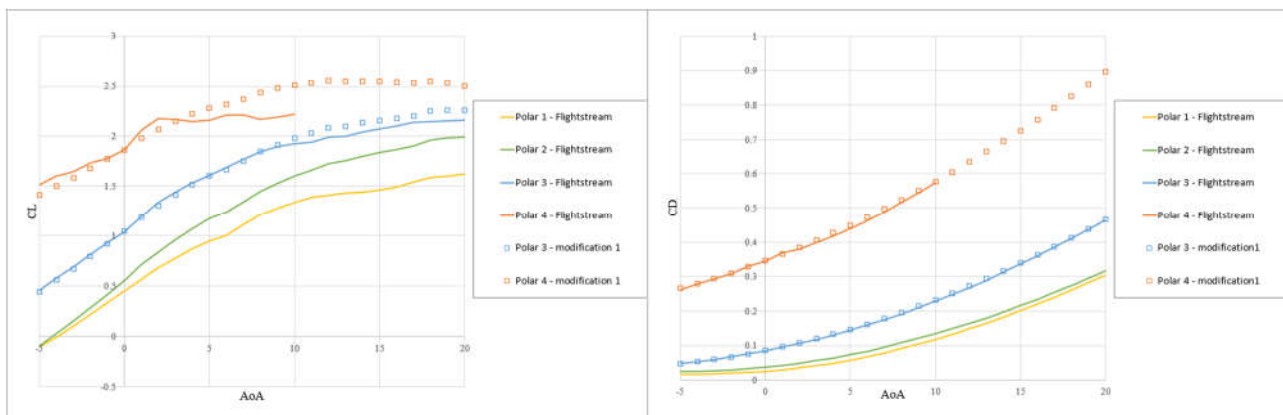


Figure 27: First step of modification of FlightStream polars.

3. Modification 2: All polars of all candidates were modified based on the verification of FlightStream results with Numeca CFD simulations. Since the basic shape of all configurations is similar to the reference configuration (tube and a wing in essence) and the CFD simulations are much more time demanding compared to FlightStream simulations, the same relative correction (based on the reference configuration) was used for all configurations. Corrections of CL(AoA) and CD(AOA) curves of the reference configuration are presented in Figure 28. Comparing Numeca and FlightStream results one can quickly conclude, that FlightStream tends to overpredict both quantities, lift and drag. Using polynomial function as a correction, FlightStream results are modified to fit the Numeca results. The same two polynomial corrections are used for all FlightStream results.

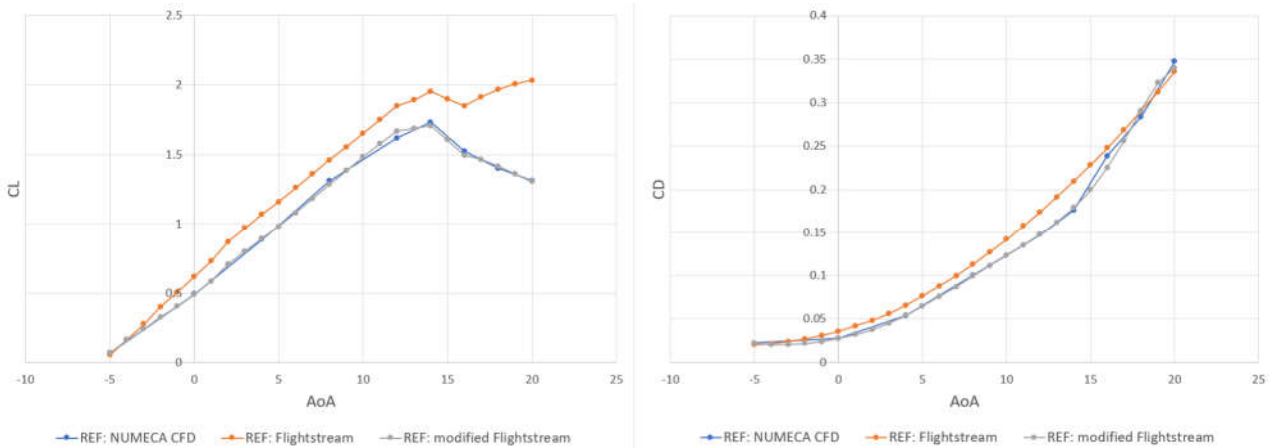


Figure 28: Relative correction of CL(AoA) and CD(AoA) curves (reference configuration) obtained with FlightStream based on the verification done with NUMECA CFD simulations.

4. Modification 3: Cooling drag (Section 2.2.7) was added as a constant on top of the drag polars from the previous step.

An example of POLIMI C7A final modified polars are compared to the baseline polars (obtained directly with FlightStream) and presented on the left-hand side of Figure 29. These modified polars were used in the Mission analysis (Section 2.2.9) done at PVS. POLIMI partner used a different set of polars in their design process. A comparison of PVS polars (modified version) and POLIMI input polars is presented on the right-hand side of Figure 29.

As can be seen, PVS's and POLIMI's Polar 1 are close at small lift coefficients, and on the other hand, Polar 3 and Polar 4 are relatively comparable between both partners at higher lift coefficients.

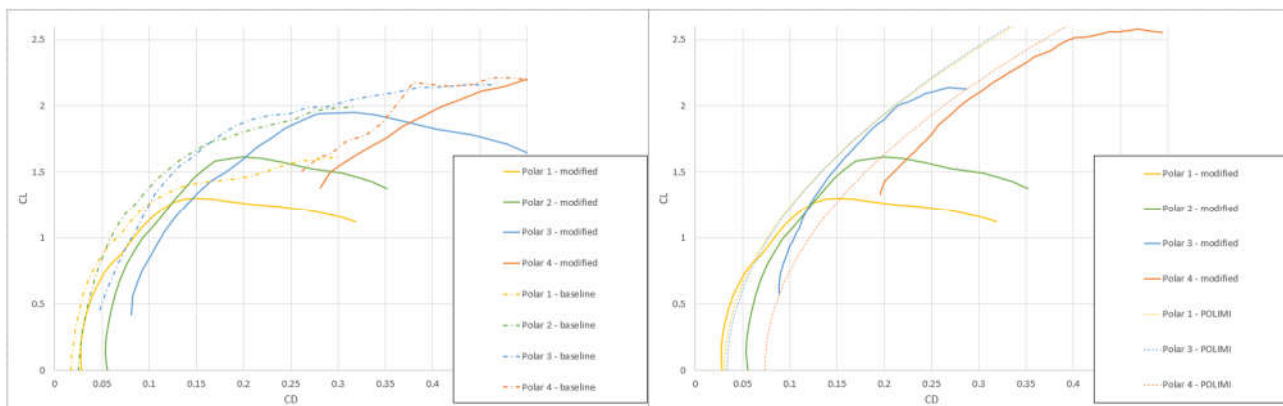


Figure 29: Comparison of baseline and modified polars for C7A candidate (left), and modified polars and POLIMI polars (right)

### 2.2.9 Mission Analysis

Mission analysis was done using the mission requirements presented in Table 14 and in Figure 30. Besides this data, also polar curves (Section 2.2.8) and propeller efficiency (Section 2.2.3) are needed in order to calculate all the required outputs, such as flight distance, required power, L/D, etc.



The analysis divides each leg of the mission into 100 small segments. For each segment a constant speed (no acceleration) is presumed and at each point of the mission, a force equilibrium is calculated. Resulting lift force allows to define the lift coefficient, which, based on the polar input, allows to define the drag coefficient. As presented in Section 2.2.8, different polar curves are used at different stages of the mission.

Since all the inputs for the force equilibrium are known for most of the mission stages, this calculation is relatively straight forward. The only exception is the loiter segment, where a maximal endurance speed is anticipated. Maximal endurance speed is defined as the speed at the minimal required power. A power minimization procedure therefore must be applied in this leg of the flight.

Table 14: Mission requirements.

Leg	Type	Value	Note
<b>Take-off</b>	Runway length	800 m	Runway type: Grass
<b>Climb</b>	Initial gradient	7 degrees	Up to 1000ft, airport near populated area
	ROC	850 ft/min	
<b>Cruise</b>	Block range	350 km	Climb + cruise + descend → <b>One “hop”</b>
	Altitude	4000 ft	
	Speed	150 kts	
<b>Descent</b>	ROD	350 ft/min	Passenger comfort
<b>Landing</b>	Runway length	800 m	
<b>Reserves</b>	Diversion	100 km	@150 kts; 90% of secondary aerodrome within 100 km
	Loiter	45 min	@maximum endurance speed
<b>General</b>	Number of “hops”	6	To avoid having refuelling infrastructure on all small airports
	Turnaround time	30 min	Ground time between hops

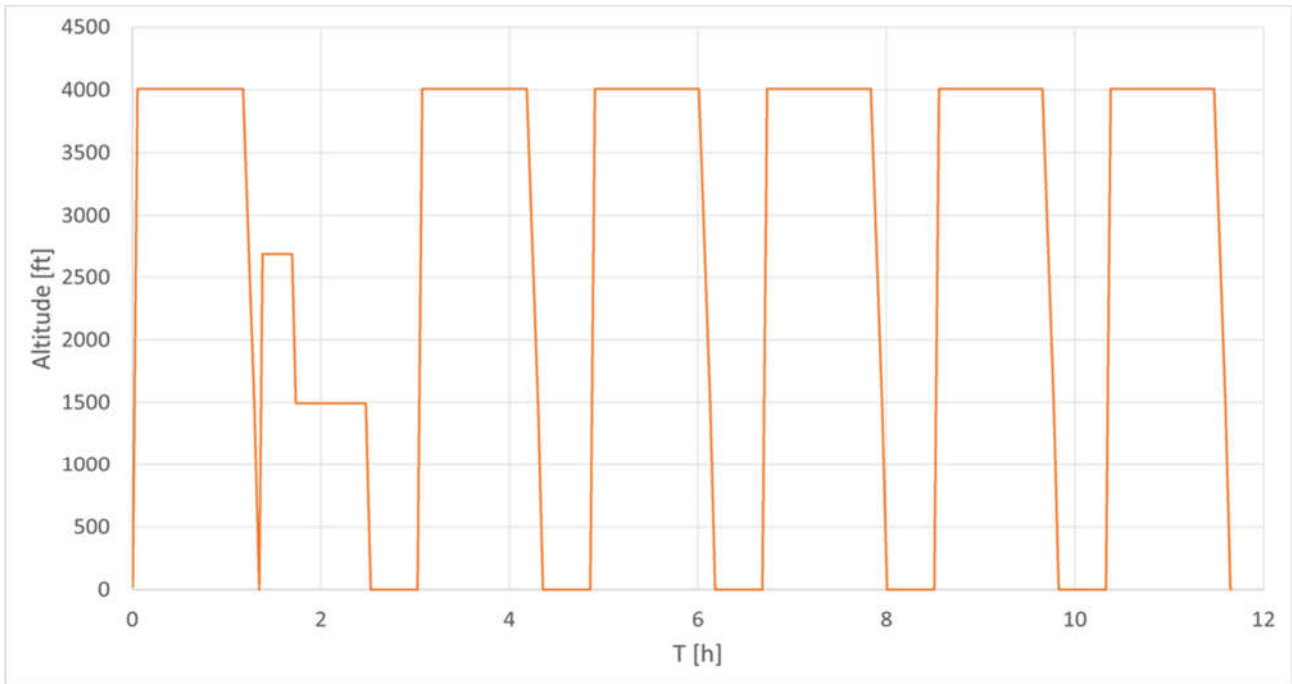


Figure 30: Prescribed mission, altitude vs time of the aircraft.

Comparison of flight speed during the mission for C7A candidate between POLIMI and PVS mission analysis and for PVS1 candidate is presented in Figure 31. PVS analysis always uses the same speed profile, only loitering speed is calculated for each candidate separately. That is why C7A (PVS analysis) and PVS1 (PVS analysis) more or less coincide. On the other hand, POLIMI and PVS mission speeds for C7A candidate directly coincide only during cruise. The rest of the flight speed are close (except for the loiter leg), but not exactly the same. POLIMI uses more detailed analysis with acceleration and deceleration transitions between main mission regimes, whereas PVS uses a simple analysis with instantaneous “jumps” from one speed to another while changing the regime of flight. This is also the reason for a small offset on the time scale seen in Figure 31. Time needed for climb and descend is not exactly the same in both analyses.

As already stated, the biggest difference in speed distribution is during loiter flight, which results from the fact that POLIMI prescribed the best L/D flight speed in that part of the mission, whereas PVS prescribed the best endurance speed. The second reason is the slight difference in polar curve inputs, which differs the used speed in both analyses even further.

One of the most important outputs of the mission analysis is the shaft power requirement, which can be used to design or verify the power plant installation, and also to compare POLIMI and PVS mission analysis. PVS used this quantity to verify the performance of all candidates that were already analysed by POLIMI.

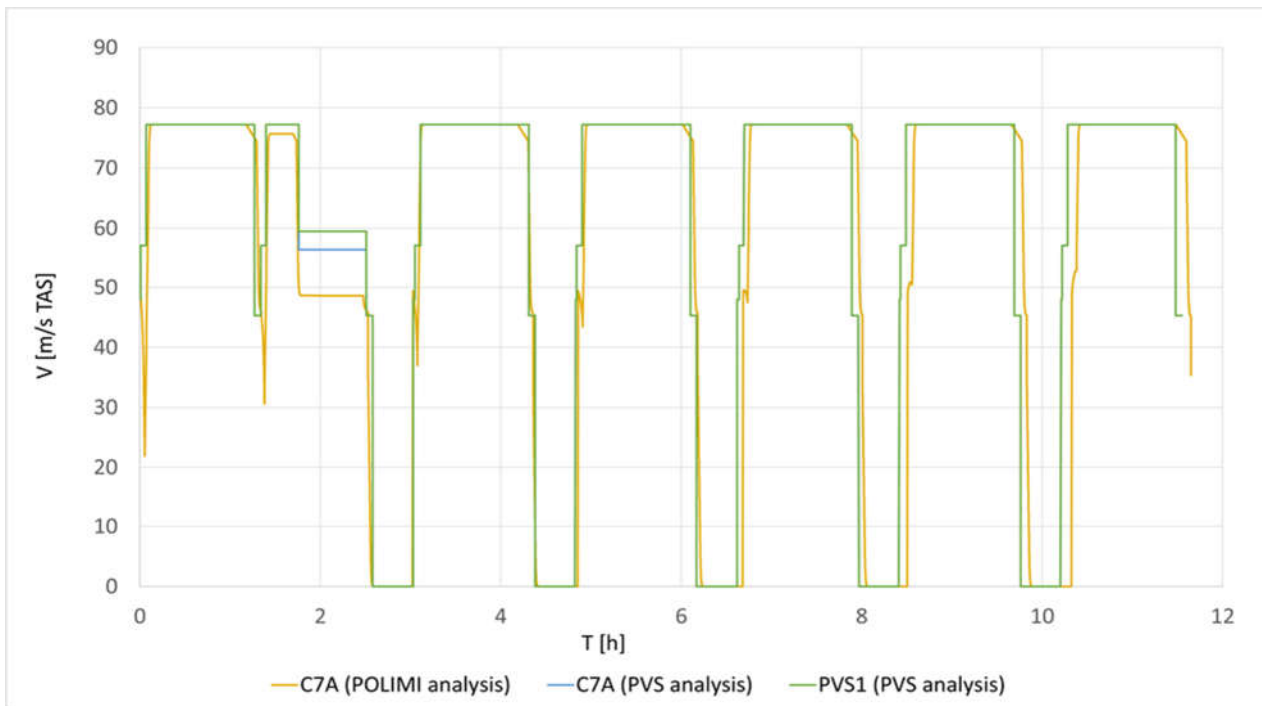


Figure 31: A/C speed comparison during the mission.

## 2.2.10 Noise assessment

In this section the methodology for assessing noise ground footprint of each candidate is presented. Then, the results are presented. Because propeller generated noise is the major noise source it was the one considered for comparison of UNIFIER19 candidates. Some theoretical background on propeller noise is given first, followed by details on modelling procedure.

### 2.2.10.1 Methodology

#### 2.2.10.1.1 Propeller noise theory

The propeller noise theory presented in this section is summarized from Hubbard (1991), if not stated otherwise. Generally, acoustic signature of the propeller can be defined by the following sources (their relative importance depends on propeller design and operating conditions):

- thickness noise,
- steady-loading noise,
- unsteady-loading noise,
- quadrupole (high-speed-impulsive noise source) noise,
- broadband noise.

Thickness noise stems from the volume displacement of the propeller blades. Its maximum magnitude is in the propeller plane. Thickness noise is a function of the blade volume where frequency depends on the blade cross-section shape and rotational speed (it increases with increasing blade-tip Mach number). Smaller the blade volume (thinner airfoils) and planform sweep help in reducing this kind of noise. Steady- and unsteady-loading noise are a consequence of the steady and circumferentially nonuniform blade

loading, respectively. Steady-loading noise stem from the forces that blades exert on the surrounding fluid (Villafana, 2016) and is important at low to moderate speeds. An example of the unsteady-loading noise is blade vortex interaction (BVI) noise. It is especially important for counter-rotating propellers where the blades of the second propeller hitting tip vortex created by the first propeller. Thickness and loading noise are known together as rotational noise (S. Brentner & Farrasat, 2003). When propeller advancing tip speed is so high that flow becomes transonic, the quadrupole noise (related to nonlinearities) occurs. Broadband noise results from the turbulence. We should be aware that for the operational propeller the total noise depends also on various distortions of the flow field, e.g., due to aircraft angle-of-attack or wakes generated upstream (both cause unsteady loading).

Propeller noise spectrum has tonal or harmonic component (discrete frequency noise) generated by the regular rotation of the blades. Thus, the time trace we can measure is periodic, where first harmonic is fundamental and higher harmonics are integer multiples of the fundamental frequency. On the other hand, the broadband noise results from the turbulent flow conditions at the leading edge (interaction of inflow turbulence with leading edge of the blade), at the trailing edge, and at the tip of each blade. The broadband noise is random in nature and contains many nonharmonic frequencies. In general, it's frequency range is between 1 kHz and 5 kHz and for this frequency band the human ear is very sensitive (Villafana, 2016). We also distinguish a narrow-band random noise. This kind of noise is almost periodic, but the energy is not concentrated at isolated frequencies.

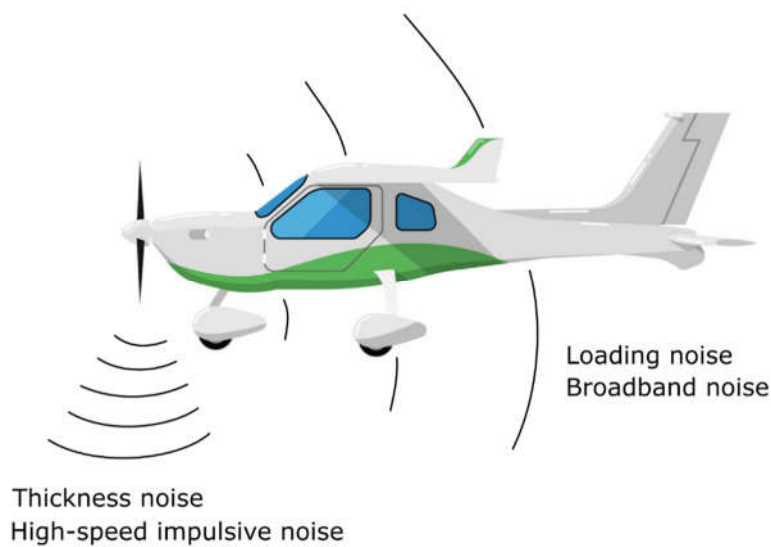


Figure 32: Directivity of thickness, loading, and broadband noise.

### 2.2.10.1.2 Modelling

To estimate propeller noise ground footprint, first, an acoustic pressure due to thickness and loading noise for a given observer/sensor location is calculated by XROTOR (Drela & Youngren). XROTOR calculation method originates from the works by Succi et al. (1979, 1982) and is based on the retarded-time concept. Result of the calculation is an instantaneous acoustic pressure as seen by the observer or sensor located at a given point (x, y, z) in space over one blade-passing period. Using XROTOR, propeller thickness noise,

steady-loading noise, and their sum can be predicted. The method requirement is that blade speed along the observer’s line of sight to be subsonic.

Our perception of loudness highly depends on the sound frequency (Ginsberg, 2018). Although XROTOR can provide sound pressure level (SPL), i.e., a common measure of the loudness of an acoustic signal, predictions, it lacks the calculation of the A-weighted SPL which accounts for the human perception of loudness. A-weighting function is shown in Figure 33. Therefore, the XROTOR output we are interested in is only the acoustic pressure trace over one blade-passing period. The signal analysis is done afterwards using separate routines developed in Python. Next, broadband noise is estimated applying Pegg’s broadband noise prediction method (Pegg, 1979) programmed in Python environment. For details on methods implementation, the interesting reader shall see *D1.1 – The design framework for an NZE 19-seater* (UNIFIER19, 2020).

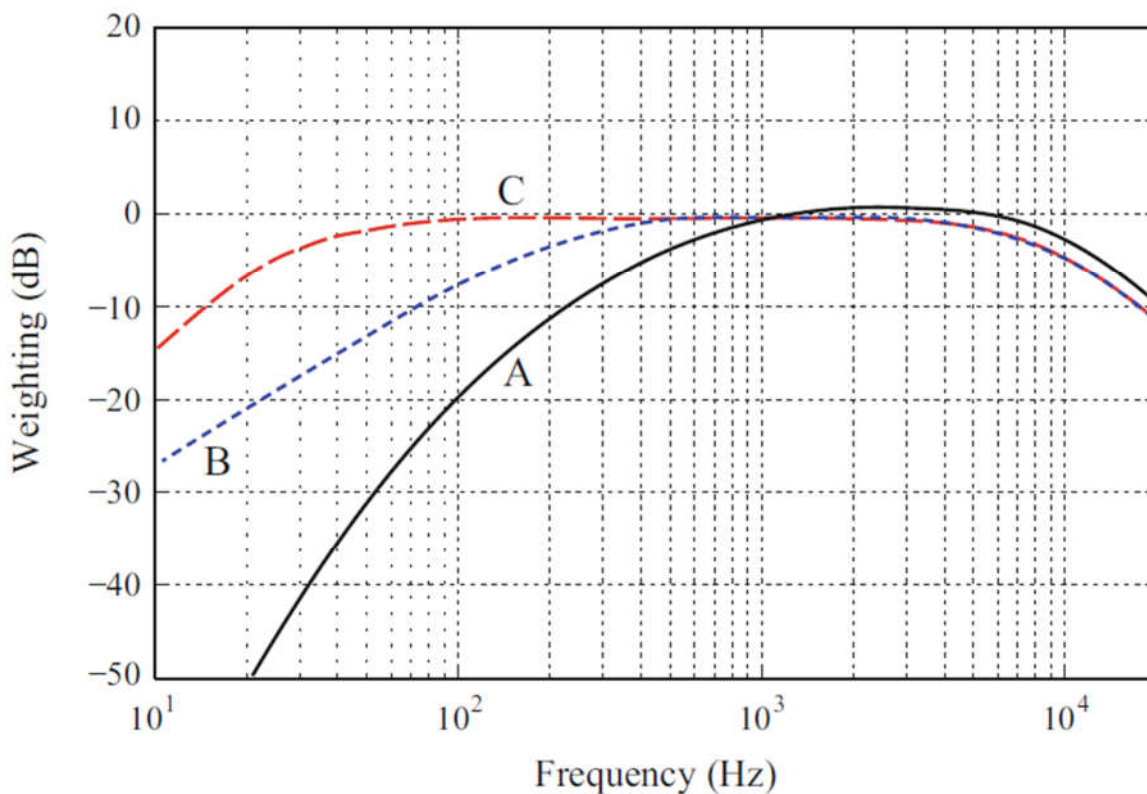


Figure 33: A-, B-, and C-weighting. (Ginsberg, 2018)

Calculation is done for multiple sensors located at points  $(x_i, y_i)$  and considers following variables:

- x coordinate of the ground sensor,
- y coordinate of the ground sensor,
- flight altitude,
- climb angle,
- propeller power,

- propeller thrust,
- propeller rpm's,
- aircraft speed,
- propeller geometrical properties (e.g., radius, blade platform, number of blades).

The output is written to simple text files (used for generation of noise ground contour maps):

- x coordinate of the ground sensor,
- y coordinate of the ground sensor,
- flight altitude,
- climb angle,
- slant distance from propeller to the ground sensor,
- azimuth angle between propeller and ground sensor,
- rotational noise SPL (dB),
- rotational noise SPL (dBA),
- broadband noise SPL (dB),
- broadband noise SPL (dBA),
- total noise SPL (dB),
- total noise SPL (dBA).

## 2.2.11 Marketability – Life-cycle cost estimation

Each candidate design has been also evaluated from its marketability potential through its direct operating costs (DOC) analysis. As this cost is highly dependent on the acquisition cost, i.e., aircraft price, the development and manufacturing cost for the whole programme had to be estimated as well. The methodology has been explained and detailed in the WP1 deliverable D1.1 (UNIFIER19, 2020).

### 2.2.11.1 Modifications after WP1

During WP1, the DOC and aircraft price estimation models were tuned to be as accurate as possible, using as a reference the average figures of existing 19-seater turboprop aircraft on a 300 km mission flight. The costs that have seen adaptations or updates, are defined in the following subsections.

#### 2.2.11.1.1 Powertrain costs

Technology evolution and better information from potential suppliers have allowed to gather more accurate data for the cost of powertrain components, especially fuel cells, LH2 tanks, electric engines, and batteries. Unfortunately, most of this information is protected by non-disclosure agreements, which does not allow to reveal the sources.

**Electric engine** costs were recalculated to 400 \$/kW for a certified motor and 250 \$/kW for the inverter, from the previous 250 and 200 \$/kW, respectively. Electric engine time between overhaul (or replacement) is now at 12 000 hours, as per Pipistrel experience and estimations, from the previously estimated 10 000 hours.

**Fuel cell** costs were extremely inaccurate in WP1. A well-known fuel cell manufacturer is giving the price of an aviation-grade fuel cell pack, including the balance of plant (BOP), at 2271 \$/kW. This price is for low volume production and will eventually decrease once production ramps up. Fuel cell lifespan, according to the same manufacturer, is set at 20 000 hours before replacement is needed.

From a supplier developing **cryogenic liquid hydrogen tanks** for aviation, we calculated a fairly linear cost of 30 \$ per litre of capacity. This cost was unknown at the end of WP1.

Pipistrel experience raised certified **battery pack** costs at 700 \$/kWh, from the previous 300 \$/kWh, which considered only the battery cells without the surrounding cooling and BMS. The lifespan of a battery pack is estimated to reach 800 full cycles between replacement, as per Pipistrel experience. A reduced usage, i.e., recharging before the battery is depleted, can increase this lifespan to up to 4000-5000 cycles.

The values that were used in the powertrain cost calculations are:

$$C_{\text{motor + inverter}} = FN_{0 \text{ kW}} (400 \text{ $/kW} + 250 \text{ $/kW})$$

$$C_{\text{fuelcell}} = FN_{0 \text{ kW}} (2271 \text{ $/kW})$$

$$C_{\text{tankLH2}} = V_{\text{H2}} (30 \text{ $/liter})$$

$$C_{\text{batt}} = E_{\text{batt}} (700 \text{ $/kWh})$$

where  $FN_{0 \text{ kW}}$  is the maximum power of the motor or fuel cell, in kW;  $V_{\text{H2}}$  is the liquid hydrogen volume, in litres; and  $E_{\text{batt}}$  the energy, in kWh, needed for a typical mission flight.

#### **2.2.11.1.2 Distributed Electric Propulsion (DEP)**

The cost models already allowed the adoption of new powertrain technologies, such as hydrogen fuel-cell, hybrid turbo-electric, and fully electric propulsion. However, as some candidate designs include distributed electric propulsion (DEP), a feature not included in the cost model at end of WP1, this capability has been added during WP2. The DEP electric engines were considered separately from the existing electric engine to allow having two different types of electric engines on the same aircraft, which is often the case for DEP architectures (one or two main electric engines used during the whole flight, the smaller DEP engines used only at low speeds). Nevertheless, the cost calculations associated to the DEP electric engines follow the same approach as the main electric engines in terms of price, maintenance, etc.

**Maintenance and durability:** As the DEP engines are used only during the low-speed phases of flight, which translates into around 7 minutes per flight hour for the UNIFIER19 mission calculated by POLIMI, the DEP motors lifespan is significantly high. Considering the time between replacement (TBR) of electric engines at 12 000 hours, and an aircraft utilisation of 1800 hours per year, this translates into an expected lifetime of the DEP engines of 57 years! On the contrary, a motor operating throughout the whole flight would have a lifetime of 6.7 years before needing replacement. This significantly decreases the maintenance costs with respect to a turboprop engine. With a time between overhaul (TBO) of 6000 hours<sup>3</sup> at best, a turboprop engine would require an overhaul every 3.3 years and a hot section inspection (HSI) almost every year.

---

<sup>3</sup> Beechcraft 1900D's Pratt & Whitney PT6A-67D has a TBO of 6.000 hours and an HSI of 2.000 hours. <https://www.pt6a.aero/maintenance/pt6a-tbo-hsi-service-intervals/>

### 2.2.11.1.3 Materials distribution

Although the candidates did not specify the percentage of materials used in the construction, which will be better defined in WP3, the following distribution (Table 15) has been assumed following the state-of-the-art:

Table 15 Material distribution for all UNIFIER19 candidate designs

Aircraft	Material	%	$F_{mat\ ref.}$	$F_{mat\ partial}$	$F_{mat\ total}$
<b>All UNIFIER19 Candidates</b>	Aluminium	30%	1.00	0.30	<b>1.32</b>
	Carbon-Epoxy	51%	1.45	0.74	
	Fiberglass/Others	7%	1.15	0.08	
	Steel	10%	1.75	0.18	
	Titanium	2%	1.45	0.03	

Where % is the percentage of each material in the entire airframe;  $f_{mat\ ref}$  is the reference cost factor for each material considering current technology;  $f_{mat\ partial}$  is the weighted material factor ( $\% * f_{mat\ ref}$ ) of each material in this airframe; and  $f_{mat\ total}$  is the resulting total material factor that is used in the manufacturing cost calculations.

Even if the percentage of materials is not exact, and the  $f_{mat\ ref}$  changes with the evolution of each technology and expertise of the manufacturer, the variations will have a rather low impact on the overall cost of the aircraft and will be good for comparative matters.

### 2.2.11.1.4 Economy parameters

Price of “green” (produced from clean energy) liquid hydrogen has reduced and shows an estimated cost by entry-into-service of 2.00 €/kg.

Salaries and wages for crew, maintenance, and engineering personnel have not been changed.

The conversion rate from USD to EUR, where applicable, has been kept at 2020 values. Also, calculations requiring the addition of inflation rates (e.g., to adapt reference salaries from 2012) have been kept to estimate their cost in 2020.

## 2.3 TUDELFT

In order to perform a full conceptual design of an aircraft, several iteration loops need to be run involving different level of fidelity. First a so-called Class-I loop is needed where statistical regression are mostly used in order to determine a first design point of the aircraft. Then, the design proceeds to a Class-II procedure where the subsystem are sized according to initial physics-based analysis. In order to start with the design of a non-conventional Fuel-Cell based aircraft, a first Class I estimation model has been developed whose the overall procedure is reported in the block Diagram of Figure 34: TUD CS23-FC Class I estimation procedure.



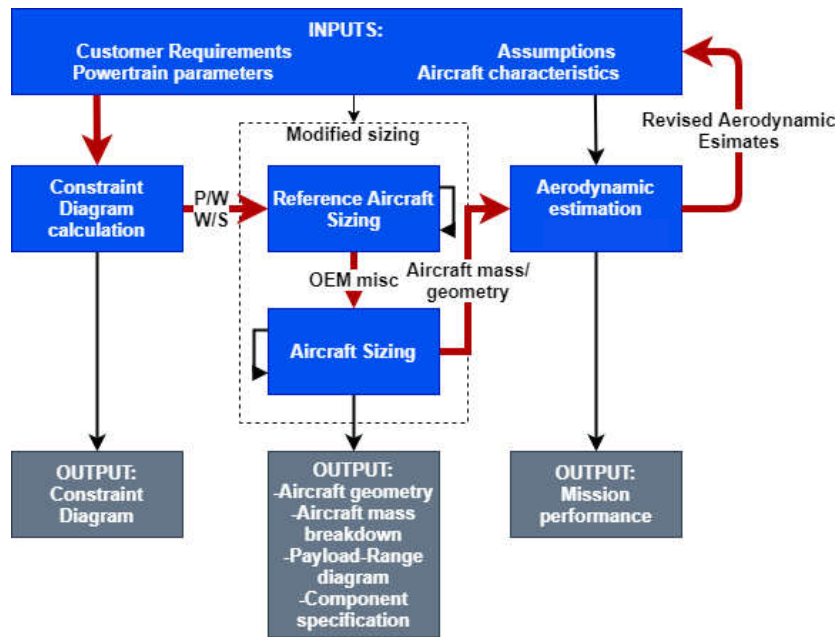


Figure 34: TUD CS23-FC Class I estimation procedure

When looking at the diagram, the procedure consists of several steps briefly described in the following list:

1. The customer requirements, together with preliminary performance parameters such as energy specific power, gravimetric indexes etc..., are used to construct a constraint diagram with the aim to identify the most suitable design point in term of Power-to-Weight ratio (P/W) and Wing Loading (W/S).
2. A reference aircraft featuring a conventional propulsion is sized according to the same requirements inputted at point 1. Once the aircraft is sized through a closed loop, a mass breakdown is computed using more refined Class II methods. In this way the Empty Operative Weight is decomposed in the components reported in Figure 35 : the first components contain all the masses of the conventional powertrain and masses of the main structural items such as the wing and fuselage. The second contribution  $EOW_{misc}$ , takes into account miscellaneous contribution and it is simply calculated by subtracting the  $EOW_{misc}$  from the total EOW of the reference aircraft.

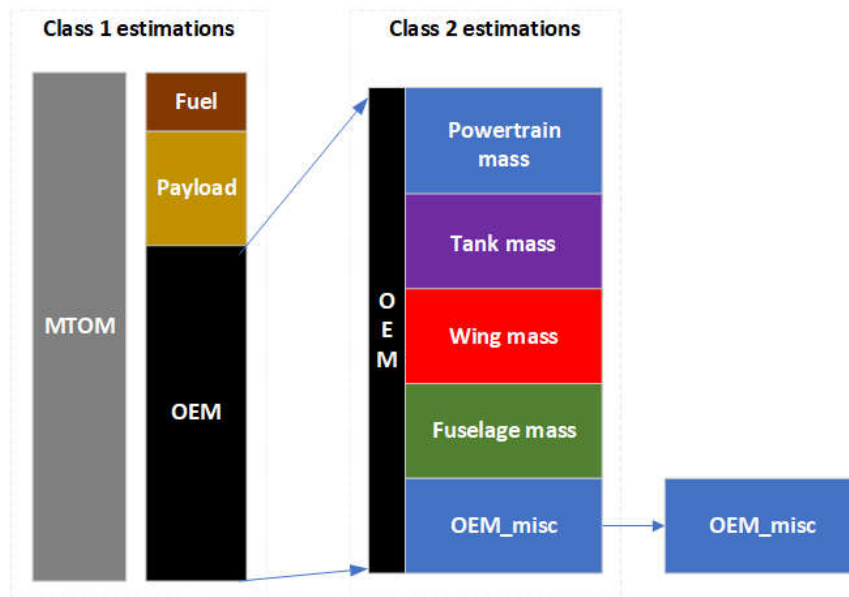


Figure 35: reference aircraft mass breakdown

3. Using the obtained  $OEM_{misc}$ , the mass of the hydrogen fuel cell aircraft can be built up by considering the masses for the wing, fuselage, fuel cell powertrain and tank specifically recomputed for the FC-Hydrogen case. The sizing routine for the harmonic mission consists of several iterative loops. The main loop converges on the mass of the entire aircraft. A smaller loop converges on the power required from the fuel cell, based on the power required for flight, and possible additional contributions required for the balance of plants.
4. To improve the validity of the results, A panel method is used to revise the estimates for the minimum drag coefficient ( $CD_{min}$ ), lift induced drag constant ( $k$ ) and the Lift to Drag ( $L/D$ ) ratio.
5. These revised aerodynamic estimations are fed back into the assumptions, and used go through the sizing routine again. This iterative loop is run until there is convergence on the sizing of the aircraft. After this final round of fidelity improvements, a feasible aircraft design is obtained.

The sizing of the FC powertrain consists of a first estimation of the power according to the requirements, and then extracting the mass of the powertrain and the overall efficiency, using specific power estimates as inputted. During the class I loop, the powertrain mass depends on the power system specific power as well as other initial technologic parameter such as: tank gravimetric and volumetric indexes, fuel cell nominal efficiency, electric motor efficiency, electric motor specific power etc... In this case, the total powertrain mass includes all components that transform the fuel energy into useful propulsion energy as reported in the subsystem components diagram of Figure 36

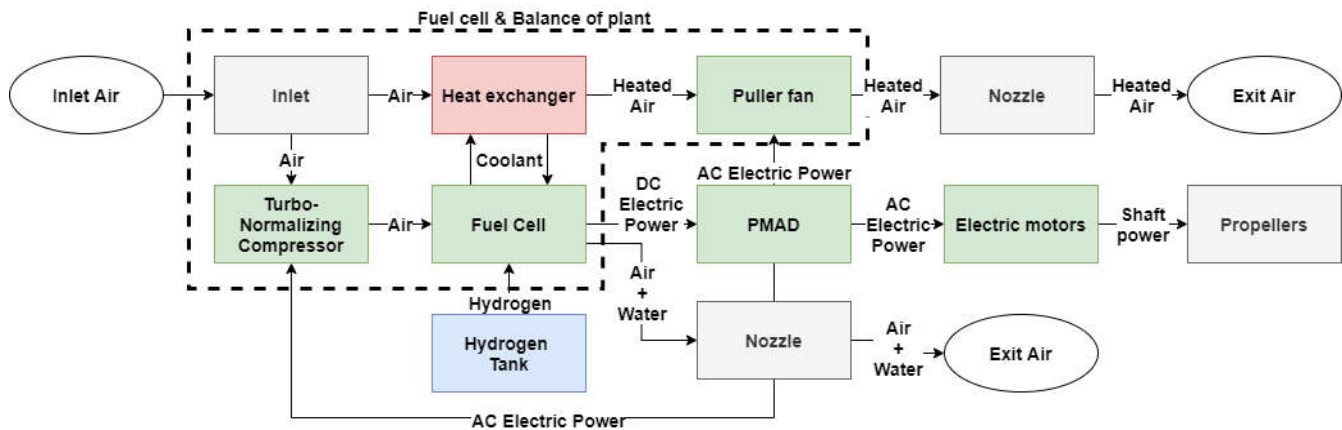


Figure 36: powertrain components of the FC powertrain

In addition to the usual primary power components (Fuel Cells, PMAD, Inverters, Electric Motors), the model is capable to preliminary size the so-called balance-of-plant components that, in this case, consists of: a Cooling System dedicated to maintain the Fuel Cell at the nominal operating temperature; a turbo-normalized compressor that ensures 1 bar atmospheric pressure so that the Fuel Cell can operate correctly without detriments of its performance in terms of efficiency and delivered power. For each component, class II models allow to estimate both their size, mass, efficiency, and when it occurs, the absorbed power.

Masses of the components are calculated by considering proper specific power  $\hat{p}$  values for each one of them; hence those mass can be easily calculated with the following equation for a generic i-th powertrain component:

$$m_i = \frac{P_i}{\hat{p}_i}$$

In the first loop, constant efficiencies are considered for most of the components with the following exceptions:

- A possible efficiency curve for a (fixed pitch) propeller has been extrapolated from a disk actuator model
- The Fuel Cell efficiency is dependent mainly on the required power by following a possible polarization curve.

In addition, also the required power levels are calculated for the elements of the balance-of-plants so that it is assumed that the total power is calculated as follows:

$$P_{tot} = \frac{P_{shaft}}{\eta_{EM}\eta_{INV}\eta_{FC}} + P_{compr} + P_{cool}$$

The first term represents the actual power spent for the motion of the aircraft whereas the second and third terms refers to the power necessary to supply the compressor and the cooling system. The compressor power is determined by the temperature rise caused by the compression of the air, and the amount of airflow through the compressor. The temperature rise is calculated using the pressure ratio

(PR) the compressor must produce. As this compressor is meant to be turbonormalizing, the pressure ratio is related to altitude directly. Furthermore, it is assumed that there is an added 5% pressure drop through the fuel cell.

The cooling system is sized to dissipate the waste heat from the powertrain to the atmosphere. The cooling system power is determined by a model provided by NASA where a preliminary sizing was performed which resulted in a relationship between the heat power to be rejected by the cooling system, and the cooling system power, mass and thrust. An important assumption is that the cooling fan always ensures positive pressure at the exit of the cooling channel, thus preventing backwards flow and even producing thrust.

As a proof that all the power terms can have an important effect on the overall sizing of the powertrain, a preliminary result is reported in Figure 37 for a case of a commuter aircraft. The reported power breakdown shows that cooling and compressor can absorb up to 15% of the total power.

For this reason, an additional loop is constructed in order to converge the produced power according to both flight and system requirements.

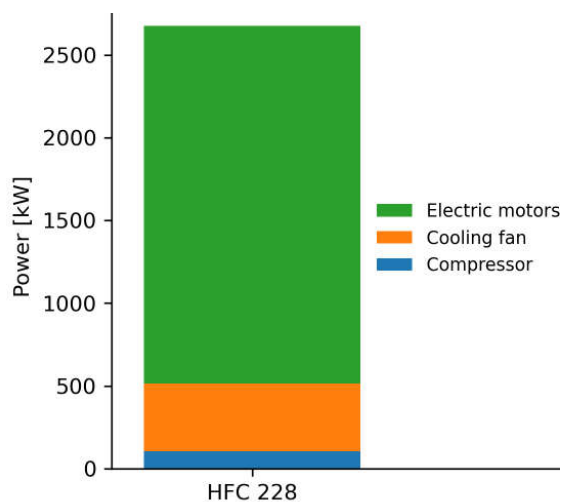


Figure 37: Power breakdown for a preliminary study case

Additional models have been built to take into account the extra weight and volume needed by the Hydrogen tank. Those preliminary models rely again on user-inputted values for both gravimetric and volumetric indexes. In addition, it is assumed that the hydrogen is stored in the fuselage so that its total length (and hence volume) is recomputed to host both cargo and hydrogen.

The tool has been validated for a variety of conventional CS23 aircraft, ranging from 2 seats LSA, to a 19 passengers commuter. Results in terms of weight breakdown show a satisfying agreement with actual data reporting a maximum deviation of 8.8% in the calculation of the MTOW. Bigger errors are appreciated in the calculation of the design fuel due to the fact that the design point of most of the actual aircraft is not exactly known and the harmonic mission has been considered instead.

As an example of the design capability of the design procedure, the main general results from the code are reported in the Figure 38 where a conventional commuter Benchmark (the Dornier Do228) is compared to its redesigned version featuring a FC powertrain.

The design method returns key parameters such as MTOW, EOW, and the design point from the constraints diagram (available but not shown here). The dimension of the fuselage and the wing are also scaled in order to converge the design; it worth to note that the wing size is recomputed by assuming some input parameters (e.g. the Aspect Ratio) to be constant during the design convergence. Other important results are related to the weight breakdown and to the payload-range diagram of the resulting aircraft.

Parameter	Do 228	HFC 228	[%]
$MTOM$ [kg]	5866.4	10113.1	72.39
$OEM$ [kg]	3629.5	8061.2	122.10
$Max\ m_{fuel}$ [kg]	1384.7	459.3	-66.83
$W/S$ [ $N/m^2$ ]	1953.1	1953.1	0.00
$P/W$ [ $W/N$ ]	18.3	17.6	-3.83

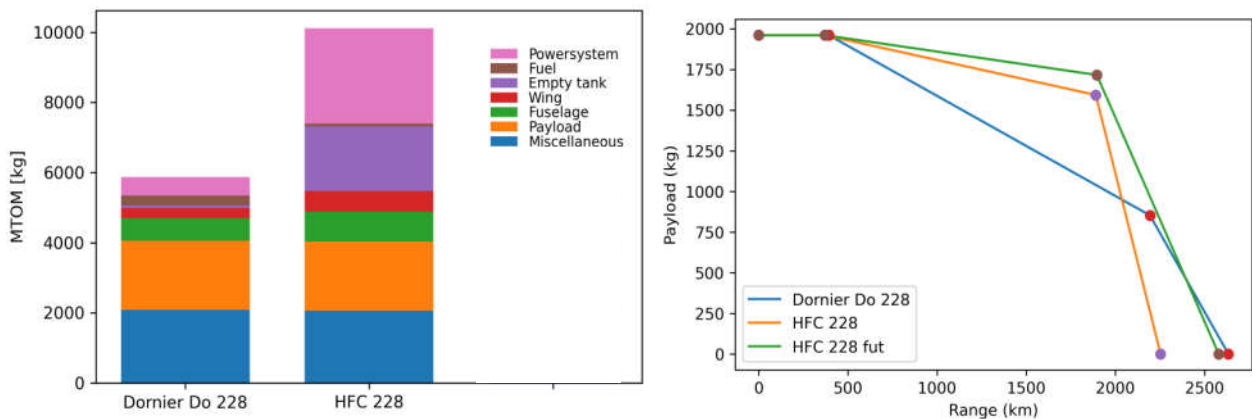


Figure 38: Output from the sizing procedure

The solution carried out from the present procedure is then fed to a more precise design procedure that makes use of higher fidelity models to refine the solution and to include the possible effects of non-conventional solution for both the wing configuration and the aero-propulsive configurations. Those full Class II analyses are being implemented in-house-developed design tool "Initiator".

## 3 Preliminary candidate solutions

### 3.1 Framework

This section describes the framework of the final phase in the concurrent design competition carried out in WP2.

#### 3.1.1 POLIMI candidates

##### 3.1.1.1 Further down-selection

The down-selection process described in Chapter 4.3 provided a solid base for the determination of the solutions to be presented for the final phase of the concurrent design competition. As noted from Table 7, the five top-ranking configurations amount to the two canard solutions C2 and C3 and to the set of TBW aircraft that give rise to configurations C7, C12, C15.

The subsequent analysis was then carried out by applying the HYPERION preliminary sizing tool to the short-listed candidates. This implied the integration of some modelling improvements to take into due account the relevant configuration options. It was noted that a reliable modelling of a tailless aircraft (C12) and a three-surface aircraft (C15) at a preliminary sizing level was not achievable and that the application of the HYPERION tool would have brought the same results for C7, C12 and C15.

Furthermore, after a mid-fidelity modelling of a truss-braced wing was developed and integrated, it was seen that the effect of the enhancement in lift-to-drag ratio was not enough to offset the weight penalty associated with this special structure. As a result, a decision was taken to consider a variant of C7, named C7A, with the same features of C7, but a cantilever wing, for further development.

##### 3.1.1.2 Additional studies

In addition to the configurations emerged in the process described above, a decision was made to include another potential candidate, named REF, which shares the fuel-cell hybrid electric power-train, but features a traditional thrust-production system made of two electric motors with their propellers on each wing, close to the root. This configuration, traditionally-looking and devoid of additional innovative features such as aero-propulsive interaction, was considered as a relatively low-risk backup candidate in case of difficulties in integrating the more exotic competitors.

Furthermore, a preliminary analysis was made by applying the HYPERION tool to a configuration inspired by the initial studies carried out at TUDELFT. This configuration, termed CTUD, features DEP and WTPs in a traditional aft-tail configuration.

##### 3.1.1.3 Final setup

The final candidate set devised by POLIMI amounts to the following:

- **Configuration C2** – Canard with drag-optimized fuselage, variable-incidence wing (VIW) and tail-cone propeller (TCP). This configuration has been developed first using HYPERION and then fully sized using TITAN.
- **Configuration C3** – Canard with distributed electric propulsion (DEP) including small wing-tip propellers (WTP) and tail-cone propeller (TCP). This configuration has been developed first using HYPERION and then fully sized using TITAN.

- **Configuration C7A** – Aft-tail with distributed electric propulsion (DEP) including small wing-tip propellers (WTP) and tail-cone propeller (TCP). This configuration has been developed first using HYPERION and then fully sized using TITAN.
- **Configuration REF** - Aft-tail with concentrated propulsion. This configuration has been developed first using HYPERION and then fully sized using TITAN. It is not discussed in the following as it has been developed as a backup solution in case of difficulties.
- **Configuration CTUD** - Aft-tail with distributed electric propulsion (DEP) including large wing-tip propellers (WTP). This configuration has been developed using HYPERION only and was not considered further.

### 3.1.2 PVS candidate

Another variant of C7A was considered, where the tail-cone propeller was substituted with ducted fan and V-tail was placed on top the duct. This seems like a structural complexity; however, ducted fan brings other advantages to the configuration:

- stators can provide sufficient structural support also to the V-tail surfaces
- ducted fan experiences higher thrust at low speeds than propeller with equal diameter, which reduces required take-off distance,
- fan noise is shielded by the duct which results in a quieter aircraft at low altitudes,
- ducted fan represents a “counter-weight” for the propeller configuration concepts.

#### 3.1.2.1 Final setup

- **Configuration PVS1** – High aspect ratio wing with distributed electric propulsion (DEP) and wingtip propellers, tail-cone ducted fan with v-tail. This configuration was fully sized with PVS Class II design loop.

### 3.1.3 Final candidate set

As the set provides by considering the multiple POLIMI candidates (C2, C3, C7A) and the PVS candidate (PVS1) exceeds the initial requirement of two competing solutions and given the wide variation in configurations spanned, a decision was taken decided to proceed.

The enlarged breadth of the competition was considered a significant benefit, fully compensating for the unavailability of a mature candidate from TUDELFT.

The following sections detail each candidate configuration, in view of the final decision for the design solution to be brought to maturity in WP3.

## 3.2 Configuration C3

This configuration ranks among the original list of the top five POLIMI candidates, selected based on the qualitative and quantitative analysis process detailed in Section 4. The following section explains the general description of the configuration, the results of sensitivity analysis and the cross-checking assessment.

### 6.2.1 General description

The candidate design consists of a canard configuration with counter-rotating pusher propellers mounted at the tail. Placing motors at the tail cone helps reducing the vehicle wake dissipation by ingesting the fuselage boundary layer (BLI). Although the thrust unit has not been designed specifically for BLI, certain enhancement may be expected due to such placement. One of the unique features of this configuration is the inclusion of a Variable Incidence Wing or VIW. This means that the main wing can change its rigger's angle of incidence relative to the fuselage on command. This may be exploited to allow take-off without the rotation manoeuvre. The result is a streamlined fuselage without a tail upsweep angle for preventing tail strike in the take-off rotation, which results in drag reduction. An added advantage of this setup is the improved visibility for pilots during take-off and landing, because the fuselage remains nearly parallel to the runway. The main wing is mounted high, towards the rear of fuselage, which means a structurally efficient continuous spar and an unobstructed main cabin. The liquid hydrogen tank is placed below the wing near the centre of gravity location. The overall configuration is displayed in Figure 39. Table 16 provides a comprehensive list of the C3 design specifications.

This is the result of the application of the TITAN design loop, which couples the HYPERION preliminary sizing tool with the ARGOS Class I design procedures. The convergence of the process is very quick, with only five iterations necessary from the HYPERION initial guess. Figure 40 shows the Sizing Matrix Plot, which allows appreciating the design point location at the intersection of the stalling speed and take-off distance requirements. Figure 41 provides the resulting mass breakdown. Finally, Figure 42 and Figure 43 show the time histories of the energy and power quantities during the sizing mission, along with its altitude profile.

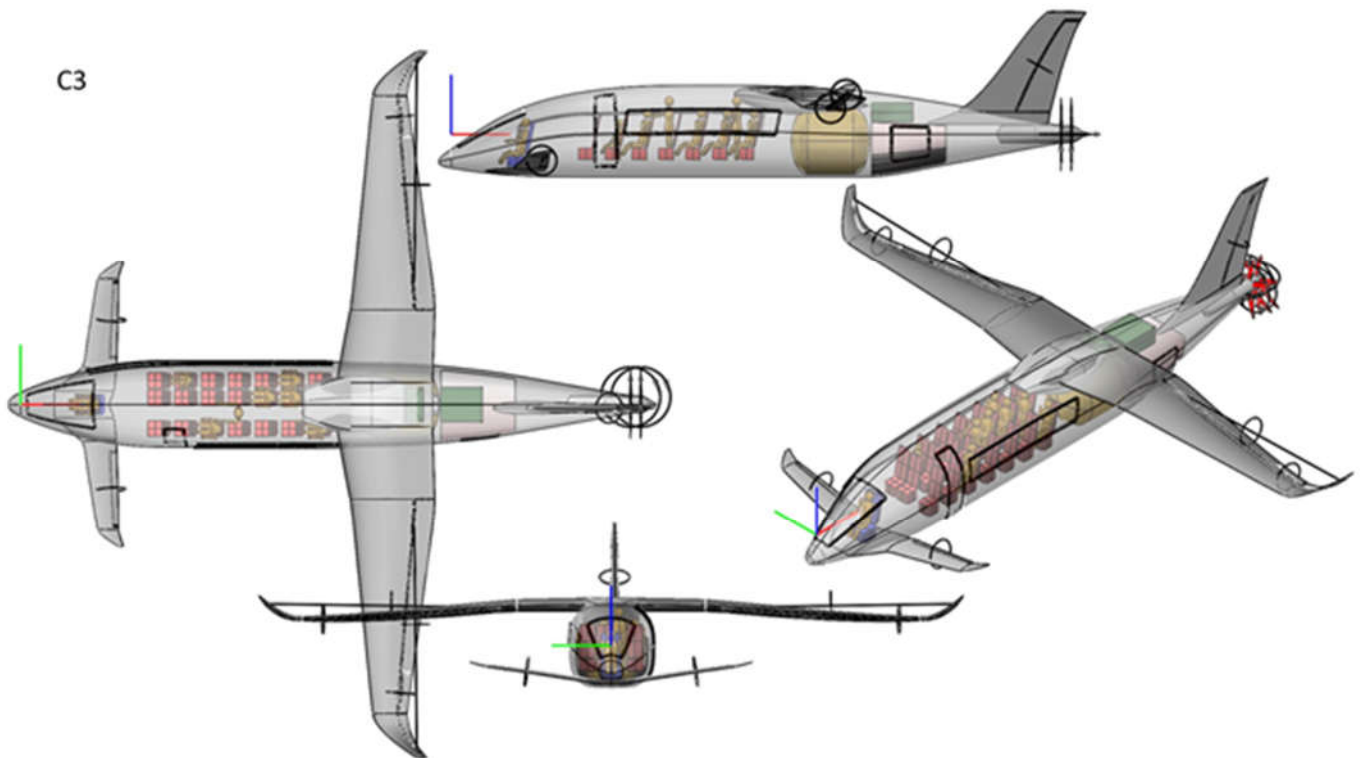


Figure 39 : Candidate C3 top, side, front and ISO view.



Table 16 Complete specifications of candidate C3.

Parameter Name	Value	Units
Payload	2280	kg
Number of passengers	19	-
Number of pilots	1	-
Design Power Loading	0.0671	N/W
Design Wing Loading	1958	N/m <sup>2</sup>
Max. take off field length	800	m
Max. landing distance	800	m
Max. stall speed	34.98	m/s
Rate of climb	6.79	m/s
Climb speed	55.25	m/s
Cruise speed	72.74	m/s
Cruise altitude	1219	m
Cruise range	350	km
Rate of descent	-1.78	m/s
Descent speed	72.74	m/s
Loiter altitude	457	m
Loiter time	45	min
Diversion range	100	km
Electric motor efficiency	92.0	%
Electric motor power density	7533	W/kg
Electric motor overrating	1.25	-
PGS power density	2130	W/kg
PGS efficiency	95.0	%
Minimum fuel level	5.0	%
Fuel cell voltage	600	V
Compressor efficiency	88.0	%
Number of FC systems	2	-
Battery power density	1670	W/kg
Battery energy density	936000	J/kg
Minimum charge level	25.0	%
Maximum charge level	85.0	%
Engine thrust	22634	N
Engine power	1088.7	kW
Propeller efficiency (non-DEP)	80.0	%
Number of engines	1	-
Propeller diameter (non-DEP)	2.81	m
Number of blades	4	m
EM maximum cont. power	1088.7	kW
PGS power	603.0	kW
H2 tank volume	5.22	m <sup>3</sup>
Gravimetric index	0.60	-
H2 tank diameter	2.04	m
H2 tank length	2.27	m
Total number of tanks	1	-
Tank ins. thickness	0.0580	m
Tank wall thickness	0.0045	m

<b>Maximum take off</b>	7438.1	kg
<b>Operative empty</b>	4806.7	kg
<b>Empty</b>	4188.6	kg
<b>Airframe</b>	3501.0	kg
<b>Lost H2</b>	10.659	kg
<b>Wing</b>	644.8	kg
<b>Fuselage</b>	894.3	kg
<b>Horizontal Tail</b>	32.4	kg
<b>Vertical Tail</b>	87.7	kg
<b>Fuel (wing)</b>	0.0	kg
<b>Fuel (fuselage)</b>	351.4	kg
<b>Landing Gear</b>	329.8	kg
<b>Pilot</b>	100.0	kg
<b>Flight Assistant</b>	0.0	kg
<b>Cargo</b>	836.0	kg
<b>Control Surf.</b>	156.2	kg
<b>Propulsion 1</b>	0.0	kg
<b>Propulsion 2</b>	244.5	kg
<b>APU</b>	0.0	kg
<b>Instr. &amp; Nav. Sys.</b>	46.7	kg
<b>Hydr. &amp; Pneu. Sys.</b>	7.7	kg
<b>Electric Sys.</b>	214.2	kg
<b>Electronics</b>	140.1	kg
<b>Air cond. &amp; Anti-ice</b>	445.1	kg
<b>Furnishing</b>	415.9	kg
<b>Battery</b>	524.7	kg
<b>PGS</b>	298.0	kg
<b>Hydrogen Tank</b>	238.5	kg
<b>Airfoil</b>	ATR72_Airfoil	-

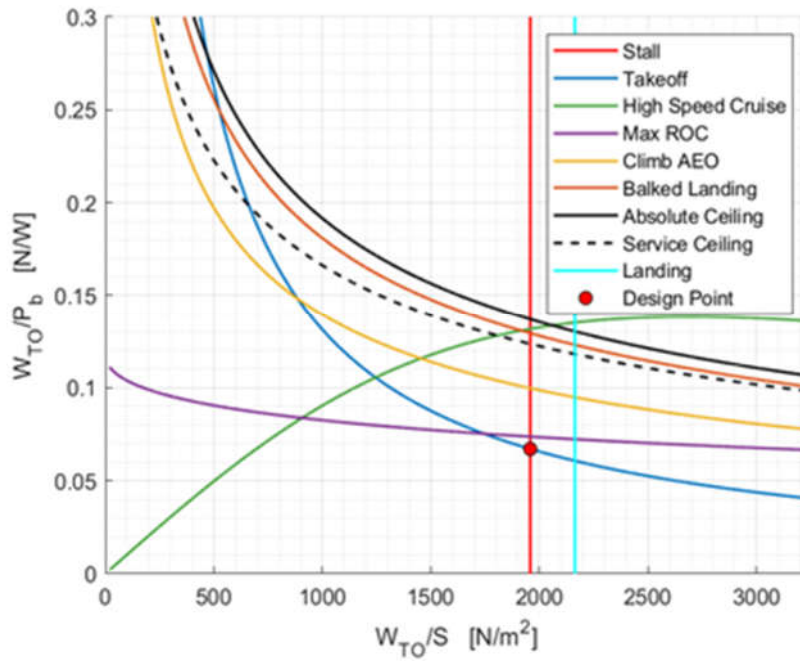


Figure 40 Sizing matrix plot for candidate C3.

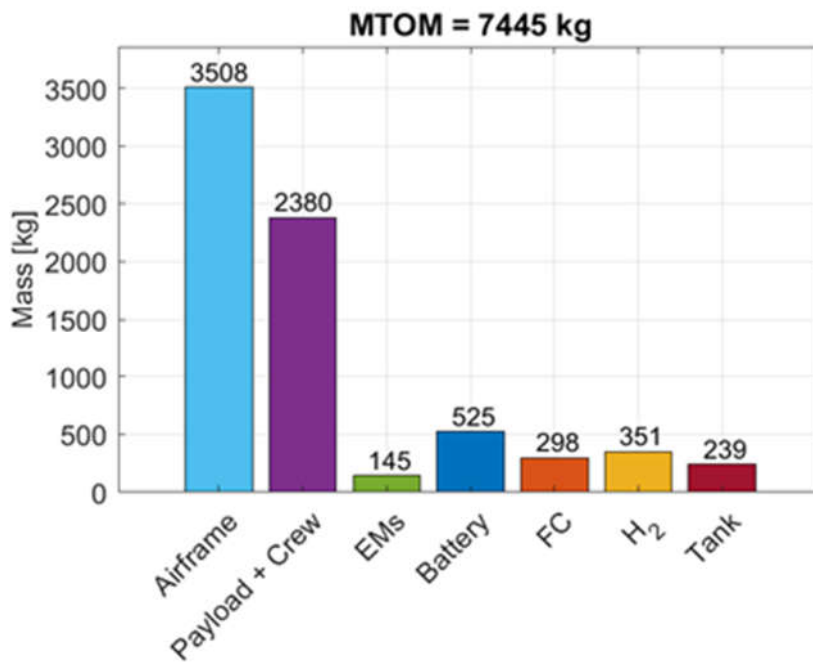


Figure 41 Mass breakdown of candidate C3.

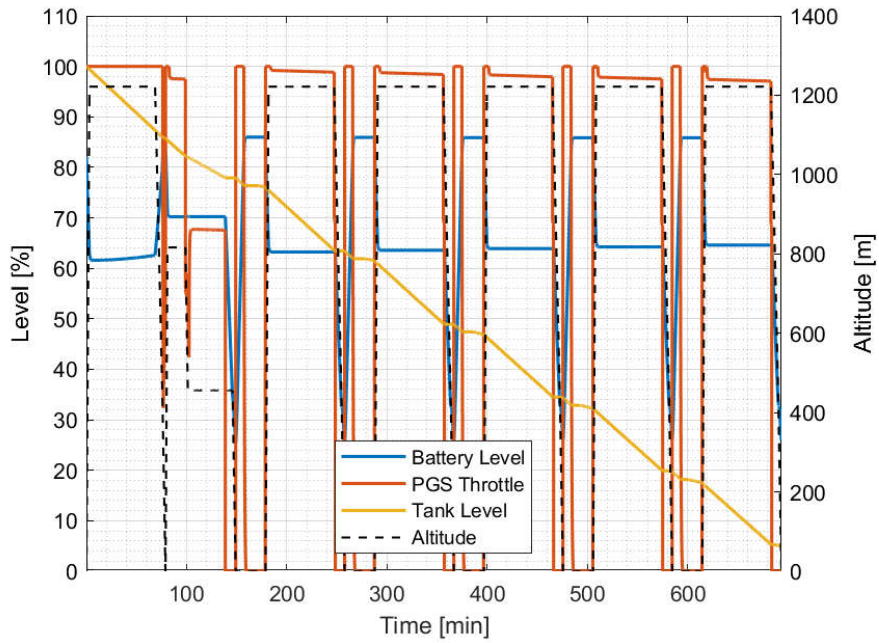


Figure 42 Battery and tank level during the sizing mission for candidate C3.

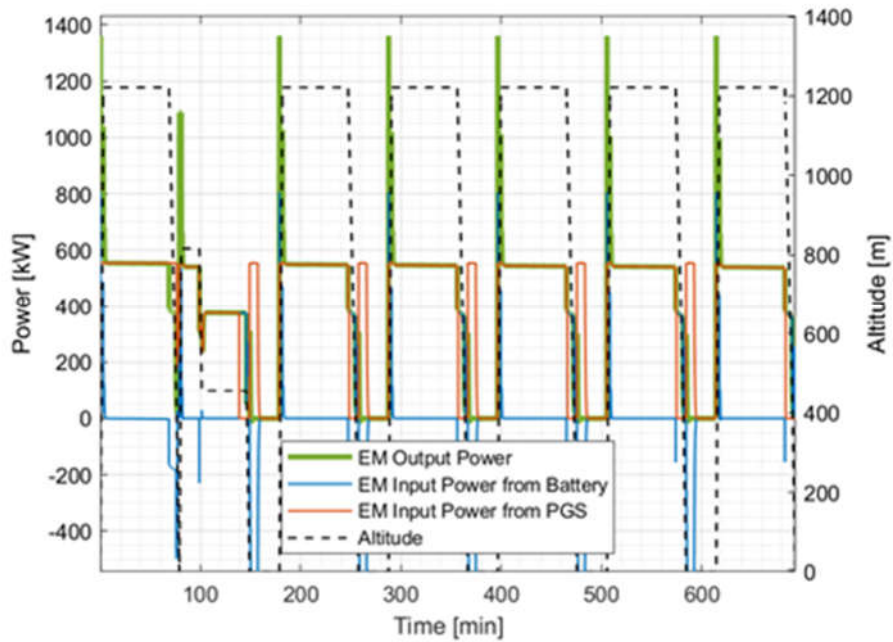


Figure 43 Power utilization during the sizing mission for candidate C3.

## 6.2.2 Sensitivity analysis

A thorough sensitivity analysis was carried out, including the variation of several parameters belonging to three broad categories: technological, global design, and operational parameters. These are varied above

and below the baseline values corresponding to the candidate solution illustrated above, to observe the changes in the selected candidate configuration. Table 17, Table 18 and Table 19. Tables list the parameters with their respective ranges of variations.

Table 17 Variation of technological parameters for sensitivity analysis.

Parameter	Units	Year						
		2020	2022	2025	2027	2030	2032	2035
Battery specific energy	Wh/kg	210	230	260	286.4	304	322.4	350
Battery specific power	W/kg	1365	1487	1670	1850	1970	2092	2275
FC specific power	W/kg	800	1332	2130	2928	3460	3996	4800
EM specific power	W/kg	5750	6463.2	7533	8603.4	9317	10030.2	11100

Table 18 Variation of global design parameters for sensitivity analysis.

Parameter	units	Percentage change						
		B-20%	B-12%	B-5%	Baseline	B+5%	B+12%	B+20%
Range	km	280	308	332.5	350	367.5	392	420
Rate of climb	ft/min	1068.8	1175.7	1269.2	1336	1402.8	1496.3	1603.2
Cruise speed	kn	113.1	124.4	134.3	141.4	148.5	158.4	169.7

Table 19 Variation operational parameters for sensitivity analysis.

Parameter	Units	Change						
		30	35	40	45	-	-	-
Loiter	min	30	35	40	45	-	-	-
Turnaround time	min		15	22	30	38	45	
Airport altitude	ft	-	-	-	0	250	500	750
Payload mass	kg		1900	2090	2280	2470	2660	

The sensitivity analysis is carried out using the HYPERION tool by running it in a batch mode for each configuration. The result of these case studies is a large collection of plots and tables which cannot be included here in entirety. Therefore, a selection of representative plots and tables are presented below (Table 20, Figure 46 - Figure 53). In order to help the evaluation of the economic viability of these configurations, the following global performance parameters are defined:

- $f_{TOT}$ : this is the total energy divided by the mission range multiplied by the number of passenger, so it is expressed in J/km/pax.
- $e_{TOT}$ : this is the total energy divided by the sum of the masses of batteries and hydrogen, so it is measured in J/kg.
- $g_{TOT}$ : this is the total mass of the propulsion system (i.e. mass of PGS + mass of batteries + mass of tank + mass of hydrogen + mass of electric motors) divided by the mission range multiplied by the number of passenger, it is measured in kg/km/pax.

Table 20 : Variation of aircraft range for C3 configuration and respective parameter changes.

<b>Range</b>	<b>[km]</b>	<b>280.0</b>	<b>308.0</b>	<b>332.5</b>	<b>350.0</b>	<b>367.5</b>	<b>392.0</b>	<b>420.0</b>
<b>Empty mass</b>	[kg]	5021	5114	5198	5257	5320	5408	5511
<b>Main motor power</b>	[kW]	1218	1237	1254	1266	1279	1298	1319
<b>Battery mass</b>	[kg]	644.5	654.6	663.8	670.3	677.1	686.7	698
<b>FC mass</b>	[kg]	285.5	290.3	264.3	297.2	300.2	304.5	309.5
<b>LH2 mass</b>	[kg]	281.8	309.5	334.4	652.2	370.9	398.2	429.1
<b>LH2 tank volume</b>	[m3]	4.180	4.590	4.960	5.230	5.500	5.910	6.370

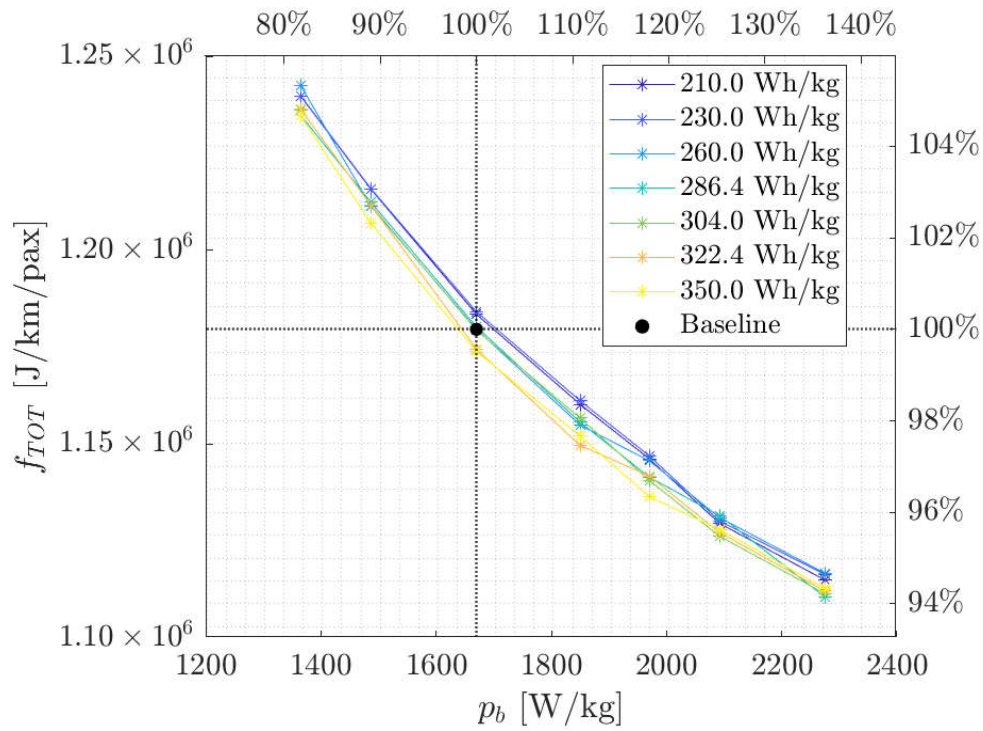


Figure 46  $f_{tot}$  versus battery specific power

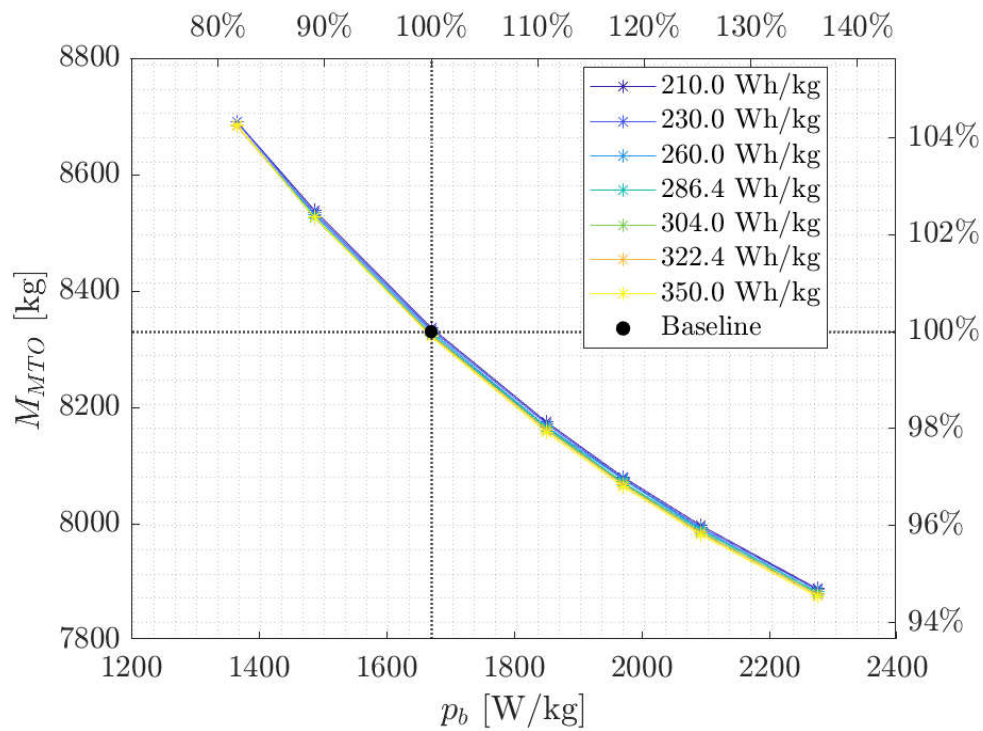


Figure 47 MTOM versus battery specific power

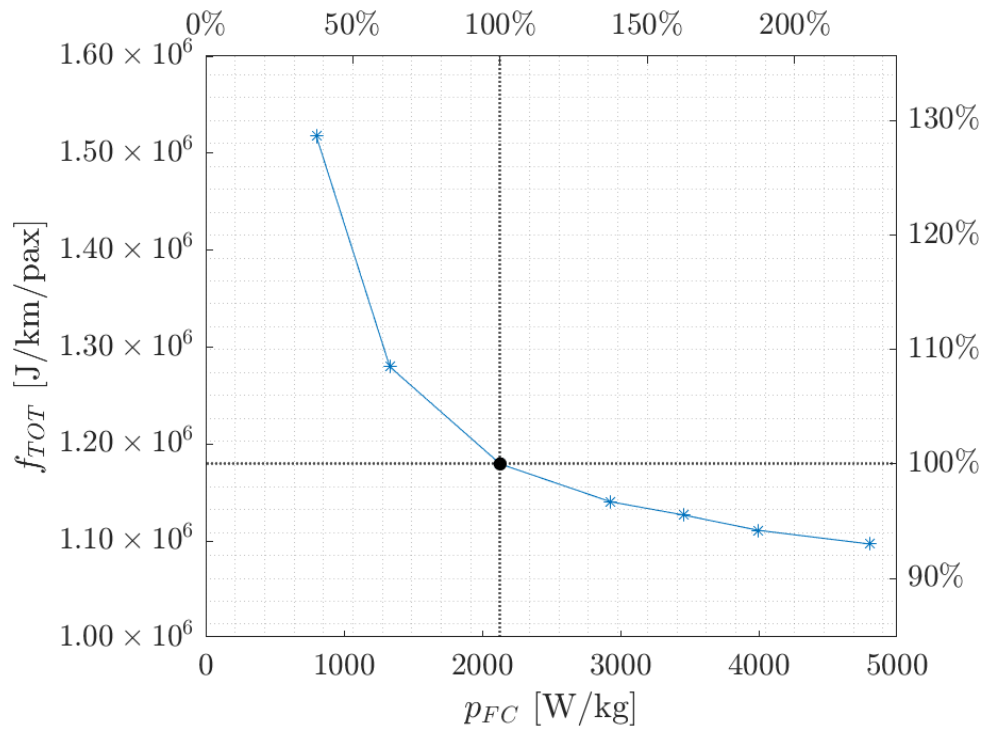


Figure 48  $f_{tot}$  versus fuel-cells specific power

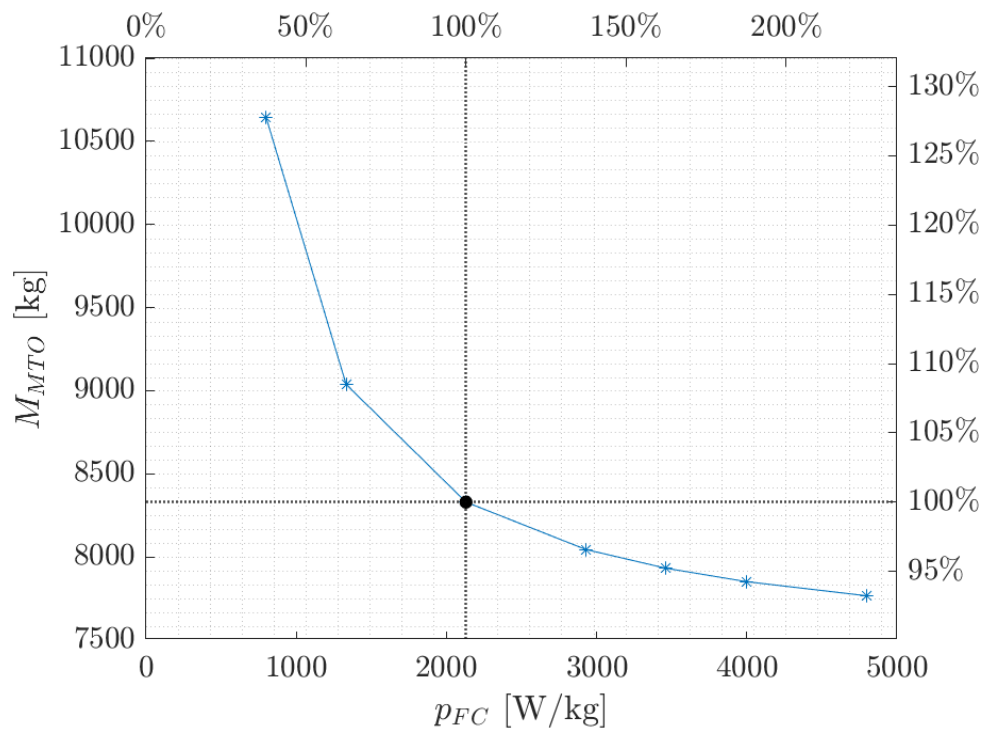


Figure 49 MTOM versus fuel-cells specific power



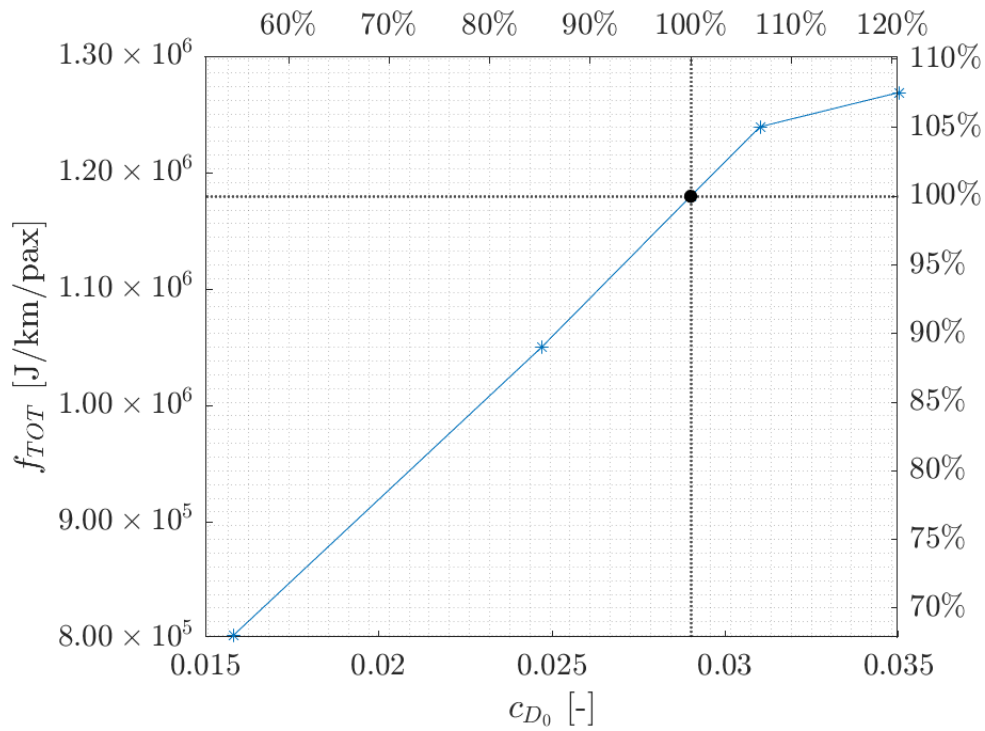


Figure 50  $f_{tot}$  versus  $CD_0$

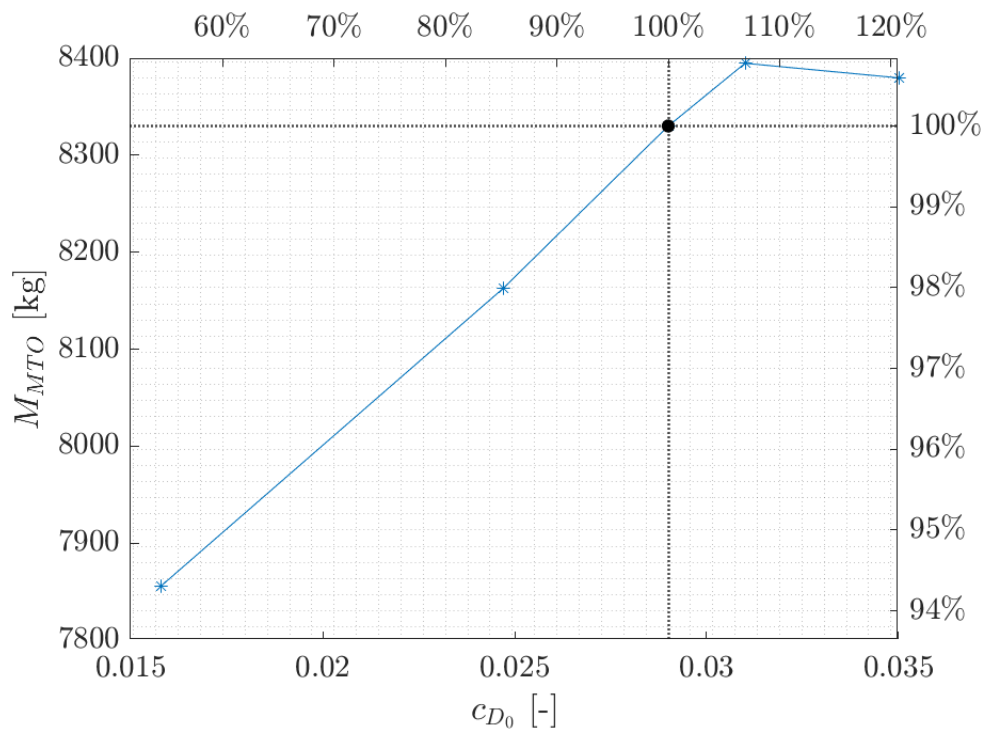


Figure 51  $MTOM$  versus  $CD_0$

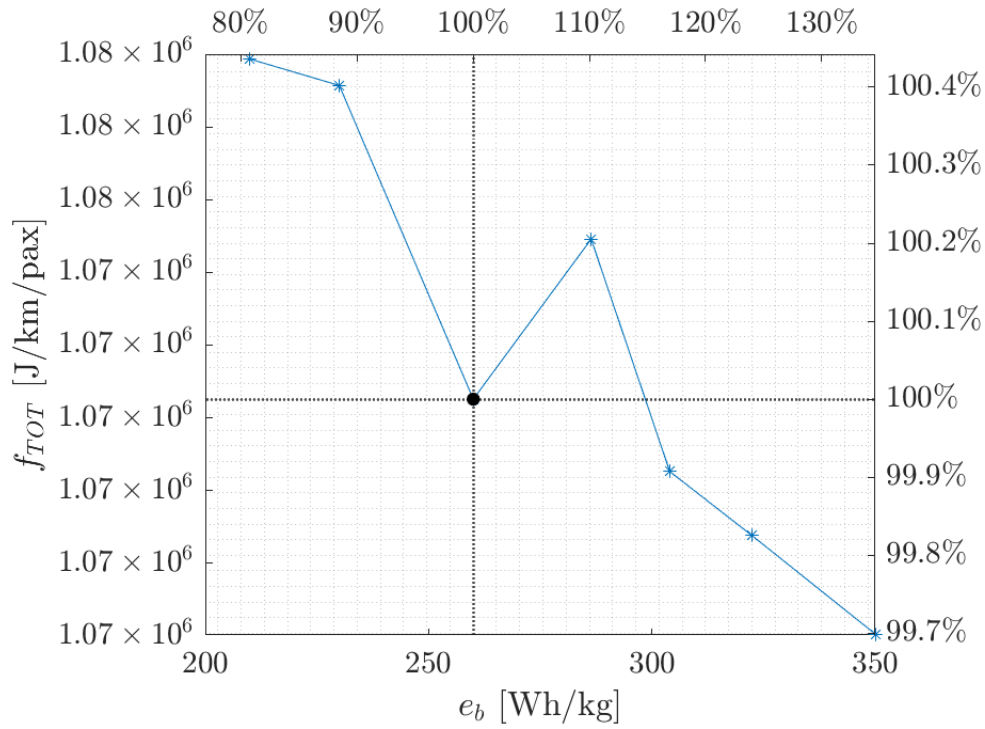


Figure 52  $f_{tot}$  versus battery specific energy

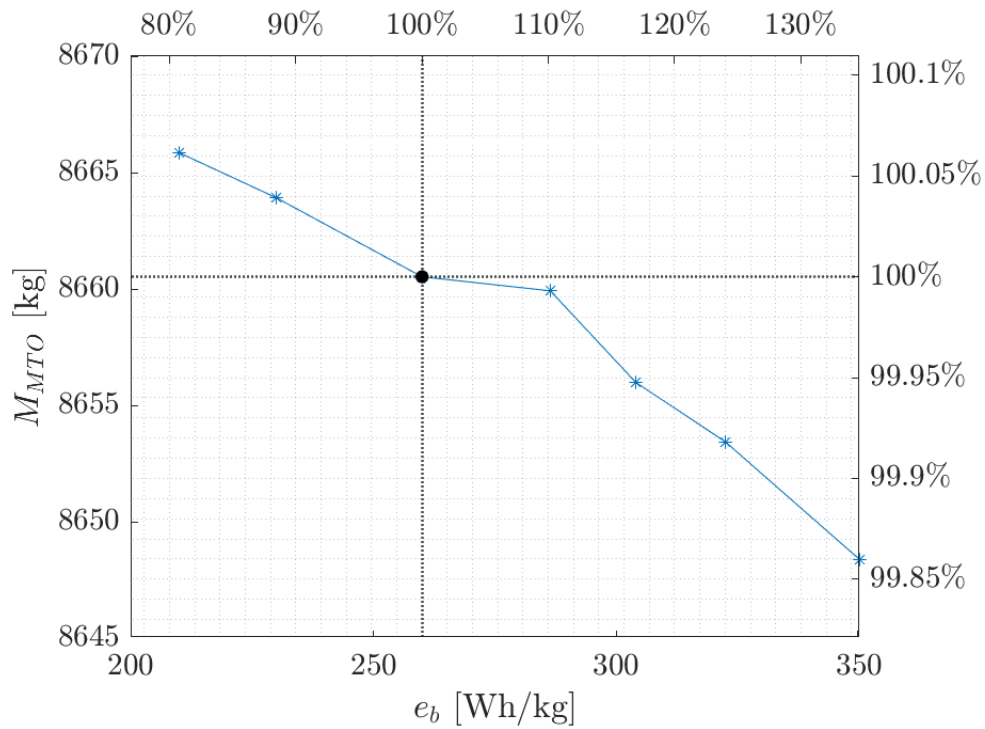


Figure 53 MTOM versus battery specific energy

### 3.2.1 Cross-check & assessment

#### pConcept

The aerodynamic performance was estimated with a single glide ratio value at first, but as the FlightStream results became available, polars were used instead. All other parameters, like battery energy density and fuel cell efficiency, were synchronised with POLIMI, thus the same technology was used. The results are in Table 21.

Table 21: pConcept results.

Mass [kg]	Total	Airframe	El. Motors	Battery	Fuel Cells	LH2	LH2 Tank
Hyperion	<b>7392</b>	<b>3464</b>	<b>144</b>	<b>521</b>	<b>296</b>	<b>350</b>	<b>237</b>
pConcept	<b>7321</b>	<b>3429</b>	<b>142</b>	<b>506</b>	<b>387</b>	<b>341</b>	<b>227</b>

#### FlightStream Analysis

Figure 55, Figure 56, and Figure 57 show the lift, lift-to-drag ratio, and pitching moment of the POLIMI C3 candidate. The candidate contains no propulsion with aero-propulsive interactions and hence only different flap settings are evaluated. The geometry of the aircraft used in the aerodynamic analysis is presented in the Figure 54.

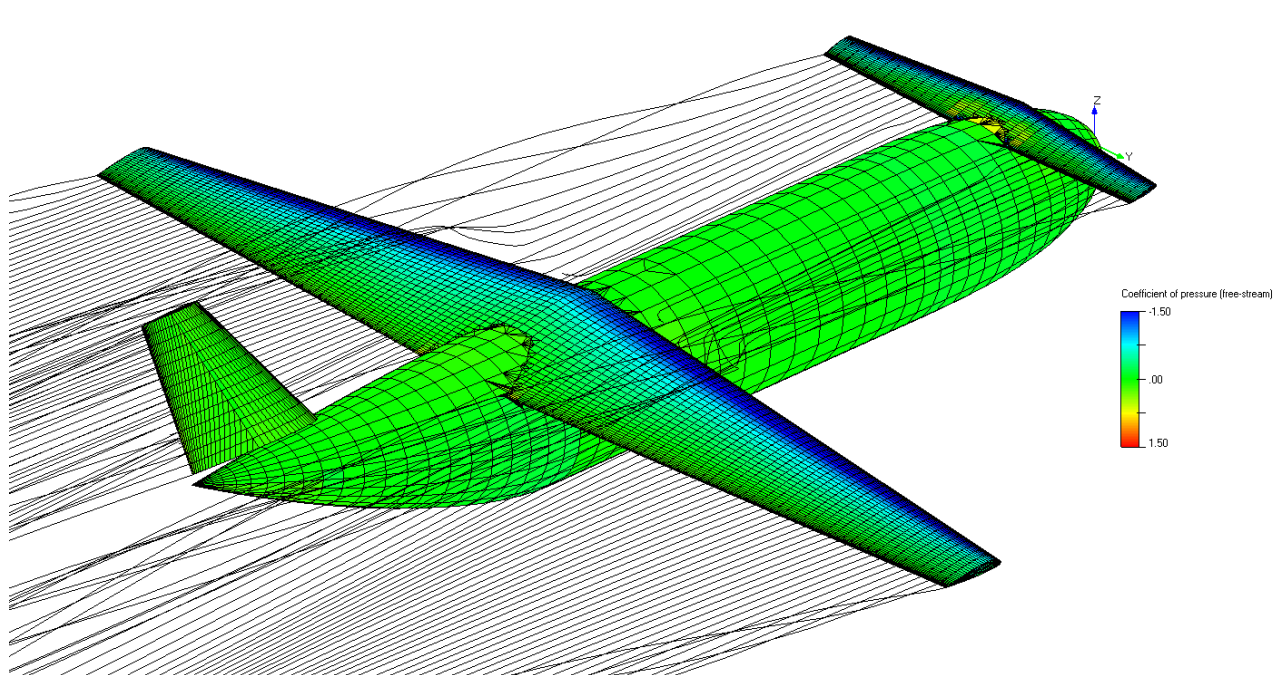


Figure 54 The geometry of the POLIMI C3 candidate used in the aerodynamic analysis.

Table 22 shows the analysis points of the candidate. Reference chord length for the candidate is 2.04 m, reference surface area 37.3 m<sup>2</sup>, and x-C.G. location 9.792 m (datum located at the fuselage nose).

Table 22 The analysis points of the POLIMI C3 candidate.

ANALYSIS POINT	AIRSPEED (m/s)	FOWLER FLAPS (deg)
Cruise	70	0, 12, 39

Similarly, to the POLIMI C2 candidate, the canard configuration has significant shift in the pitching moment coefficient due to flap deployment. No analysis on the trimmability were performed. Additionally, the longitudinal static stability is neutral and slightly negative for the candidate, hence, the centre of gravity would likely need to be shifted further forward. Similarly to the POLIMI C2 and C7A candidates, the candidate contains a fowler flap, which is modelled as continuous due to limitation in the geometric modelling capabilities.

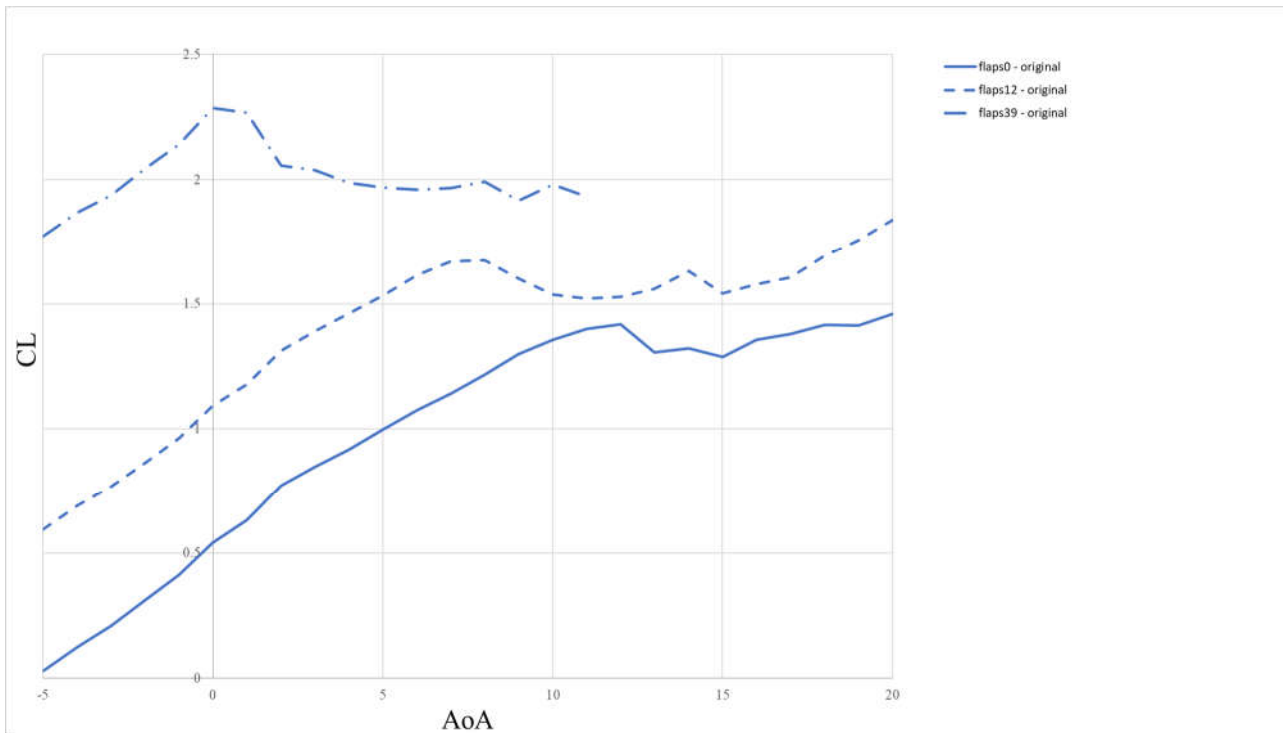


Figure 55 The lift coefficient of the POLIMI C3 candidate.

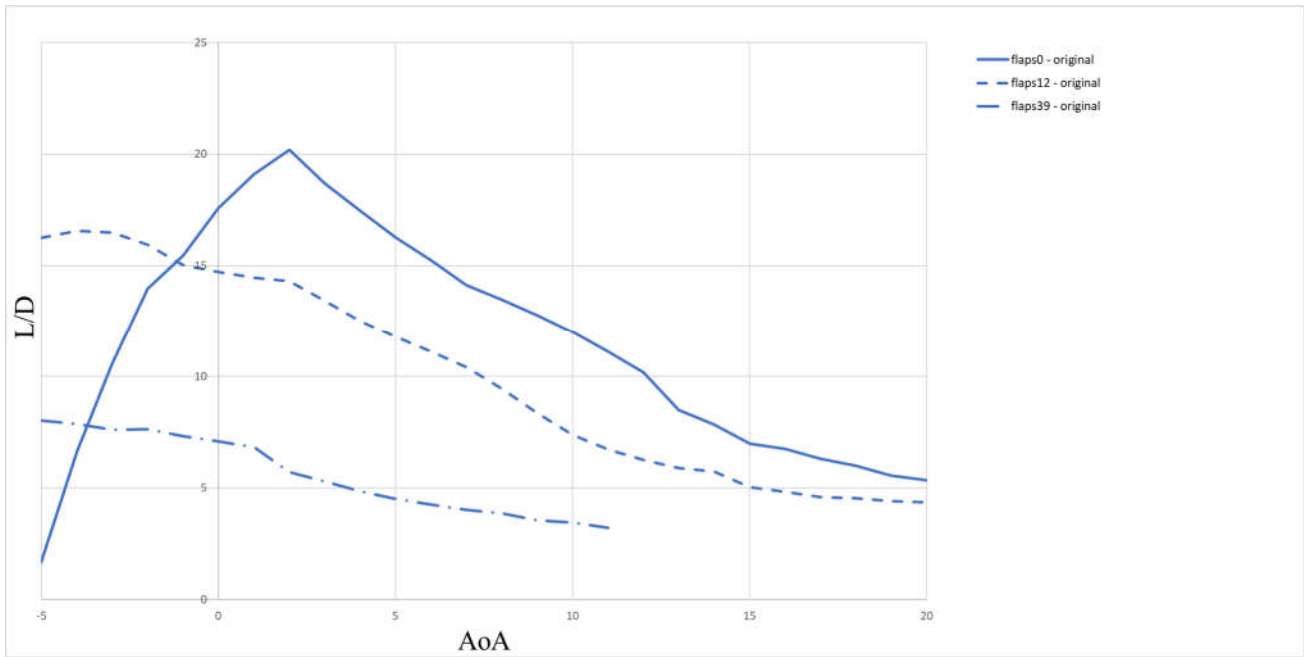


Figure 56 The lift-to-drag coefficient of the POLIMI C3 candidate.

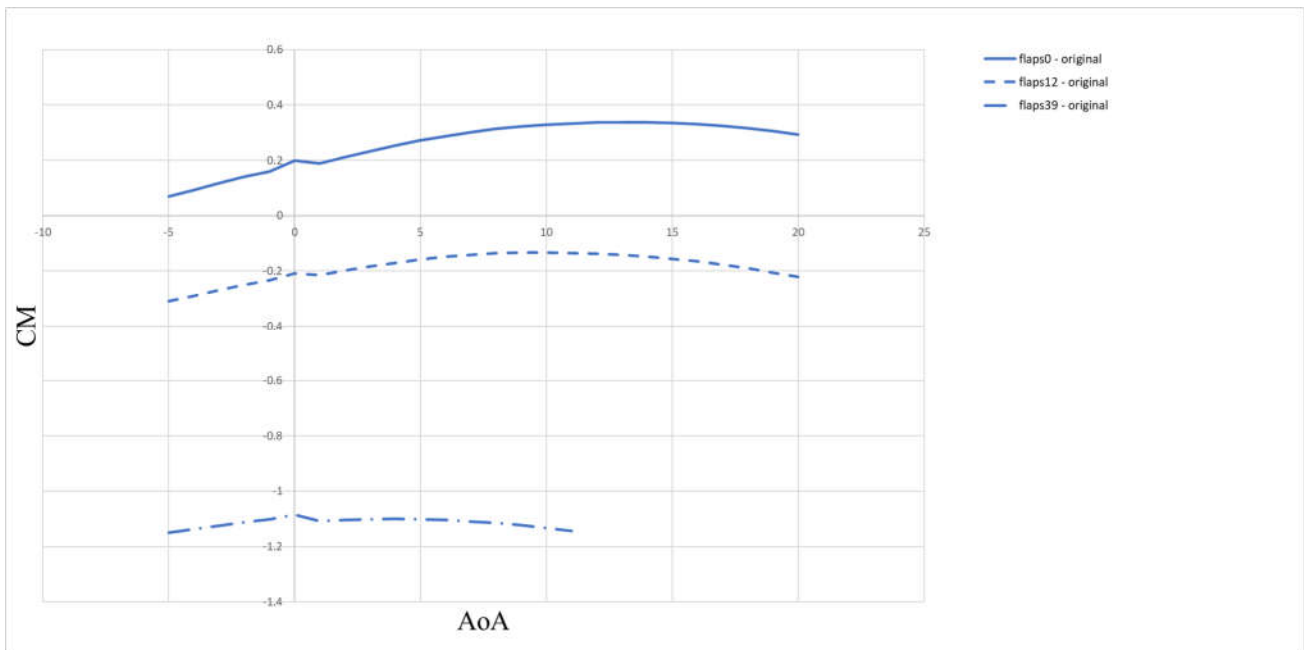


Figure 57 The pitching moment coefficient of the POLIMI C3 candidate.

**Cooling Drag Assessment**

For the POLIMI C3 candidate the input data for cooling drag estimation is presented with Table 23 and Table 25. The estimated size of radiators is given in Table 25. Total face area of radiators is **2.07 m<sup>2</sup>**. Total cooling drag of **1269.5 N** and **753.4 N** was estimated for climb and cruise regime, respectively.

Table 23: Input data (POLIMI 4) for cooling drag estimation – main electric powertrain.

	CLIMB	CRUISE
<b>Electric power (kW)</b>	972.3	524.2
<b>El. motor efficiency (/)</b>	0.95	0.95
<b>Power-controller efficiency (/)</b>	0.97	0.97
<b>Speed (m/s)</b>	48	77
<b>Coolant volumetric flow rate, el. motor (l/min)</b>	62	34
<b>Coolant volumetric flow rate, power-contr. (l/min)</b>	32	18
<b>Coolant inlet temp, el. motor (°C)</b>	60	60
<b>Coolant inlet temp, power-controller (°C)</b>	55	55
<b>Coolant</b>	50/50 MEG	50/50 MEG

Table 24 Input data (POLIMI C3) for cooling drag estimation – FC.

	CLIMB	CRUISE
<b>Total electric power out (kW)</b>	600	600
<b>FC efficiency (/)</b>	0.52	0.52
<b>Speed (m/s)</b>	48	77
<b>Coolant volumetric flow rate (l/min)</b>	130	130
<b>Coolant inlet temp (°C)</b>	45	45
<b>Coolant</b>	50/50 MEG	50/50 MEG

Table 25: POLIMI C3 radiators size.

Cooling system for	# of radiators	Height (mm)	Width (mm)	Face area (m <sup>2</sup> )
<b>Main el. powertrain</b>	1	470	600	0.282
	1	400	470	0.188
<b>FC system</b>	2	800	1000	1.6

### Mission Analysis

Comparison of required shaft power during the mission between POLIMI and PVS mission analysis for C3 is presented in Figure 58. The figure depicts only the first two hops with the diversion in between, for the sake of visibility. A small offset in time scale can be observed, originating from different times needed for climb and descend.

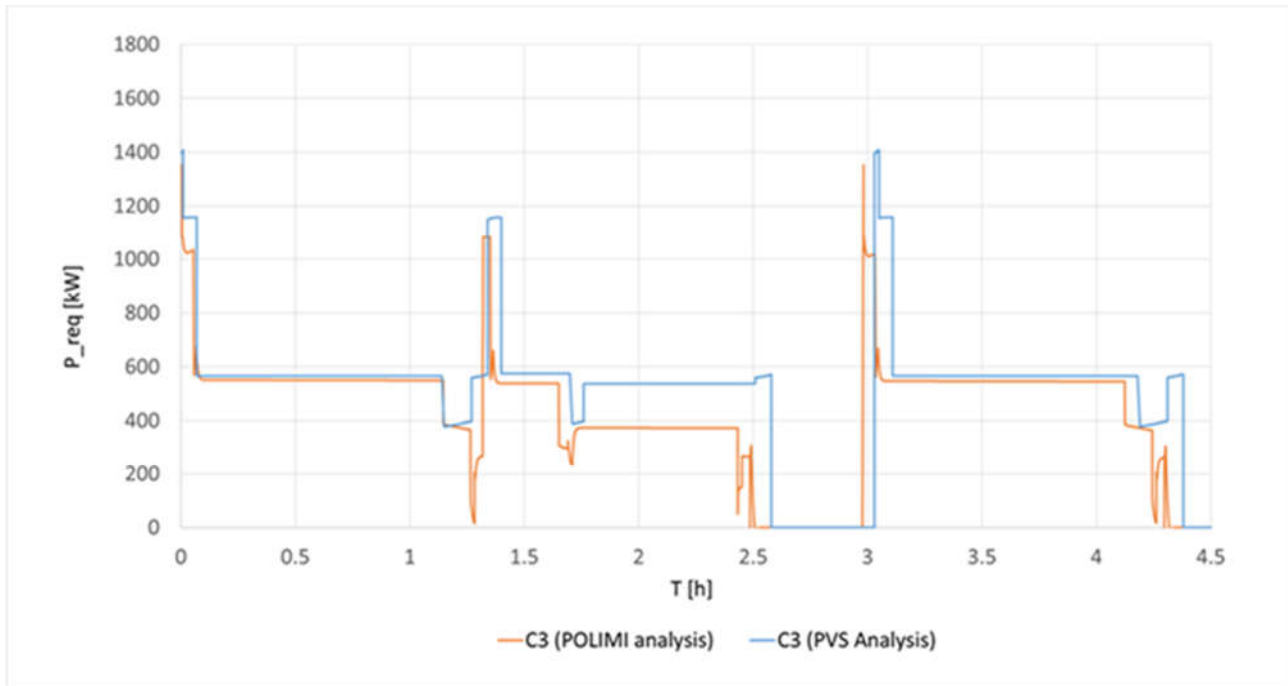


Figure 58: Shaft power requirement comparison for C3 candidate between PVS and POLIMI analysis.

Two notable differences in power requirements in loiter and second descend phase are visible, for which a more detailed clarification can be found in Section 1.1.1.

### Qualitative structural design assessment

The table below summarizes the advantages and disadvantages of the C3 configuration w.r.t. to other configurations from a qualitative structural standpoint. A more detailed and general qualitative structural assessment is presented in Section 1.1.1.

Section	Pros	Cons
<b>Fuselage</b>	Reduced weight due to canard configuration	/
<b>Main Wing</b>	Simpler structural design due to no engines mounted on the wing	-No bending load alleviation as with DEP concepts -More complicated planform and wingtip shapes may prove suitable only for composite structure
<b>Empennage</b>	No horizontal stabilizer simplifies the design	Presence of pusher engine complicates design and increases weight

## 3.3 Configuration C7A

### 3.3.1 General description

As discussed at the beginning of the present Chapter, this configuration emerged as a result of a further down-selection and reconsideration of the TBW candidates included the original top five POLIMI candidate list. The following section explains the general description of the configuration, the results of sensitivity analysis and the cross-checking assessment.

This configuration entails the traditional lifting surface layout with a tail aft of the main wing. The distinguishing features include an array of multi-functioning distributed electric propulsion (DEP) units on the leading edge of the main wing and a powerful pusher propeller on the tail (TCP). This innovative propulsion setup helps improving the wing design which is optimized for cruise and yet it can achieve lift requirements for take-off and landing. This is accomplished by blowing the main wing with the help of distributed propellers which increase the coefficient of lift without the need of large high-lift devices. The blowing propellers also provide additional thrust required during the take-off phase. During the cruise phase, DEP is turned off and the pusher propeller provides the cruise thrust. The propellers in the DEP array are assumed to fold backwards when non-operating, to reduce drag in cruise. The terminal phases of final approach and landing call for activation of DEP once again.

The internal arrangement of the fuselage includes a liquid hydrogen fuel tank under the wing, while the passenger cabin is in the front section and the baggage compartment is in the rear. The optimized hydrogen tank shape and size is such that it cannot be placed inside the wings. Hence a position close to centre of gravity is selected in the fuselage. The overall configuration is displayed in Figure 59. Table 26 provides a comprehensive list of the C7A design specifications.

This is the result of the application of the TITAN design loop, which couples the HYPERION preliminary sizing tool with the ARGOS Class I design procedures. The convergence of the process is very quick, with only five iterations necessary from the HYPERION initial guess. Figure 60 shows the Sizing Matrix Plot (SMP), which allows appreciating the design point location at on the take-off distance requirement. It is remarked that several curves in the SMP have a strikingly different appearance than in the case of non-DEP aircraft solutions, due to the aerodynamic impact of DEP on various terminal and point performance. Figure 61 provides the resulting mass breakdown. Finally, Figure 62 and Figure 63 show the time histories of the energy and power quantities during the sizing mission, along with its altitude profile.

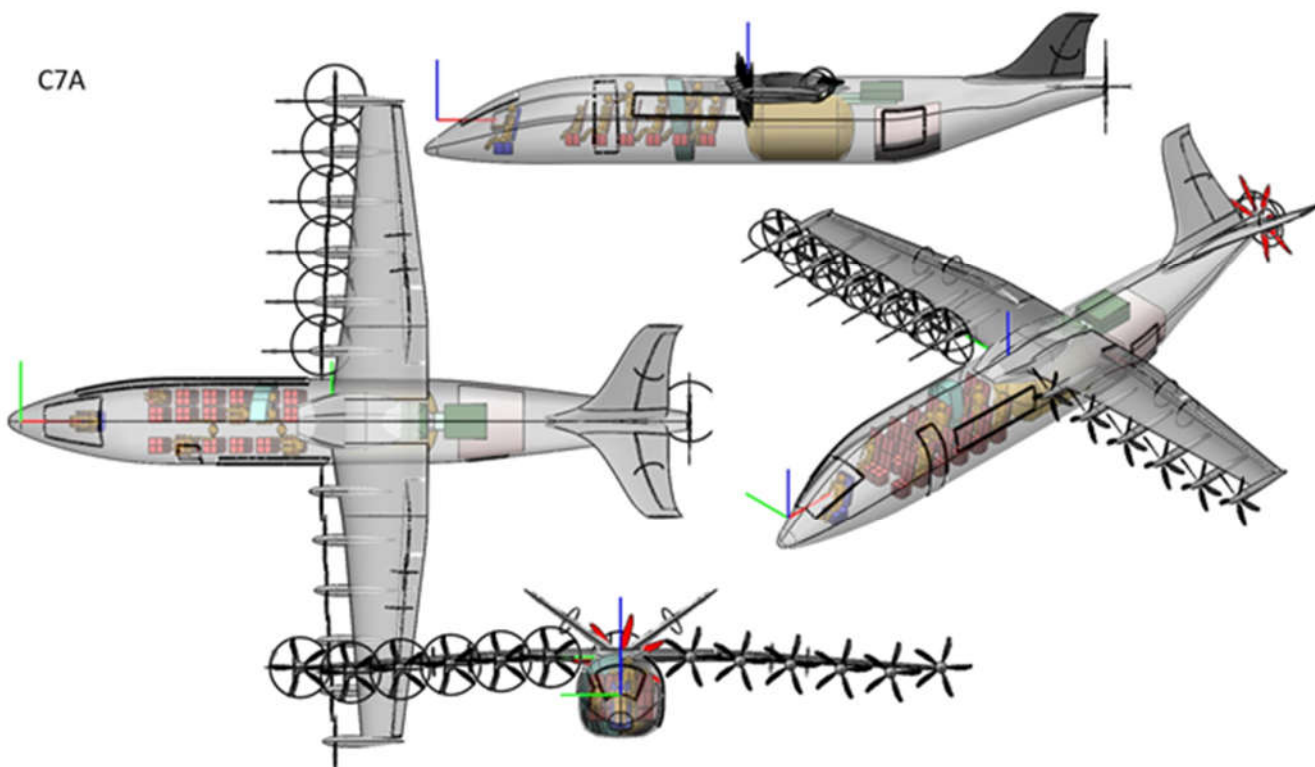


Figure 59 Candidate C7A top, side, front and ISO view.



Table 26 Complete specifications of candidate C7A

Name	Value	Units
Payload	2280	kg
Number of passengers	19	-
Number of pilots	1	-
Pressurization	No	-
Regulation	CS23	-
Use DEP	Yes	-
Wing position	High	-
Flap type	Fowler	-
Design Power Loading	0.0657	N/W
Design Wing Loading	1999	N/m <sup>2</sup>
Max. take off field length	800	m
Max. landing distance	800	m
Max. stall speed	35.35	m/s
Airport altitude	0	m
Rate of climb	6.79	m/s
Climb speed	55.25	m/s
Cruise speed	72.74	m/s
Cruise altitude	1219	m
Cruise range	350	km
Rate of descent	-1.78	m/s
Descent speed	72.74	m/s
Loiter altitude	457	m
Loiter time	45	min
Diversion range	100	km
Field Name	Propulsion	
Windmill efficiency	0.0	%
Electric motor efficiency	92.0	%
Electric motor power density	7533	W/kg
Electric motor overrating	1.25	-
PGS power density	2130	W/kg
PGS efficiency	95.0	%
Hybrid transition altitude	0	m
Minimum fuel level	5.0	%
Fuel cell voltage	600	V
Compressor efficiency	88.0	%
Number of FC systems	2	-
Battery power density	1670	W/kg
Battery energy density	936000	J/kg
Minimum charge level	25.0	%
Maximum charge level	85.0	%
Engine thrust	24443	N
Engine power	1188.2	kW
Propeller efficiency (non-DEP)	80.0	%

Number of engines	1	-
Propeller diameter (non-DEP)	2.88	m
Number of blades	4	m
EM maximum cont. power	1188.2	kW
PGS power	635.3	kW
H2 tank volume	5.58	m3
Gravimetric index	0.60	-
H2 tank diameter	2.09	m
H2 tank length	2.32	m
N. of tanks on length	1	-
N. of tanks on width	1	-
Total number of tanks	1	-
Tank ins. thickness	0.0580	m
Tank wall thickness	0.0046	m
DEP power	786.1	kW
DEP propeller diameter	1.47	m
DEP Electric motor efficiency	92.0	%
DEP Electric motor power density	7533	W/kg
DEP Electric motor overrating	1.25	-
DEP propeller efficiency	60.0	%
Number of DEP propellers	12	-
DEP propeller separation	0.00	-
DEP propeller tilt angle	0.0	deg
DEP propeller offset	0.310	-
Field Name	Weights - General/Special	
Maximum take off	7953.7	kg
Operative empty	5297.8	kg
Empty	4614.6	kg
Airframe	3886.0	kg
Wing	665.5	kg
Fuselage	974.5	kg
Horizontal Tail	74.6	kg
Vertical Tail	118.3	kg
Fuel (wing)	0.0	kg
Fuel (fuselage)	375.9	kg
Landing Gear	352.7	kg
Pilot	100.0	kg
Flight Assistant	0.0	kg
Cargo	836.0	kg
Control Surf.	239.0	kg
APU	0.0	kg
Instr. & Nav. Sys.	45.4	kg
Hydr. & Pneu. Sys.	8.0	kg
Electric Sys.	202.0	kg
Electronics	136.1	kg
Air cond. & Anti-ice	447.4	kg
Furnishing	433.6	kg

<b>Passengers</b>	1444.0	kg
<b>Battery</b>	586.3	kg
<b>PGS</b>	314.0	kg
<b>Hydrogen Tank</b>	253.8	kg
<b>DEP</b>	104.4	kg
<b>Airfoil</b>	NACA 0006	-

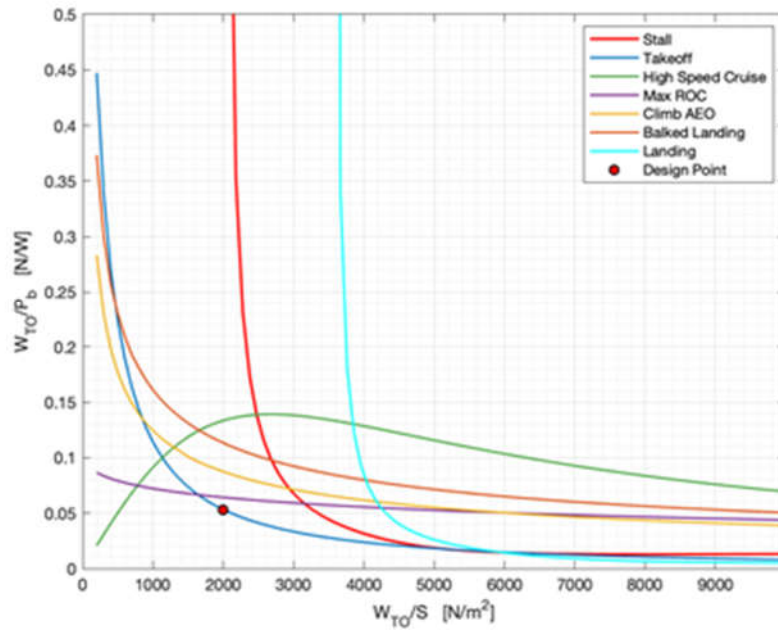


Figure 60 Sizing matrix plot for candidate C7A.

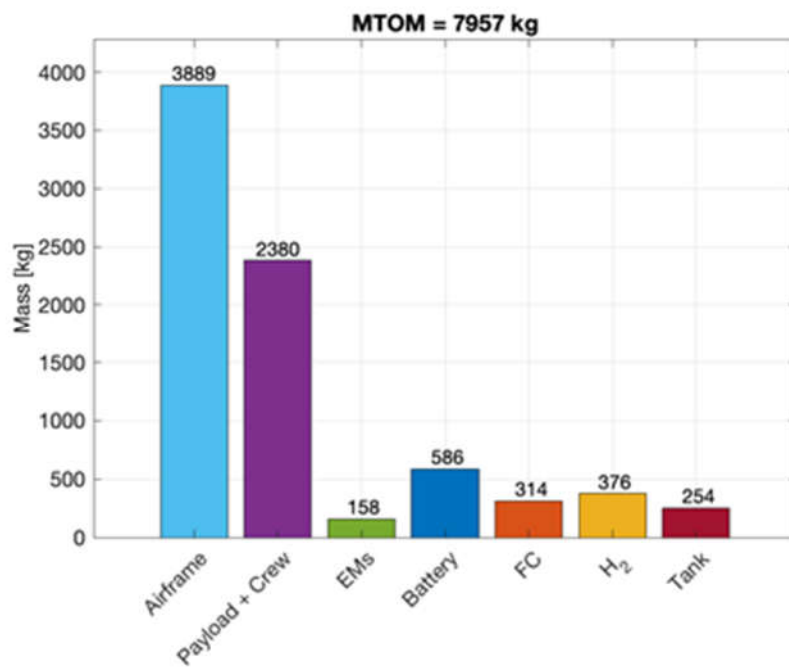


Figure 61 Mass breakdown of candidate C7A.

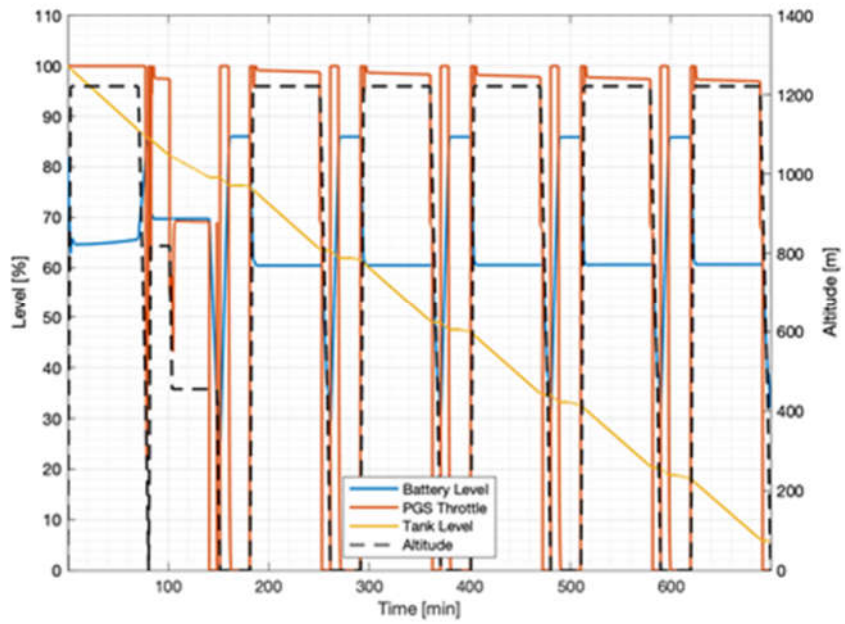


Figure 62 Battery and tank level during the sizing mission for candidate C7A.

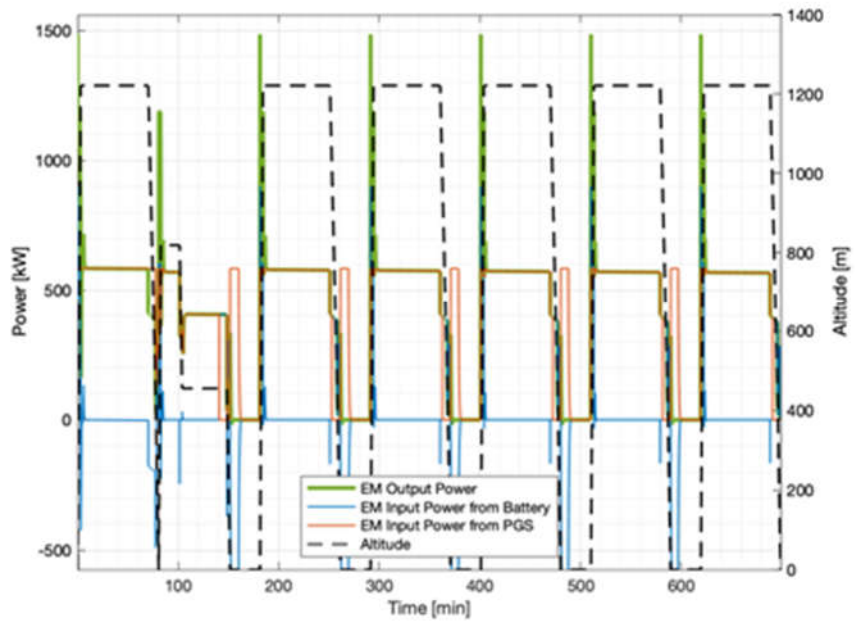


Figure 63 Power utilization during the sizing mission for candidate C7A.

### 3.3.2 Sensitivity analysis

A thorough sensitivity analysis was carried out along the same lines discussed for candidate C3. The result of these case studies is a large collection of plots and tables which cannot be included here in entirety. Similarly, a selection of representative plots and tables are presented below (Table 27, Figure 64 - Figure 71).

Table 27 Variation of aircraft range for C7A configuration and respective parameter changes.

Range	[km]	280.00	308.00	332.50	350.00	367.50	392.00	420.00
MTOM	[kg]	8040.3	8152.2	8254.2	8330.0	8406.8	8520.1	8652.9
Empty mass	[kg]	4731.2	4867.6	4946.7	5005.9	5064.4	5151.4	5254.0
Main motors power	[kW]	1197.4	1211.4	1224.2	1233.7	1243.2	1257.8	1274.5
DEP motors power	[kW]	598.72	605.70	612.10	616.89	621.62	628.93	637.25
Battery mass	[kg]	569.50	563.50	558.40	555.10	550.70	547.30	541.30
FC mass	[kg]	310.60	316.30	321.50	325.30	329.30	335.00	341.80
LH2 mass	[kg]	309.30	340.70	368.70	388.70	411.50	440.80	477.20
LH2 tank volume	[m3]	4.5900	5.0600	5.4700	5.7700	6.1100	6.5500	7.0800

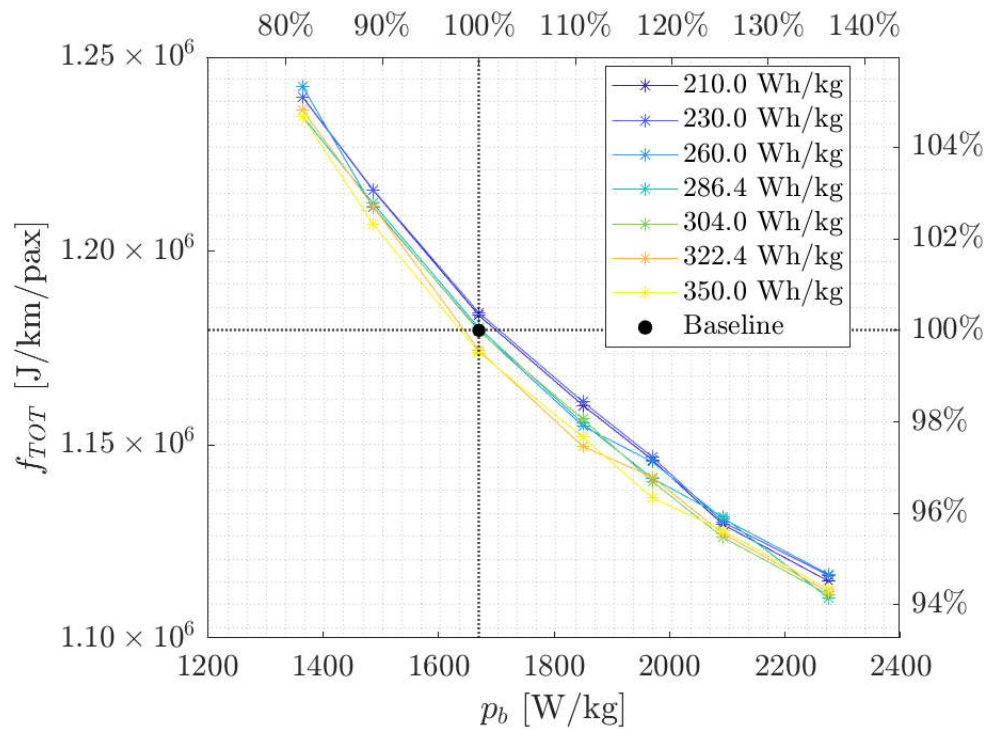


Figure 64  $f_{tot}$  versus battery specific power

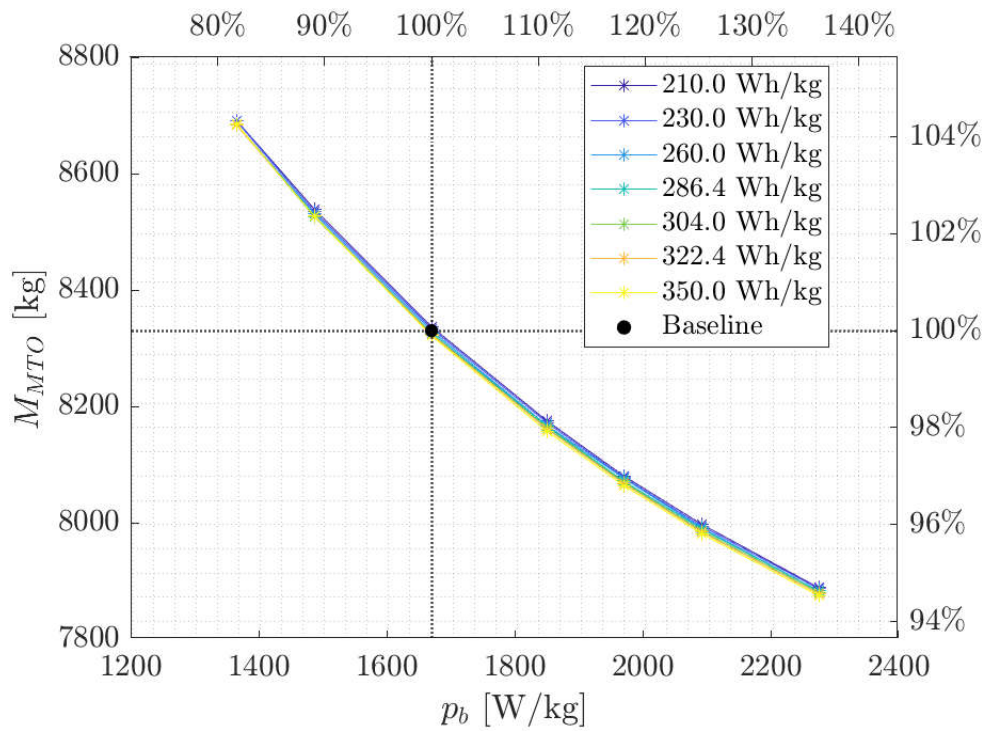


Figure 65 MTOM versus battery specific power

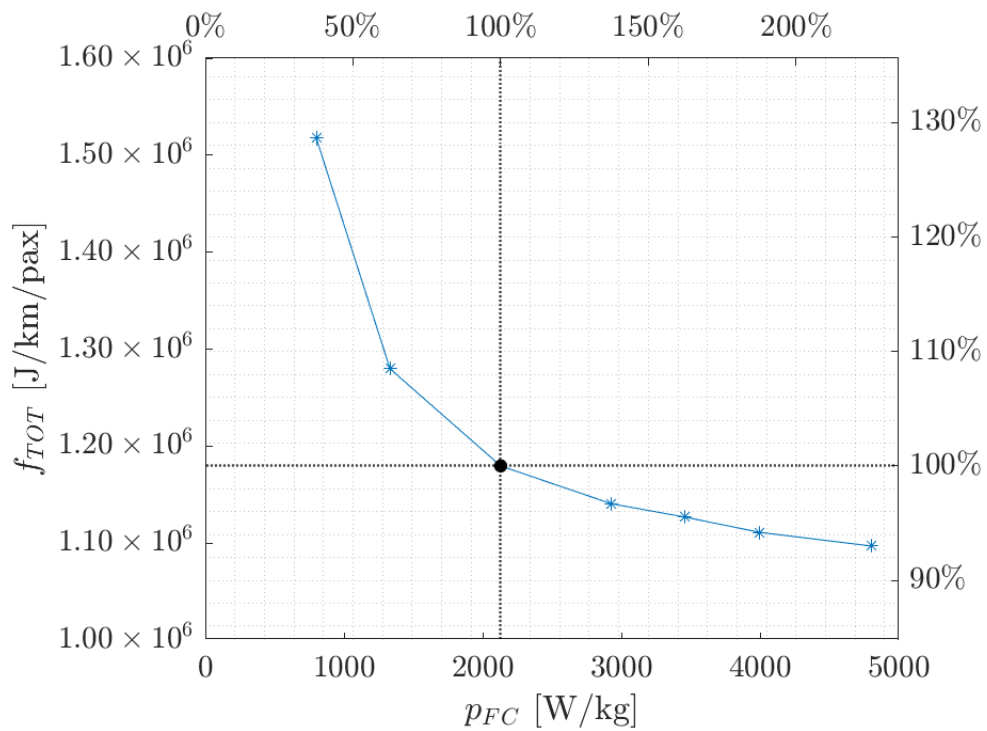


Figure 66  $f_{tot}$  versus fuel-cells specific power

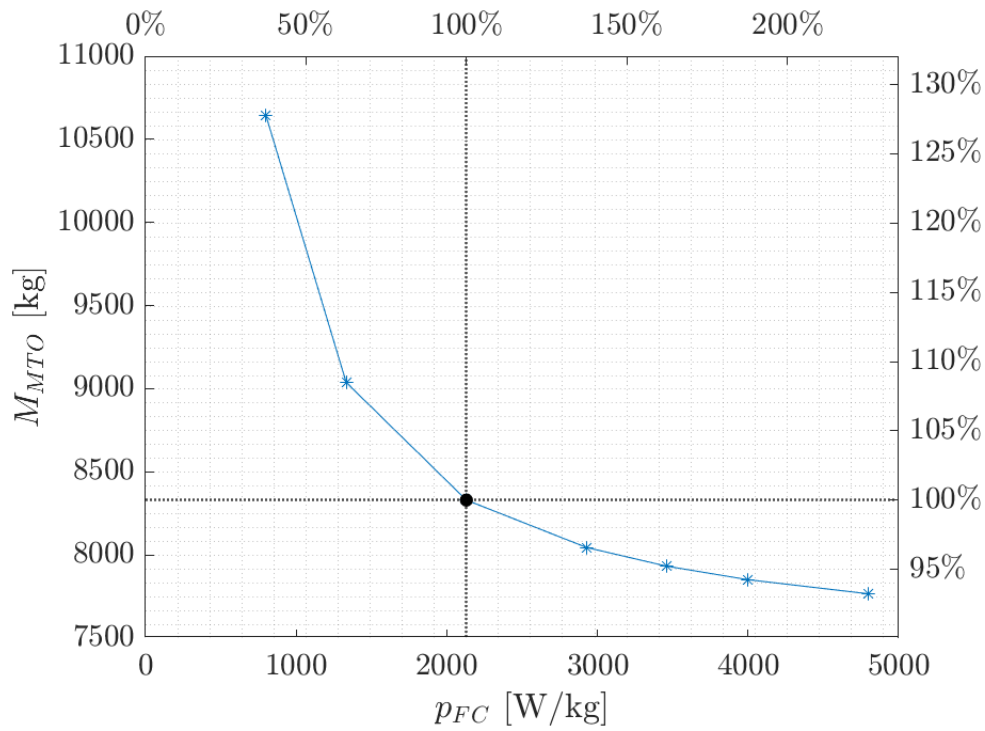


Figure 67 MTOM versus fuel-cells specific power

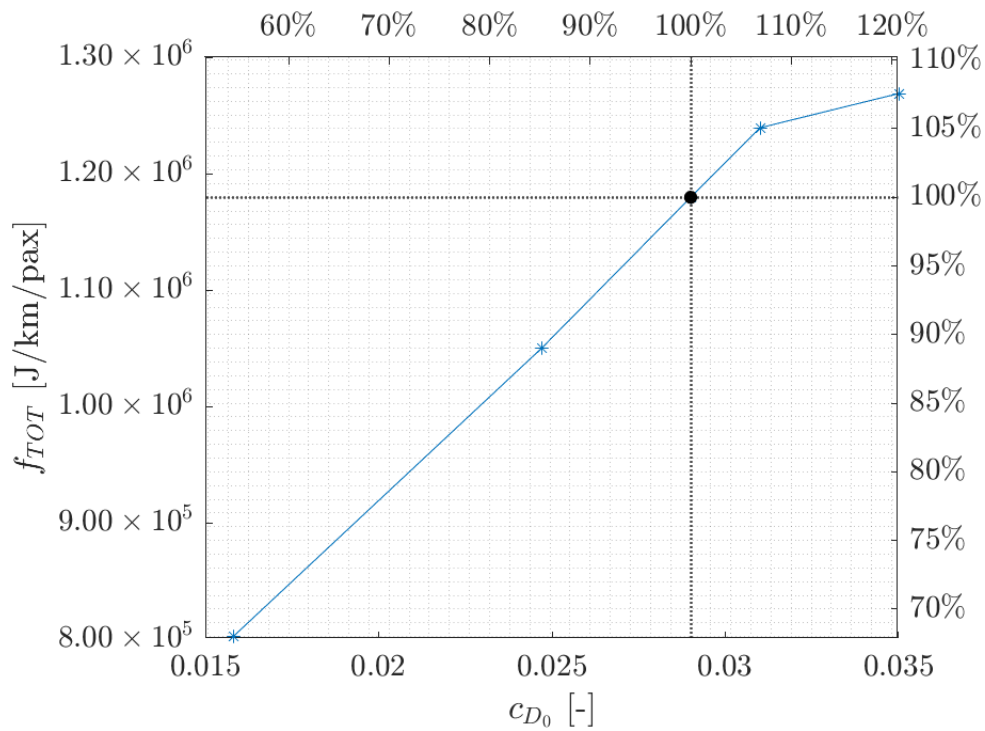


Figure 68  $f_{tot}$  versus  $CD_0$

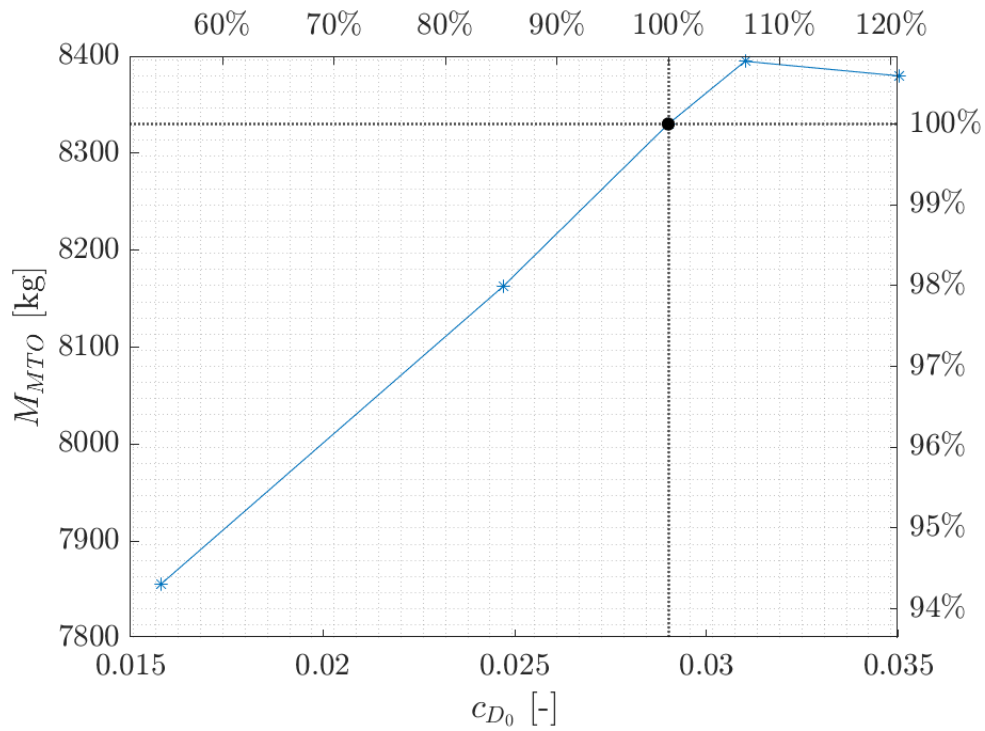


Figure 69 MTOM versus CD0

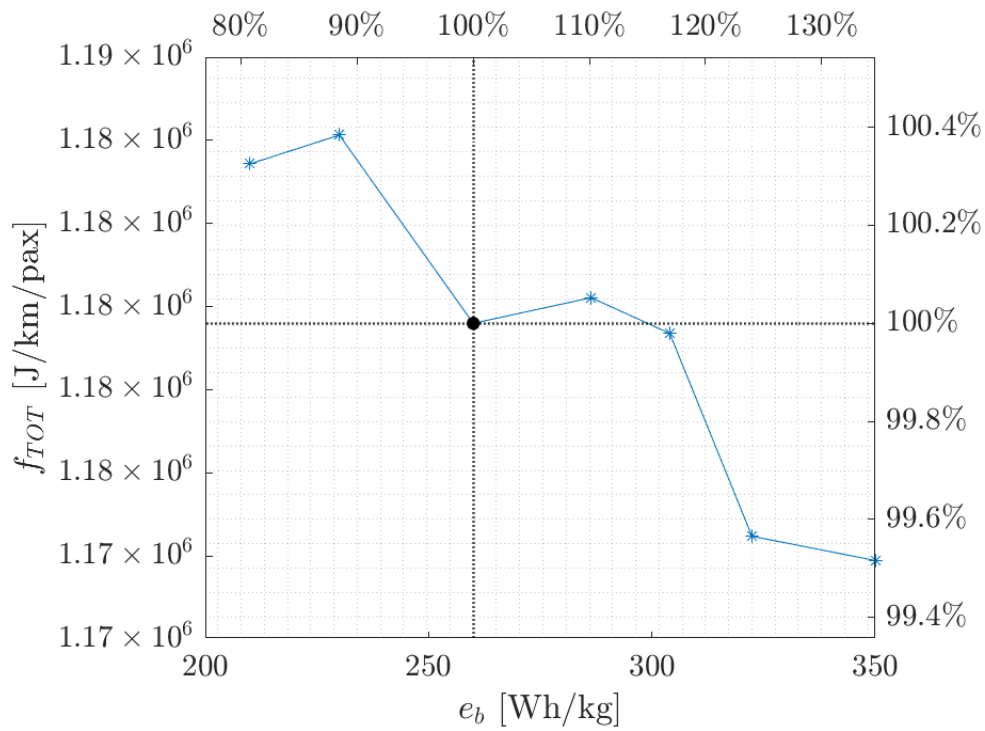


Figure 70  $f_{tot}$  versus battery specific energy



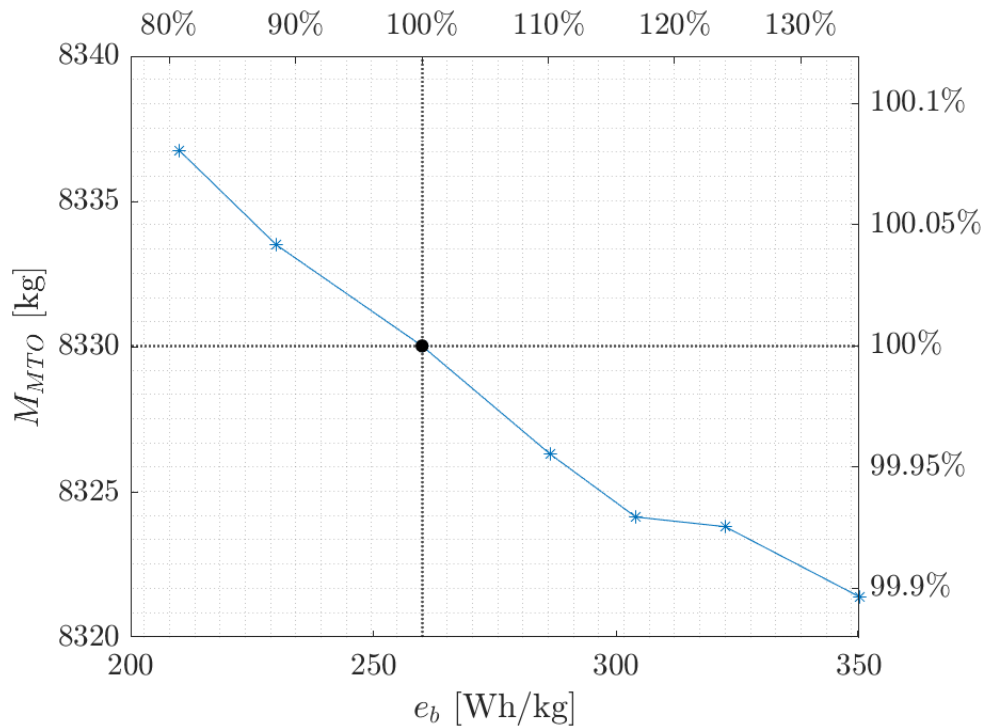


Figure 71 MTOM versus battery specific energy

### 3.3.3 Cross-check & assessment

#### pConcept

The aerodynamic performance was estimated with a single glide ratio value at first, but as the Flight Stream results became available, polars were used instead. All other parameters, like battery energy density and fuel cell efficiency, were synchronised with POLIMI, thus the same technology was used. The results are in Table 28.

Table 28: pConcept results.

Mass [kg]	Total	Airframe	El. Motors	Battery	Fuel Cells	LH2	LH2 Tank
<b>Hyperion</b>	7957	3889	158	586	314	376	254
<b>pConcept</b>	7868	3855	156	574	300	361	241

#### FlightStream Analysis

The candidate contains leading edge mounted distributed electric propulsion, which is used only in the climb and take off/landing phase. The geometry of the aircraft used in the aerodynamic analysis is presented in the Figure 74.

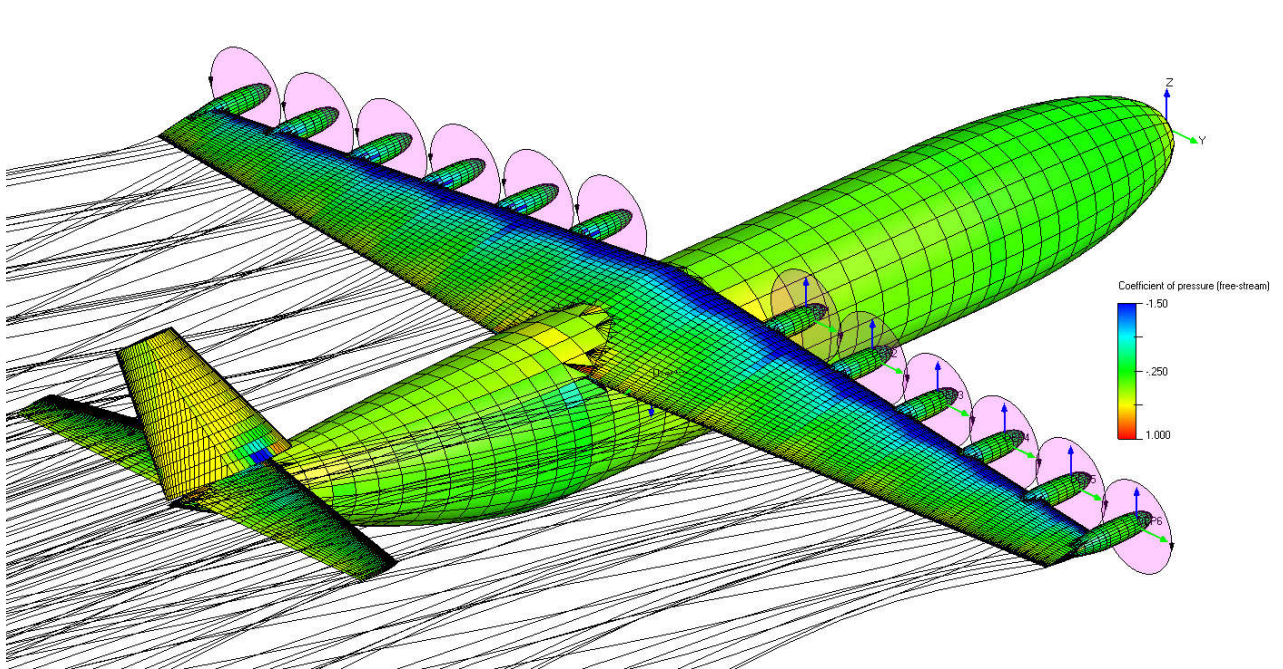


Figure 74 The geometry of the POLIMI C7A candidate used in the aerodynamic analysis.

The analysis points of the candidate can be seen in Table 29. Reference chord length for the candidate is 2.08 m, reference surface area 39.03 m<sup>2</sup>, and x-C.G. location 10.36 m (datum located at the fuselage nose).

Table 29 The analysis settings of the POLIMI C7A candidate.

ANALYSIS POINT	DEP COEFFICIENT	THRUST DEP RPM	AIRSPEED (m/s)	FOWLER FLAPS (deg)
<b>Cruise</b>	-	-	72.74	0, 12, 39
<b>Climb</b>	0.29	1400	55.25	0, 12, 39
<b>Take off/Landing</b>	0.31	1400	39	0, 12, 39

The candidate contains a fowler flap. However, due to the limitation in the geometric modelling capabilities, the fowler flap was replaced with a continuous fowler flap. The limitation is due to OpenVSP which offers no simple approach for modelling fowler flap. Due to this reason the fowler flap shows significant stalling behaviour at take-off and landing configuration, which would not exist in a fowler flap with slot as the slot is re-energizing the boundary layer over the flap. This limitation is mitigated by collecting the data only at low angles of attack. At high angles of attack, the coefficients are extrapolated. Refer to the Section 2.2.9 for future discussion of the extrapolation. Figure 75 shows the fowler flap of the candidate.

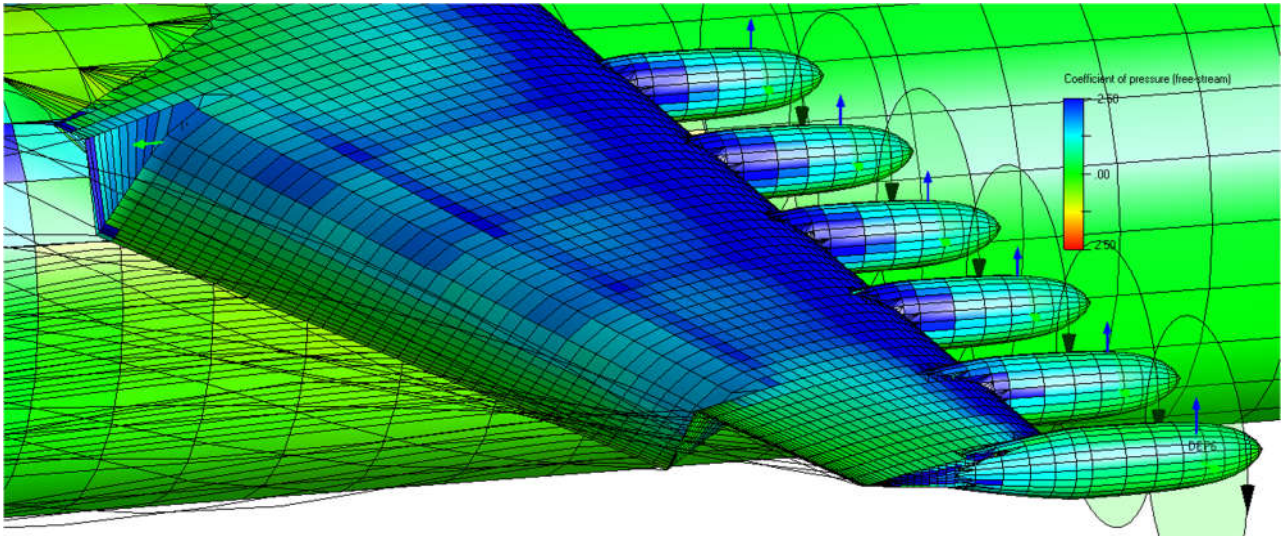


Figure 75 The fowler flap of the POLIMIC7A1 candidate. The fowler flap is modelled as continuous due to limitation in the modelling capabilities.

Figure 76, Figure 77 and Figure 78 show the lift, lift-to-drag ratio, and pitching moment coefficient of the POLIMI C7A candidate.

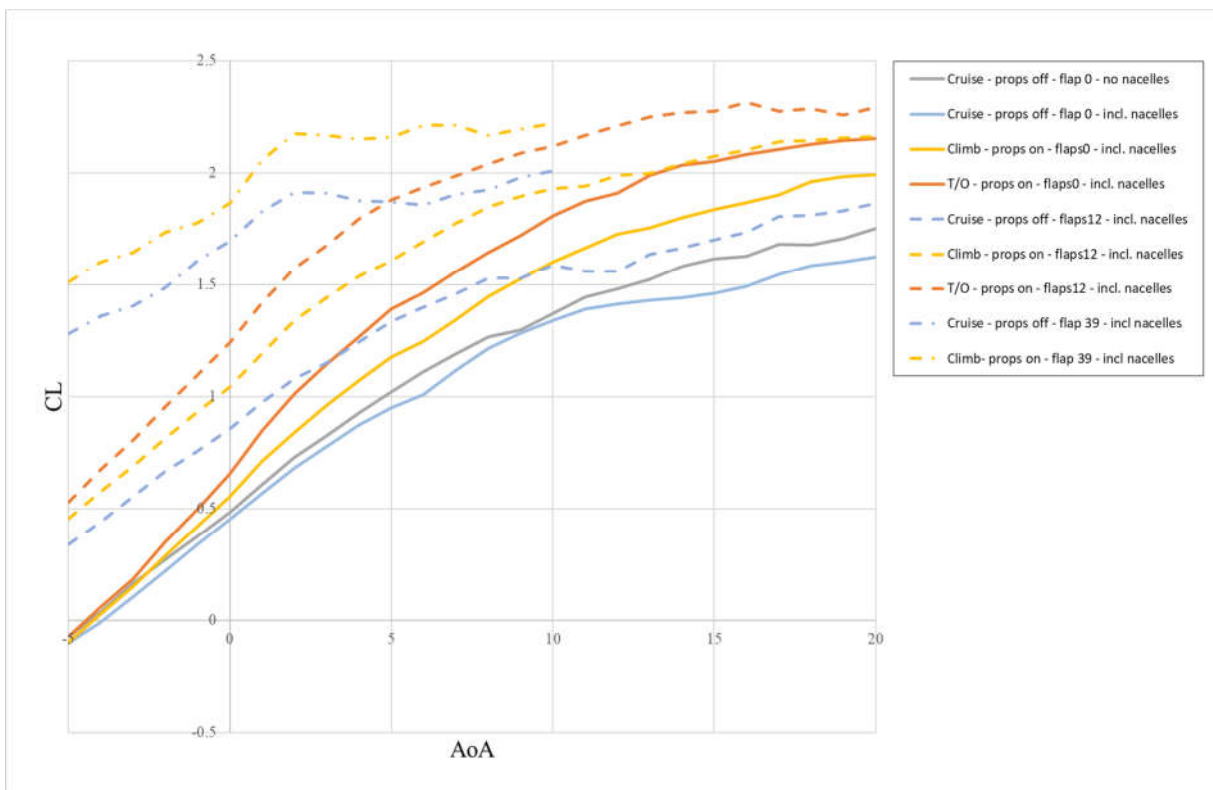


Figure 76 The lift coefficient of the Polimi C7A candidate.

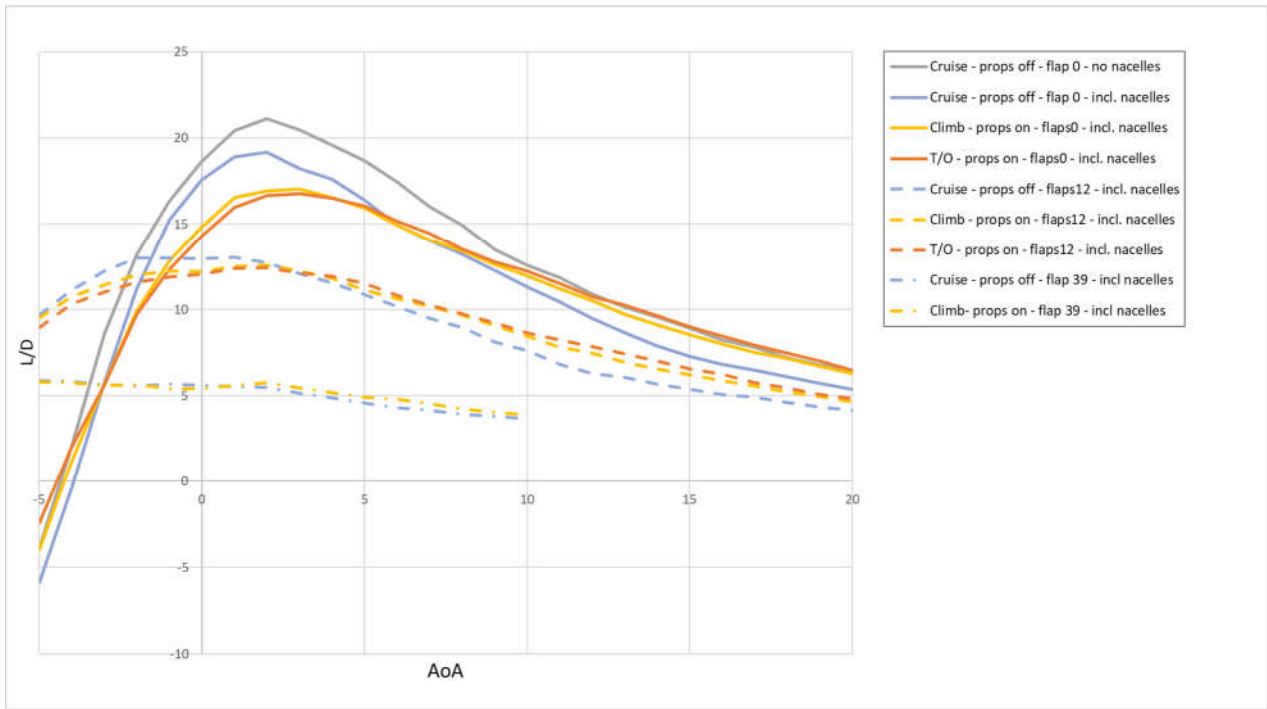


Figure 77 The lift-to-drag coefficient of the Polimi C7A candidate.

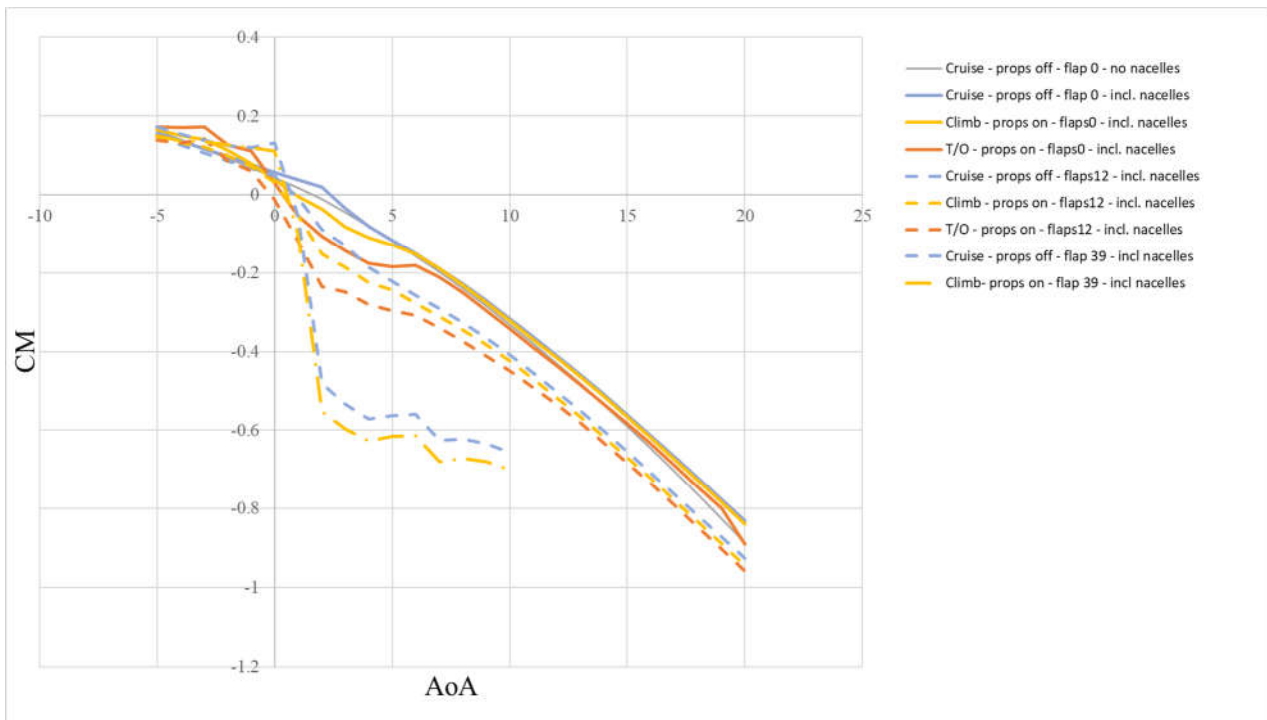


Figure 78 The pitching moment coefficient of the Polimi C7A candidate.

**Cooling Drag Assessment**

For the POLIMI C7A candidate, the input data for cooling drag estimation is presented in Table 30, Table 31 and Table 32. The estimated size of radiators is given in Table 33. Total face area of radiators is **2.3918 m<sup>2</sup>**. Total cooling drag of **1366.2 N** and **853.9 N** was estimated for climb and cruise regime, respectively.

Table 30 Input data (POLIMI C7A) for cooling drag estimation – main electric powertrain.

	CLIMB	CRUISE
<b>Electric power (kW)</b>	463.2	227.1
<b>El. motor efficiency (/)</b>	0.95	0.95
<b>Power-controller efficiency (/)</b>	0.97	0.97
<b>Speed (m/s)</b>	48	77
<b>Coolant volumetric flow rate, el. motor (l/min)</b>	26	14
<b>Coolant volumetric flow rate, power-contr. (l/min)</b>	16	8
<b>Coolant inlet temp, el. motor (°C)</b>	60	60
<b>Coolant inlet temp, power-controller (°C)</b>	55	55
<b>Coolant</b>	50/50 MEG	50/50 MEG

Table 31 Input data (POLIMI C7A) for cooling drag estimation – DEP electric powertrain.

	CLIMB	CRUISE
<b>Electric power (kW)</b>	666.1	327.2
<b>El. motor efficiency (/)</b>	0.95	0.95
<b>Power-controller efficiency (/)</b>	0.97	0.97
<b>Speed (m/s)</b>	48	77
<b>Coolant volumetric flow rate, el. motors (l/min)</b>	24	24
<b>Coolant volumetric flow rate, power-contrs. (l/min)</b>	60	60
<b>Coolant inlet temp, el. motor (°C)</b>	60	60
<b>Coolant inlet temp, power-controller (°C)</b>	65	65
<b>Coolant</b>	50/50 MEG	50/50 MEG

Table 32 Input data (POLIMI C7A) for cooling drag estimation – FC.

	CLIMB	CRUISE
<b>Total electric power out (kW)</b>	635.3	635.3
<b>FC efficiency (/)</b>	0.52	0.52
<b>Speed (m/s)</b>	48	77

Coolant volumetric flow rate (l/min)	140	140
Coolant inlet temp (°C)	45	45
Coolant	50/50 MEG	50/50 MEG

Table 33 POLIMI 1 (C7A) radiators size.

Cooling system for	# of radiators	Height (mm)	Width (mm)	Face area (m <sup>2</sup> )
Main el. powertrain	1	350	500	0.175
	1	320	350	0.112
DEP el. powertrain	2	330	440	0.2904
	2	130	440	0.1144
FC system	2	850	1000	1.7

### Mission Analysis

Comparison of required shaft power and aircraft speed during the mission between POLIMI and PVS mission analysis for C7A are presented in Figure 79 and Figure 80, respectively. The figure depicts only the first two hops with the diversion in between, for the sake of visibility. A small offset in time scale can be observed, originating from different times needed for climb and descend.

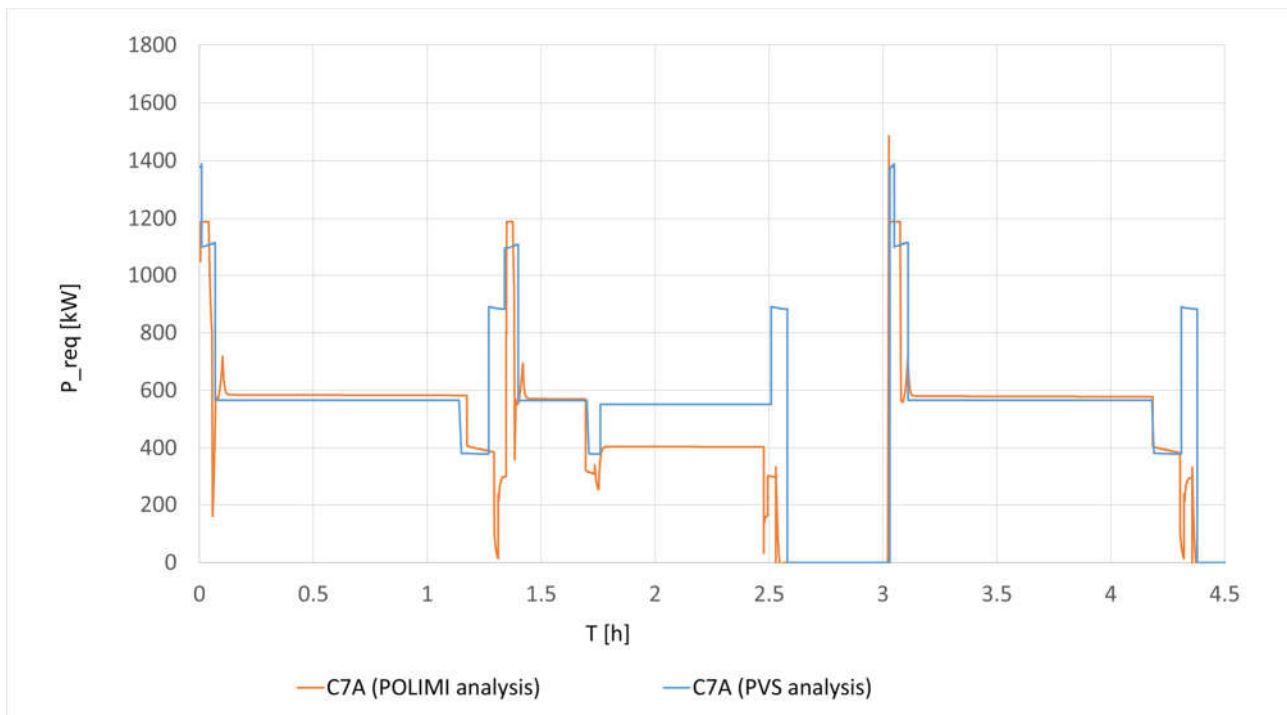


Figure 79 Shaft power requirement comparison for C7A candidate between PVS and POLIMI analysis.

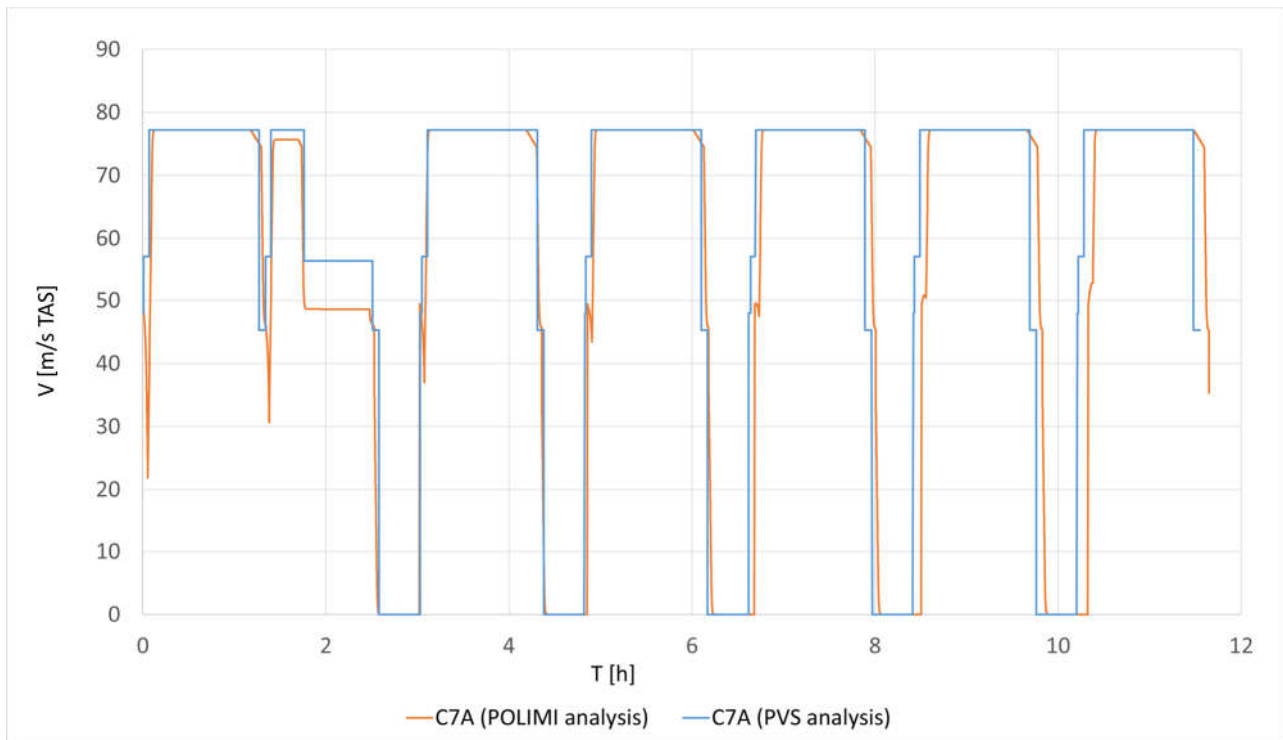


Figure 80 A/C speed comparison during the mission for C7A candidate between PVS and POLIMI analysis

From the figures it can be quickly observed that required shaft power from POLIMI and PVS analyses on average compare really well. Especially in cruise regime there is less than 10% of difference. But there are two distinctive differences that should be explained. The first one is at loiter leg of the flight. As explained above, this difference comes from different flight speed. PVS analysis uses higher speed which results in higher power requirements.

The second notable difference is at the second descend phase, descending from altitude of 1500ft AGL to the ground. At the prescribed flight speed, the required lift coefficient is approximately 1.5 (depends on MTOM of each candidate). In this phase of the mission, PVS assumes landing configuration with deflected fowler flaps and DEP system turned on. The same as POLIMI. But since all of these high lift augmentation systems are turned on, all candidates descend at highly negative angles of attack, which results in high drag forces, and consequently in higher power demand (Figure 79).

### **Qualitative structural design assessment**

#### **Introduction:**

The following sections present a short qualitative assessment of the structural design of the candidate aircraft. Each section discusses some possible high level implementations of structural design for the corresponding Assembly/Subassembly. Comments are presented for the strengths and weaknesses of the assessed design.

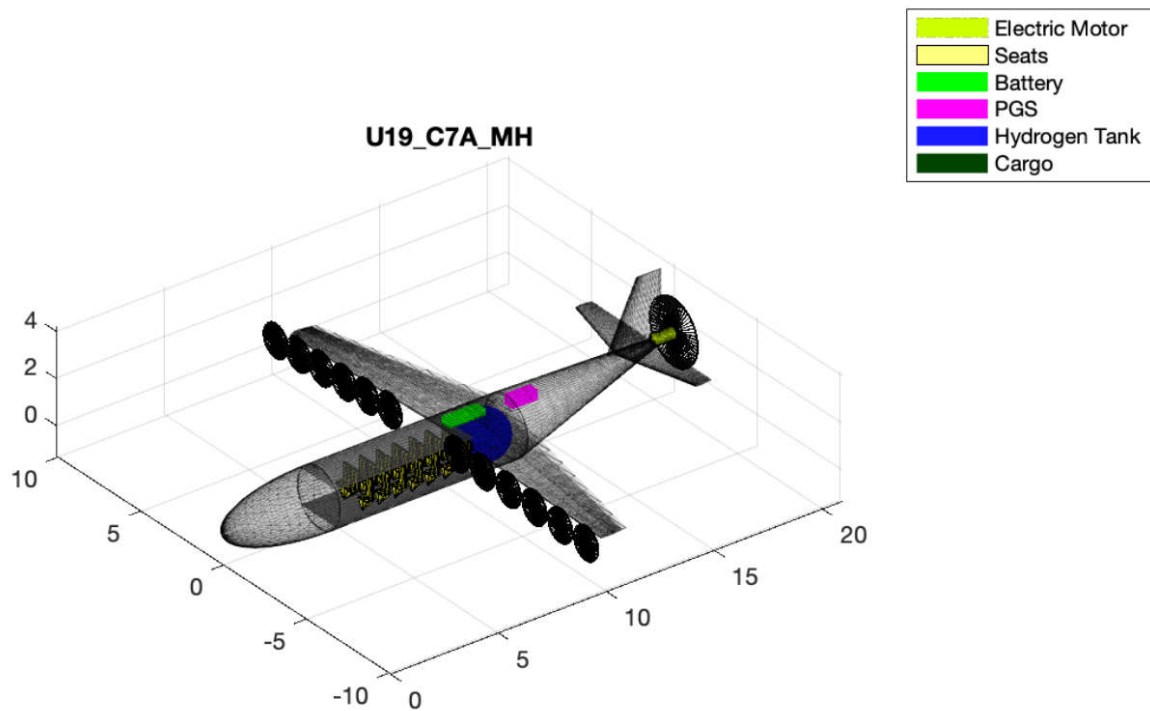


Figure 81: C7A conceptual design

From a structural perspective the A/C does not appear to have any major deviations from a »traditional« aircraft design principle. The biggest challenge is likely to arise from the integration of the large hydrogen tank, which would be subject to detailed design of the aircraft. Another sensitive area appears to be the numerous electric engines located on the wing as part of the distributed electric propulsion drivetrain. Here close collaboration between the structural and aerodynamic teams would be needed in detailed design to arrive at an efficient nacelle design.



## Fuselage - Load assumptions, dominant cases

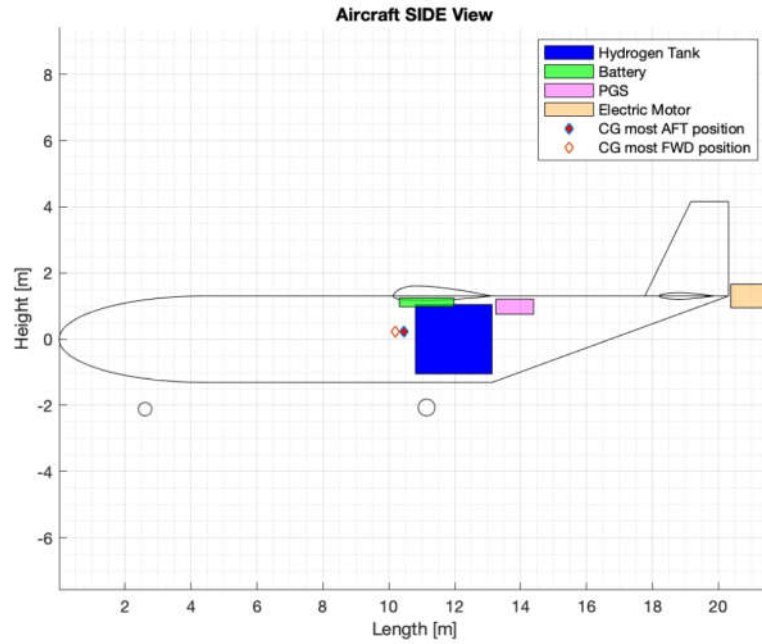


Figure 82: Position of primary powertrain components inside the fuselage

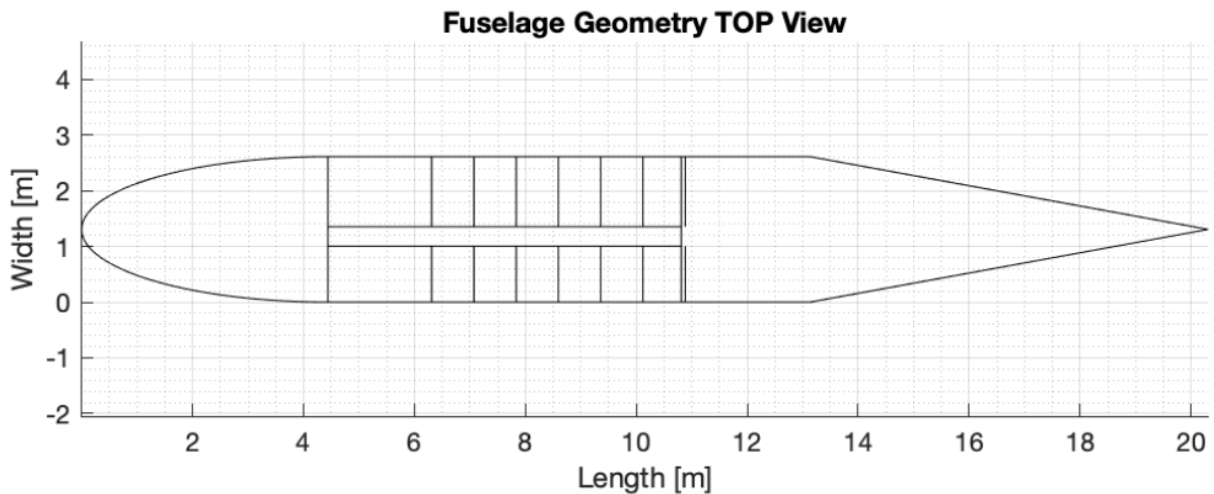


Figure 83: Passenger seating configuration

The dominant loads acting on the fuselage will likely arise from the following load cases:

- Dominant up/down bending of the front fuselage section arising from inertia loads of the passenger + cargo section in a positive/negative manoeuvre or gust
- Dominant up/down bending of the rear fuselage section resulting from vertical stabilizer trim or gust loads
- Lateral bending of the rear fuselage section due to gyroscopic loads of the pusher propeller arising from A/C pitching condition(s)
- Dominant torsional loads on the fuselage induced from the tail section in yawing manoeuvre or lateral gust

- Vertical shear forces from ground loads
- Vertical shear forces/bending moment inducted from the main wing attachments (dependant on actual design configuration)

Fuselage - Design layout

The most suitable configuration of the primary structure is a stressed skin design with bulkheads and longerons positioned throughout the fuselage. The sizing methods used in the quantitative assessment also analyse such a configuration. The Passenger floor section is attached to the bulkhead, with possible additional bracing struts added later in the design, as shown on the figure below. The aforementioned design has become a de facto standard in the design of large and medium sized civil aircraft, primarily due to the fact that it is well suited to carry the manoeuvring, gust, ground and pressurization loads which act on the fuselage, and allow for cut-outs and serviceability.

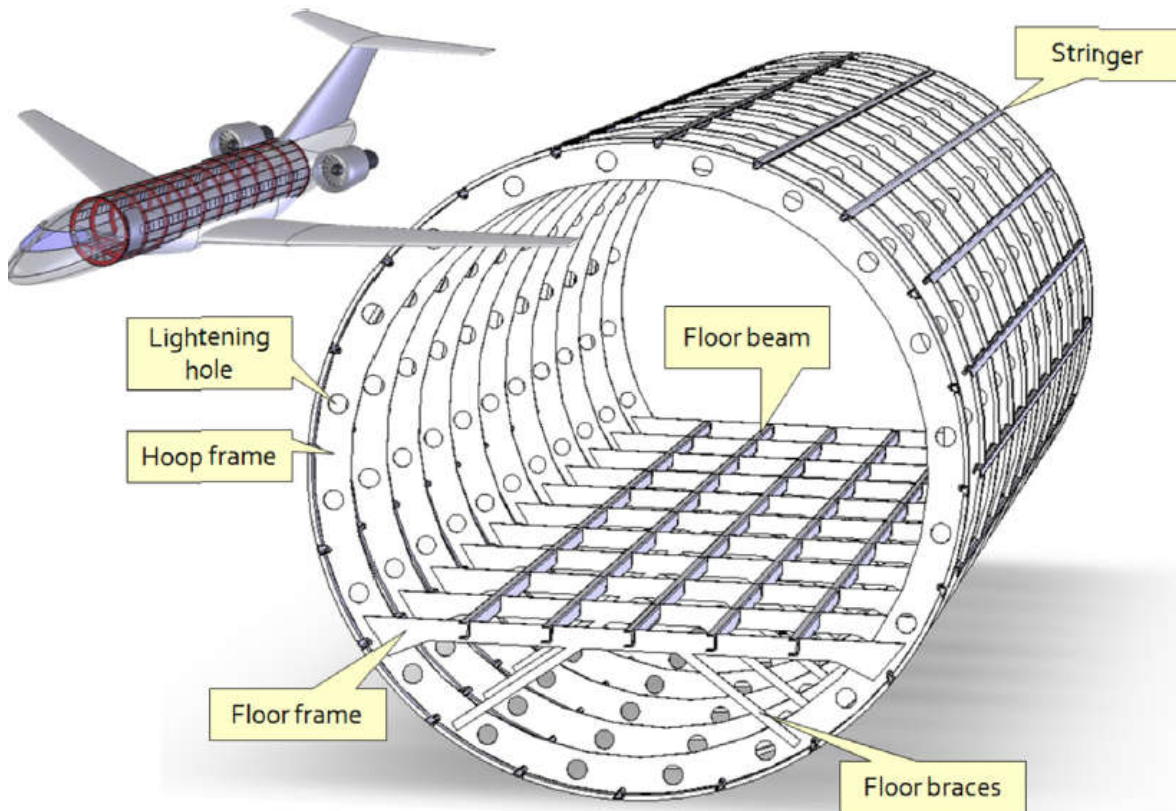


Figure 84: Schematic representation of the chosen fuselage structural concept (1)

Main wing - Wing-fuselage attachment

The attachment of the main wing onto the fuselage would be implemented via additional links. Each link would transmit a force in a certain direction, while not transferring the bending moments. This results in very deterministic and redundant load paths which simplifies the analysis and design of both the wing and the fuselage. Consequently, by not transmitting the bending moment, such a design would also reduce

the loads acting on the fuselage shell. This design also enables the wing to be manufactured as a single piece, which reduces tooling and production costs. The intersection of the wing and fuselage section would be covered with a non-structural aerodynamic fairing, reducing interference drag. The figures below present some solutions for the attachments found on other aircraft.

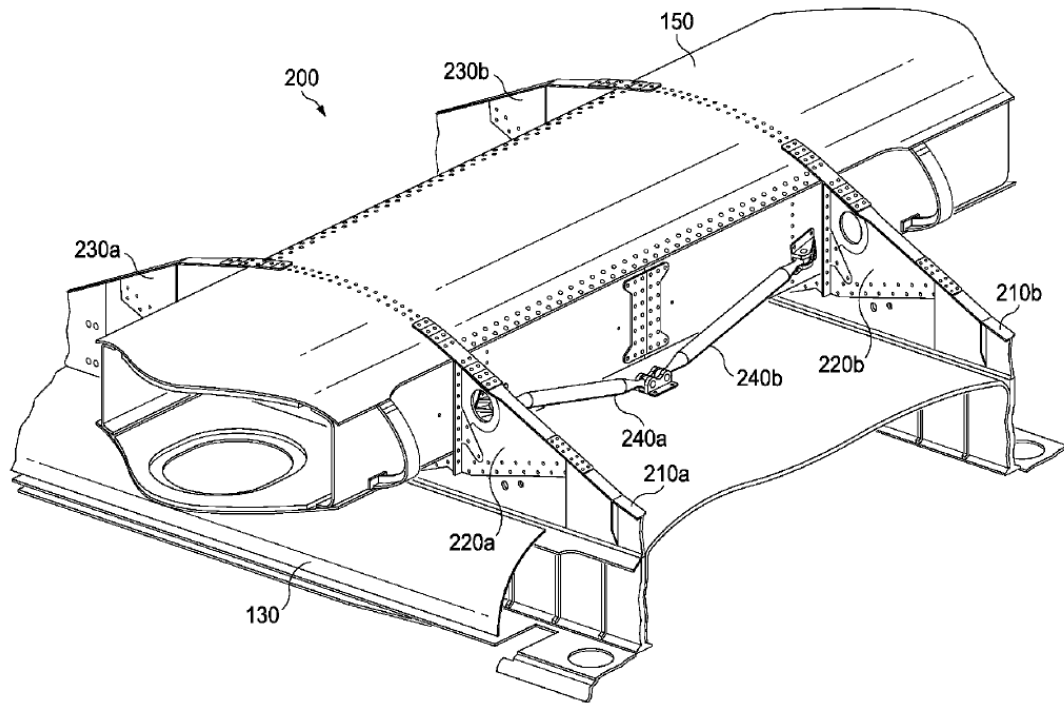


Figure 85: Wing-fuselage attachment of a tiltwing VTOL aircraft (2)

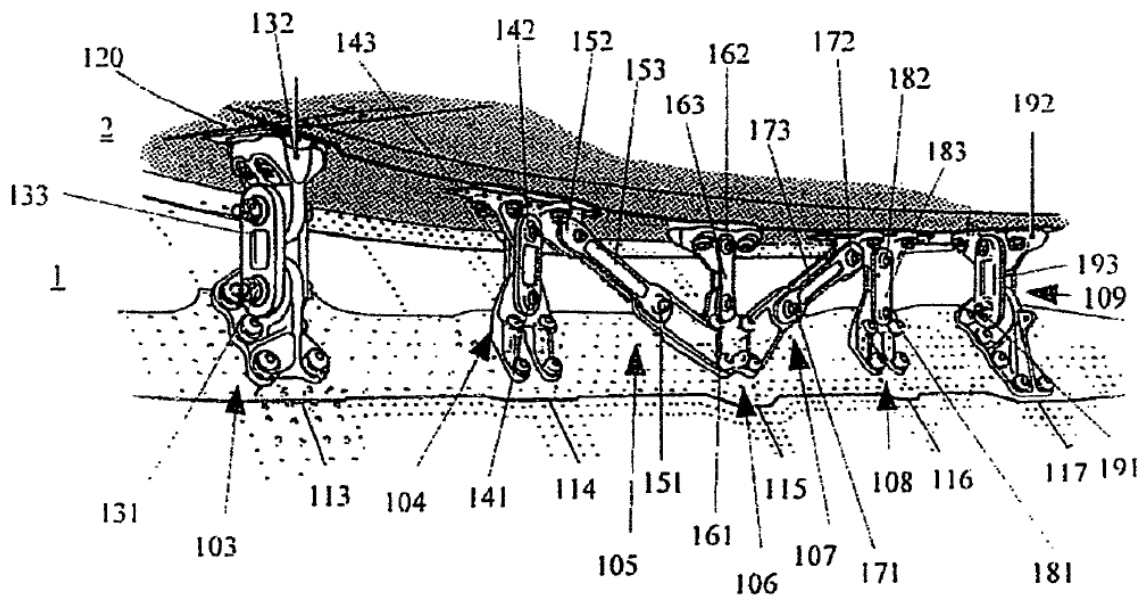


Fig. 5

PRIOR ART

Figure 86: Fuselage wing attachment concept of a high wing aircraft (3)



Figure 87: Fuselage wing attachment of military transport aircraft

## Main wing - Nacelles/pylons

As stated in the introduction the numerous engines mounted on the wing would pose additional, but not insurmountable challenges to the design of the structure. The design of the nacelles and the pylon structure would be heavily influenced by the geometry, mass, volume, as well as additional performance and integration requirements of the electric powertrain and propellers.

For a traditional 19-seater twin turboprop aircraft the expected weight of the nacelle and pylon assembly ranges from 1,5% to 3,5% of the A/C MTOM. Extrapolations could be made for the distributed electric propulsion concept(s), but it is highly likely they would produce very inaccurate results. In conceptual design it is deemed too early in the design process of the aircraft to invest a lot of engineering resources into a detailed estimation of the mass of the nacelles, given their relatively low contribution to the total A/C mass.

## Empennage

The vertical tail/V tail/horizontal stabilizer of the empennage structure will be designed using similar principles of construction as for the main wing. An example of a twin spar with stressed skin construction is shown in the figure below:

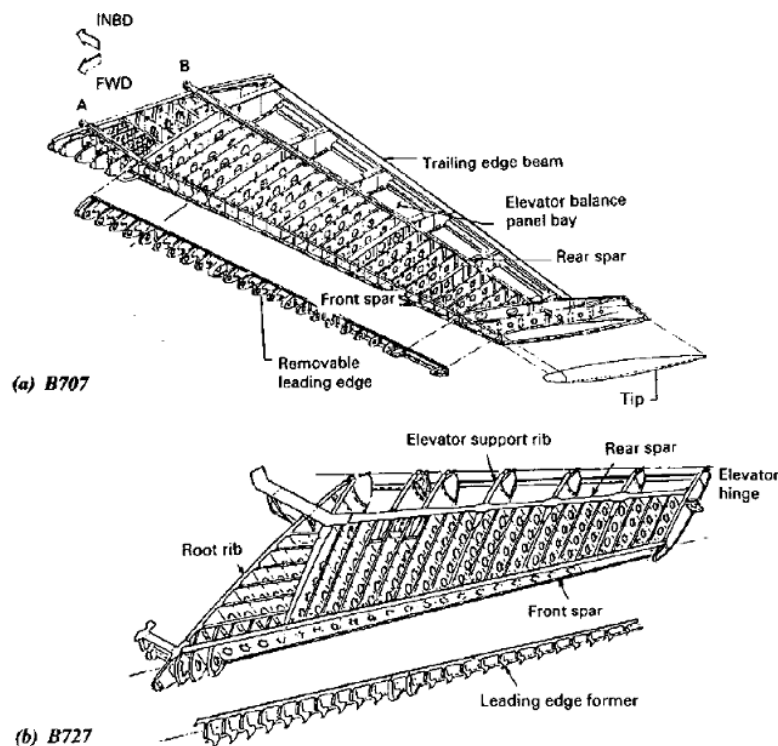


Figure 88: Example structure of the horizontal stabilizer

In the current configuration, the pusher electric engine is located right at the junction of the stabilizer surfaces, which will impose some additional challenges for the design of the attachments due to spatial, strength and stiffness constraints. For a more detailed assessment of the structural design, the control surface sizes and positions would have to be estimated, as well as the electric engine geometry and installation constraints.

Before preliminary design would begin it is worth noting an apparent critical design flaw in the layout of the pusher propeller. The axial clearance between the propeller and the vertical stabilizer, shown in the figure below, is insufficient. Such a small clearance could manifest in a significant amount of structural vibrations, which would lead to premature fatigue of the structure. These could also induce aeroelastic instabilities as well as interfere with the safe operation of the control surfaces. The vibrations would also transfer onto the electric engine bearings and/or gearbox assembly via the propeller shaft, which would require the components to be oversized or risk premature failure. The proposed alternative designs are shown on the figure below, where a) the clearance between the pusher propeller and the vertical stabilizer can simply be increased or b) the propeller is placed in front of the vertical stabilizer assembly.

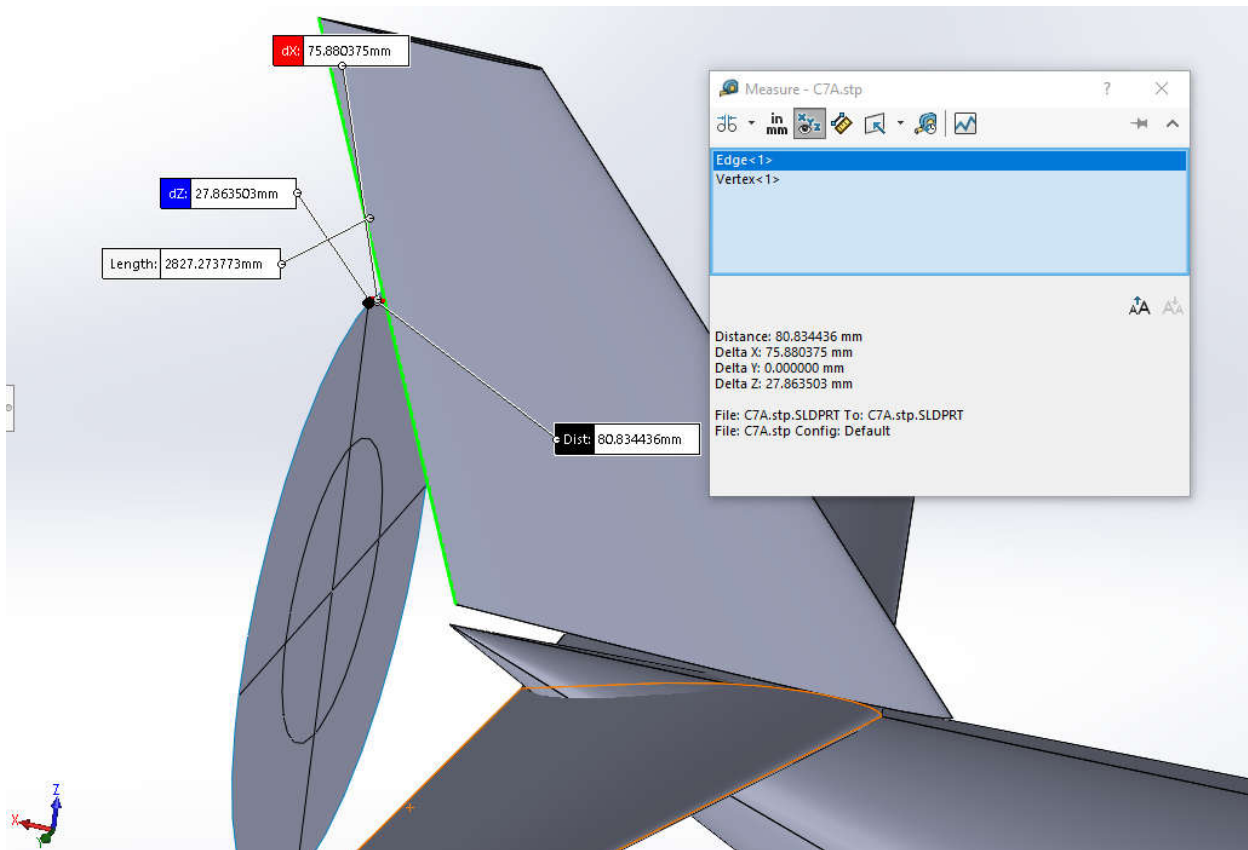


Figure 89: Critical lack of clearance between the pusher propeller and the vertical tail

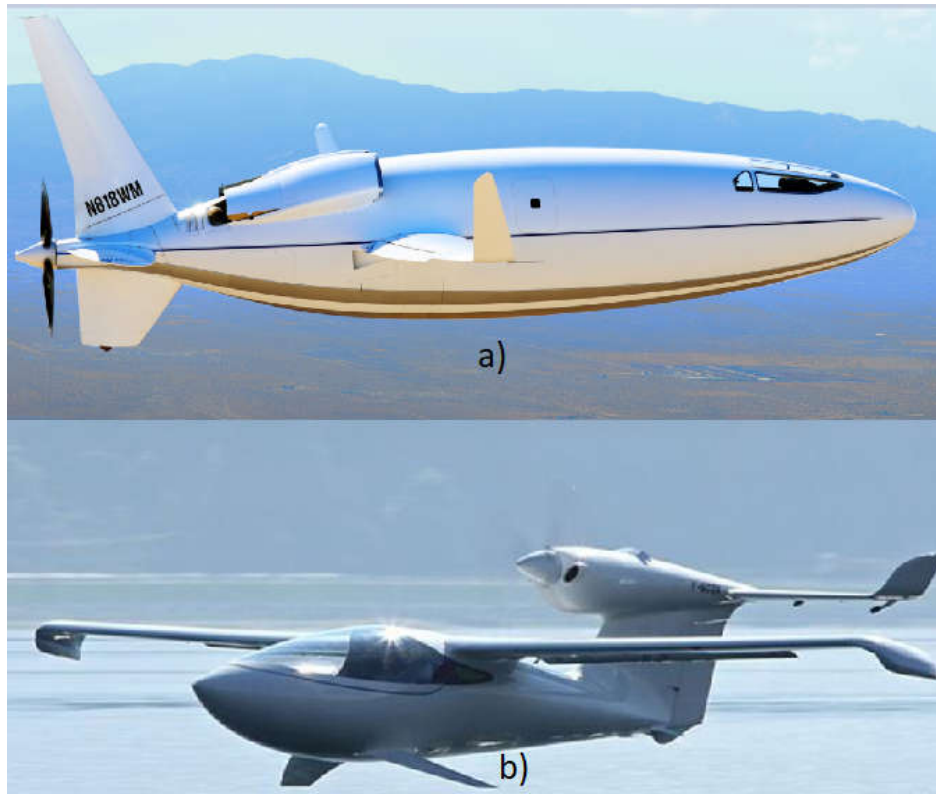


Figure 90: Proposed design changes to mitigate the insufficient clearance between the pusher propeller and the vertical stabilizer

### Landing gear

In the conceptual design phase, no particular consideration has been made regarding the landing gear, apart from the decision for a nose wheel and main landing gear configuration.

A well designed retractable landing gear for a 19 seater class of aircraft should represent between 4 and 6 % of the total A/C MTOM. This should serve as a target for the later stages of the design process. Analysing the layout of the key components of the A/C as shown on Figure 82, there may be insufficient space for stowing the landing gear under the belly of the A/C as is typically done on such aircraft, due to the presence of the large hydrogen tank and its corresponding ancillary systems. An alternative solution would be an additional aerodynamic fairing around the gear in a retracted configuration, which is a suboptimal solution due to increased drag. From the available information a »side stowing« landing gear configuration appears as the best solution, an example of which is shown in the figure below.



Figure 91: "Side stowing" main landing gear configuration on a novel VTOL aircraft design with limited space in the fuselage

The table below summarizes the advantages and disadvantages of the C7A configuration w.r.t. to other configurations from a qualitative structural standpoint.

Section	Pros	Cons
<b>Fuselage</b>	A »traditional« aircraft design principle	/
<b>Main Wing</b>	Smaller wing surface area and bending load alleviation leading to lower structural mass due to DEP concept	Increased no. of engines and nacelles complicates design and manufacturing
<b>Empennage</b>	/	Location of the main engine at the horizontal and vertical tail junction complicates design of the attachment of VT and HT.

### 3.4 Configuration C2

This configuration ranks among the original list of the top five POLIMI candidates, selected based on the qualitative and quantitative analysis process detailed in Section 4. The following section explains the general description of the configuration, the results of sensitivity analysis and the cross-checking assessment.



### 3.4.1 General description

This configuration might be able to combine the best features of the configurations C3 and C7A previously discussed. For example, it incorporates the canard design, like C3, and the DEP on the wing, like C7A, for high-lift provision only. It also includes a powerful pusher propeller on the tail (TCP). The same operational considerations about DEP activation apply as for C7A.

The internal arrangement of the fuselage includes a liquid hydrogen fuel tank under the wing, while the passenger cabin is in the front section and the baggage compartment is in the rear. The overall configuration is displayed in Figure 92. Table 34 provides a comprehensive list of the C7A design specifications.

This is the result of the application of the TITAN design loop, which couples the HYPERION preliminary sizing tool with the ARGOS Class I design procedures. The convergence of the process is very quick, with only five iterations necessary from the HYPERION initial guess. Figure 93 shows the Sizing Matrix Plot (SMP), which allows appreciating the design point location at on the take-off distance requirement, as for C7A. Figure 94 provides the resulting mass breakdown. Finally, Figure 95 and Figure 96 show the time histories of the energy and power quantities during the sizing mission, along with its altitude profile.

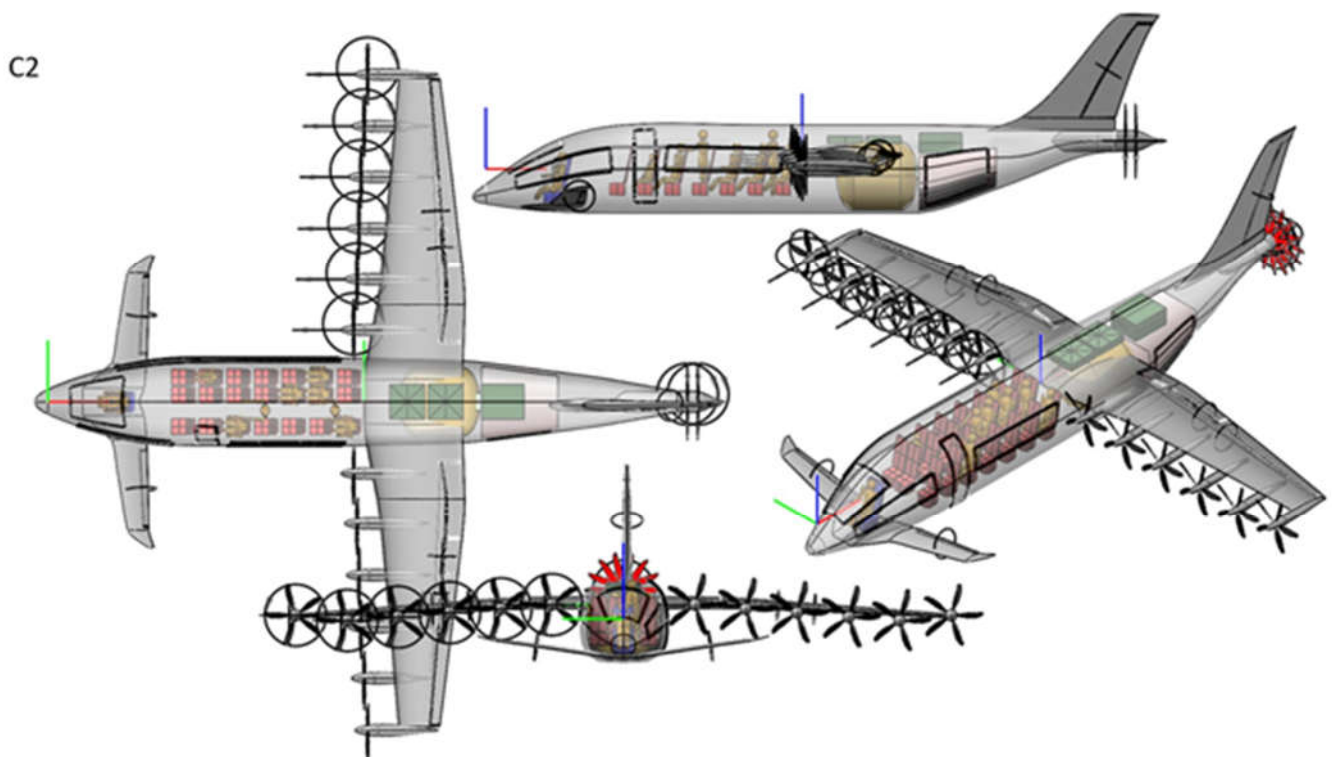


Figure 92 Candidate C2 top, side, front and ISO view.

Table 34 Complete specifications of candidate C2.

Name	Value	Units
Payload	2280	kg
Number of passengers	19	-
Number of pilots	1	-
Pressurization	No	-
Design Power Loading	0.0559	N/W
Design Wing Loading	1928	N/m <sup>2</sup>
Max. take off field length	800	m
Max. landing distance	800	m
Max. stall speed	34.98	m/s
Rate of climb	6.79	m/s
Climb speed	55.25	m/s
Cruise speed	72.74	m/s
Cruise altitude	1219	m
Cruise range	350	km
Rate of descent	-1.78	m/s
Descent speed	72.74	m/s
Loiter altitude	457	m
Loiter time	45	min
Diversion range	100	km
Windmill efficiency	0.0	%
Electric motor efficiency	92.0	%
Electric motor power density	7533	W/kg
Electric motor overrating	1.25	-
PGS power density	2130	W/kg
PGS efficiency	95.0	%
Hybrid transition altitude	0	m
Minimum fuel level	5.0	%
Fuel cell voltage	600	V
Compressor efficiency	88.0	%
Number of FC systems	2	-
Battery power density	1670	W/kg
Battery energy density	936000	J/kg
Minimum charge level	25.0	%
Maximum charge level	85.0	%
Engine thrust	28769	N
Engine power	1383.8	kW
Propeller efficiency (non-DEP)	80.0	%
Number of engines	1	-
Engine length	1.20	m
Engine diameter	0.75	m
Propeller diameter (non-DEP)	2.99	m
Number of blades	4	m
EM maximum cont. power	1383.8	kW
PGS power	632.9	kW
Gravimetric index	0.60	-
Total number of tanks	1	-

<b>Tank ins. thickness</b>	0.0600	m
<b>Tank wall thickness</b>	0.0046	m
<b>DEP power</b>	691.9	kW
<b>DEP propeller diameter</b>	1.49	m
<b>DEP Electric motor efficiency</b>	92.0	%
<b>DEP Electric motor power density</b>	7533	W/kg
<b>DEP Electric motor overrating</b>	1.25	-
<b>DEP propeller efficiency</b>	60.0	%
<b>Number of DEP propellers</b>	12	-
<b>DEP propeller separation</b>	0.00	-
<b>DEP propeller tilt angle</b>	0.0	deg
<b>DEP propeller offset</b>	0.310	-
<b>Maximum take off</b>	7879.2	kg
<b>Operative empty</b>	5228.8	kg
<b>Empty</b>	4385.5	kg
<b>Airframe</b>	3633.8	kg
<b>DEP motor</b>	7.7	kg
<b>Wing</b>	676.6	kg
<b>Fuselage</b>	877.4	kg
<b>Horizontal Tail</b>	27.0	kg
<b>Vertical Tail</b>	95.6	kg
<b>Fuel (wing)</b>	0.0	kg
<b>Fuel (fuselage)</b>	370.4	kg
<b>Landing Gear</b>	349.4	kg
<b>Pilot</b>	100.0	kg
<b>Cargo</b>	836.0	kg
<b>Control Surf.</b>	152.6	kg
<b>Instr. &amp; Nav. Sys.</b>	45.4	kg
<b>Hydr. &amp; Pneu. Sys.</b>	7.9	kg
<b>Electric Sys.</b>	201.9	kg
<b>Electronics</b>	136.1	kg
<b>Air cond. &amp; Anti-ice</b>	445.2	kg
<b>Furnishing</b>	429.3	kg
<b>Passengers</b>	1444.0	kg
<b>Battery</b>	746.8	kg
<b>PGS</b>	312.8	kg
<b>Hydrogen Tank</b>	251.6	kg
<b>DEP</b>	91.8	kg
<b>Airfoil</b>	NACA 63-012A	-

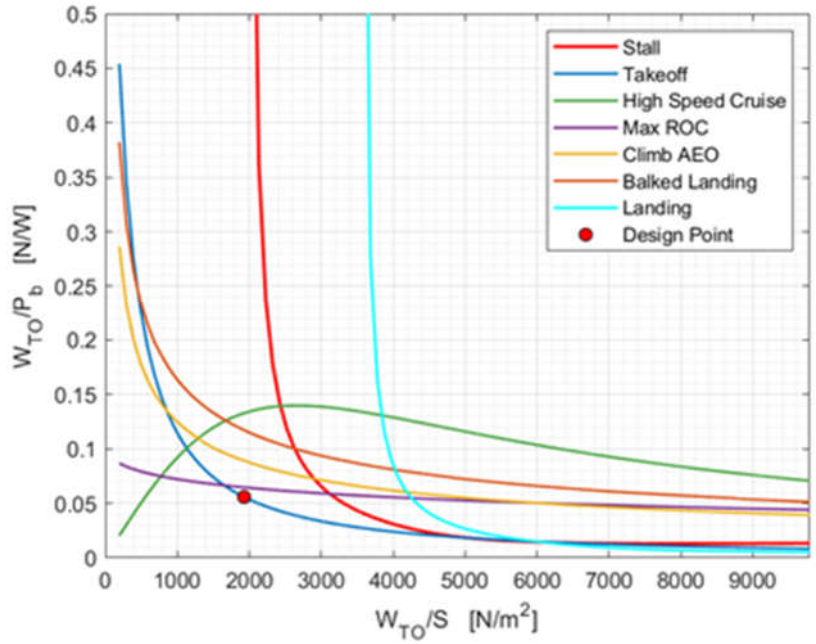


Figure 93 Sizing matrix plot for candidate C2.

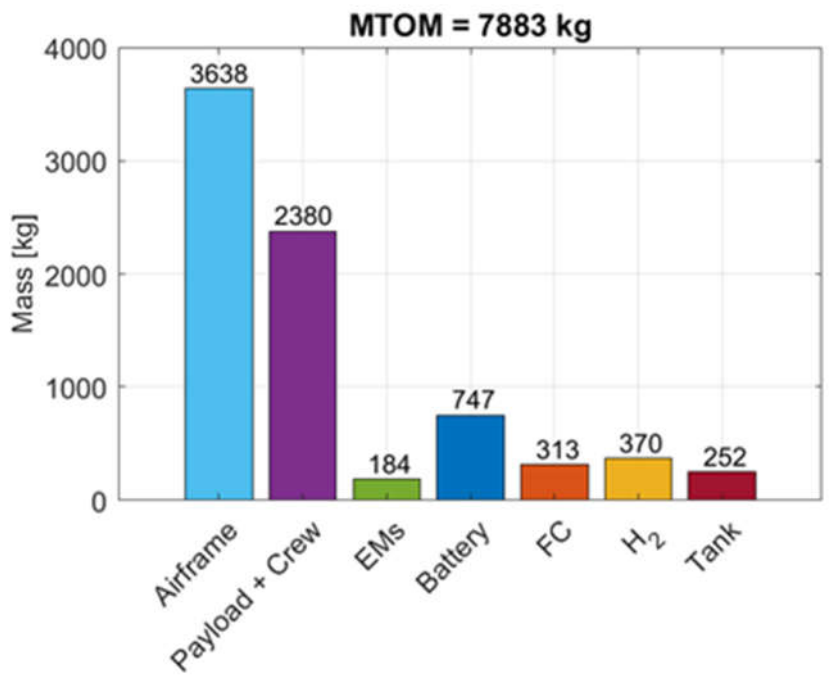


Figure 94 Mass breakdown of candidate C2.

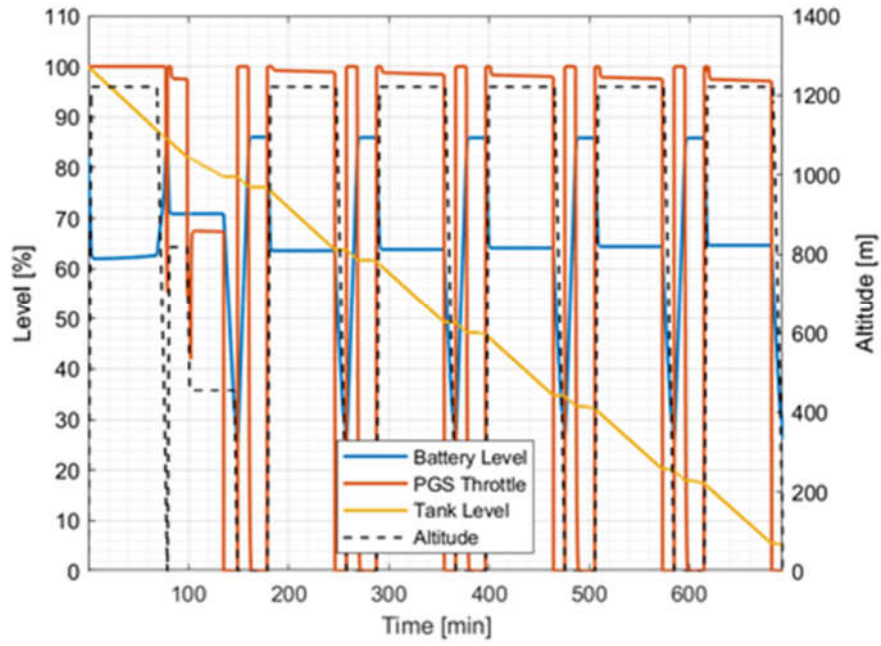


Figure 95 Battery and tank level during the sizing mission for candidate C2.

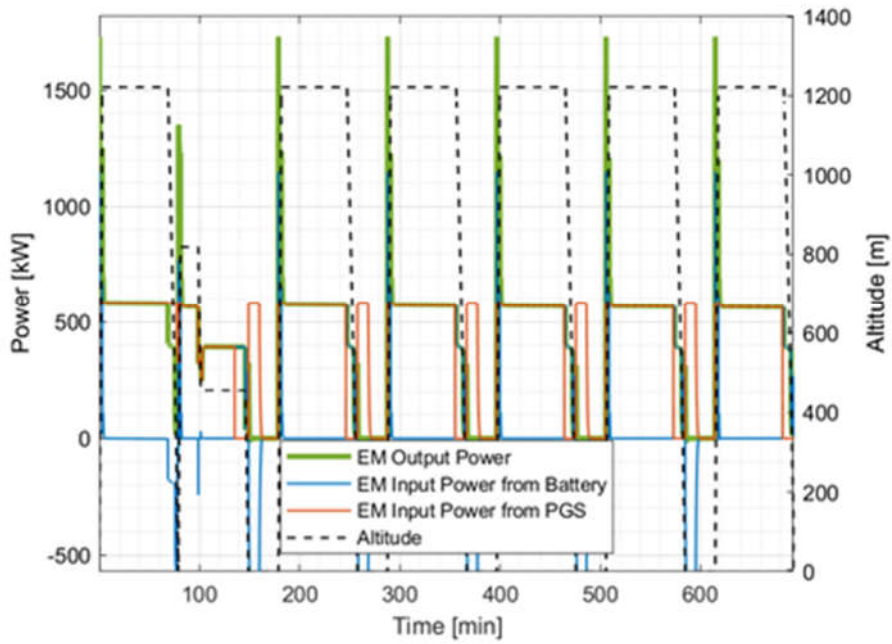


Figure 96 Power utilization during the sizing mission for candidate C2.

### 3.4.2 Sensitivity analysis

A thorough sensitivity analysis was carried out along the same lines discussed for candidate C3 and C7A. The result of these case studies is a large collection of plots and tables which cannot be included here in entirety. Similarly, a selection of representative plots and tables are presented below (Table 35, Figure 97 - Figure 104).

Table 35 Variation of aircraft range for C2 configuration and respective parameter changes.

Range	[km]	280.00	308.00	332.50	350.00	367.50	392.00	420.00
MTOM	[kg]	8040.3	8152.2	8254.2	8330.0	8406.8	8520.1	8652.9
Empty mass	[kg]	4731.2	4867.6	4946.7	5005.9	5064.4	5151.4	5254.0
Main motors power	[kW]	1197.4	1211.4	1224.2	1233.7	1243.2	1257.8	1274.5
DEP motors power	[kW]	598.72	605.70	612.10	616.89	621.62	628.93	637.25
Battery mass	[kg]	569.50	563.50	558.40	555.10	550.70	547.30	541.30
FC mass	[kg]	310.60	316.30	321.50	325.30	329.30	335.00	341.80
LH2 mass	[kg]	309.30	340.70	368.70	388.70	411.50	440.80	477.20
LH2 tank volume	[m3]	4.5900	5.0600	5.4700	5.7700	6.1100	6.5500	7.0800

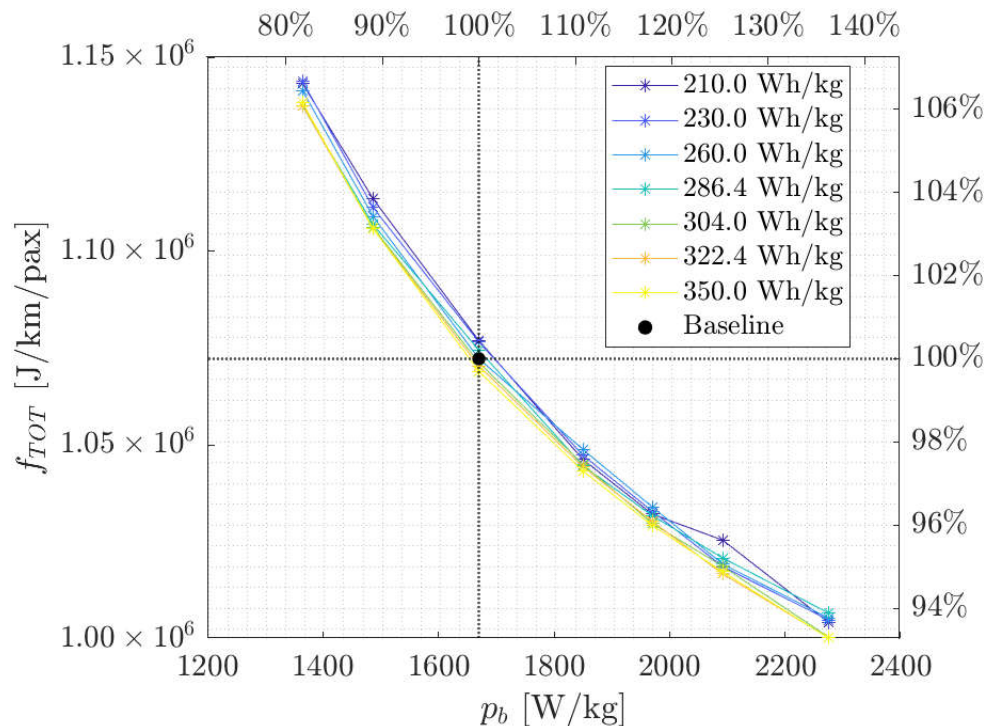


Figure 97  $f_{tot}$  versus battery specific power

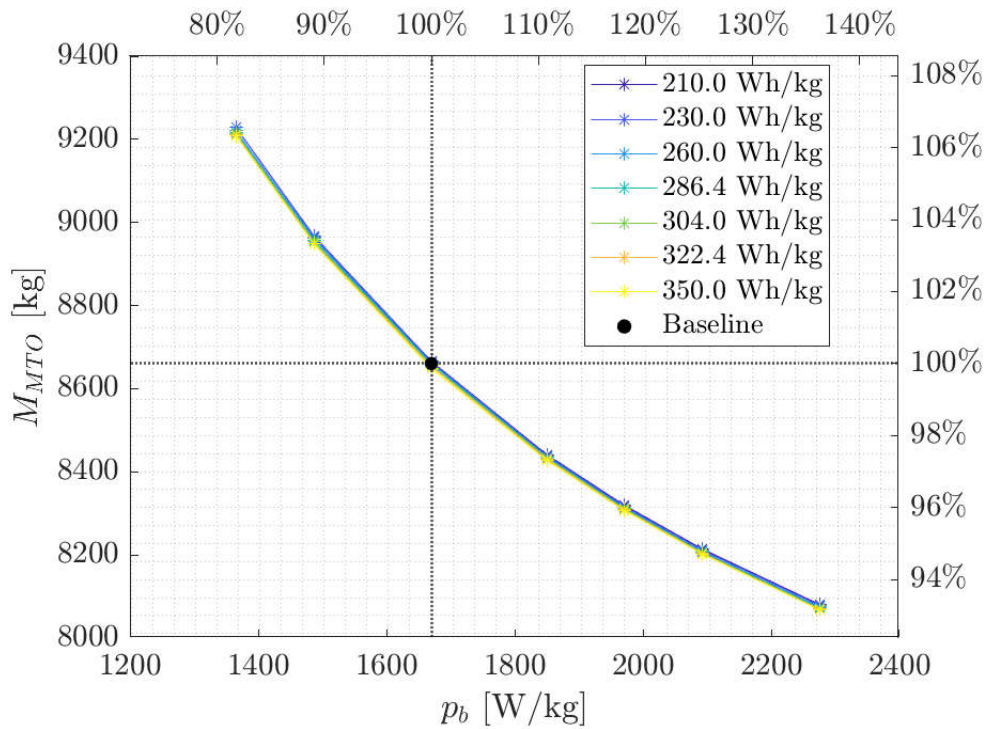


Figure 98 MTOM versus battery specific power

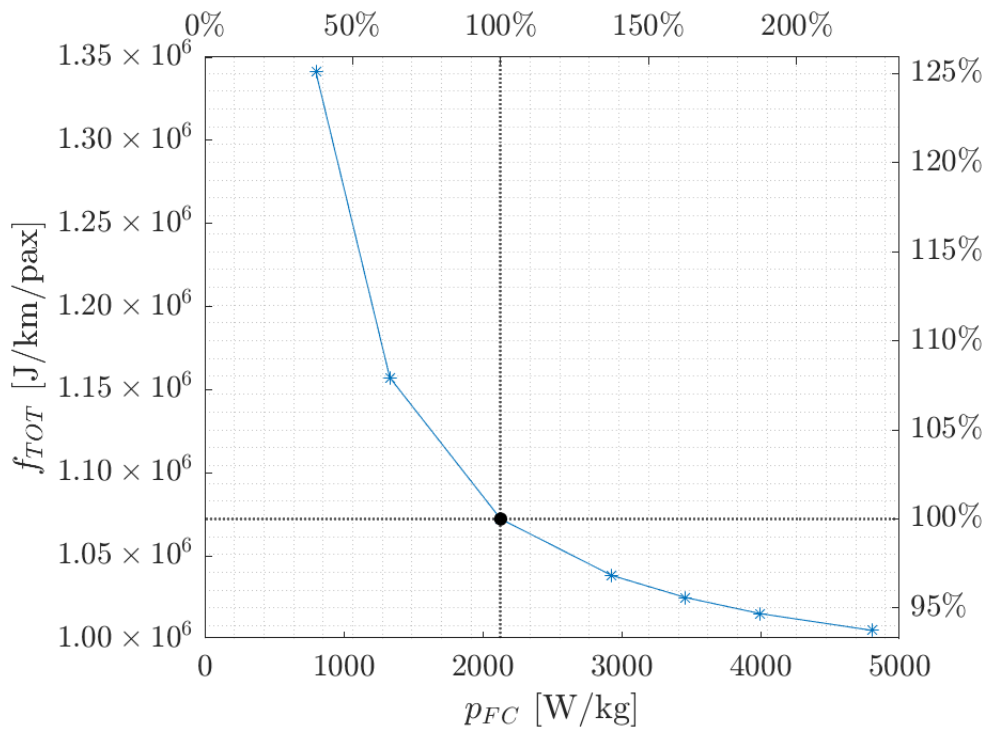


Figure 99  $f_{tot}$  versus fuel-cells specific power

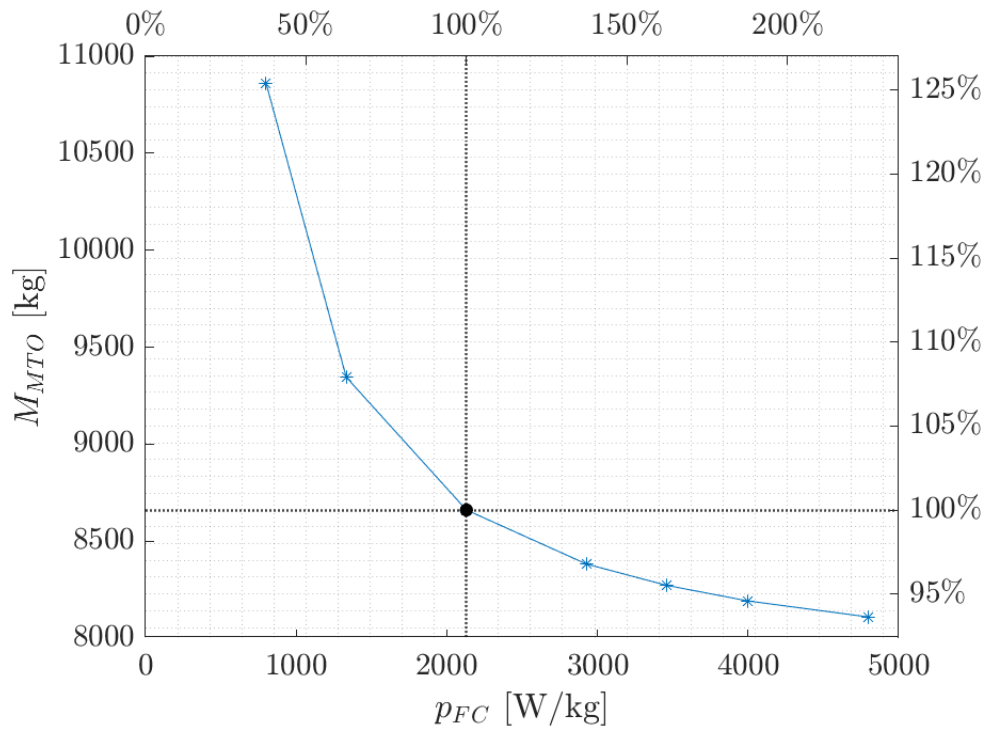


Figure 100 MTOM versus fuel-cells specific power

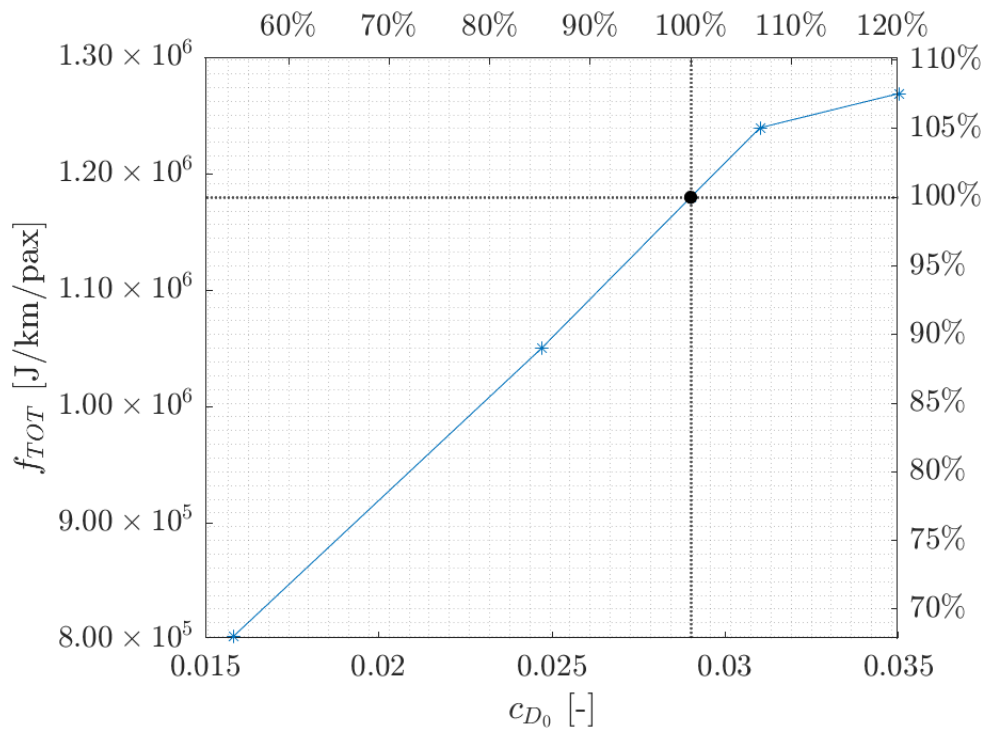


Figure 101  $f_{tot}$  versus  $C_{D0}$



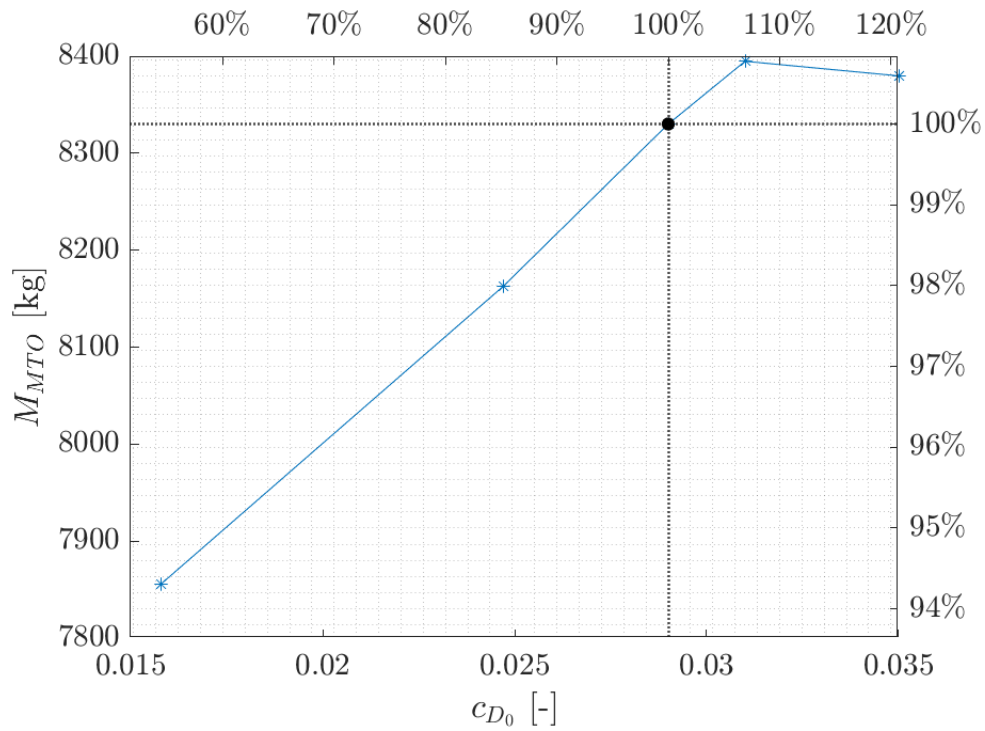


Figure 102 MTOM versus CD0

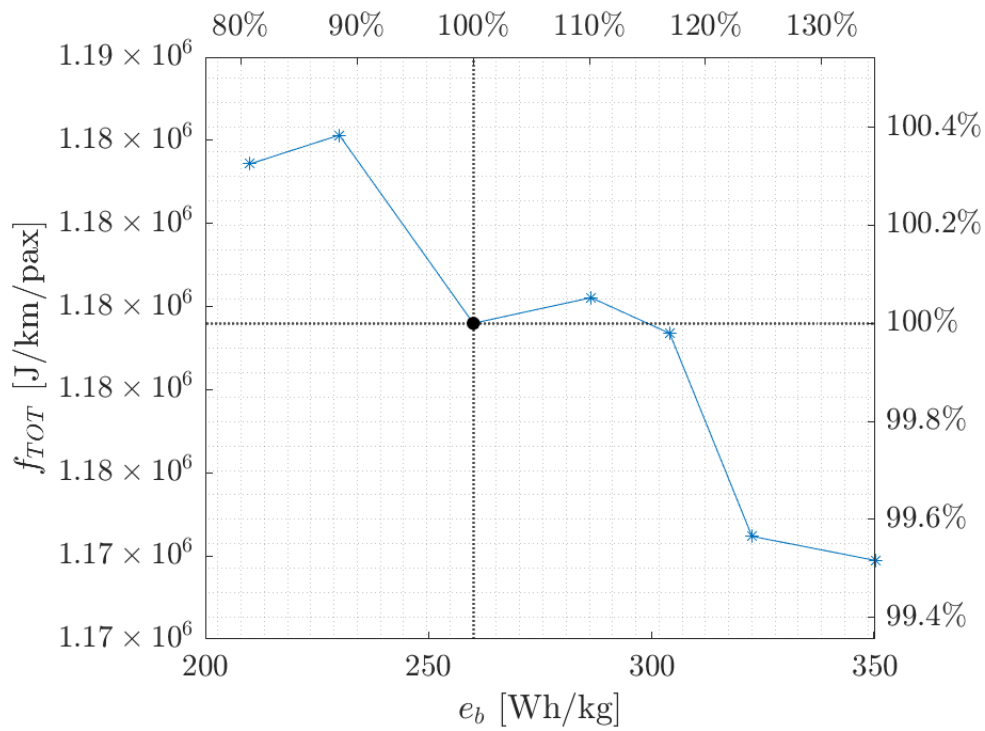


Figure 103  $f_{tot}$  versus battery specific energy

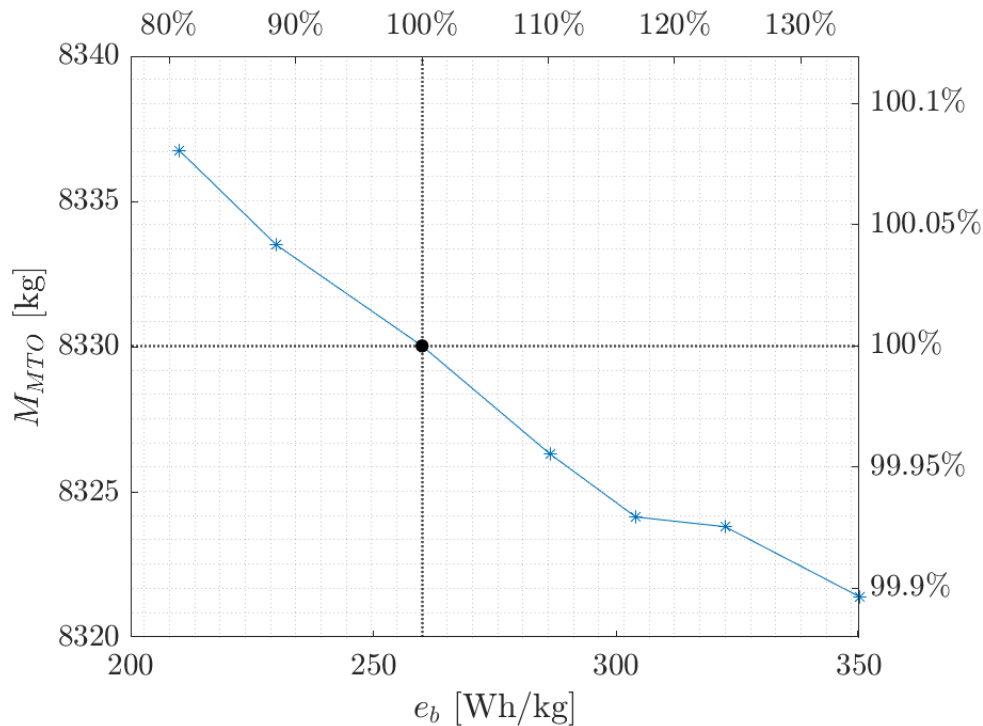


Figure 104 MTOM versus battery specific energy

### 3.4.3 Cross-check & assessment

#### pConcept

The aerodynamic performance was estimated with a single glide ratio value at first, but as the Flight Stream results became available, polars were used instead. All other parameters, like battery energy density and fuel cell efficiency, were synchronised with POLIMI, thus the same technology was used. The results are in Table 36.

Table 36: pConcept results.

Mass [kg]	Total	Airframe	El. Motors	Battery	Fuel Cells	LH2	LH2 Tank
<i>Hyperion</i>	7441	3474	148	545	297	356	241
<i>pConcept</i>	7335	3425	146	526	287	342	228

#### FlightStream Analysis

The candidate contains leading edge mounted distributed electric propulsion and hence the performance was accessed in three different configurations. The geometry of the aircraft used in the aerodynamic analysis is presented in the Figure 107.

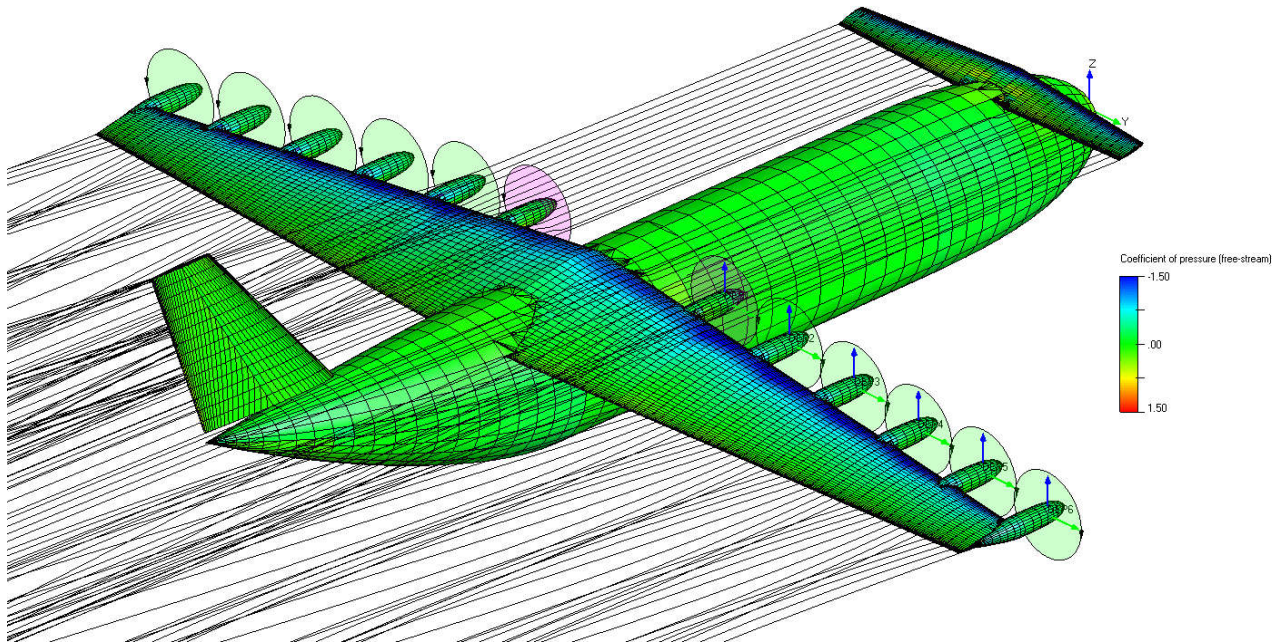


Figure 107 The geometry of the POLIMI C2 candidate used in the aerodynamic analysis.

The analysis points of the candidate can be seen in Table 37. Reference chord length for the candidate is 2.11 m, reference surface area 40.09 m<sup>2</sup>, and x-C.G. location 8.75 m (datum located at the fuselage nose).

Table 37 The analysis settings of the POLIMI 3 candidate.

ANALYSIS POINT	DEP COEFFICIENT	THRUST	DEP RPM	AIRSPEED (m/s)	FOWLER FLAPS (deg)
<b>Cruise</b>	-	-	-	70	0, 12, 39
<b>Climb</b>	0.27	1455	1455	50	0, 12, 39
<b>Take off/Landing</b>	0.34	1379	1379	40	0, 12, 39

Figure 108, Figure 109 and Figure 110 show the lift, lift-to-drag ratio, and pitching moment of the POLIMI C2 candidate.

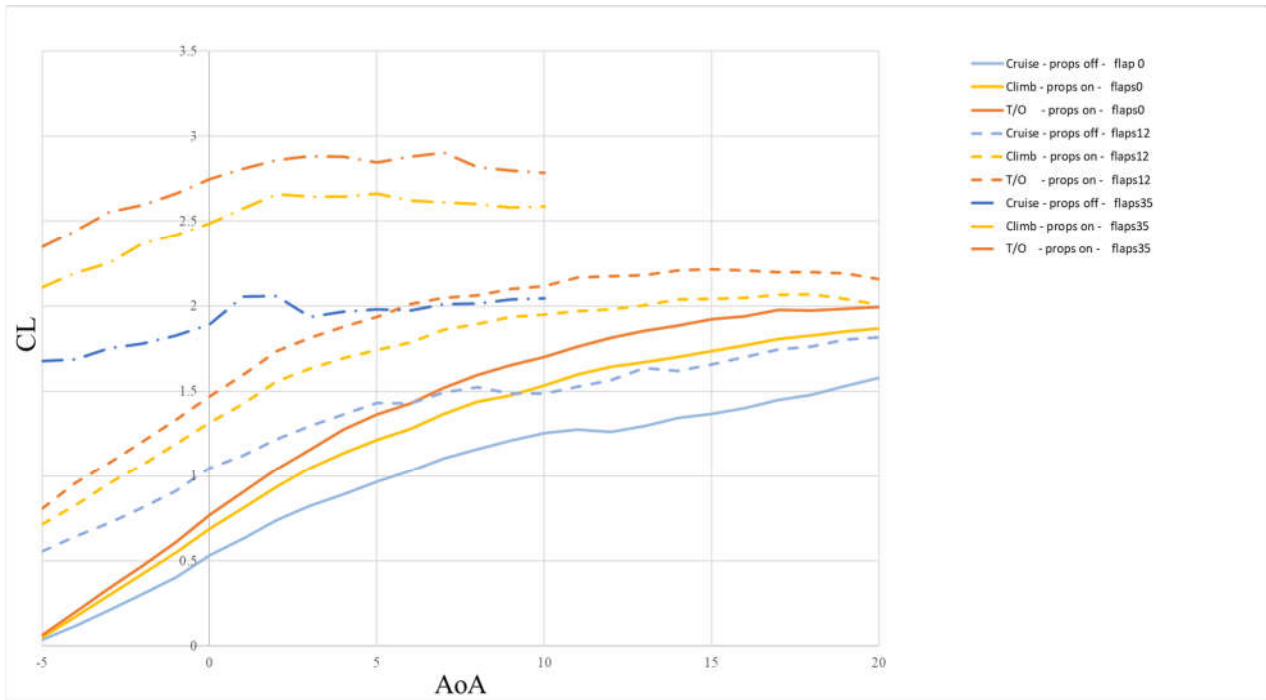


Figure 108 The lift coefficient of the POLIMI C2 candidate.

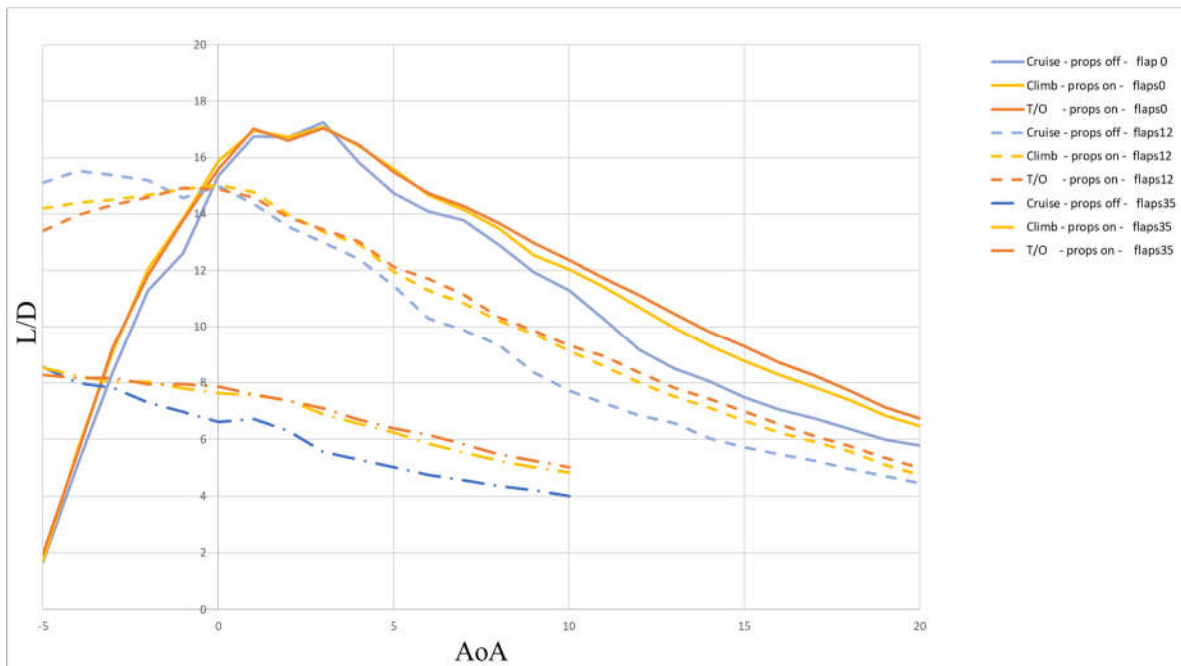


Figure 109 The lift-to-drag coefficient of the POLIMI C2 candidate.

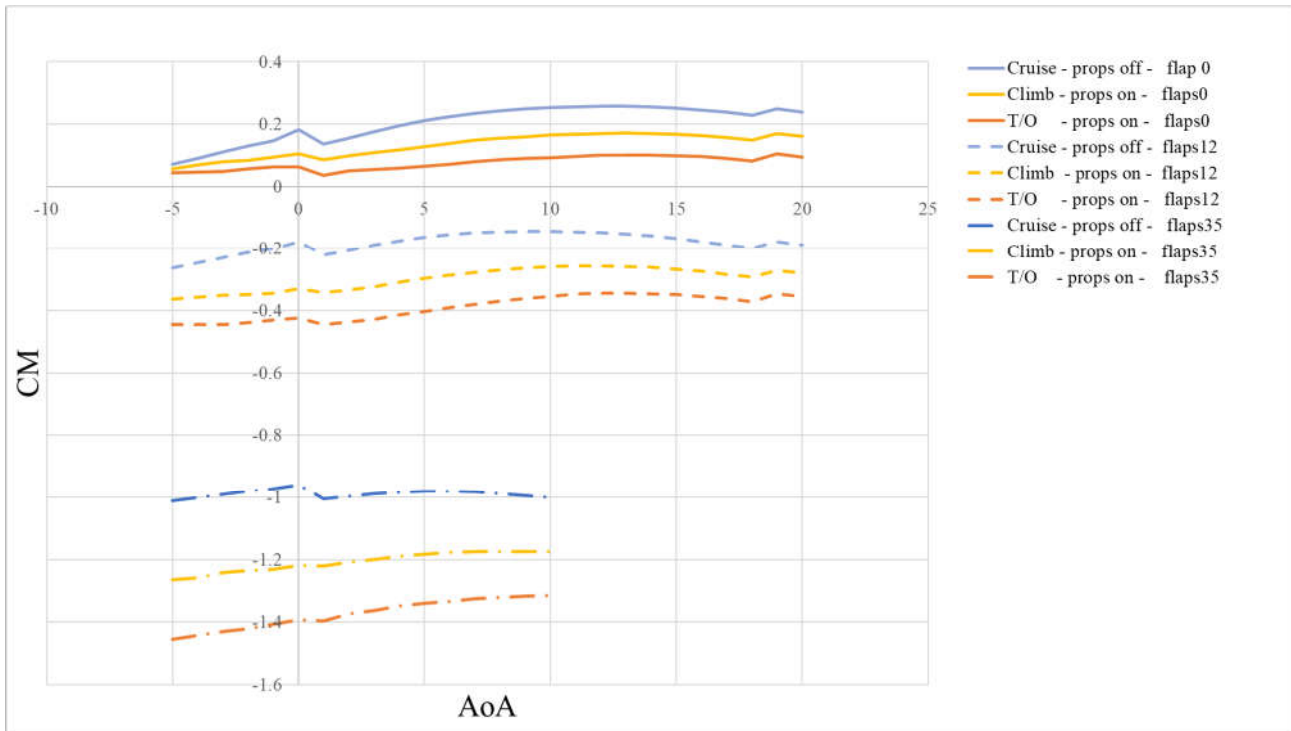


Figure 110 Pitching moment coefficient of the POLIMI C2 candidate.

It can be seen that the leading edge mounted distributed propulsion and flaps have a significant impact on the pitching moment of the aircraft. This is because for canard configurations, like this candidate, the centre of gravity must be located significantly in front of the wing to achieve longitudinal static stability. In the case of flap deployment and augmented lift from leading edge propulsion, the pitching moment of the aircraft shifts. It is seen questionable whether the canard can trim the aircraft in some of the configurations. No analysis on trimmability were performed. Additionally, the longitudinal static stability is neutral and slightly negative for the candidate, hence, the centre of gravity would likely need to be shifted further forward. Similarly to the POLIMI C3 candidate, the candidate contains a Fowler flap, which is modelled as continuous due to limitation in the geometric modelling capabilities.

### Cooling Drag Assessment

For the POLIMI C2 candidate the input data for cooling drag estimation is presented with Table 38 - Table 40. The estimated size of radiators is given in Table 41. Total face area of radiators is **2.3198 m<sup>2</sup>**. Total cooling drag of **1459.2 N** and **829 N** was estimated for climb and cruise regime, respectively.

Table 38: Input data (POLIMI C2) for cooling drag estimation – main electric powertrain.

	CLIMB	CRUISE
<b>Electric power (kW)</b>	433.7	215.7
<b>El. motor efficiency (/)</b>	0.95	0.95
<b>Power-controller efficiency (/)</b>	0.97	0.97
<b>Speed (m/s)</b>	48	77
<b>Coolant volumetric flow rate, el. motor (l/min)</b>	28	14

Coolant volumetric flow rate, power-contr. (l/min)	15	8
Coolant inlet temp, el. motor (°C)	60	60
Coolant inlet temp, power-controller (°C)	55	55
Coolant	50/50 MEG	50/50 MEG

Table 39: Input data (POLIMI C2) for cooling drag estimation – DEP electric powertrain.

	CLIMB	CRUISE
Electric power (kW)	623.5	310.2
El. motor efficiency (/)	0.95	0.95
Power-controller efficiency (/)	0.97	0.97
Speed (m/s)	48	77
Coolant volumetric flow rate, el. motors (l/min)	24	24
Coolant volumetric flow rate, power-contrs. (l/min)	36	36
Coolant inlet temp, el. motor (°C)	60	60
Coolant inlet temp, power-controller (°C)	65	65
Coolant	50/50 MEG	50/50 MEG

Table 40: Input data (POLIMI C2) for cooling drag estimation – FC.

	CLIMB	CRUISE
Total electric power out (kW)	602.2	602.2
FC efficiency (/)	0.52	0.52
Speed (m/s)	48	77
Coolant volumetric flow rate (l/min)	140	140
Coolant inlet temp (°C)	45	45
Coolant	50/50 MEG	50/50 MEG

Table 41: POLIMI C2 radiators size.

Cooling system for	# of radiators	Height (mm)	Width (mm)	Face area (m <sup>2</sup> )
Main el. powertrain	1	340	500	0.17
	1	300	350	0.105
DEP el. powertrain	2	320	440	0.2816
	2	140	440	0.1232
FC system	2	820	1000	1.64

### Mission Analysis

Comparison of required shaft power during the mission between POLIMI and PVS mission analysis for C2 is presented in Figure 58. The figure depicts only the first two hops with the diversion in between, for the sake of visibility. A small offset can be again observed, originating from different times needed for climb and descend.

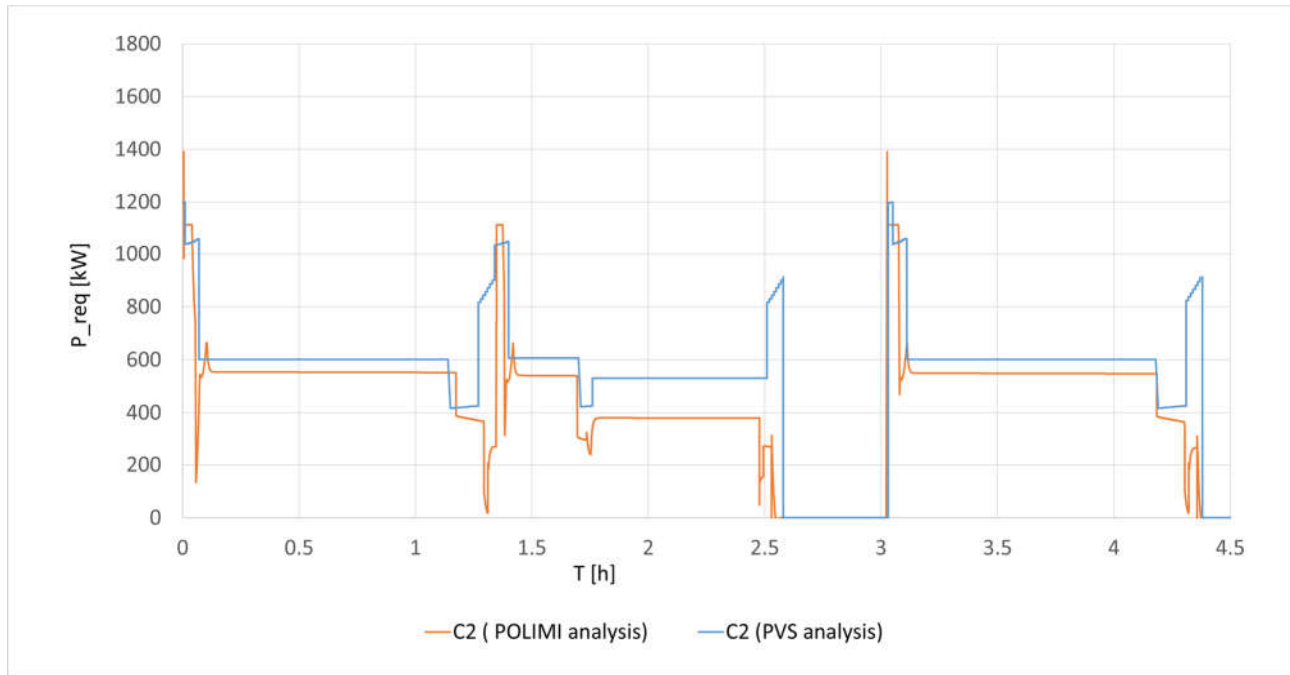


Figure 111: Shaft power requirement comparison for C2 candidate between PVS and POLIMI analysis.

Also here, two notable differences in power requirements in loiter and second descend phase are visible, for which a more detailed clarification can be found in Section 1.1.1.

### Qualitative structural design assessment

The table below summarizes the key differentiators of the structure of the concept compared to other A/C design solutions.

Section	Pros	Cons
<b>Fuselage</b>	Reduced weight due to canard configuration	/
<b>Main Wing</b>	-Smaller wing surface area and bending load alleviation leading to lower structural mass due to DEP concept	- Increased no. of engines and nacelles complicates design and manufacturing
<b>Empennage</b>	No horizontal stabilizer simplifies the design	Presence of pusher engine complicates design and increases weight

## 3.5 Configuration PVS1

### 3.5.1 General description

PVS1 candidate is a further explored version of C7A candidate, replacing pusher propeller on the tail with a ducted fan, which represents a “counterweight” to previous designs, where only propellers are considered. The main advantage of the ducted fan is high efficiency at static thrust and at low-speed conditions.

This configuration entails the traditional lifting surface layout with a v-tail placed on top of the tail cone duct. The high aspect ratio wing is optimised for cruise segment of the flight, however, a required lift enhancement during take-off and landing is provided via an array of multi-functioning distributed electric propulsion (DEP) units on the leading edge of the main wing together with a (mechanically most simple) plain flap. DEP propeller slipstream increases dynamic pressure over the wing resulting in artificial increase in wing lift coefficient. The blowing propellers also provide additional thrust required during the take-off phase. During the cruise phase, most of the DEP propellers is turned off. Only wing tip propellers remain operational and, together with the ducted fan, provide the cruise thrust. The propellers in the DEP array are assumed to fold backwards when non-operating, to reduce drag in cruise. The terminal phases of final approach and landing call for activation of DEP once again.

The internal arrangement of the fuselage includes a liquid hydrogen fuel tank under the wing, while the passenger cabin is in the front section and the baggage compartment is in the rear. The optimized hydrogen tank shape and size is such that it cannot be placed inside the wings. Hence a position close to centre of gravity is selected in the fuselage. The overall configuration is displayed in Figure 112.



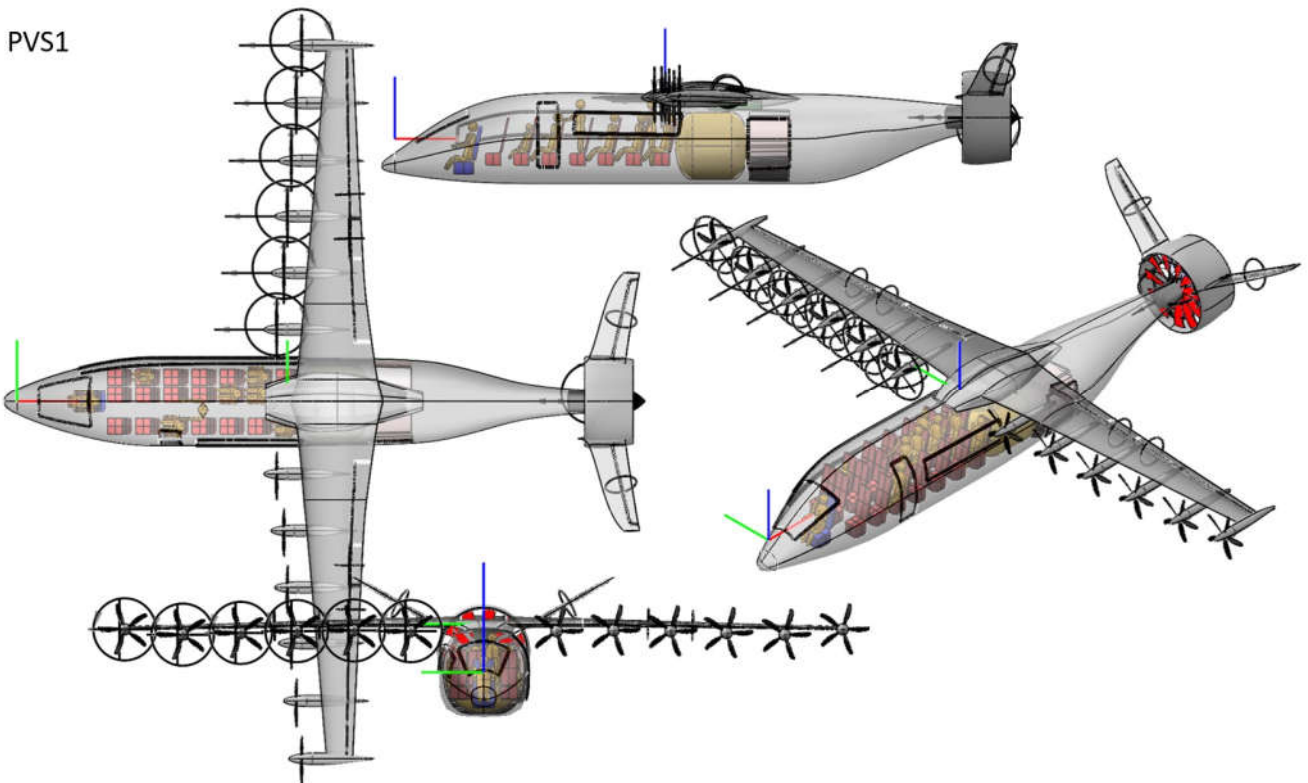


Figure 112 PVS1 top, side, front and ISO view

Main geometrical and performance characteristics are shown in Table 42

Table 42 PVS1 geometrical and performance characteristics

Geometrical characteristics		Performance	
<b>Length</b>	18.1 m	TAS @cruise	150 kts
<b>Wingspan</b>	20.1 m	L/D @cruise	15.1
<b>Wing surface</b>	28.9 m <sup>2</sup>	Take-off distance over 50 ft obstacle	562 m
<b>Aspect ratio</b>	14.1		

Mass breakdown from pConcept analysis can be seen in Table 43.

Table 43: pConcept results.

Mass [kg]	Total	Airframe	El. Motors	Battery	Fuel Cells	LH2	LH2 Tank
<b>PVS1</b>	7878	4073	139	403	367	309	206

### **FlightStream Analysis**

The candidate contains leading edge mounted distributed electric propulsion in addition to wingtip mounted propellers. The wingtip mounted propellers are operated in all the analysis points, whereas the remaining leading-edge mounted propulsors are operated only during climb take-off and landing phase.

The candidate contains plain flap, which is modelled in the FlightStream. The geometry of the aircraft used in the aerodynamic analysis is presented in the Figure 113.

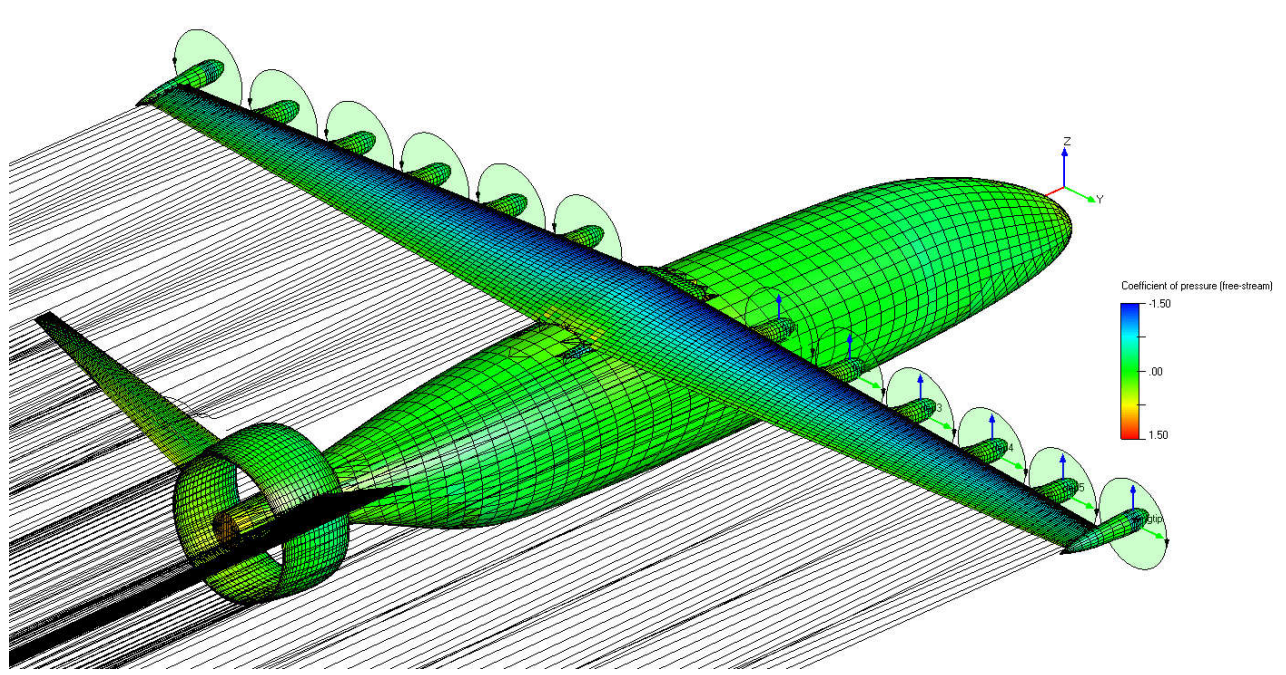


Figure 113 The geometry of the PVS 1 candidate used in the aerodynamic analysis.

The analysis points can be seen in the Table 44. Reference chord length for the candidate is 1.606 m, reference surface area 28.9 m<sup>2</sup>, and x-C.G. location 9.2 m (datum located at the fuselage nose).

Table 44 The analysis points of the PVS 1 candidate.

ANALYSIS POINT	DEP THRUST COEFFICIENT	DEP RPM	WINGTIP THRUST COEFFICIENT	WINGTIP RPM	AIRSPEED (m/s)	PLAIN FLAP (deg)
<b>Cruise</b>	-	-	0.059	2500	90	0, 15, 25
<b>Climb</b>	0.254	1475	0.254	1475	48	0, 15, 25
<b>Take off/Landing</b>	0.327	1402	0.327	1402	40	0, 15, 25

Figure 114, Figure 115 and Figure 116 show the lift, lift-to-drag, and pitching moment coefficient of the PVS 1 candidate.

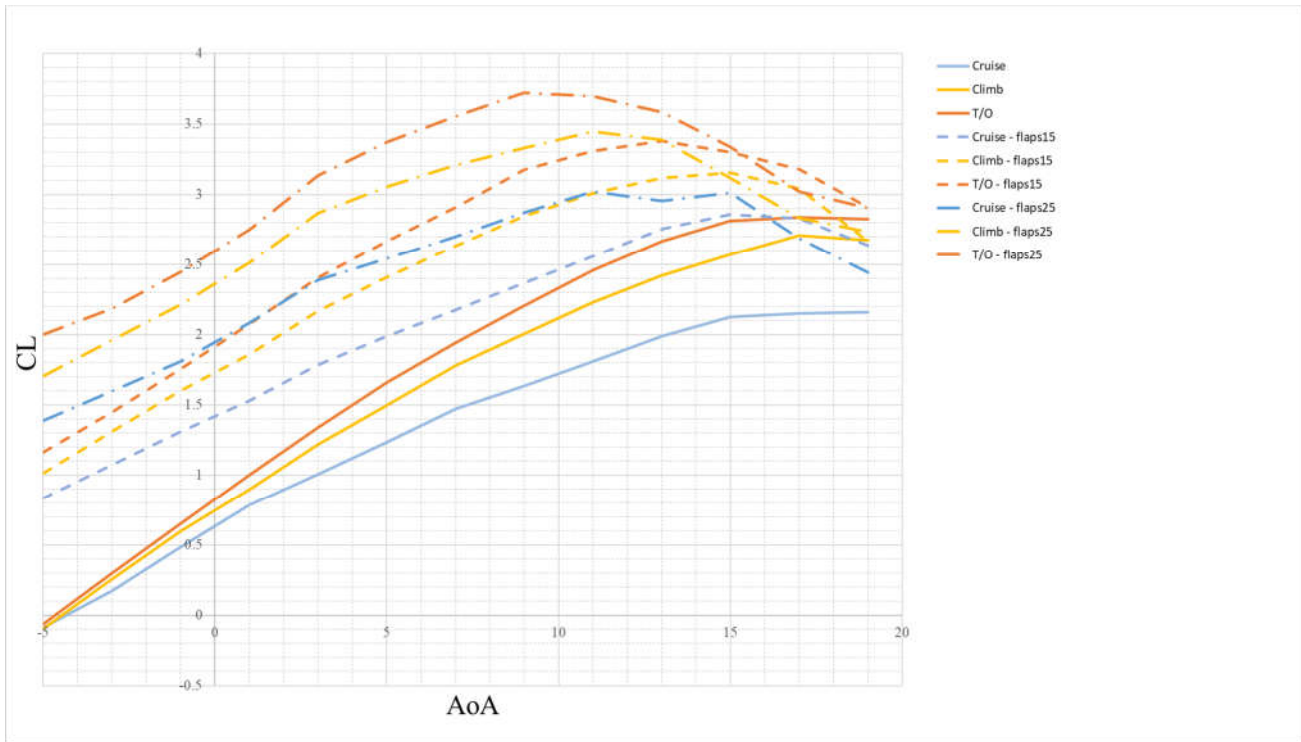


Figure 114 The lift coefficient of the PVS 1 candidate.

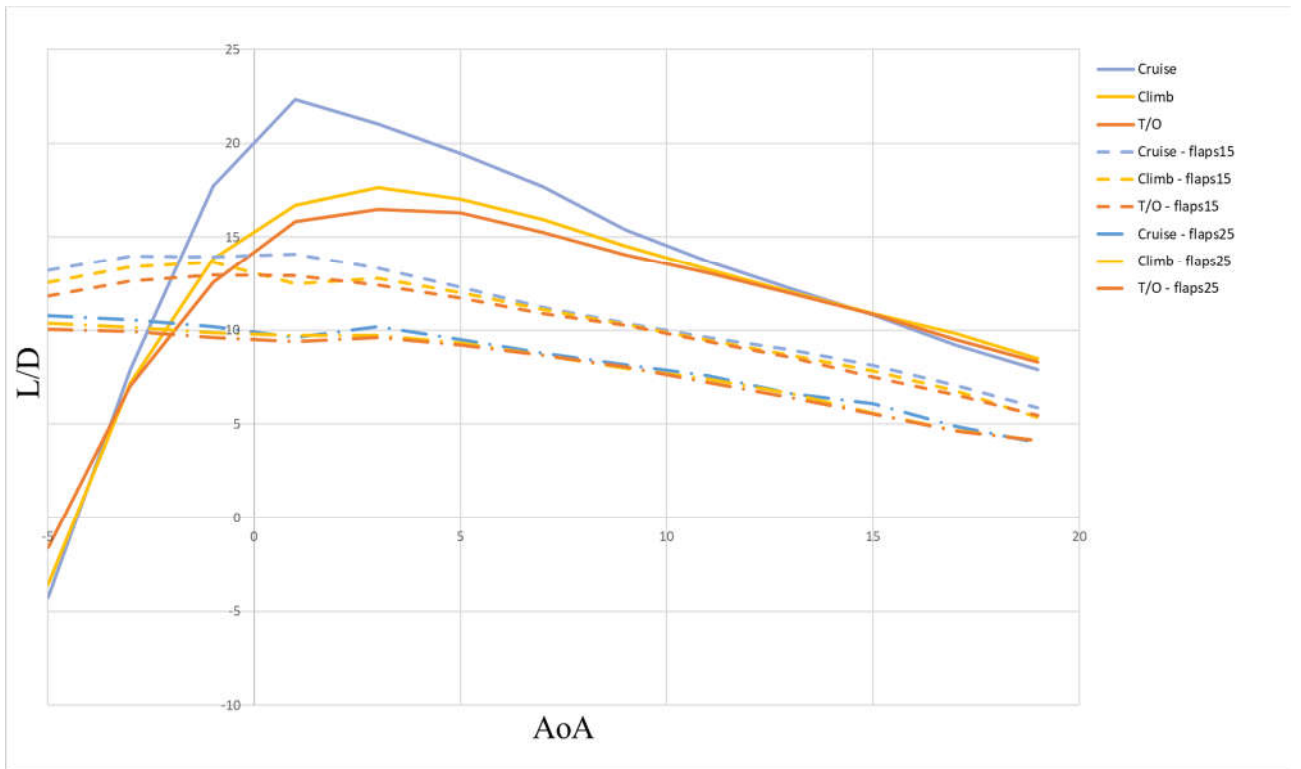


Figure 115 The lift-to-drag coefficient of the PVS 1 candidate.

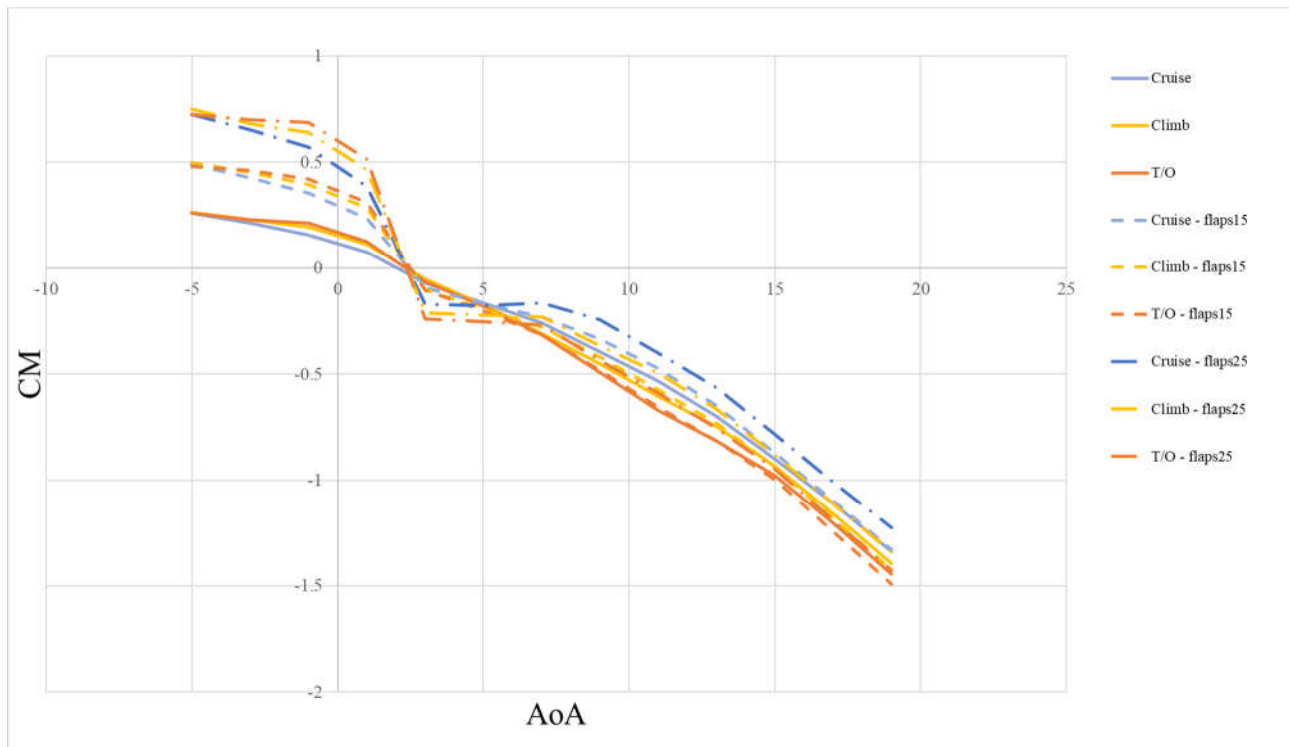


Figure 116 The pitching moment coefficient of the PVS 1 candidate

## Cooling Drag

### ***Main electric powertrain (electric motor, power-controller)***

Conceptual design of the PVS1 candidate main electric powertrain (pusher propeller) cooling circuit is shown in Figure 117. Electric powertrain consists of electric motor and power-controller. For clear comparison it is assumed that each component has its dedicated liquid cooling circuit and heat is rejected to the ambient using ducted radiator. Efficiency of intake diffuser is assumed to be 1.0. Electric motor and power-controller efficiencies of 0.92 and 0.97 were considered, respectively. Radiator sizing was done considering climb at 0 m altitude at ISA temperature offset of 24 K.

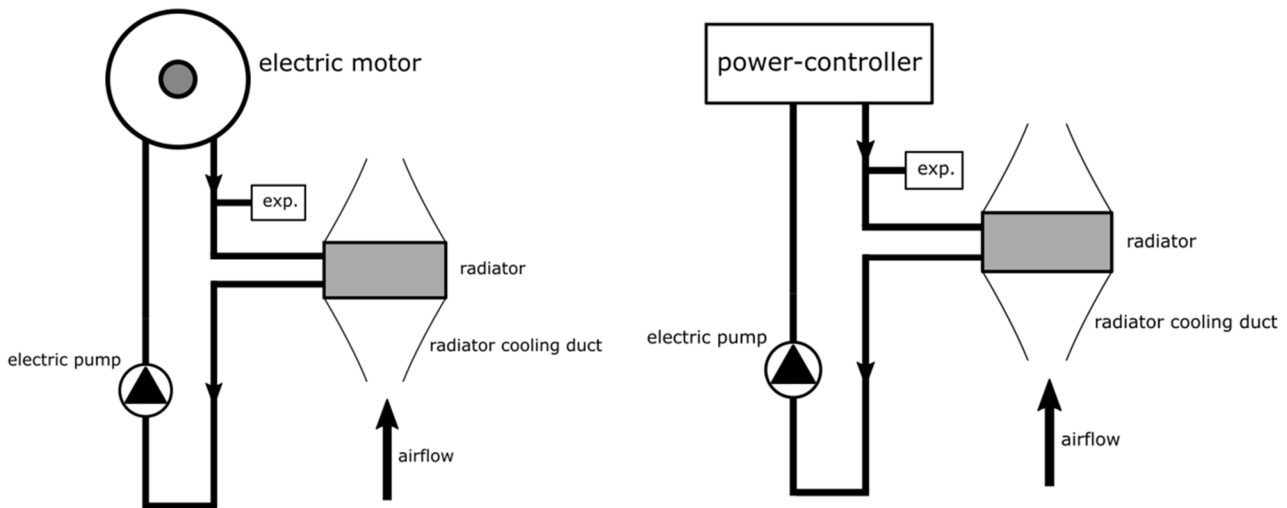


Figure 117: PVS 1 candidate main electric powertrain cooling system concept. Left: electric motor cooling circuit. Right: Power-controller cooling circuit.

Input data considered is given with Table 45.

Table 45: Input data (PVS 1) for cooling drag estimation – main electric powertrain.

	CLIMB	CRUISE
<b>Electric power (kW)</b>	286.8	399.3
<b>El. motor efficiency (/)</b>	0.95	0.95
<b>Power-controller efficiency (/)</b>	0.97	0.97
<b>Speed (m/s)</b>	48	77
<b>Coolant volumetric flow rate, el. motor (l/min)</b>	16	23
<b>Coolant volumetric flow rate, power-contr. (l/min)</b>	10	14
<b>Coolant inlet temp, el. motor (°C)</b>	60	60
<b>Coolant inlet temp, power-controller (°C)</b>	55	55
<b>Coolant</b>	50/50 MEG	50/50 MEG

### ***DEP electric powertrain (electric motor, power-controller)***

Conceptual design of the PVS1 candidate DEP electric powertrain cooling circuit (one wing) is shown in Figure 118. Electric powertrain consists of electric motor and power-controller. Components are liquid cooled, and heat is rejected to the ambient using ducted radiator. Efficiency of intake diffuser is assumed to be 1.0. Radiator sizing was done considering climb at 0 m altitude at ISA temperature offset of 24 K. Input data considered is given with Table 46.

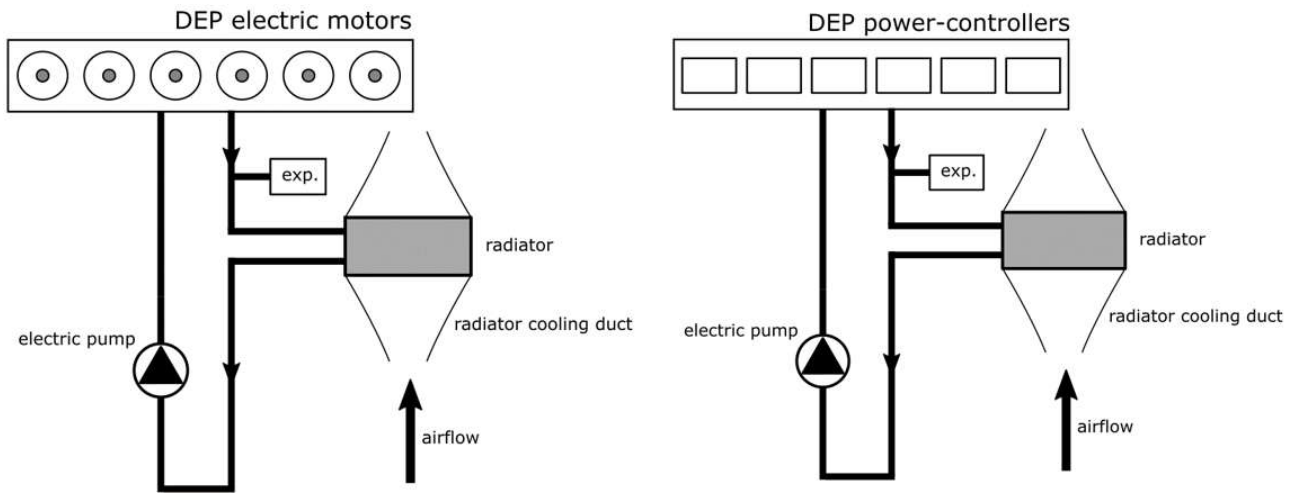


Figure 118: PVS 1 candidate DEP electric powertrain cooling system concept. Left: electric motors cooling circuit (one wing). Right: Power-controllers cooling circuit (one wing).

Table 46: Input data (PVS1) for cooling drag estimation – DEP electric powertrain.

	CLIMB	CRUISE
<b>Electric power (kW)</b>	726.1	121
<b>El. motor efficiency (/)</b>	0.95	0.95
<b>Power-controller efficiency (/)</b>	0.97	0.97
<b>Speed (m/s)</b>	48	77
<b>Coolant volumetric flow rate, el. motors (l/min)</b>	24	4
<b>Coolant volumetric flow rate, power-contrs. (l/min)</b>	60	10
<b>Coolant inlet temp, el. motor (°C)</b>	60	60
<b>Coolant inlet temp, power-controller (°C)</b>	65	65
<b>Coolant</b>	50/50 MEG	50/50 MEG

### Fuel cells system

Conceptual design of the PVS1 candidate FC system cooling circuit is shown in Figure 119. Fuel cells are liquid cooled, and heat is rejected to the ambient using ducted radiator. Efficiency of intake diffuser is assumed to be 1.0. Radiator sizing was done considering climb at 0 m altitude at ISA temperature offset of 24 K. Input data considered is given with Table 47.

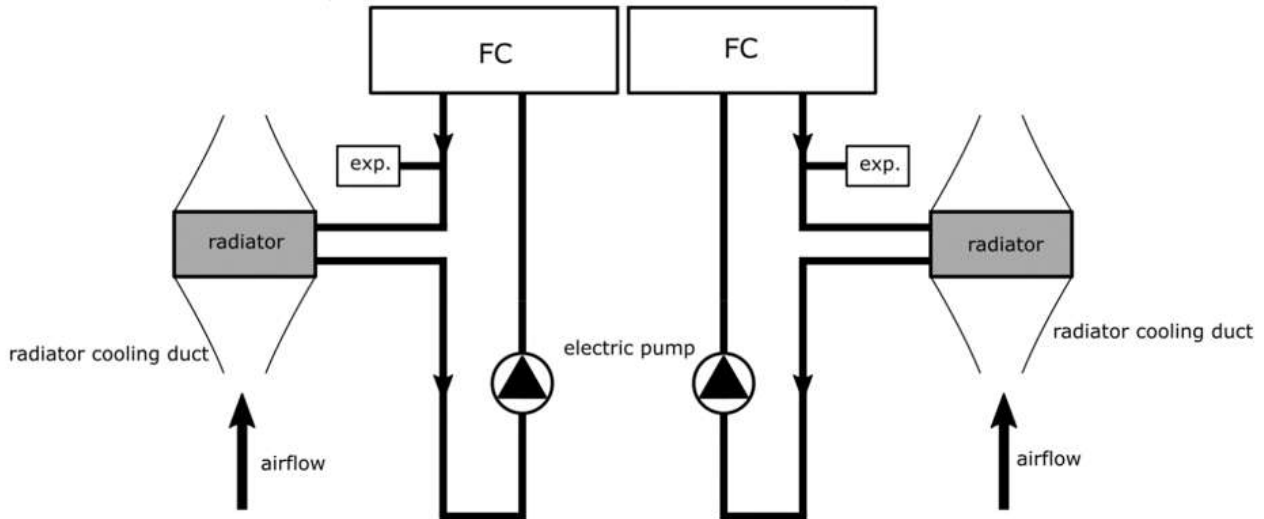


Figure 119: PVS1 candidate fuel cells cooling system concept.

Table 47: Input data (PVS1) for cooling drag estimation – FC.

	CLIMB	CRUISE
<b>Total electric power out (kW)</b>	782.3	524
<b>FC efficiency (/)</b>	0.52	0.52
<b>Speed (m/s)</b>	48	77
<b>Coolant volumetric flow rate (l/min)</b>	180	120
<b>Coolant inlet temp (°C)</b>	45	45
<b>Coolant</b>	50/50 MEG	50/50 MEG

### Batteries

To not increase cooling drag, it was assumed for all the candidates that batteries cooling is done via skin-integrated heat exchangers.

For the PVS1 candidate, the estimated size of radiators is given in Table 48. Total face area of radiators is **2.5589 m<sup>2</sup>**. Total cooling drag of **1637.6 N** and **901.3 N** was estimated for climb and cruise regime, respectively.

Table 48: PVS1 radiators size.

Cooling system for	# of radiators	Height (mm)	Width (mm)	Face area (m <sup>2</sup> )
<b>Main el. powertrain</b>	1	300	410	0.123
	1	250	310	0.0775
<b>DEP el. powertrain</b>	2	350	440	0.308
	2	130	440	0.1144
<b>FC system</b>	2	880	1100	1.936

### Mission Analysis

Required shaft power during the mission for the PVS1 candidate is presented in Figure 120. For the sake of comparison, also the comparison of required shaft power between POLIMI and PVS mission for C7A is added. The figure depicts only the first two hops with the diversion in between, for the sake of visibility. A small offset in the time scale can be again observed, originating from different times needed for climb and descend.

In this case there is no comparison with POLIMI analysis, but comparing to C7A (PVS analysis), there is one distinct difference at the landing phase of the mission. PVS1 candidate has smaller wing and also the deflection of flap is smaller, which results in smaller power demand at this phase of the flight.

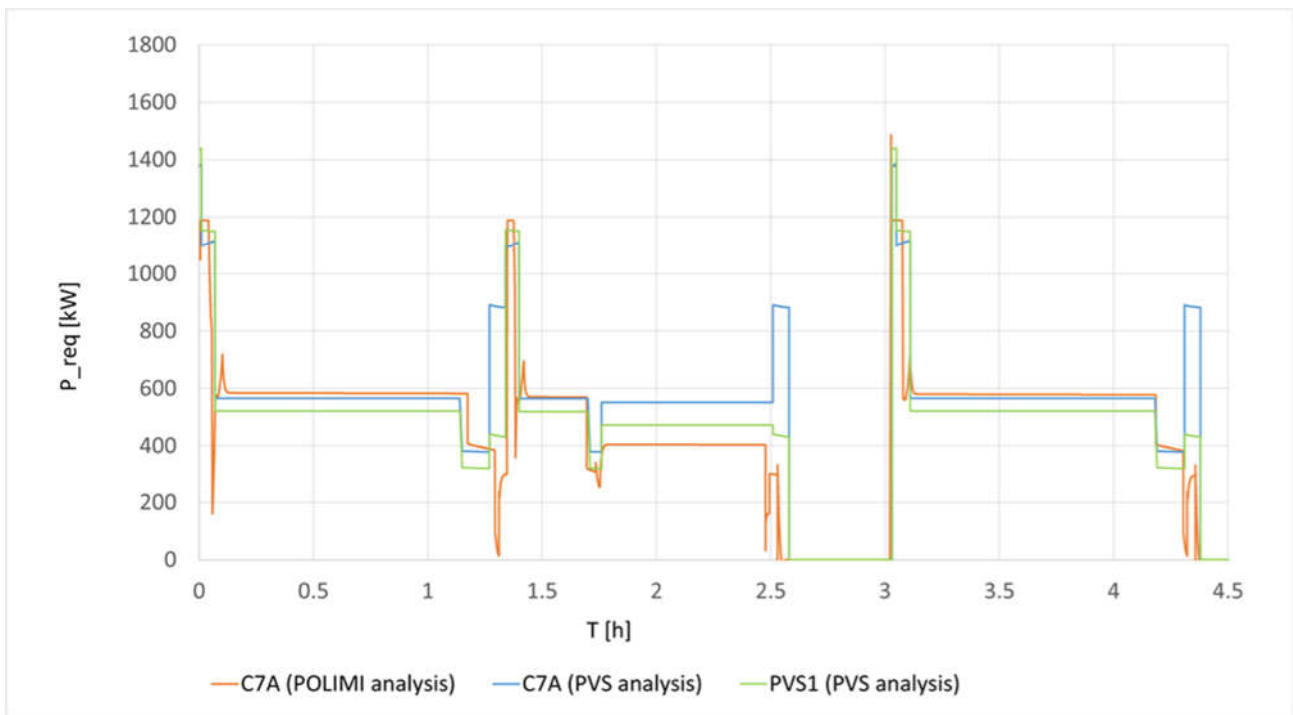


Figure 120: Shaft power requirement comparison between PVS1 candidate and C7A candidate.

### Qualitative structural design assessment

The table below summarizes the key differentiators of the structure of the concept compared to other A/C design solutions.

Section	Pros	Cons
<b>Main Wing</b>	Smaller wing surface area and bending load alleviation leading to lower structural mass due to DEP concept	Increased no. of engines and nacelles complicates design and manufacturing
<b>Empennage</b>	/	Presence of pusher engine and large ducted fan complicates design and increases weight



Fuselage	/	Great increase in weight due to large, ducted pusher prop assembly and stabilizers
----------	---	--

### 3.5.2 Sensitivity analysis

The sensitivity analysis for the PVS1 aircraft was performed with pConcept. Results are presented in the following sections.

#### **Airframe Mass Fraction**

The mass of the airframe is usually one of the biggest unknowns in the conceptual phase of the aircraft design – and the one with the greatest penalty, if assumed too low. It is therefore critical, that airframe mass fraction parameter is investigated. Figure 121 reveals, that missing this parameter by just 5% can make more than a half of tonne of difference in total aircraft weight.

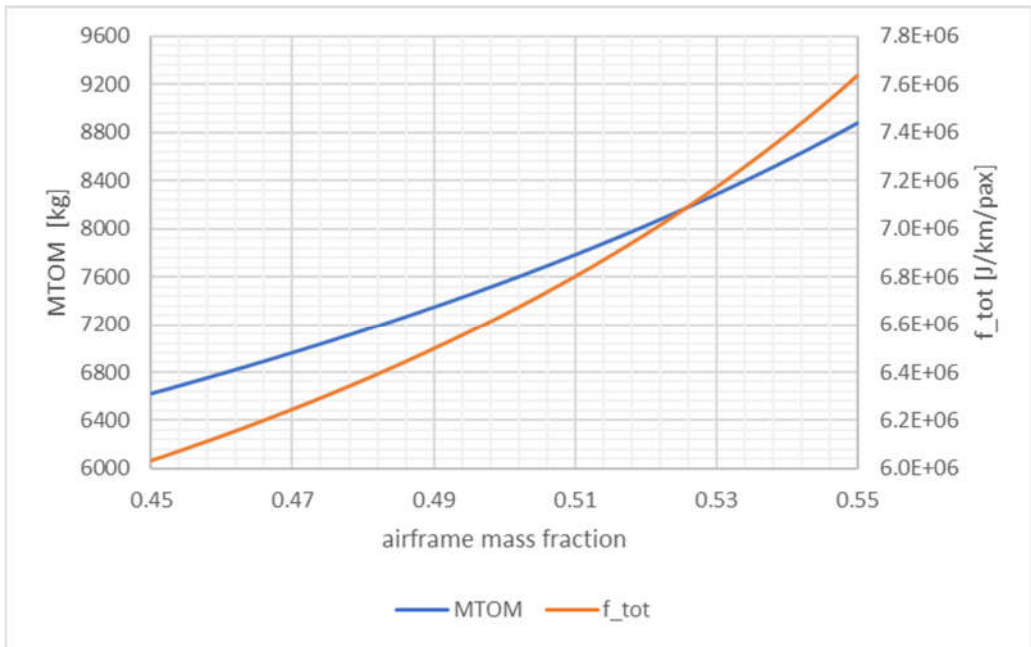


Figure 121: Aircraft PVS1 weight and f\_tot versus airframe mass fraction.

#### **Battery Power Density**

Battery is sized using the worst case of two different constraints: power and energy requirements. This is evident in the battery power density sensitivity, where at high power densities the aircraft weight does not change (Figure 122), as the energy requirements are the active constraint. At low power densities, the power constraint becomes active, and the aircraft weight starts to rise. The optimum battery pack would have specifications that correspond to the location of the kink in the sensitivity line. Keep in mind, that this curve changes with other parameters, namely battery energy density, therefore the location of the kink would change as well.

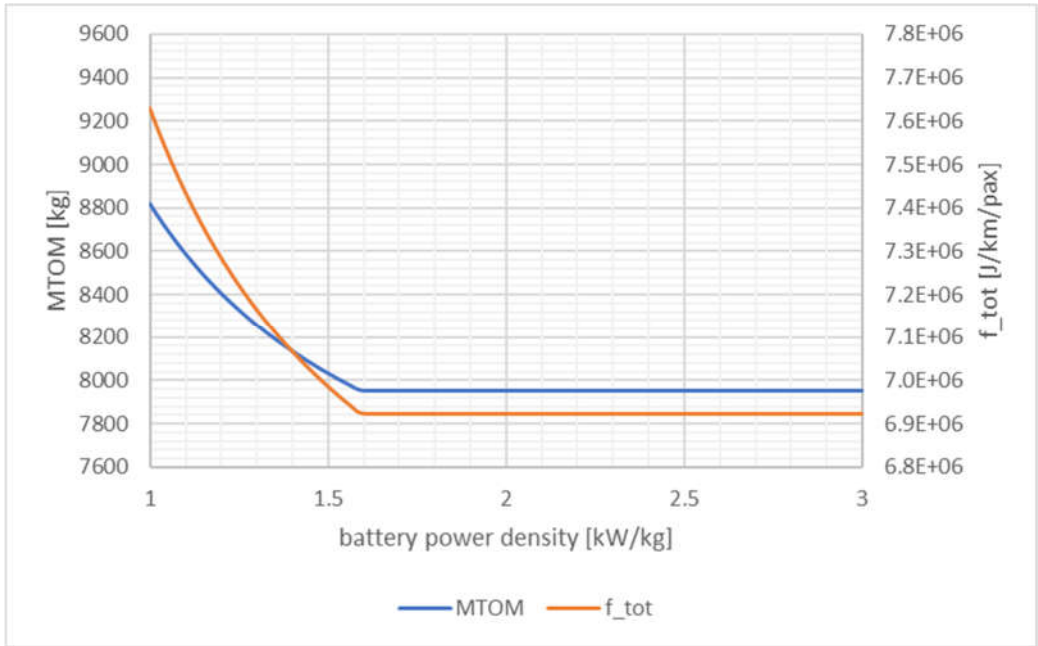


Figure 122: Aircraft PVS1 weight and  $f_{tot}$  versus battery power density.

**Battery Energy Density**

It is a similar story with battery energy density. The aircraft weight does not change at high densities; but at low densities, the energy requirements are dominant, and the aircraft weight starts to rise (Figure 123).

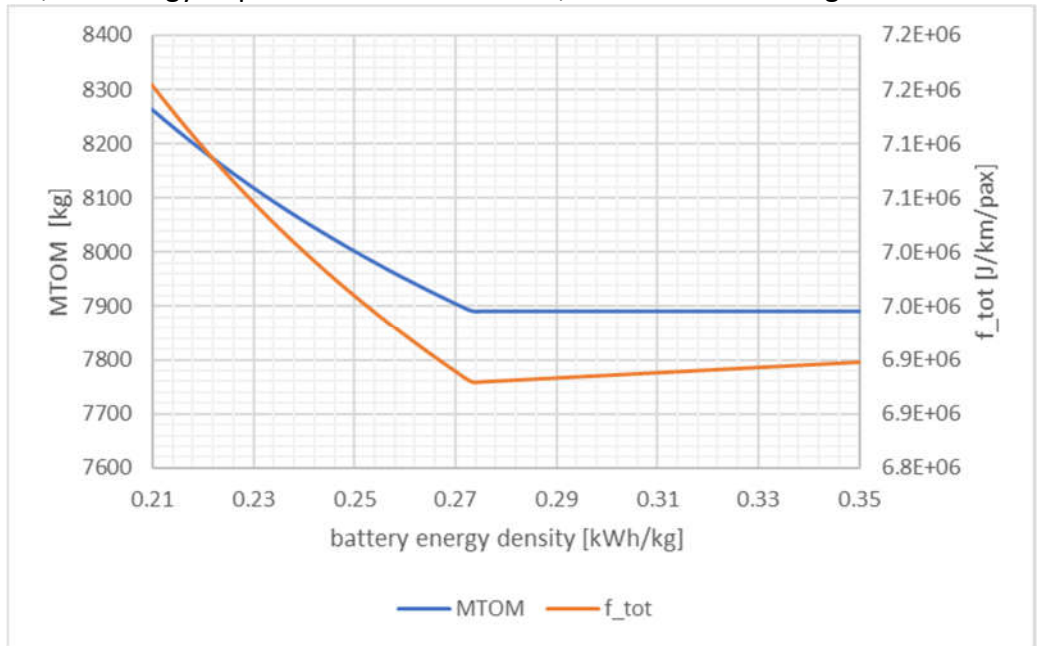


Figure 123: Aircraft PVS1 weight and  $f_{tot}$  versus battery energy density.

### Fuel Cell Efficiency

Fuel cell efficiency is another value, which is somewhat harder to estimate, due to the novelty of the fuel cell use in aircrafts. Figure 124 reveals that the aircraft mass changes quite fast with fuel cell efficiency.

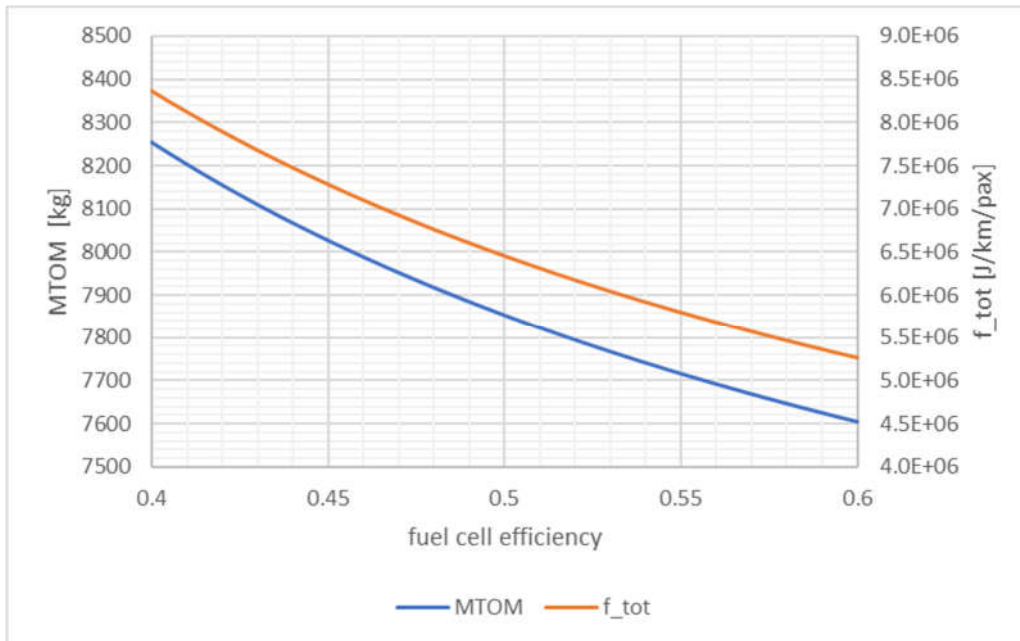


Figure 124: Aircraft PVS1 weight and  $f_{tot}$  versus fuel cell efficiency.

### Fuel Cell Power Density

The same goes for fuel cell power density. The dependence gets stronger at lower power density values, where it becomes quite important (Figure 125).

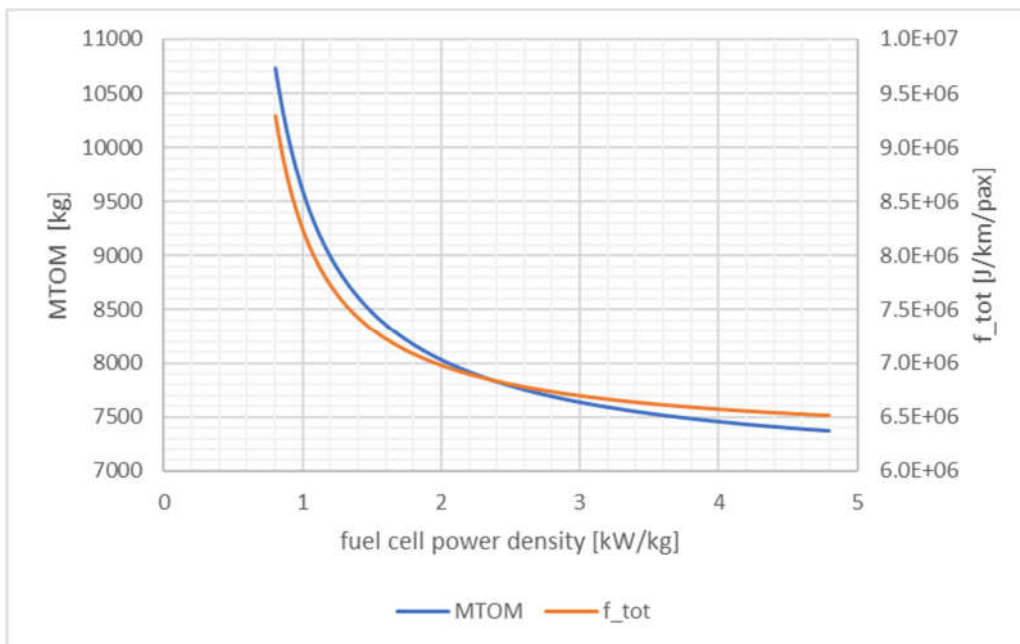


Figure 125: Aircraft PVS1 weight and  $f_{tot}$  versus fuel cell power density.

### Glide Ratio

A better glide ration means aircraft with less drag, which in turn means lower power requirements, which finally leads to lower fuel consumption and lower mass.

The kink in the line (Figure 126) is there because the battery sizing transitions from energy constrained to power constrained.

The higher glide ratio provides aircraft with lower mass, however, once the glide ratio is high enough, the difference is not too dramatic.

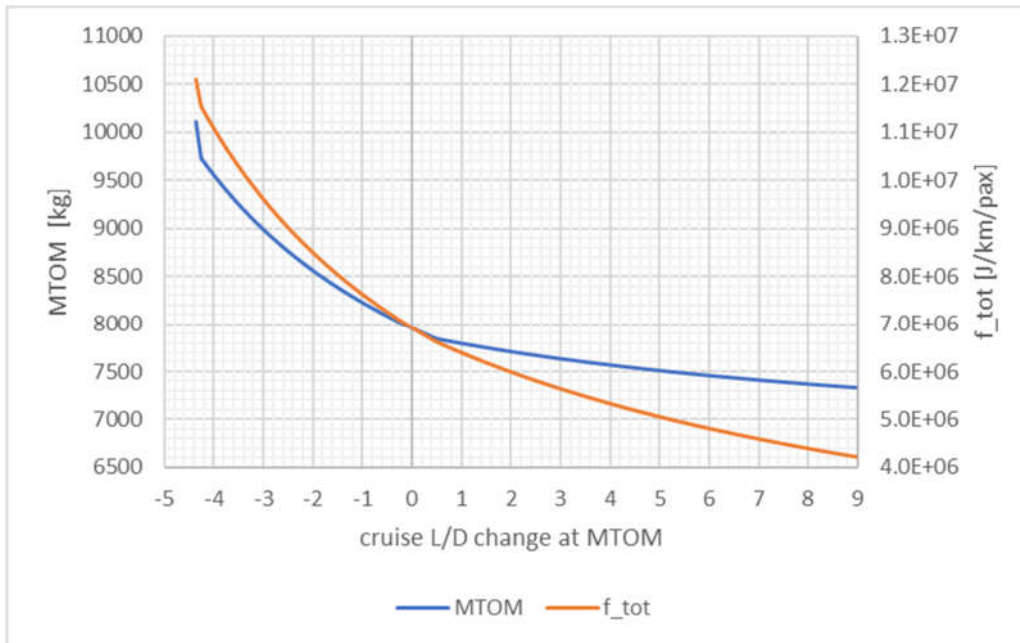


Figure 126: Aircraft PVS1 weight and  $f_{tot}$  versus glide ratio.

### 3.5.3 Cross-check & assessment

#### Hyperion

PoliMI cross-checked the PVS1 candidate by applying the Hyperion tool, seeking a preliminary sizing solution. This is motivated by the good performance of this tool in delivering general sizing and mission simulation data for a conceptual design solution. Indeed, while the Titan design loop allows achieving a more detailed solution with the sizing of the aircraft geometry and main subsystems, the general sizing data are typically updated only slightly.

The sizing was carried out using the same technological data as used by PVS. This includes the power and energy densities of propulsion components such as motors, fuel cells and batteries.

In a first attempt, a design solution based on the PVS1 requirements and design options (such as tail aft, DEP, etc.) was obtained. This solution does not take into account any PVS derived data and is to be considered as a “clean-sheet” approach to the preliminary sizing. The general sizing data for this solution are shown in Table 49 in the row marked “Hyperion – Clean sheet” and can be contrasted with the PVS design data in the “pConcept” row. As seen, there is a significant difference between the two solutions, with a significantly lower MTOM (9% difference) and mass components in the case of the Hyperion data. This is interpreted mainly as the result of the significantly lower non-propulsive airframe mass (6% difference) and of different design assumptions in deriving polar data, various system efficiencies, and other characteristics, including mission profile phase attributes.

Concerning the difference in non-propulsive airframe mass, it is noted that, in Hyperion, this is evaluated by resorting to a combination of statistical estimations involving aircraft empty weight and thermal engine weight, and this process is known to be prone to some uncertainties, especially within the very diverse CS-23 category. Additionally, it is remarked that the estimation of the weight related to the large tail ducted fan and its supporting structures are very difficult to model in general terms at conceptual level.

Table 49 Results of PVS1 cross-check using Hyperion.

Mass [kg]	Total	Airframe	El. Motors	Battery	Fuel Cells	LH2	LH2 Tank
<b>pConcept</b>	7980	4037	227	406	371	309	206
<b>Hyperion - Clean sheet</b>	7271	3809	119	262	266	257	179
<b>Hyperion - Retrofit</b>	7736	4037	125	464	245	286	198

To provide more insight and get a better comparison between the sizing approaches of pConcept and Hyperion, a second attempt was pursued by applying Hyperion in “retrofit” mode. This implies that the non-propulsive airframe mass is kept constant (equal to the pConcept output value) during the sizing iterations, while all other component masses are free to evolve to satisfy the design requirements. This application led to the results in Table 49 in the row marked “Hyperion – Retrofit”. The results indicate a better match now, with a difference in MTOM decreased from 9% to 3%. Such difference is now a result of the discrepancies in the modelling approach related to aerodynamics and system efficiencies. Indeed, the mass of the electric motors and that of the fuel cell system are quite lower, standing at 55% and 66%, respectively, while other components show a different trend: the battery pack mass is increased by 14%, the fuel cell system mass is decreased by 7%, and the fuel tank mass is decreased by 4%.

Interestingly, the values of the overall mass efficiency of the two aircraft solutions for the same sizing mission are very close, as the pConcept version uses 0.038 kg of hydrogen per kg of all-up aircraft mass, while for the Hyperion version the value is 0.037. Based on the results discussed and the inevitable uncertainties inherent to the two independent sizing processes, the cross-check is considered satisfactory. To complete the discussion, the sizing matrix plot and the graphs showing the energy and power plots for the sizing mission are reported, in connection to the retrofit solution only.

In Figure 127, the design point for the considered solution is shown. It is seen that the active performance constraint is the maximum rate of climb requirement, while both the stalling speed and the landing distance requirements are satisfied with a significant margin. It is remarked that both the latter requirements, as well as the take-off requirement, are formulated in a novel way, which takes into account the effect of DEP. For this reason, the stalling speed and the landing distance curves are not vertical lines as usual, but become highly non-linear as the power loading is reduced, with the “conventional” vertical lines as asymptotes.

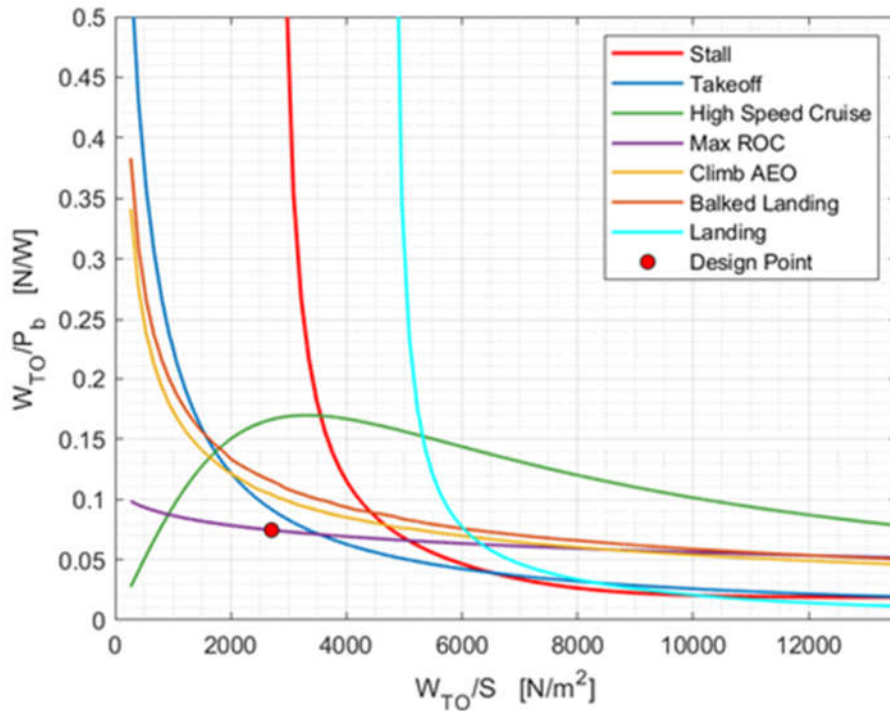


Figure 127 Sizing matrix plot for PVS1 obtained by Hyperion

Figure 128 and Figure 129 show the time histories of the energy and power quantities during the sizing mission, along with its altitude profile. These fully prove the suitability of the design solution in providing the six 350 km hops with due reserves.

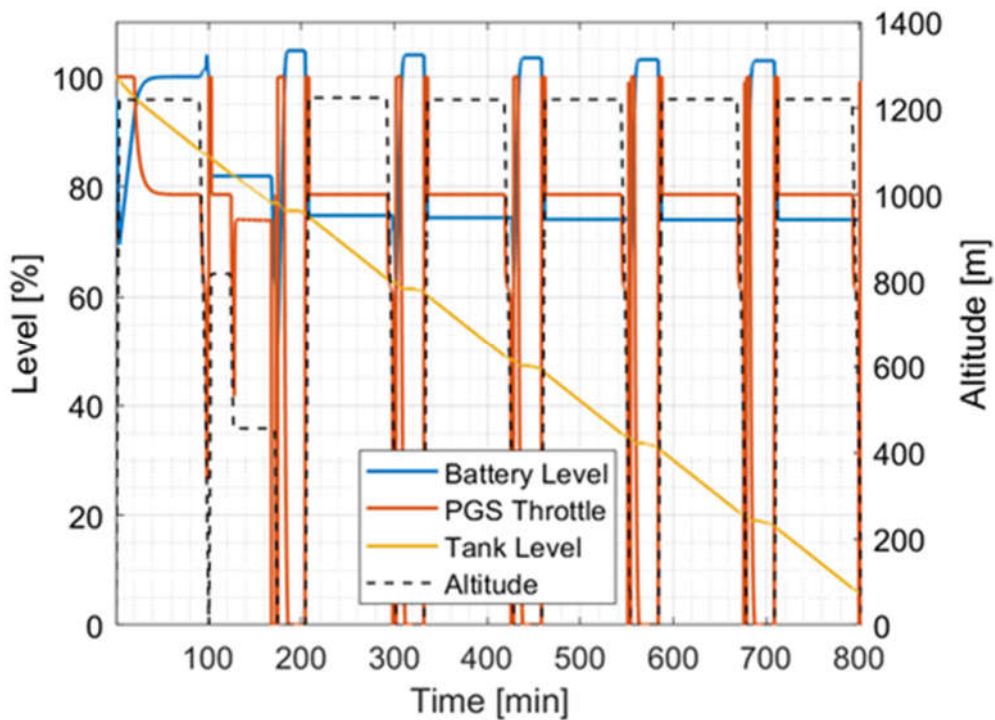


Figure 128 Fuel, battery, and throttle level plot for PVS1 obtained by Hyperion

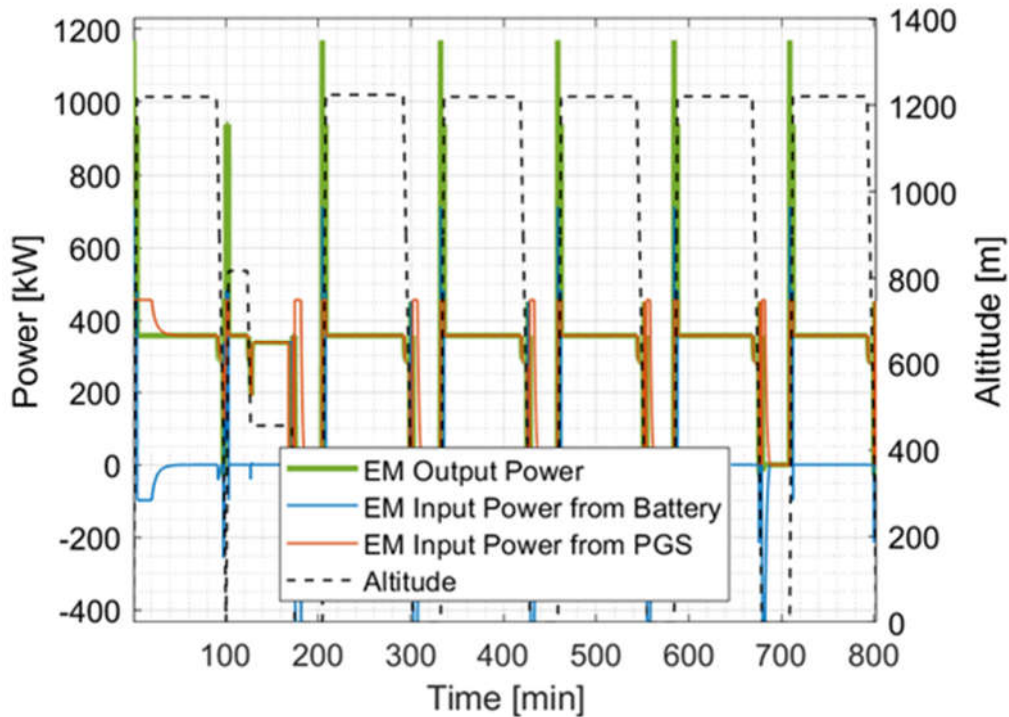


Figure 129 Power utilization during the sizing mission for PVS1 obtained by Hyperion.

### Qualitative structural considerations

Table 50 synthetically reports a qualitative assessment provided by PoliMI in relation to structural issues for PVS1. As seen the main considerations concern the unusual tail ducted fan system, which inevitably carries along pros and cons.

Table 50 Qualitative structural design assessment

Section	Pros	Cons
Fuselage	/	Ducted fan at the tail may strike during take-off roll
Main Wing	-Smaller wing surface area and bending load alleviation leading to lower structural mass due to DEP concept	- Increased no. of engines and nacelles complicates design and manufacturing
Empennage	No horizontal stabilizer simplifies the design	Presence of pusher engine with ducted fan shroud complicates design and increases weight

### 3.6 FlightStream General Discussion

In this section some observations about the aerodynamic performance and viability of each candidate are made. No ranking of the candidates is provided.

Firstly, the distributed electric configurations are discussed. POLIMI C7A, POLIMI C2 and PVS1 leveraged from the leading edge mounted distributed propulsion during landing, take off and climb phase of the flight. It can be seen that PVS1 can reach significantly higher lift coefficient values than the other candidates. This is merely due to the reason that the wing area and hence the reference area used to non-dimensionalize the candidates is lower. Hence, the maximum lift coefficient value does not address the take-off performance or landing performance directly. However, conventionally the distributed electric propulsion is leveraged to allow for reduction of drag through the reduction of the wing size. This reduction is not directly visible in some of the candidates as the wing area is close to the reference aircraft wing size.

The aerodynamic cruise performance can be estimated from the lift-to-drag ratio of the candidates. It is seen that the highest lift-to-drag coefficient at cruise angle of attack (1-2 degrees) is achieved by the PVS1 concept. This is explained mostly due to the fact that the wing area of the candidate is the smallest. However, it must be noted that the lift-to-drag ratio of the PVS 1 candidate is not significantly better than the reference aircraft. This is mainly due to the reason that even though the drag can be reduced by reducing the wing area, additional drag is introduced in the forms of nacelles. In the PVS1 concept the nacelles are mounted slightly below the wing, whereas for the POLIMI C7A and POLIMI C2 candidates the nacelles are mounted to the leading edge of the wing. However, a brief analysis was performed in FlightStream regarding the mounting location and no large difference was seen between these two mounting options.

The candidate with canard and no distributed electric propulsion, POLIMI C3, did not perform better from lift-to-drag performance point of view than the reference aircraft. It must be noted that the modelling of the canard in this candidate was relatively rudimentary, and with more detailed design of the canard, some performance gains could be achieved. Also, the wake of the canard was interacting with the main wing during the cruise flight which likely also contributed to the lift-to-drag performance.



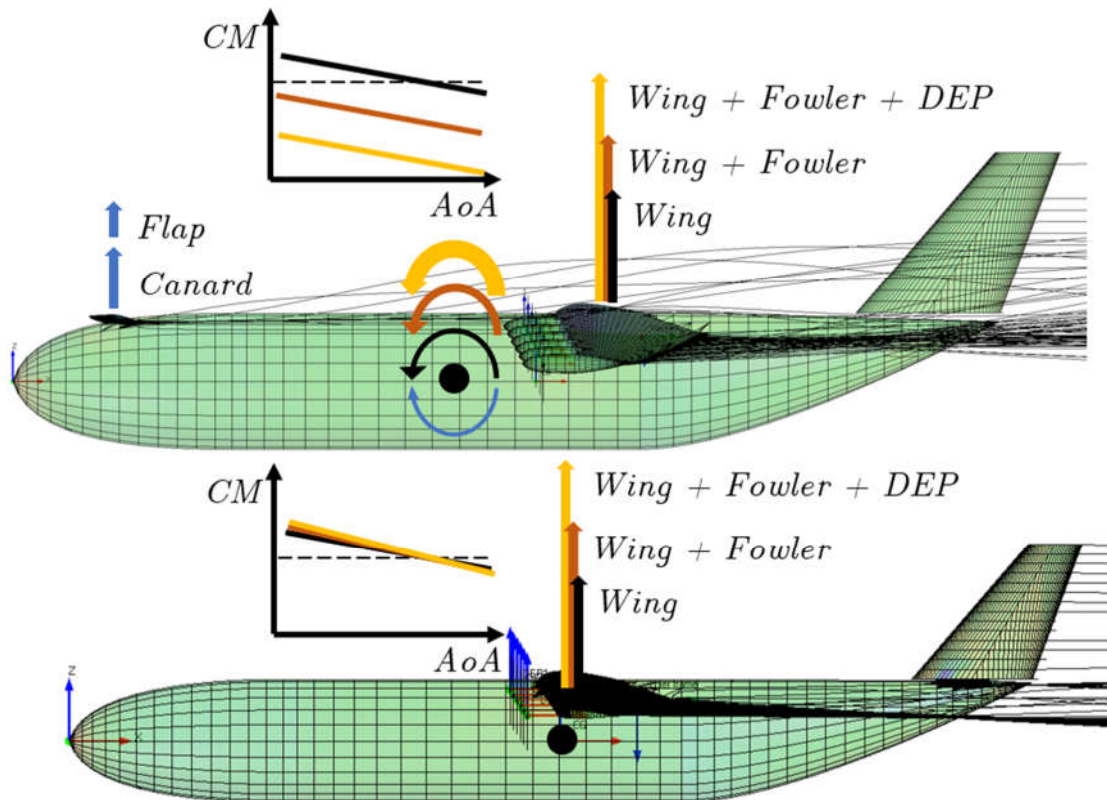


Figure 130 The pitching moment behaviour between canard and conventional configuration.

The configurations with canard and with conventional tail have a significant difference in the pitching moment behaviour. This is due to the reason that the centre of gravity is placed in front of the leading edge for aircraft using canard. Hence, changes on the wing lift have also significant changes on the pitching moment. This is illustrated in Figure 130. This imposes a demand for the canard design to be able to provide sufficient pitch-up moment with a control surface or via variable geometry of the canard. No analysis was performed to investigate whether the canard can meet this requirement. Secondly, it is seen that the candidates with canard configurations have neutral to negative longitudinal static stability. This can be corrected by shifting the centre of gravity further or shifting the wing more aft. Due to the required shift, it is seen that also the size of the canard needs to be increased, which will impact adversely to the lift-to-drag performance.

In conclusion, it can be seen that all of the candidates offer a viable option from the aerodynamic analysis point of view. It is seen that the canard candidates will require further design of the canard size to address the pitching moment issue, however, this is expected at the conceptual design phase. Additionally, a challenge is seen with the canard configuration regarding the trimmability of the aircraft, however similarly to the pitching moment issue, this can be addressed with further analysis of the canard design.

## 4 Noise assessment

### 4.1 Approach

For all candidates, the point of interest (POI) was defined according to ICAO Annex 16 – Volume 1 (see Figure 131): the ground noise contour map is calculated for airplane in climb at height that is reached 2500 m (horizontal direction) after brake release. For all candidates climb angle of  $7^\circ$  was considered.

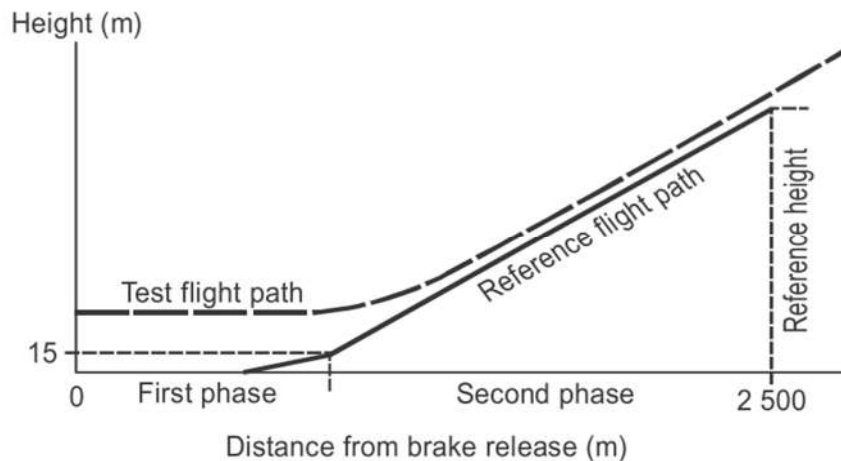


Figure 131: Point of interest for generation of ground noise contour maps.

### 4.2 Example application

Figure 132 - Figure 134 show PVS1 candidate main rotor rotational, broadband, and total noise ground footprint, respectively. Similarly, Figure 135 - Figure 137 show PVS1 candidate DEP propellers rotational, broadband, and total noise ground footprint.

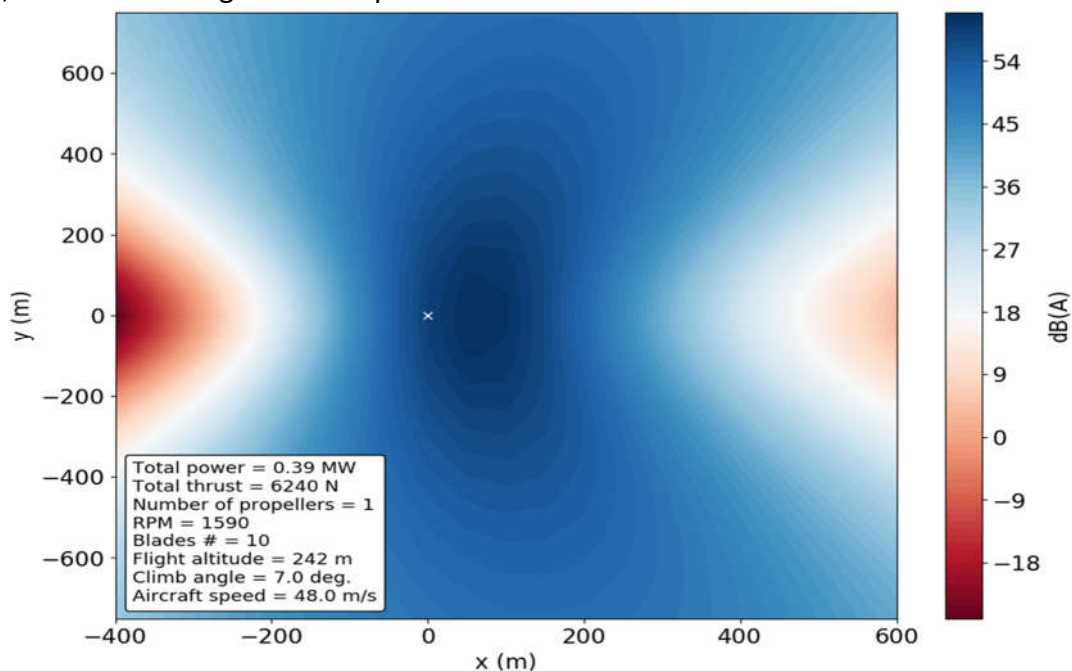


Figure 132: PVS1 candidate main propeller **rotational** noise ground contour map.

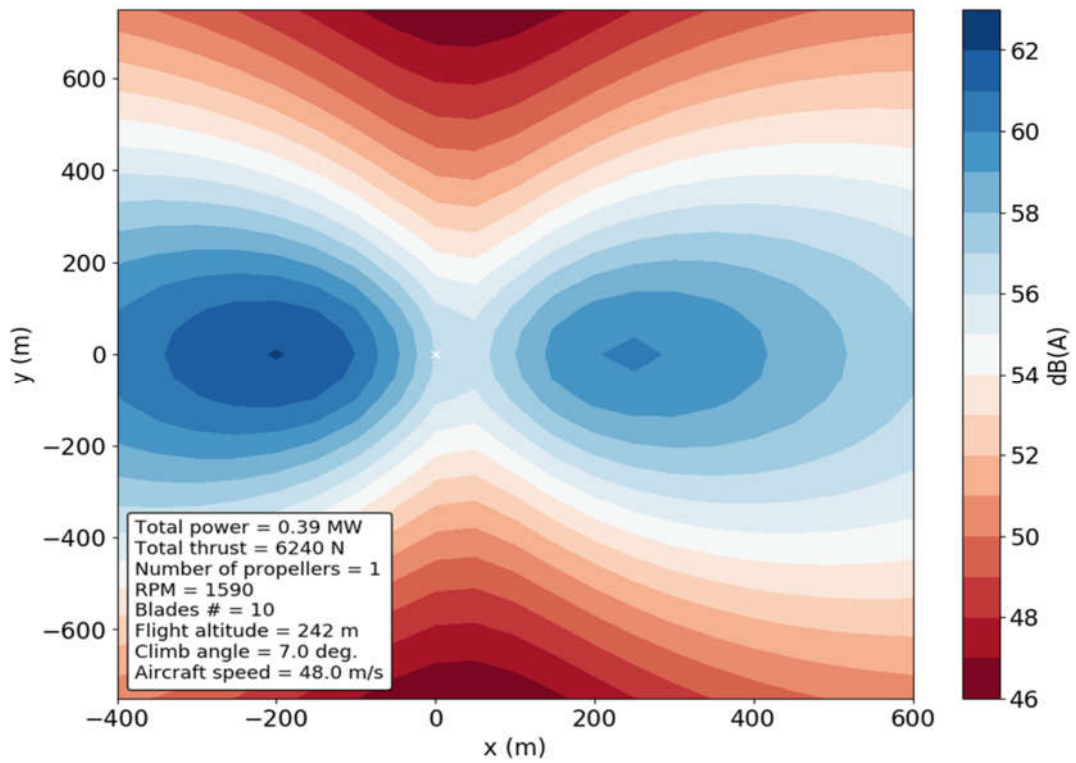


Figure 133: PVS1 candidate main propeller **broadband** noise ground contour map.

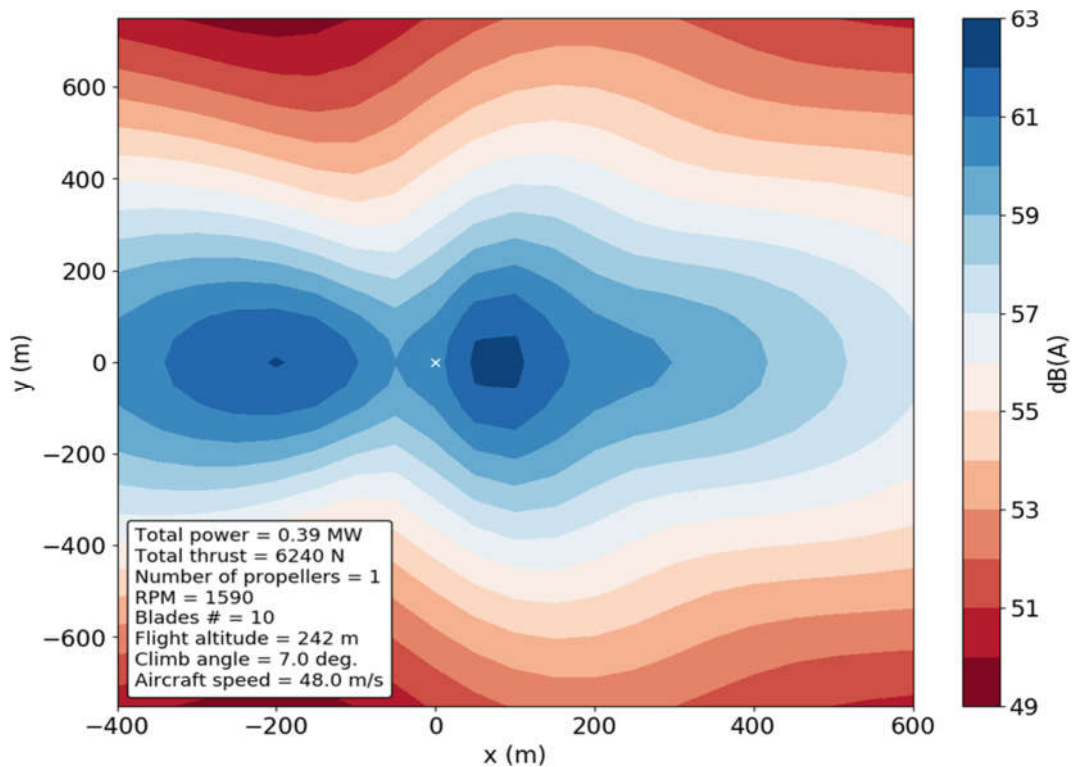


Figure 134: PVS1 candidate main propeller **total** noise ground contour map.

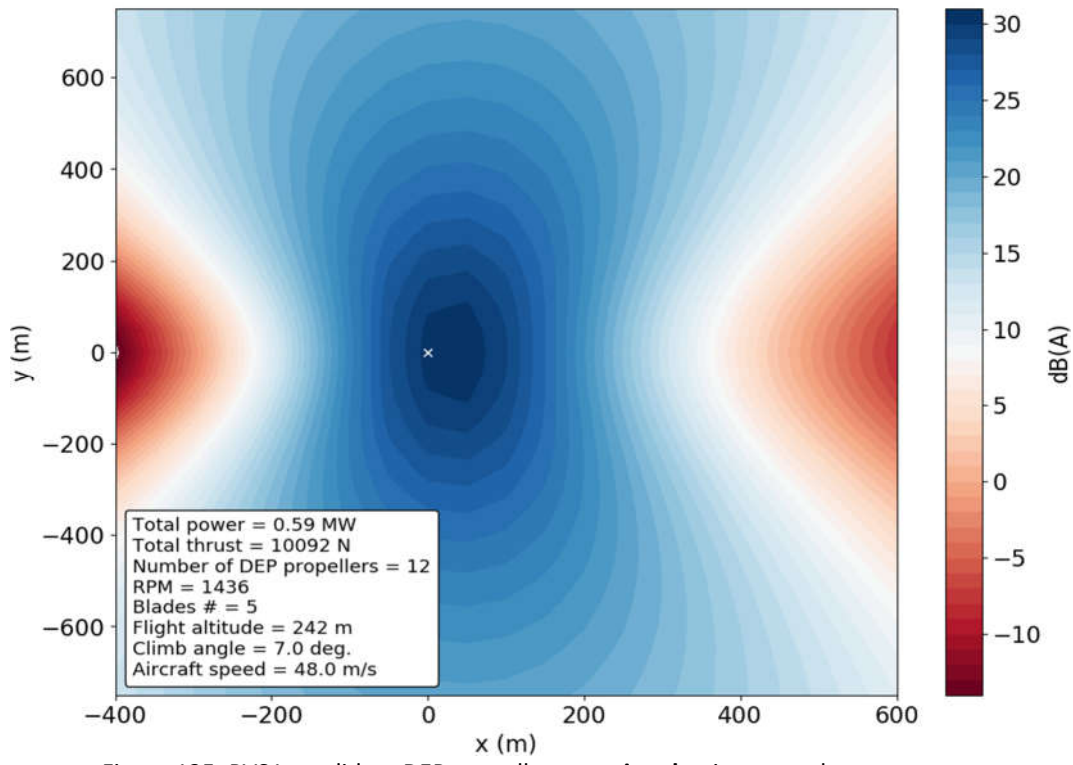


Figure 135: PVS1 candidate DEP propellers **rotational** noise ground contour map.

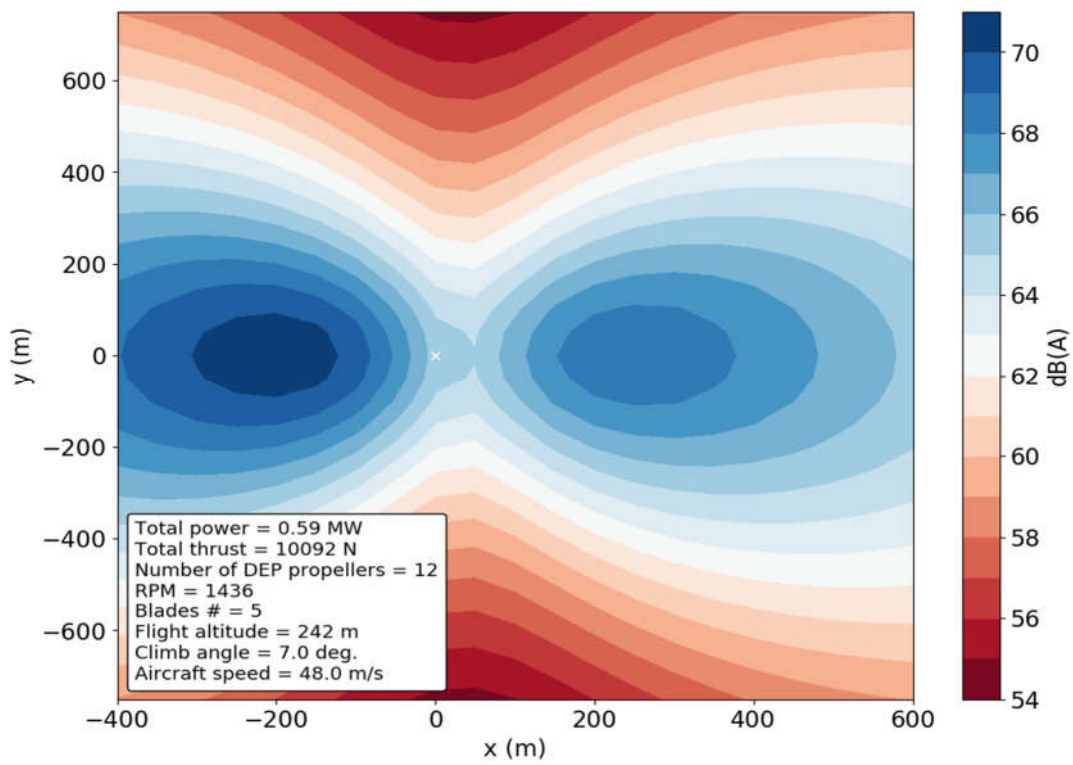


Figure 136: PVS1 candidate DEP propellers **broadband** noise ground contour map.

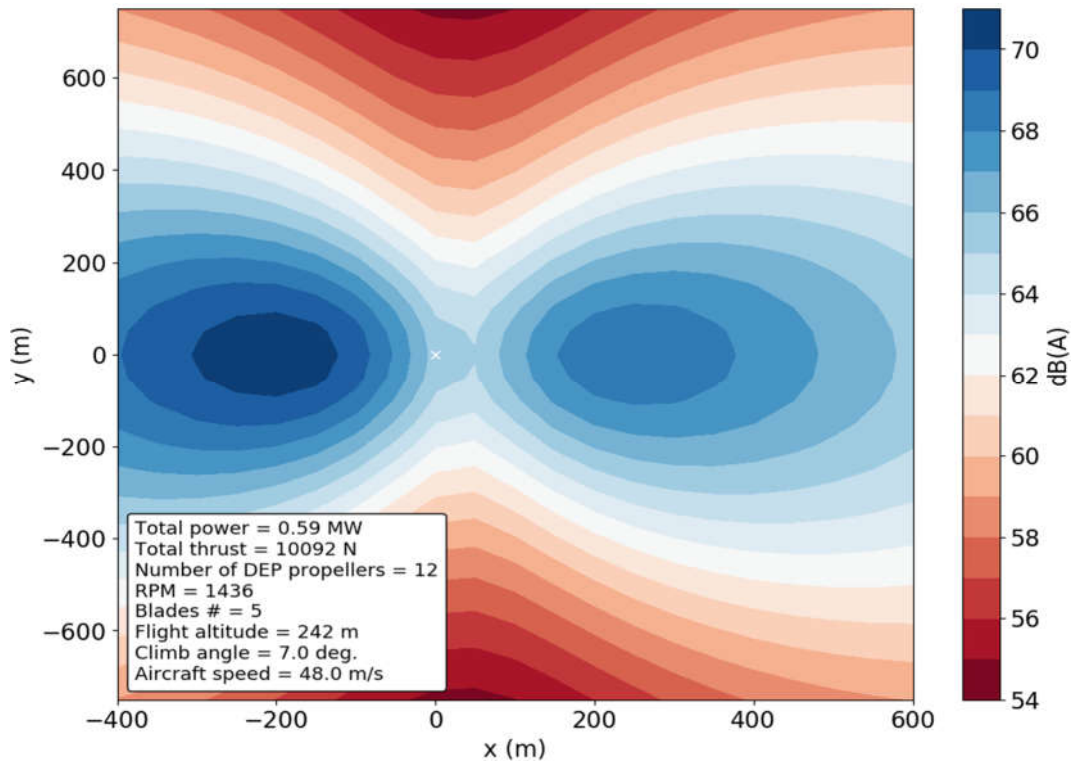


Figure 137: PVS1 candidate DEP propellers **total** noise ground contour map.

### 4.3 Candidate analysis and comparison

Operational data for all candidates is reported in Table 51 - Table 55.

Table 51: PVS1 operational data for propellers noise estimation.

	PVS1 – main	PVS1 - DEP
<b>Total power (MW)</b>	0.39	0.59
<b>Total thrust (N)</b>	6240	10092
<b>Number of propellers</b>	1	12
<b>Propeller diameter (m)</b>	2.44	1.47
<b>RPM</b>	1590	1436
<b>Number of blades</b>	10	5
<b>Flight altitude (m)</b>	242	242
<b>Climb angle (°)</b>	7	7
<b>Aircraft speed (m/s)</b>	48	48

Table 52: POLIMI C7A operational data for propellers noise estimation.

	POLIMI C7A – main	POLIMI C7A – DEP
<b>Total power (MW)</b>	0.5	0.59
<b>Total thrust (N)</b>	8034	10212
<b>Number of propellers</b>	1	12
<b>Propeller diameter (m)</b>	2.88	1.47
<b>RPM</b>	1500	1443
<b>Number of blades</b>	5	5
<b>Flight altitude (m)</b>	238	238
<b>Climb angle (°)</b>	7	7
<b>Aircraft speed (m/s)</b>	47.3	47.3

Table 53: POLIMI C2 operational data for propellers noise estimation.

	POLIMI C2 – main	POLIMI C2 – DEP
<b>Total power (MW)</b>	0.47	0.56
<b>Total thrust (N)</b>	7542	9504
<b>Number of propellers</b>	1	12
<b>Propeller diameter (m)</b>	2.83	1.41
<b>RPM</b>	1400	1438
<b>Number of blades</b>	5	5
<b>Flight altitude (m)</b>	239	239
<b>Climb angle (°)</b>	7	7
<b>Aircraft speed (m/s)</b>	47.1	47.1

Table 54: POLIMI C3 operational data for propellers noise estimation.

	POLIMI C3 – main
<b>Total power (MW)</b>	0.96
<b>Total thrust (N)</b>	12657
<b>Number of propellers</b>	1
<b>Propeller diameter (m)</b>	2.81
<b>RPM</b>	1500
<b>Number of blades</b>	5
<b>Flight altitude (m)</b>	223

<b>Climb angle (°)</b>	7
<b>Aircraft speed (m/s)</b>	54

Table 55: POLIMI REFERENCE operational data for propellers noise estimation.

POLIMI REF – main	
<b>Total power (MW)</b>	1.13
<b>Total thrust (N)</b>	15944
<b>Number of propellers</b>	2
<b>Propeller diameter (m)</b>	2.52
<b>RPM</b>	2000
<b>Number of blades</b>	5
<b>Flight altitude (m)</b>	221
<b>Climb angle (°)</b>	7
<b>Aircraft speed (m/s)</b>	54.2

To compare all candidates, the intersection of contour map at  $y = 0$  (below the airplane) was selected. Comparison is shown in Figure 138. It can be seen that PVS1 candidate has the lowest the noise ground footprint. The pusher propeller is ducted - shielding noise. This should have a beneficial effect on radial propagation of propeller thickness noise as well.

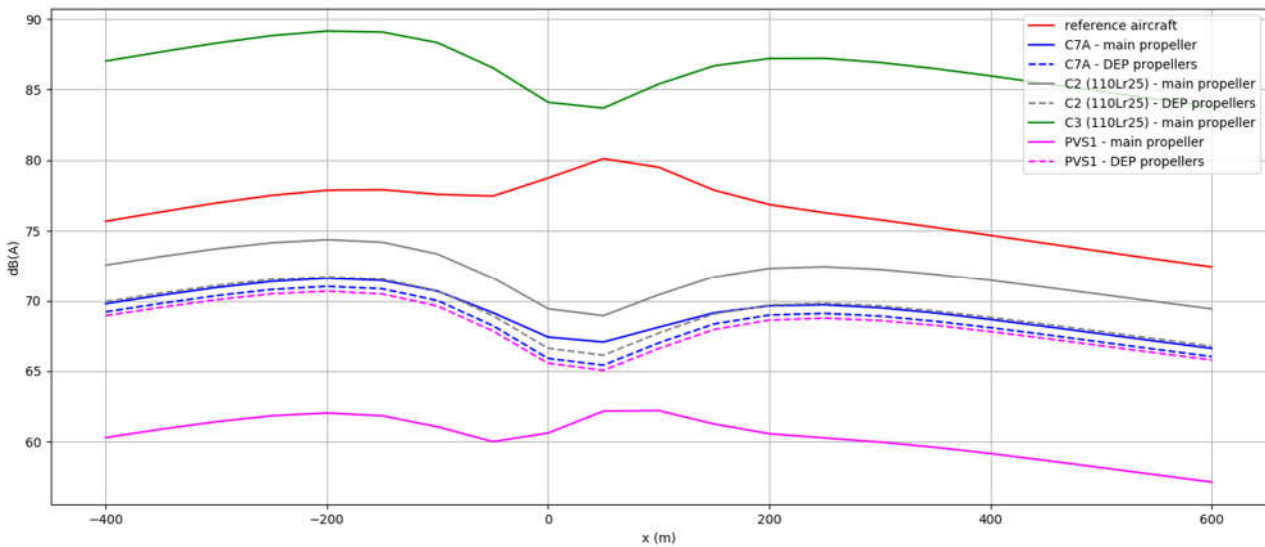


Figure 138: Comparison of candidates - noise ground footprint at  $y = 0$  m (below aircraft).

## 5 Cost and marketability analysis

Each candidate design has been also evaluated from its marketability potential through its direct operating costs (DOC) analysis. As this cost is highly dependent on the acquisition cost, i.e., aircraft price, the development and manufacturing cost for the whole programme had to be estimated as well. The methodology has been explained and detailed in the WP1 deliverable D1.1 (UNIFIER19, 2020).

### 5.1 Modifications after WP1

During WP1, the DOC and aircraft price estimation models were tuned to be as accurate as possible, using as a reference the average figures of existing 19-seater turboprop aircraft on a 350 km mission flight. The costs that have seen adaptations or updates, are defined in the following subsections.

#### 5.1.1 Powertrain costs

Technology evolution and better information from potential suppliers have allowed to gather more accurate data for the cost of powertrain components, especially fuel cells, LH2 tanks, electric engines, and batteries. Unfortunately, most of this information is protected by non-disclosure agreements, which does not allow to reveal the sources.

**Electric engine:** Project was able to obtain information for electric motor at 400 \$/kW and for the inverter at 250 \$/kW. Electric engine time between overhaul (or replacement) is now at 12 000 hours, as per Pipistrel experience and estimations, from the previously estimated 10 000 hours.

**Fuel cell** costs were extremely inaccurate in WP1. Project was able to obtain information for fuel cell pack, including the balance of plant (BOP), at 2300 \$/kW and for fuel cell lifespan at 20 000 hours.

**Cryogenic liquid hydrogen tank** cost was unknown at the end of WP1. Project was able to obtain information for tanks at 30 \$ per litre of capacity.

**Battery pack:** Project was able to obtain information for cost for pack at 700 \$/kWh and the lifespan at 800 full cycles between replacement. A reduced usage, i.e., recharging before the battery is depleted, can increase this lifespan to up to 4000-5000 cycles.

The values that were used in the powertrain cost calculations are:

$$\begin{aligned}C_{motor + inverter} &= FN_{0\ kW} (400\ \$/kW + 250\ \$/kW) \\C_{fuelcell} &= FN_{0\ kW} (2271\ \$/kW) \\C_{tankLH2} &= V_{H2} (30\ \$/liter) \\C_{batt} &= E_{batt} (700\ \$/kWh)\end{aligned}$$

where  $FN_{0\ kW}$  is the maximum power of the motor or fuel cell, in kW;  $V_{H2}$  is the liquid hydrogen volume, in litres; and  $E_{batt}$  the energy, in kWh, needed for a typical mission flight.



### 5.1.2 Distributed Electric Propulsion (DEP)

The cost models already allowed the adoption of new powertrain technologies, such as hydrogen fuel-cell, hybrid turbo-electric, and fully electric propulsion. However, as some candidate designs include distributed electric propulsion (DEP), a feature not included in the cost model at end of WP1, this capability has been added during WP2. The DEP electric engines were considered separately from the existing electric engine to allow having two different types of electric engines on the same aircraft, which is often the case for DEP architectures (one or two main electric engines used during the whole flight, the smaller DEP engines used only at low speeds). Nevertheless, the cost calculations associated to the DEP electric engines follow the same approach as the main electric engines in terms of price, maintenance, etc.

**Maintenance and durability:** As the DEP engines are used only during the low-speed phases of flight, which translates into around 7 minutes per flight hour for the UNIFIER19 mission calculated by POLIMI, the DEP motors lifespan is significantly high. Considering the time between replacement (TBR) of electric engines at 12 000 hours, and an aircraft utilisation of 1800 hours per year, this translates into an expected lifetime of the DEP engines of 57 years! On the contrary, a motor operating throughout the whole flight would have a lifetime of 6.7 years before needing replacement. This significantly decreases the maintenance costs with respect to a turboprop engine. With a time between overhaul (TBO) of 6000 hours<sup>4</sup> at best, a turboprop engine would require an overhaul every 3.3 years and a hot section inspection (HSI) almost every year.

### 5.1.3 Materials distribution

Although the candidates did not specify the percentage of materials used in the construction, which will be better defined in WP3, the following distribution has been assumed following the state-of-the-art:

Table 56: Assumed material distribution for all UNIFIER 10 candidate designs.

Aircraft	Material	%	$f_{mat} \text{ ref.}$	$f_{mat} \text{ partial}$	$f_{mat} \text{ total}$
UNIFIER19 Candidates	Aluminium	30%	1.00	0.30	1.32
	Carbon-Epoxy	51%	1.45	0.74	
	Fiberglass/Others	7%	1.15	0.08	
	Steel	10%	1.75	0.18	
	Titanium	2%	1.45	0.03	

Where % is the percentage of each material in the entire airframe;  $f_{mat} \text{ ref}$  is the reference cost factor for each material considering current technology;  $f_{mat} \text{ partial}$  is the weighted material factor ( $\% * f_{mat} \text{ ref}$ ) of each material in this airframe; and  $f_{mat} \text{ total}$  is the resulting total material factor that is used in the manufacturing cost calculations.

<sup>4</sup> Beechcraft 1900D's Pratt & Whitney PT6A-67D has a TBO of 6000 hours and an HSI of 2000 hours. <https://www.pt6a.aero/maintenance/pt6a-tbo-hsi-service-intervals/>

Even if the percentage of materials is not exact, and the  $f_{mat\ ref}$  changes with the evolution of each technology and expertise of the manufacturer, the variations will have a rather low impact on the overall cost of the aircraft and will be good for comparative matters.

### 5.1.4 Economy parameters

Price of “green” (produced from clean energy) liquid hydrogen has reduced and shows an estimated cost by entry-into-service of 2.00 €/kg.

Salaries and wages for crew, maintenance, and engineering personnel have not been changed. The conversion rate from US dollars (\$) to euros (€), where applicable, has been kept at January 2020 values. Also, calculations requiring the addition of inflation rates (e.g., to adapt reference salaries from 2012) have been kept to estimate their cost in 2020.

## 5.2 Results

### 5.2.1 Cost comparison

The candidate designs and the Reference Turboprop (REF TP) show similar DOC values per flight, with slight differences depending mainly on the powertrain configuration and power. The flight distance is set at 350 km, and flying all at the same speed, the flight time does not give advantages to any of the candidates.

Figure 139 gives an indication of the relative cost efficiency of each design, segmented by type of cost. It can be observed that the biggest share – around 40% of the total DOC- corresponds to the capital cost (acquisition, depreciation, insurance, etc.), followed by maintenance, operation fees, and crew salaries, all slightly below 20%, and finally the fuel which accounts for 5% of the DOC.

This changes in the case of the REF TP which is cheaper to manufacture, but consumes more fuel (in kg). The capital is still the most important cost at 28%, and all the other costs slightly below 20% of the total DOC.

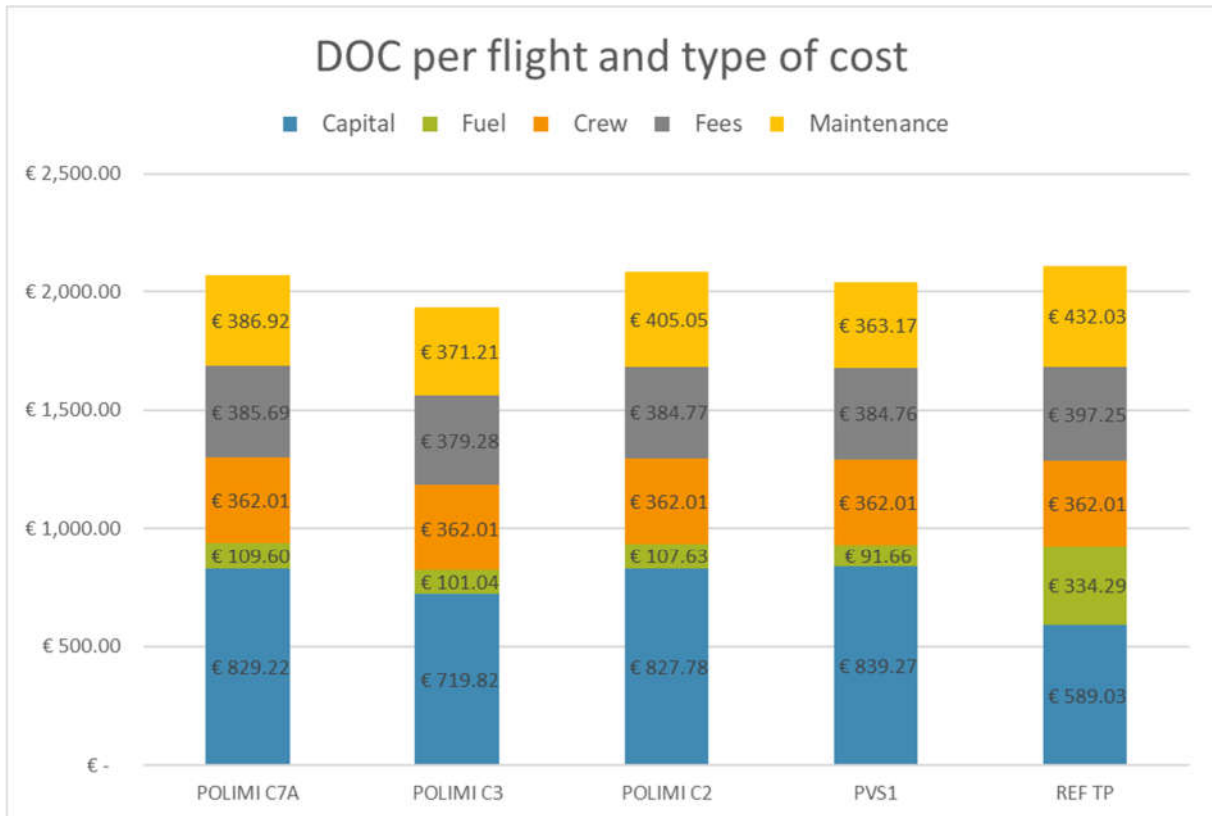


Figure 139: Total DOC per flight, detailed per type of cost.

The POLIMI C3 aircraft is the only candidate that can do the 350 km flight for less than 2000 €, while all the others slightly exceed that value.

When divided by the cabin capacity and flight distance, **the Cost per Available Seat and Kilometre (CASK) is the lowest for the C3, followed by the PVS1, then the C7A, and finally the C2. All the H2-powered candidates are more cost efficient than the Reference Turboprop designed for the UNIFIER19 mission.** The CASK values are shown in Figure 140.

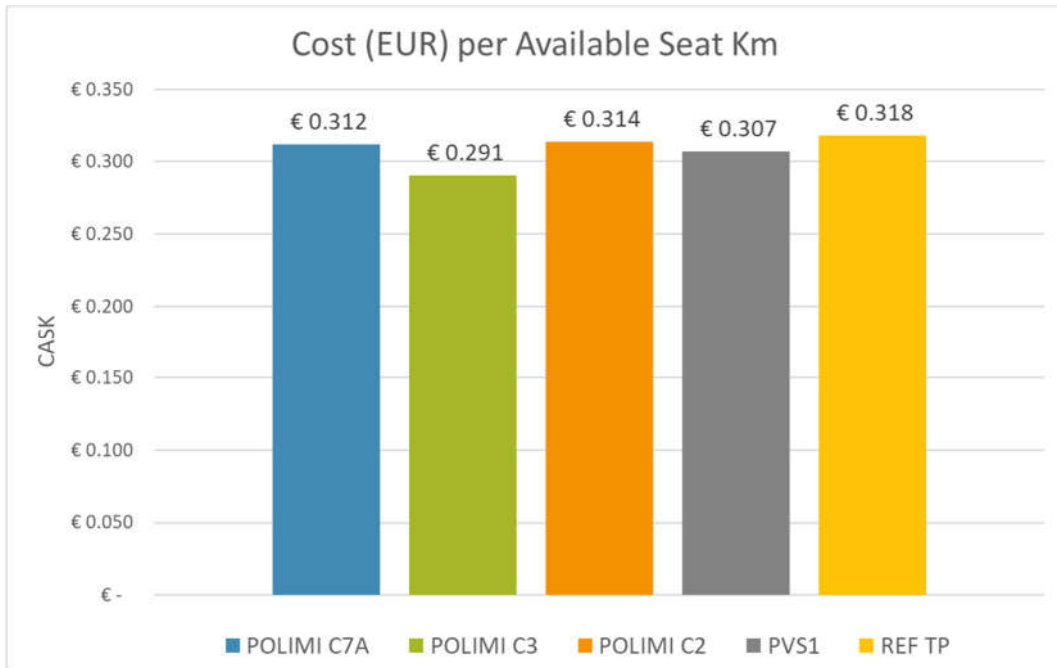


Figure 140: DOC expressed in terms of Cost per Available Seat and Kilometre.

As mentioned, in this case the aircraft acquisition price is the main factor driving the operating costs. Figure 141 clearly shows that the C3 is the least expensive of all the designs in terms of acquisition. The estimation is given for a production run of 500 aircraft, with an overhead profit margin of 35%, and 10% extra for spare parts.

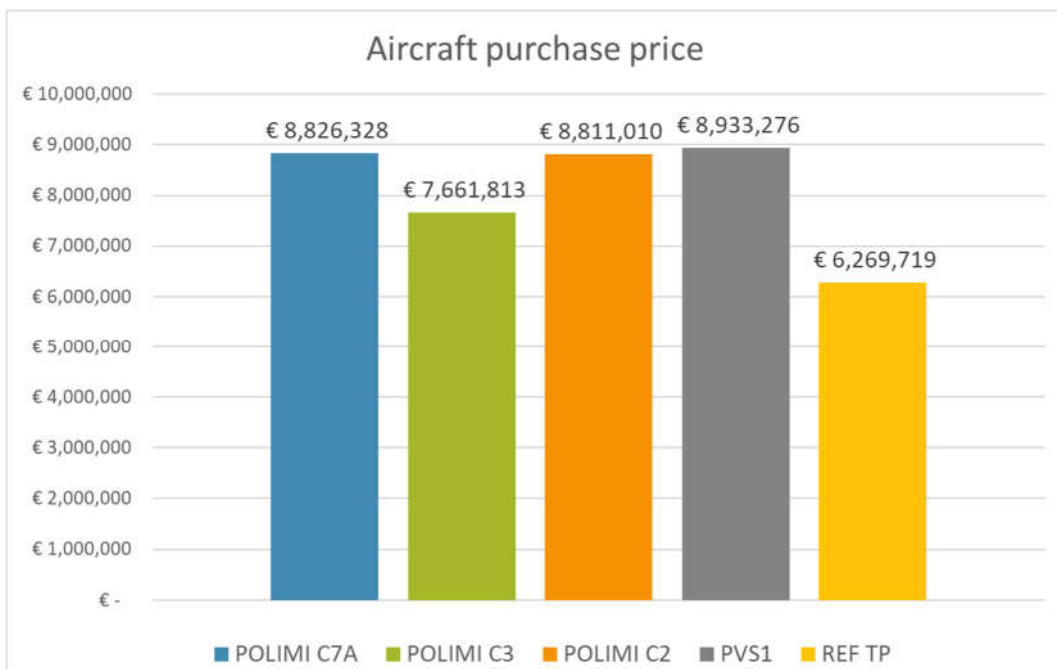


Figure 141: Aircraft purchase price for 500 units, including overhead margin and extras.

The differences in aircraft price can be explained by looking at the total engine power needed for each design. The C3 is the less powerful aircraft at 1088 kW of total engine power, compared to the C2 and C7A, each with around 2000 kW.

Despite having only 1307 kW of power, the PVS1 is the most expensive to acquire due to a more powerful fuel-cell, which is the most expensive component in terms of \$ per kW. However, PVS1 manages to keep the DOC lower than the C2 and C7A by relying highly on the DEP. The DEP, together with the fuel-cells, are the components with the longest lifetime and therefore lowest maintenance costs.

It is important to clarify that all these values are used for comparison purposes only, and the final direct operating costs will depend considerably on the aircraft operator's commercial strategy, the airports operators' infrastructure and fees, and the governments' will to support clean aviation through incentives and subsidies.

### 5.2.2 Sensitivity studies

The candidate designs were subject to sensitivity studies to evaluate which design parameters affect the operating costs more significantly. The following parameters and values were analysed (case 4 is the design baseline value):

Case number	1	2	3	4	5	6	7	8
Range [km]	280.0	308.0	332.5	350.0	367.5	392.0	420.0	
Speed [km/h]	222.3	244.5	264.1	277.3	291.8	311.3	333.5	
Payload [kg]		1900.0	2090.0	2280.0	2470.0	2660.0		
Battery specific energy [Wh/kg]		210.0	230.0	260.0	286.4	304.0	322.4	350.0
Fuel Cell specific power [W/kg]		800.0	1332.0	2130.0	2928.0	3460.0	3996.0	4800.0

The results show the DOC have an important direct dependence with the payload. Higher capacities imply higher costs, but the higher payload also means higher revenues! Therefore, the payload level will need to be carefully chosen based on market analysis and operator's needs.

The battery specific energy practically does not affect the DOC.

The rest of the parameters mainly show an inverse relation to the DOC: the higher the values, the lower the DOC.

As it was already mentioned, higher speeds would signify shorter flights and advantages in the costs based on hourly rates, such as crew costs. However, for each design there is a sweet spot beyond which the DOC increases again with speed. This can be clearly seen for the candidate C3; there is an ideal cruise speed between cases 5 and 6, at around 300 km/h (see Figure 142).

Longer flight distances are also a factor that reduces the DOC. More time spent in cruise require lower fuel consumption and airport fees spread throughout a longer time. The final value will depend on the market needs.

An important factor is the fuel cell specific power. Low specific powers will greatly increase weight, power and therefore operating costs. As technology evolves, the DOC related to the fuel cell will improve.

Additionally, it is important to note that the cost of each of these technologies (battery, fuel cell, motors, etc.) will probably have a far greater impact on DOC than the performance of the powertrain itself.

Sensitivity study – Configuration C3

C3	1	2	3	4	5	6	7	8
Range [km]	0.310	0.301	0.295	0.291	0.287	0.283	0.280	
Speed [km/h]	0.311	0.299	0.293	0.291	0.289	0.289	0.293	
Payload [kg]		0.267	0.279	0.291	0.303	0.314		
Battery specific energy [Wh/kg]		0.290	0.290	0.291	0.291	0.292	0.292	0.293
Fuel Cell specific power [W/kg]		0.333	0.304	0.291	0.285	0.283	0.282	0.280

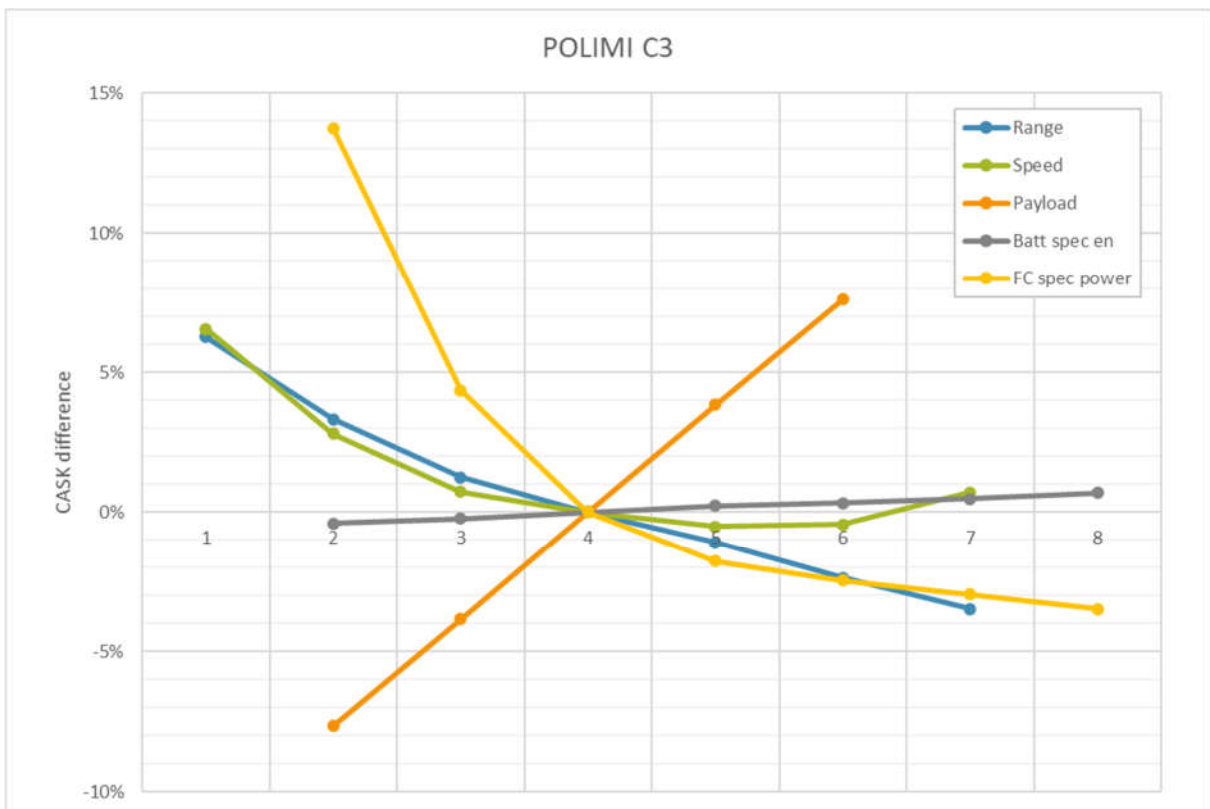


Figure 142: Sensitivity study for C3, in percentages from the baseline DOC.

Sensitivity study – Configuration C7A

C7A	1	2	3	4	5	6	7	8
Range [km]	0.331	0.324	0.316	0.312	0.308	0.304	0.301	
Speed [km/h]	0.326	0.317	0.313	0.312	0.308	0.303	0.299	
Payload [kg]		0.287	0.299	0.312	0.324	0.337		
Battery specific energy [Wh/kg]		0.311	0.311	0.312	0.312	0.313	0.313	0.314
Fuel Cell specific power [W/kg]		0.362	0.327	0.312	0.306	0.303	0.302	0.299

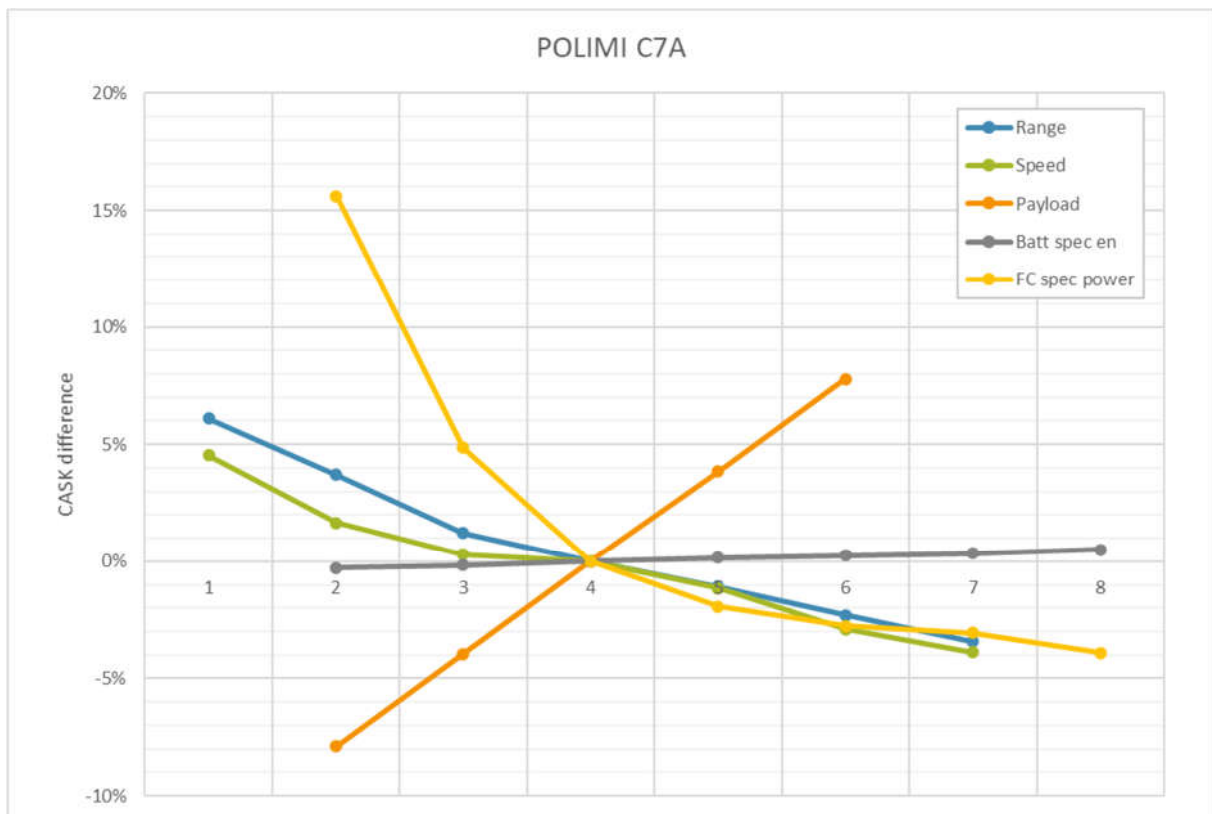


Figure 143: Sensitivity study for C7A, in percentages from the baseline DOC.



Sensitivity study – Configuration C2

C2	1	2	3	4	5	6	7	8
Range [km]	0.333	0.326	0.318	0.314	0.310	0.307	0.303	
Speed [km/h]	0.328	0.319	0.315	0.314	0.310	0.305	0.301	
Payload [kg]		0.289	0.301	0.314	0.326	0.339		
Battery specific energy [Wh/kg]		0.313	0.313	0.314	0.314	0.315	0.315	0.316
Fuel Cell specific power [W/kg]		0.364	0.329	0.314	0.308	0.305	0.304	0.301

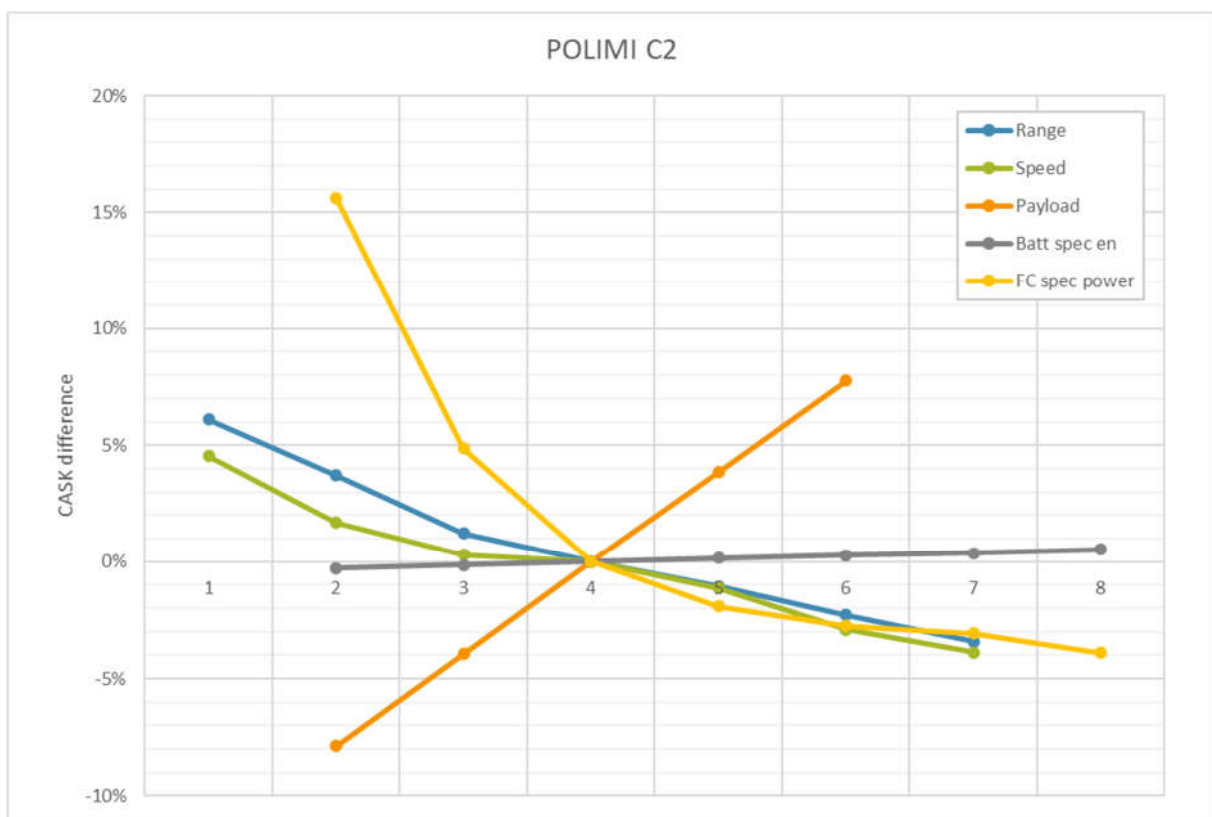


Figure 144: Sensitivity study for C2, in percentages from the baseline DOC.

Sensitivity study – Configuration PVS1

PVS1	1	2	3	4	5	6	7	8
Range [km]	0.325	0.316	0.310	0.307	0.304	0.301	0.298	
Speed [km/h]	0.346	0.327	0.314	0.307	0.300	0.292	0.285	
Payload [kg]		0.286	0.296	0.307	0.318	0.330		
Battery specific energy [Wh/kg]		0.314	0.311	0.307	0.306	0.306	0.306	0.307
Fuel Cell specific power [W/kg]		0.366	0.315	0.307	0.301	0.298	0.297	0.298

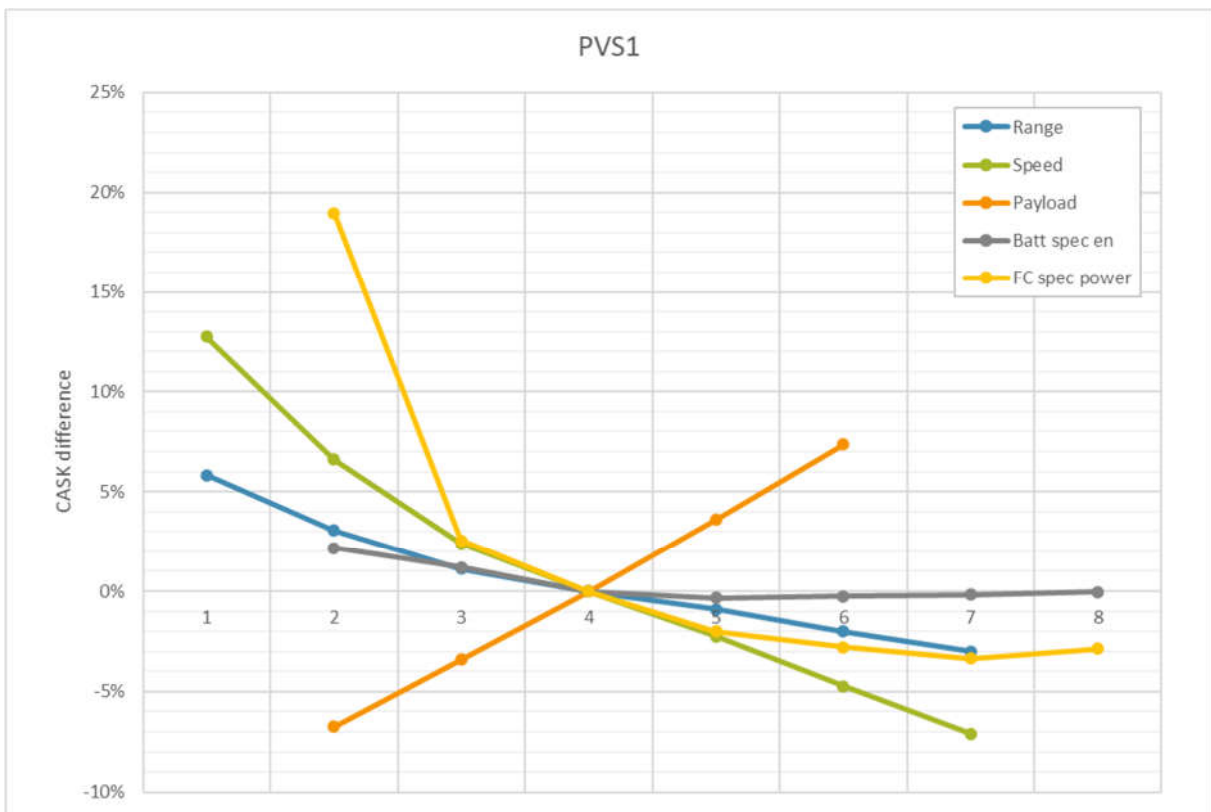


Figure 145: Sensitivity study for PVS1, in percentages from the baseline DOC.

## 6 Gaseous Emissions

### 6.1 Approach

In this section, the evaluation of the gaseous emissions is discussed. The methodology developed in Task T1.4 lies at the basis of this evaluation. As the UNIFIER19 selected candidates are all based on a fuel-cell hybrid-electric powertrain using hydrogen, only water vapour is created as the result of the electric power production process. Therefore, any carbon and nitrogen oxides are null.

In order to provide an estimation of the savings in chemical pollution allowed by the UNIFIER19 zero-emission solutions, the methodology is applied to a reference conventionally powered aircraft devised by POLIMI.

### 6.2 Reference aircraft

A reference aircraft has been defined for the present task, trying to match all the UNIFIER19 TLAR with a conventional hydrocarbon fuel-burning powertrain. To this end, a turboprop aircraft was sized using HYPERION, under the same hypothesis for technology maturity adopted for the candidate configurations described in Section 6., i.e. 2020 technology level.

As the full TLAR could not be matched without exceeding the CS-23 MTOM limitations, the multi-hop requirement was changed and a single-hop mission was defined, with a range of 1700 km. In fact, this value is the maximum that – with all other requirements unchanged – allows to comply with the MTOM certification limit. We remark that this amounts to a significant relaxation in the required mission range, since the UNIFIER19 candidate solutions provide a much larger value with their six hops, each of 350 km, as the corresponding single-hop range clearly exceeds 2100 km.

Table 57 shows the main specifications of the conventionally powered reference aircraft, termed CO.

Table 57 Conventionally powered reference aircraft main specifications.

Description	Value	Units
Takeoff Mass	8,733	kg
Wing Loading	1,945.7	N/m <sup>2</sup>
Power Loading	45.9	N/kW
Total Range	1,600.4	km
Total Range + Diversion	1,701.7	km
Wing Surface	44.02	m <sup>2</sup>
Wingspan	19.9	m
Drag Polar	$CD = 0.0290 + 0.0442 CL^2$	
Peak Power	1,866.31	kW
Takeoff Power	1,866.31	kW
High speed cruise	662.58	kW
PGS Power	1,866.31	kW
Average ESFC	0.0915	mg/s/W
PGS Weight	876.2	kg
Time to Climb	3.3	min

<b>Cruise Time</b>	335.3	min
<b>Time to Descent</b>	7.2	min
<b>Loiter Time</b>	0	min
<b>Total Flight Time</b>	419.32	min
<b>Empty Weight</b>	4,904.1	kg
<b>Payload + Crew Weight</b>	2,380	kg
<b>Battery Weight</b>	0.02	kg
<b>Fuel Weight</b>	1,448.59	kg
<b>Total Takeoff Distance</b>	800	m
<b>Landing Distance</b>	800	m
<b>High speed cruise EAS</b>	72.74	m/s
<b>High speed cruise altitude</b>	1,219.2	m
<b>Max ROC at sea level</b>	6.79	m/s
<b>Range</b>	1,701.71	km
<b>Payload</b>	2280	kg
<b>Cruise altitude</b>	1,219.2	m
<b>Cruise EAS</b>	72.74	m/s
<b>Hybrid Transition Altitude</b>	0	m
<b>BATTERY PARAMETERS</b>	0	0
<b>Battery Specific Power</b>	100,000	kW/kg
<b>Battery Specific Energy</b>	100,000	kWh/kg

Figure 146 depicts the Sizing Matrix Plot for this solution, which completely matches the POLIMI UNIFIER19 candidates, having assumed the same point and field performance requirements.

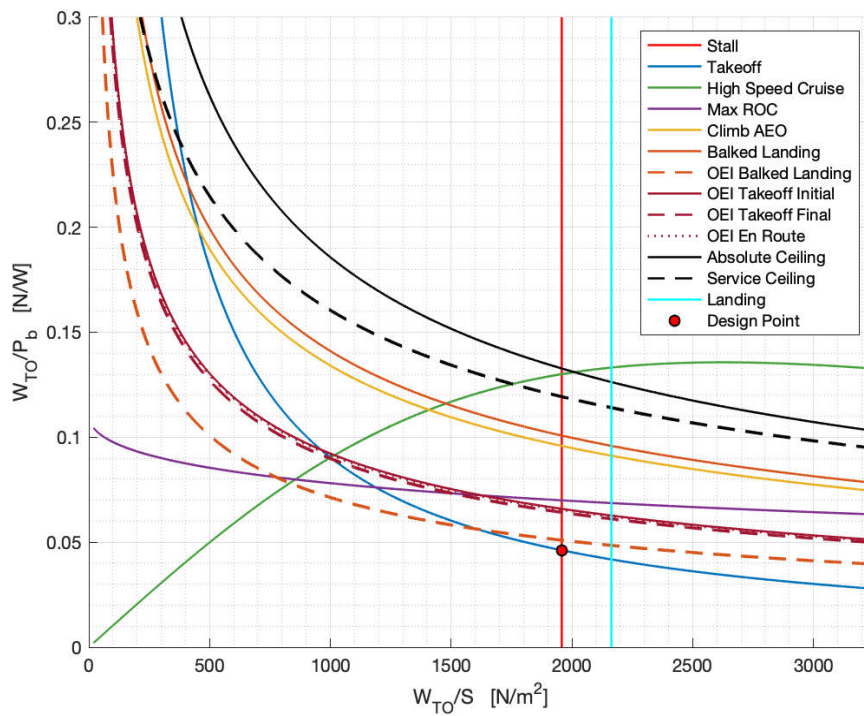


Figure 146 Conventionally powered reference aircraft sizing matrix plot.

Figure 147 provides the mass breakdown, while Figure 148 and Figure 149 show the time histories of the energy and power quantities during the sizing mission.

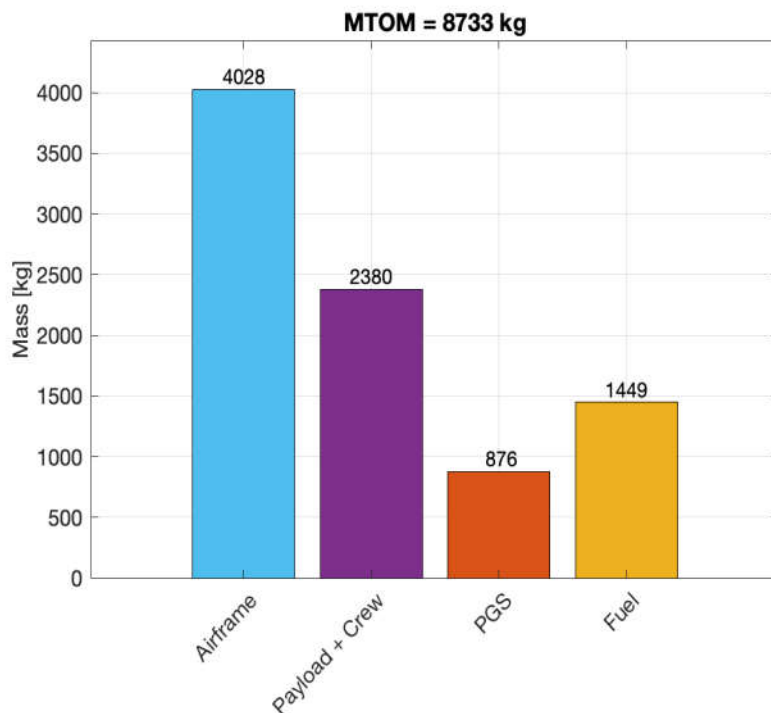


Figure 147 Conventionally powered reference aircraft mass breakdown.

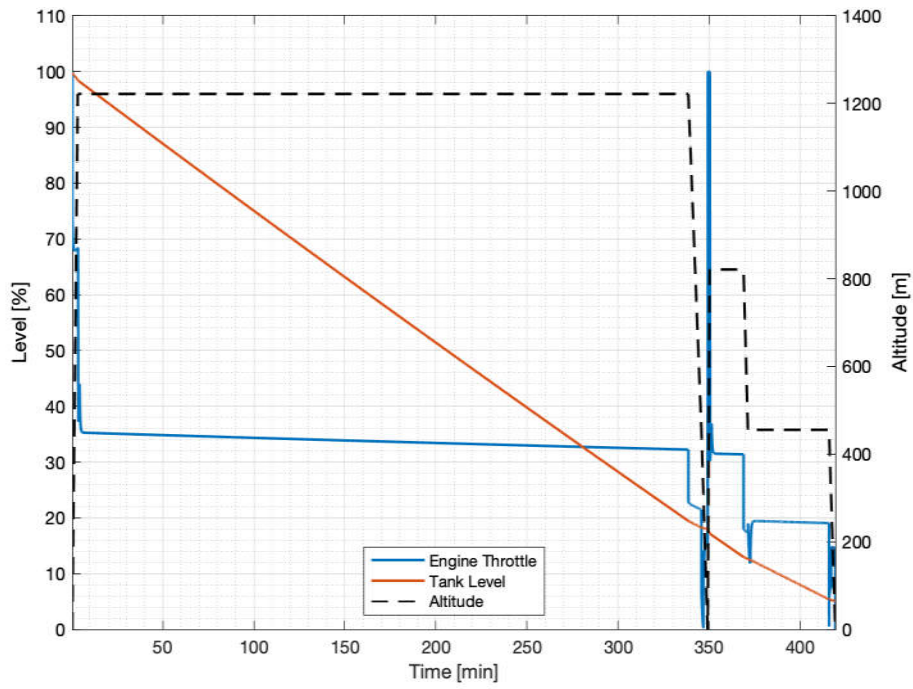


Figure 148 Conventionally powered reference aircraft sizing mission simulation: altitude profile (black dashed), engine throttle (blue) and fuel tank level (red).

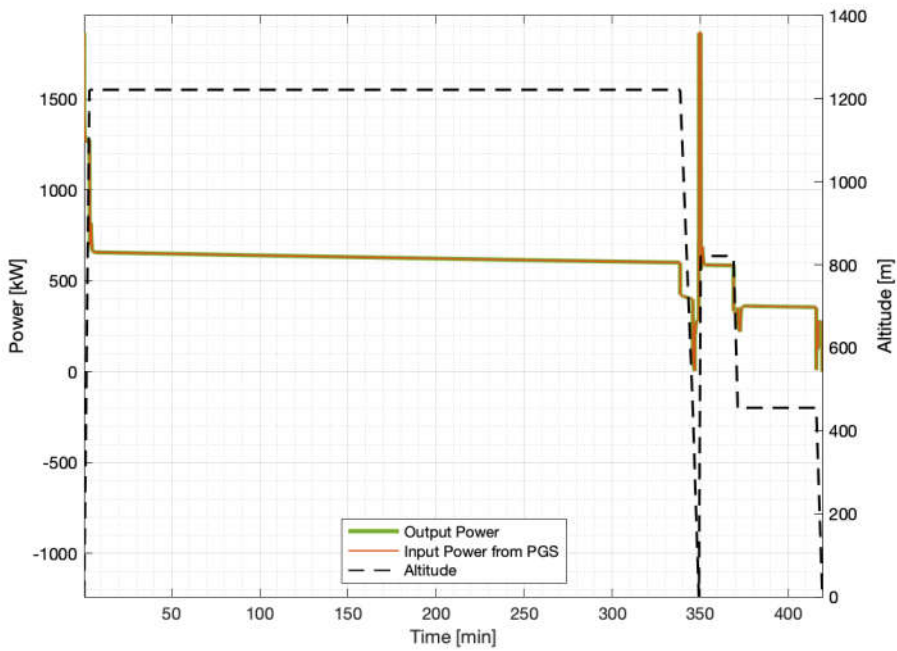


Figure 149 Conventionally powered reference aircraft sizing mission simulation: altitude profile (black dashed), electric motor input power (red) and output power (green).

### 6.3 Gaseous emission estimation methodology and results

In this section, the evaluation of the gaseous emissions is discussed. At the basis of this evaluation stands the methodology developed in task T1.4. As the selected candidates are all based on hybrid-electric technology, the only aircraft that needs to be evaluated in task T2.1 is the conventional reference aircraft using a fuel-burning engine.

The reference mission includes:

- Take-off segment that takes 16.3 seconds at full throttle
- (initial) Climb segment up to 1200m altitude
- Enroute segment that includes final climb, cruise and initial descend
- Approach phase from 1200m till touchdown.
- Taxi phase for the duration of 13 minutes at 7% throttle.

In the conceptual design loops, the flight mechanics of these segments are solved. As part of these calculations, the engine performance is modelled using a conceptual level approximation. Therefore, for each moment in time the fuel flow is known. The relationship between fuel flow and the emission index of NOx is given by the relationship in Figure 150

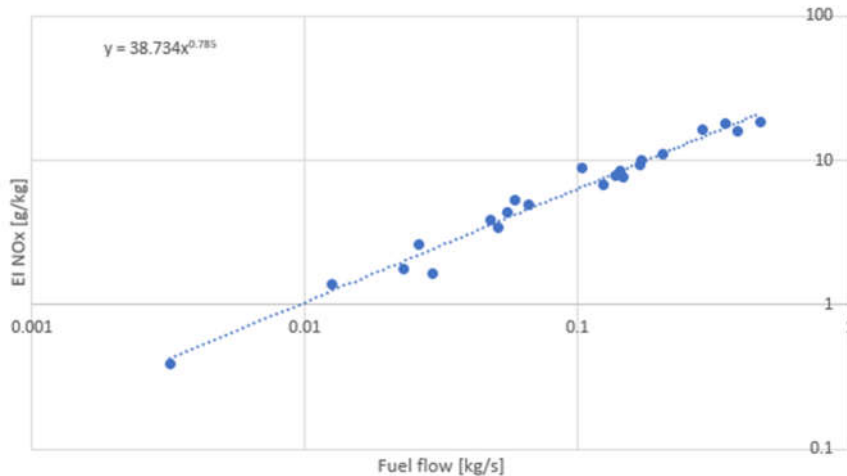


Figure 150 NOx emissions of turbine engines as a function of fuel flow

The resulting figures of the **gaseous emissions per passenger per km** are listed in the Table 58.

Table 58 Gaseous emissions of the conventional reference aircraft per passenger kilometer

Phases	Fuel burn	CO2	H2O	NOx
Landing, Take-Off [g/seat]	2.3	7.3	2.85	0.01
Enroute [g / seat / km]	35.9	113	44.2	0.15

## 7 Final selection

The analysis of the candidate design solutions described in Section 6 allowed the consortium to draw a decision concerning the configuration to be chosen as the best one for maturation in the preliminary design process to be carried out in WP3.

Indeed, the characteristics of the candidate solutions span a wide array of design options, including canard and traditional aft-tail arrangement, variable-incidence wing (VIW), tail-cone propeller (TCP), tail-cone ducted fan, distributed electric propulsion (DEP), as well as other elements. Notwithstanding such large differences in the candidate configurations, the conceptual design process showed that all candidates are not only feasible, but not much different in terms of achieved flight and field performance. They all appear capable to improve on conventionally powered solutions in terms of range, thanks to the overall higher energy efficiency of the LH2 powertrain, and no special worries arise in relation to the capability to satisfy the mass constraints imposed by the CS-23 requirements.

For this starting point, attention was focused on their foreseen environmental impact, cost and marketability. With respect to noise emissions, the main results are found in Figure 147, which shows generally good performance, except for the case of configuration C3. Indeed, configuration C3 is the worst, being the only one for which noise at take-off exceeds that of a conventionally arranged, concentrated propulsion competitor (REF). This is due to the use of a TCP only, without any split of the installed power with the adoption of wing-located DEP. This was considered an important drawback of configuration C3.

In terms of costs, an important result expressed in Section 8.2.1 is the general improvement in DOC with respect to the reference conventionally powered competitor. This was not at all to be taken for granted, given the degree of innovation considered in the present project and is considered to be a very promising and motivating result. It is seen that the candidate configurations do not differ much in terms of expected DOC, although configuration C3 stands out with the lower value, due to the absence of DEP. While this is an important element, it must be considered that the costs associated to production, maintenance and operation related to the VIW are necessarily uncertain due to the inherent novelty of this design option. For this reason, the cost advantage is not considered enough to compensate the noise drawback. This is the main reason for discarding configuration C3, compared to the others.

Another important element of choice is related to the relative difficulty in harmonizing the longitudinal trim and stability characteristics of canard configurations (C3, C2, PVS1) with respect to traditional tail-aft ones (C7A). Indeed, the canard configurations typically impose center-of-gravity travel restrictions which, in addition to difficulties in design, translate into lower flexibility in loading and operating the aircraft. As the general comparison between the candidates does not provide any striking element in favour of canard configurations, the above considerations were taken as a reason for preferring C7A over the competitors.

However, C7A (as well as C3 and C2) was preliminarily sized with a relatively conservative assumption of a typical wing aspect ratio of 9, which is not necessarily the best in taking advantage of the DEP. On the other hand, PVS1 was designed more aggressively, assuming an aspect ratio of 14, which appears to be more capable to take advantage of the presence of DEP, with a possible optimization of cruise aerodynamic performance without low-speed drawbacks. Therefore, the C7A solutions was resized with an aspect ratio of 14 without changes in the design requirements, showing negligible differences in MTOM



and mass breakdown. This motivates the choice of a wing optimized C7A solution for the subsequent phase of the UNIFIER19 project.

In the first phases of WP3, this solution shall be further analysed not only from the point of view of wing aerodynamics and propulsive interactions, but also with respect to the detailed propulsive configurations, seeking the best trade-off between the C7A approach, which provides a DEP layout in which all EMs and propellers are the same, including the wing tip ones, and are not operate in cruise, and the PVS1 approach, in which the wing tip propellers are operated in cruise, mainly to reduce the power load on the main tail propeller.

## 8 Reply to M12 Assessment Report Comments and Recommendations

One-year review has been performed and this is how we tackled the recommendations and comments, received in the review:

- a) **Recommendation:** The reference A/C is not well defined at this stage. Similarly, a comparison with CS2 SAT green A/C is missing. Recovery actions need to be implemented to measure the project ambition against a well-defined reference A/C.  
**Reply:** Existing, state-of-the-art aircraft are not optimised for UNIFIER19 specific mission requirements (multi-hops) and thus not suitable to be a well-defined reference aircraft. Therefore, we will define our own reference aircraft, a conventionally powered (i.e. turboprop) aircraft that comes closer to our design solutions, sized according to the following global requirements:
- state-of-the-art propulsion / aerodynamics / structural characteristics
  - CS-23 and operational regulation compliance (not only MTOW, but also diversion, loiter, etc.)
  - same performance requirements (point performance, field length) as UNIFIER19 or satisfy them as much as possible (number of hops)
- b) **Recommendation:** Forecast in terms of environmental benefits is not clearly presented. Explanations on the assumptions made needs to be presented.  
**Reply:** Liquid hydrogen fuel-cell system gaseous emissions consist of water vapours only. Therefore, CO<sub>2</sub> and NO<sub>x</sub> emission reduction will be 100%. Due to the use of distributed electric propulsion, we also anticipate a 10dB noise emission reduction (as per standard certification measurement procedure).
- c) **Recommendation:** Different design approaches are ongoing; Methodologies for the multi-disciplinary optimization loop need to be presented with explanation of the different weight assigned to the different objectives.  
**Reply:** the optimization loop methodologies and selection of winning configuration based on emission/cost metrics will be presented in deliverable D2.1
- d) **Recommendation:** Assumption made for integration of technology at A/C level needs to be better highlighted.  
**Reply:** Technology assumptions for integration at A/C level will be highlighted in deliverable D2.1.
- e) **Recommendation:** At the end of the first year, few dissemination actions have been implemented. EU project portal needs to be updated accordingly.  
**Reply:** Dissemination actions in EU project portal shall be updated.

## 9 References

- Ahuja, V., & Hartfield, R. (2016). Aerodynamic loads over arbitrary bodies by method of integrated. *Journal of Aircraft*, 1719.
- Ashby, D., Dudley, M., Iguchi, S., & Browne, L. K. (1999). *Potential flow theory and operation guide for the panel code PMARC*. NASA.
- Conway, J. (1995). Analytical solutions for the actuator disk with variable radial distribution of load. *Journal of Fluid Mechanics*, 327.
- Curle, N. (1967). A twoparameter method for calculating the twodimensional incompressible laminar boundary layer. *The Aeronautical Journal*, 117.
- Dungen, N. v. (2017). *Synthesis of an Aircraft Featuring a Ducted-Fan Propulsive Empennage*, Master Thesis.
- M, D., & H, Y. (2005). *Axisymmetric Analysis and Design of Ducted Rotors*. Retrieved from <http://web.mit.edu: http://web.mit.edu/drela/Public/web/dfdc/DFDCtheory12-31.pdf>
- M., D. (2005). *DFDC*. Retrieved from [https://web.mit.edu/drela/Public/web/dfdc/](http://web.mit.edu: https://web.mit.edu/drela/Public/web/dfdc/)
- M., D., & H., Y. (2003). *xrotor*. Retrieved from [http://web.mit.edu: http://web.mit.edu/drela/Public/web/xrotor/xrotor\\_doc.txt](http://web.mit.edu: http://web.mit.edu/drela/Public/web/xrotor/xrotor_doc.txt)
- M., N. (2010). *Fundamentals of Aircraft and Airship Design*.
- McDonald, R. A. (2016). Advanced Modeling in OpenVSP. *16th AIAA Aviation Technology, Integration, and Operations Conference*.
- Michael D. Patterson, \*. J. (2016). High-Lift Propeller System Configuration Selection for NASA's SCEPTOR Distributed Electric Propulsion Flight Demonstrator.
- Raymer, D. P. (2018). *Aircraft Design: A Conceptual Approach* (6th ed.). Washington, D.C., USA: AIAA, Inc.
- Soikkeli, J. (2020). Vertical Tail Reduction Through Differential Thrust: An Initial Assessment of Aero-Propulsive Effects on LateralDirectional Stability and Control in Engine Inoperative Conditions. *Master Thesis*. TU Delft.



UNIFIER19 COMMUNITY FRIENDLY MINILINER

**UNIFIER19**  
COMMUNITY FRIENDLY MINILINER

Imagine a new way to travel,...  
no noise,...  
no emissions,...  
**just flying.**

**MAIN SPECIFICATIONS**

Payload	19 pax (2280 kg)
Powertrain	fuel-cell hybrid
Fuel	liquid hydrogen
Emissions	zero
Runway type	grass, tarmac
Runway length	800 m
Take-off noise	more than 3 times lower than a turboprop aircraft at equal performance
Climb angle	7 degrees
Cruise speed	150 kts
Typical trip	350 km
Total range	over 2000 km



Turn hours of car drive into a short hop flight from a



"door step" airfield...

...as easy as taking a bus.

Four competing candidates have been downselected for the final UNIFIER19 configuration

CONCEPT C3

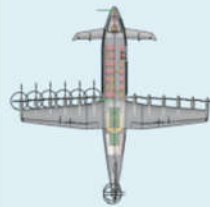


CONCEPT C7A

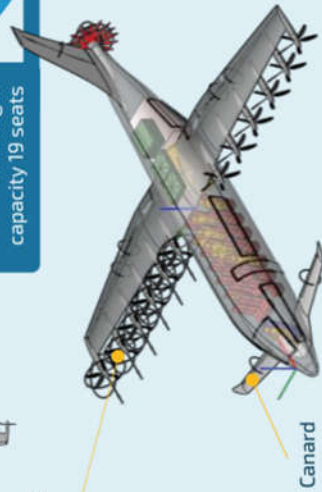


Liquid hydrogen electric power system  
Only emission - pure water

Innovative configuration space exploration  
High efficiency fuel cell technology



CONCEPT C2



Distributed electric propulsion



CONCEPT PVS1



Distributed Electric Propulsion

Futuristic look  
Passenger capacity 19 seats

Ducted fan propulsion

Distributed electric propulsion